NASA CR-54327

Thermo Electron Engineering Corporation, 85 First Avenue, Waltham, Massachusetts 02154

FINAL REPORT
FOR
SURFACE AND ADSORBATE STUDIES

March 25, 1963, to March 25, 1964

by

S. S. Kitrilakis
D. Lieb
L. van Someren
J. H. Weinstein

N66 19482

Report No. TE 19-65
Contract No. NAS 3-2539

Technical Management
NASA-Lewis Research Center
Nuclear Power Technology Branch
Gerald R. Brendel

Approved by: S. Kitrilakis
S. S. Kitrilakis
Research Manager

TABLE OF CONTENTS

Chapter		Page
I	INTRODUCTION	I-1
II	SUMMARY AND CONCLUSIONS	II-1
III	THE THERMIONIC SCANNING DEVICE	III-1
	A. Principle of Operation	III-1
	B. Test Vehicle Design	III-2
	C. Deflection System	III-4
	SCANNER REFERENCES	III-6
IV	PHOTOELECTRIC SCANNING DEVICE	IV-1
	A. Principle of Operation	IV-1
	B. Test Vehicle Design	IV-2
	C. Deflection System	IV-3
	D. Signal Circuits	IV-4
V	TEST PROCEDURES AND INSTRUMENTATION	V-1
	A. Display System	V-1
	B. Heater Controls	V-2
	C. Output Equipment	V-2
	D. Outgassing and Charging	V-4
	E. Thermionic Scanner	V-5
	F. Photoelectric Scanner	V-9
	G. General Procedure	V-10

TABLE OF CONTENTS (continued)

Chapter		Page
VI	EXPERIMENTAL RESULTS	VI-1
	A. General	VI-1
	B. Methods of Data Analysis	VI-1
	Thermionic Scanner Typical Calculation	VI-2
	Photoelectric Scanner Typical Calculation	VI-2
	Distributions of Work Function Typical Calculation	VI-7
	C. Data Analysis	VI-9
	Photoelectric Data	VI-9
	Thermionic Data	VI-11
	Tungsten	VI-11
	Molybdenum	VI-13
	D. Interrelation of Emission Data and Metallurgy	VI-16
VII	NON-EQUILIBRIUM EFFECTS	VII-1
	A. General	VII-1
	B. Induction Time Phenomena	VII-2
	C. Short Term Effects	VII-3
VIII	METALLURGICAL ASPECTS OF THE PROGRAM	VIII-1
	Introduction	VIII-1
	A. Preparation of Surfaces Studied	VIII-1
	Tungsten (W3)	VIII-1
	Molybdenum (M1)	VIII-2
	B. Observation of Surfaces	VIII-2
	1. Tungsten	VIII-2
	2. Molybdenum	VIII-5
	C. X-Ray Analysis	VIII-7

TABLE OF CONTENTS (continued)

Page

APPENDIX A A-1

"Orientation Determination of Large Grains in Polycrystalline Mo"
by Advanced Metals Research Corporation
for Thermo Electron Engineering Corporation

APPENDIX B B-1

Original Data

APPENDIX C C-1

Wiring Diagrams for Scanner Operation

LIST OF ILLUSTRATIONS

Figure	Title	Page
II-1	Correlation of Various Surface Examination Techniques	II-5
II-2	Display Photo (No. 6), $T = 1280\,°K$, $T_R = 425\,°K$	II-6
II-3	Display Photo (No. 21), $T = 1280\,°K$, $T_R = 425\,°K$, $T_A = 520\,°K$	II-7
II-4	Summary of Work Function Variations on Tungsten and Molybdenum Surfaces	II-8
III-1	Elementary Scanner in Magnetic Field	III-7
III-2	Magnetic Scanner Test Vehicle	III-8
III-3	Magnetic Scanner Partially Assembled	III-9
III-4	Thermionic Scanner on Stand	III-10
III-5	Schematic of Thermionic Scanner Coil	III-11
III-6	Scanner under Vacuum with Coils	III-12
IV-1	Photoelectric Scanner Test Vehicle	IV-6
IV-2	Emitter Assembly (Photoelectric Scanner)	IV-7
IV-3	Shell (Photoelectric Scanner)	IV-8
IV-4	Top View (Photoelectric Scanner)	IV-9
IV-5	Photoelectric Scanner on Test Stand	IV-10
IV-6	Schematic of Photoelectric Scanner	IV-11
V-1	Block Diagram of Display System	V-12
V-2	Additive Capsule	V-13
V-3	J-V Curve	V-14
V-4	Pulse Timing	V-15
V-5	Pulse Cross Scan	V-16
V-6	Pulse Scanning Instrumentation	V-17

LIST OF ILLUSTRATIONS (continued)

Figure	Title	Page
VI-1	Typical Thermionic Scanner Display Photograph	VI-20
VI-2	Cross Scan (No. 55), $T = 1060\,°K$, $T_R = 425\,°K$, Thermionic Scanner	VI-21
VI-3	ϕ vs T/T_R, $T_R = 425\,°K$, Tungsten Surface	VI-22
VI-4	Typical Single-Line Cross Scan (Photoelectric Scanner)	VI-23
VI-5	Quantum Effect Plot	VI-24
VI-6	Xenon Lamp Spectrum	VI-25
VI-7	Integrated Xenon Lamp Spectrum	VI-26
VI-8	Relative Photocurrent vs T/T_R	VI-27
VI-9	Normalized ϕ vs T/T_R for Photoscanner	VI-28
VI-10	Work Function Distribution for Tungsten	VI-29
VI-11	Scanner Display Photograph	VI-30
VI-12	Relative Current vs T/T_R for Photoscanner	VI-31
VI-13	Relative Work Function vs T/T_R	VI-32
VI-14	Display Photo (No. 12), $T = 1280\,°K$, $T_R = 425\,°K$, $T_A = 425\,°K$	VI-33
VI-15	Display Photo (No. 19), $T = 1080\,°K$, $T_R = 425\,°K$, $T_A = 425\,°K$	VI-33
VI-16	Work Function Plots of Two Patches	VI-34
VI-17	ϕ vs T/T_R, $T_R = 425\,°K$	VI-35
VI-18	ϕ vs T/T_R, $T_R = 475\,°K$	VI-36
VI-19	Summary of Work Function Variations on Tungsten Surface	VI-37
VI-20a	Work Function Distribution for Tungsten	VI-38
VI-20b	Work Function Distribution for Tungsten	VI-39
VI-21	Overall Display of Molybdenum Emitter	VI-40
VI-22	Enlarged Display of Central Region	VI-40
VI-23	Composite Metallograph of Central Region	VI-41

LIST OF ILLUSTRATIONS (continued)

Figure	Title	Page
VI-24	Concentric Ring Pattern at High Electric Fields	VI-42
VI-25	Central Region with Increased Cesium Pressure, Showing Loss of Resolution	VI-42
VI-26	Same as VI-26 with Increased Collimating Field, Showing Improved Resolution	VI-43
VI-27	Central Region of Molybdenum Surface, Showing Resolution with High Cesium Pressure and Large Magnetic Field	VI-43
VI-28	Typical Molybdenum Test Surface Cross Scan	VI-44
VI-29	Typical High Cesium Pressure Cross Scan	VI-45
VI-30	Work Function Plot for Molybdenum Surface	VI-46
VI-31	Cross Scan Showing Collector Emission	VI-47
VI-32	Molybdenum Display Photograph with Additive Present	VI-48
VI-33	Cross Scan Showing Stray Collector Current	VI-49
VI-34	Metallograph of Local Contamination of Molybdenum Surface, 75x	VI-50
VII-1	Work Function Variation on Tungsten Surface	VII-7
VII-2	Time Effect with Additive	VII-8
VII-3	Work Function Change vs Time	VII-9
VII-4	Exponential Decay of Current	VII-10
VII-5	Desorption Time Constant vs Temperature	VII-11
VII-6	Cross Scan (No. 99), $T = 1100\,°K$, $T_R = 425\,°K$, $T_A = 520\,°K$	VII-12
VII-7	Cross Scan (No. 113), $T = 1100\,°K$, $T_R = 425\,°K$, $T_A = 520\,°K$	VII-13
VII-8	Cross Scan (No. 119), $T = 1100\,°K$, $T_R = 425\,°K$, $T_A = 520\,°K$	VII-14
VIII-1	Tungsten Test Surface (W3), Electropolished and Lightly Etched, 75x	VIII-12
VIII-2	Tungsten Test Surface (W3), Electropolished and Lightly Etched, 560x	VIII-13

LIST OF ILLUSTRATIONS (continued)

Figure	Title	Page
VIII-3	Tungsten Test Surface (W3), after Operation, 75x	VIII-14
VIII-4	Tungsten Test Surface (W3), after Operation, 560x	VIII-15
VIII-5	Molybdenum Test Surface (M1), after Outgassing, Showing Supposed Precipitate, 75x	VIII-16
VIII-6	Same as VIII-5, 310x	VIII-16
VIII-7	Molybdenum Test Surface (M1) after Operation in Photoelectric Scanner, 75x	VIII-17
VIII-8	Same as VIII-7, 310x	VIII-17
VIII-9 VIII-10	⟨110⟩ Tungsten Surface at 1084x with Green Light. A pair of photographs of an etch pit before and after firing at 2000°C for 1 hour	VIII-18
VIII-11	Electropolished ⟨100⟩ Tungsten Etched in $K_3Fe(CN)_6$ to Develop Square Etch Pits with Structure Visible on Sloping Sides, Photographed at 560x after 5 minutes at 2100°C	VIII-19
VIII-12	Electropolished ⟨100⟩ Tungsten Etched in $K_3Fe(CN)_6$, after 7 hours at 2550°C, 560x	VIII-20
VIII-13	Photograph of Tungsten Emitter before Firing, 5x	VIII-21
VIII-14	Free Energy of Formation of Molybdenum and Cesium Oxides as a Function of Temperature	VIII-22
VIII-15	Molybdenum Test Surface (M1) after Thermionic and Photoelectric Operation, 75x	VIII-23
VIII-16	Same as VIII-15, 7x	VIII-23
VIII-17	Orientation of Large Grains on Molybdenum Emitter on Unit Stereographic Triangle	VIII-24
VIII-18	Laué Back Reflection X-Ray of Grain #1, Test Surface (M1)	VIII-25
VIII-19	Laué Back Reflection X-Ray of Grain #8, Test Surface (M1)	VIII-26
VIII-20	Laué Back Reflection X-Ray of Grain #9, Test Surface (M1)	VIII-27
VIII-21	Laué Back Reflection X-Ray of Grain #10, Test Surface (M1)	VIII-28

LIST OF ILLUSTRATIONS (continued)

Figure	Title	Page
B-1	Typical Photoelectric Cross Scans Nos. PM14, PM15, PM16, PM17	B-5
B-2	Typical Thermionic Cross Scans Nos. 59, 61, 71, 95	B-9
B-3	Typical Thermionic Cross Scans Nos. 240, 250, 253, 263	B-17
C-1	Circuitry for X-Y Recording of Cross Scans using Thermionic Scanner (Includes Pulse Scanning Instrumentation)	C-3
C-2	Circuitry for X-Y Recording of Cross Scans using Photoelectric Scanner	C-4
C-3	Circuitry for Sweep Data (Display) using Thermionic Scanner	C-5
C-4	Circuitry for Sweep Data (Display) using Photoelectric Scanner	C-6

ABSTRACT

19482

The adsorption of Cs and CsF on refractory metal surfaces has been studied using a new emission scanning device. Experimental results are presented in the form of thermionic emission display photographs and point by point work function measurements. A definite correlation is shown to exist between crystal orientation and emission properties. The effect of CsF is to shift the minimum value of work function to lower surface to reservoir temperature ratio values. In transient tests, exceptionally low collector work function values were obtained.

author

CHAPTER I
INTRODUCTION

The thermionic converter has shown considerable promise as a means of energy conversion. In fact, for certain applications it appears to be the only feasible means of conversion. The usefulness of the process can be increased, however, if the emitter temperatures can be lowered and the conversion efficiencies increased. One approach to improving performance in these respects is the use of a so-called additive in the interelectrode space.

Several workers in the field have reported an enhancement of thermionic emission in the presence of cesium vapor and compounds of cesium with electro-negative elements. Langmuir[1] observed this with cesium oxide, Aamodt[2] reported on the effects of cesium fluoride, and more recently Jester[3] reported also on cesium fluoride.

Beginning in November 1962, Thermo Electron, under sponsorship by the Air Force Aero Propulsion Laboratory of the Air Force Systems Command, conducted a one-year program aimed at determining experimentally whether the lowering of the electrode work function in the presence of cesium halides could be achieved in an actual thermionic converter and whether it would result in an increase in performance for a given emitter temperature. The results of that program[4] were affirmative.

---

1. I. Langmuir, D. S. Villars, "Oxygen Films on Tungsten," JACS 53 486 (1931).
2. R. L. Aamodt, L. J. Brown, and B. D. Nichols, "Thermionic Emission from Molybdenum in Vapors of Cesium and Cesium Fluoride," Power Information Center Conference, December 6 and 7, 1961.
3. "Electron Emission of Tungsten in a Cesium Fluoride Atmosphere." AIAA Conference Paper, Paris, France, August 1963.
4. S. S. Kitrilakis and J. H. Weinstein, "Additive Converter Studies," Technical Documentary Report No. APL-TDR-64-2, USAF, January 1964.

The program reported herein was undertaken as a means of gathering more detailed information on the effects produced upon electrode surfaces by cesium plus cesium fluoride under various conditions of coverage. The scanning type of device was used, rather than a power-producing converter, so that the relationship between surface characteristics and emission characteristics could be observed. To enhance this portion of the work, one of the test surfaces used was monocrystalline tungsten. Polycrystalline molybdenum characteristic of thermionic collector surfaces was also studied.

The experimental work made use of work function scanners, which are unique in that they allow scanning to be performed on surfaces which are in equilibrium with the cesium vapor environment. Two types of scanners had been developed at Thermo Electron. One is a photoelectric scanner suitable for low temperatures, where thermionic currents are small. The other is a thermionic scanner for high surface and cesium reservoir temperatures, where thermionic currents are significant. One scanner of each type was fabricated for this program after design changes had been made to accommodate the addition of the reservoir required to contain the additives.

For each test surface, series of data in the form of photographs, cross scans and I-V curves were made at several combinations of cesium and cesium fluoride reservoir temperatures. In a number of cases key runs were repeated to check reproducibility and equilibrium. Non-equilibrium tests were also performed.

More than 250 cross scans were taken covering surface temperatures from 350°K to 1400°K, Cs reservoir temperatures from 325°K to 475°K, and additive reservoir temperatures up to 750°K. A sample group of these cross scans, as well as a sample group of emission photographs, is shown in Appendix B.

CHAPTER II
SUMMARY AND CONCLUSIONS

The ability of the thermionic photoelectric scanners to examine test surfaces on a point-by-point basis has brought out new facets of the additive behavior. Orientation of the surface grains apparently influences both the time constants in the adsorption process and the final work function obtained when equilibrium is reached. Uniform results in the application of additives require that these factors be understood and controlled. A start in this direction has been made through the study of activation energies and the effects of grain orientation on work function.

The obvious correspondence between various techniques of surface examination, shown in Figure II-1, underlines the success in the experimental treatment of the problem and engenders confidence in the results. This figure includes: (a) a photomicrograph, (b) an emission picture taken with the thermionic scanner, (c) a cross scan, and (d) a diagram of the crystal structure identifying the grains.

Specific experimental results of the program follow.

1. The presence of the additive resulted in non-uniform emission from a nominally single-crystal tungsten surface which exhibited uniform emission in the presence of cesium only. This is graphically illustrated by Figures II-2 and II-3 and documented in Chapter VI.

2. The cross-scan experiments showed that the non-uniformity over a given surface seldom exceeded 0.2 volt. (See Chapter VI.)

3. The introduction of additives causes a shift of the important work function-vs-T/T_R dependence to lower values of T/T_R. This is of extreme importance to improved converter performance. Figure II-4[1] illustrates the change. (See Chapter VI.)

4. Figure II-4 also shows evidence that the adsorption of additive on the surface is characterized by long time constants and the existence of equilibrium conditions not always easy to attain. A detailed discussion of the equilibrium problems is contained in Chapter VII.

5. The nature of emitting surfaces resulting from various thermal and chemical treatments has been defined and is discussed in Chapter VIII.

6. As clearly shown by Figure II-1, a definite relationship appears to exist between grain orientation and cesiated work function. Again, Chapters VI and VIII provide considerable discussion and experimental evidence to support this conclusion.

7. The operation of a thermionic electrode in a cesium-only environment has been thoroughly explored and documented.[2,3,4,5]

---

1. The molybdenum data in this figure was obtained under Contract AF33(657)-10130 with the Air Force Aero Propulsion Laboratory, Research & Technology Div., Air Force Systems Command, Wright-Patterson Air Force Base, Ohio (see Report No. APL-TDR-64-2).

2. S. S. Kitrilakis, M. E. Meeker and N. S. Rasor, Annual Technical Summary Report for the Thermionic Emitter Materials Research Program, 1 July 1961 through 30 June 1962, Contract NONR-3563(00), Report No. TE2-63, prepared for Office of Naval Research, Power Branch, Dept. of the Navy, Washington, D. C.

3. A. Shavit and S. S. Kitrilakis, Third Annual Technical Summary Report, "Effect of Electrode Configuration on Thermionic Converter Output Characteristics," March 1963 - March 1964, Contract AF19(604)-8453, Report No. TE7-65, prepared for Air Force Cambridge Research Laboratories, Office of Aerospace Research, Bedford, Mass.

4. N. S. Rasor, "Correlation of Emission Processes for Adsorbed Alkali Films on Metal Surfaces," J. Appl. Phys., Vol. 35, No. 9, pp. 2589-2600, Sept. 1964.

5. G. Miskolczy et al., Final Technical Report, "Emitter Crystal Structure Study," February 1964, Contract No. 950338, Report No. TE36-64, prepared for Jet Propulsion Laboratory, Pasadena, California.

The unique correlation between the surface work function ϕ, and the surface-to-cesium-reservoir temperature T/T_R has also been well documented. The use of an additive, in this case cesium fluoride, has been shown to change the nature of the correlation so that a unique relationship between ϕ and T/T_R no longer exists. This result was anticipated and is certainly logical. It was hoped that the data derived from this program would allow the nature of the additive effect to be documented sufficiently to allow a new correlation to be developed, and investigations were performed in an attempt to confirm the expectation that the ratio T/T_A would act as a parameter to establish a series of similar-shaped curves in the ϕ-vs-T/T_R plane. Unfortunately, the experimental difficulties encountered, especially obtaining equilibrium at operating conditions, prevented this goal from being realized. Considerable additional work will be required before the parametric relationship of the additive effect can be delineated.

Item 3 above defines the primary and most interesting effect of the additive from the point of view of the converter designer. Many converter applications could be more effectively met if the collector could be operated at a higher temperature, making more effective use of the heat rejection area. This would result in a less weighty converter, which is of obvious benefit to operation in spacecraft.

The observed shift of the minimum work function with respect to the value of T/T_R appears to furnish an additional degree of freedom to future converter designers, which may allow them to vary collector work function over some useful range without changing collector temperature.

Finally, the experiments have revealed that, under transient conditions, the additive can reduce the collector work function to lower values than have been maintained in the equilibrium case, and there is the possibility that further experiments will enable those low values of collector work function to be stabilized. Such a result will have a very substantial effect upon the future performance of thermionic conversion systems.

a. Photomicrograph.

b. Emission Picture from Thermionic Scanner.

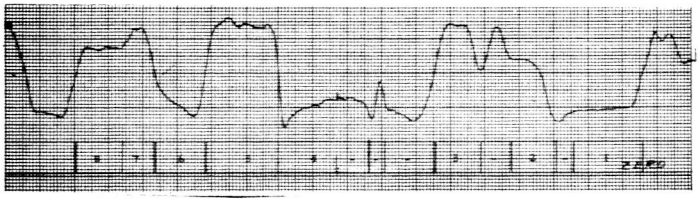

c. Cross Scan.

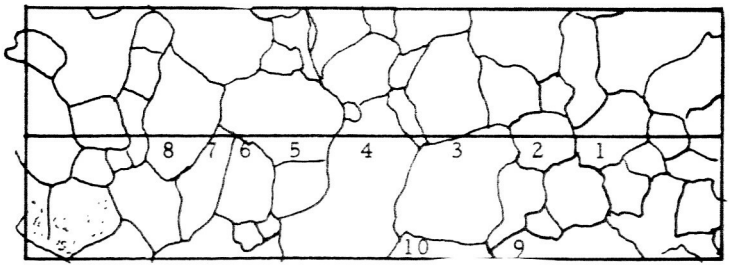

d. Diagram of Grain Structure.

Figure II-1. Correlation of Various Surface Examination Techniques.

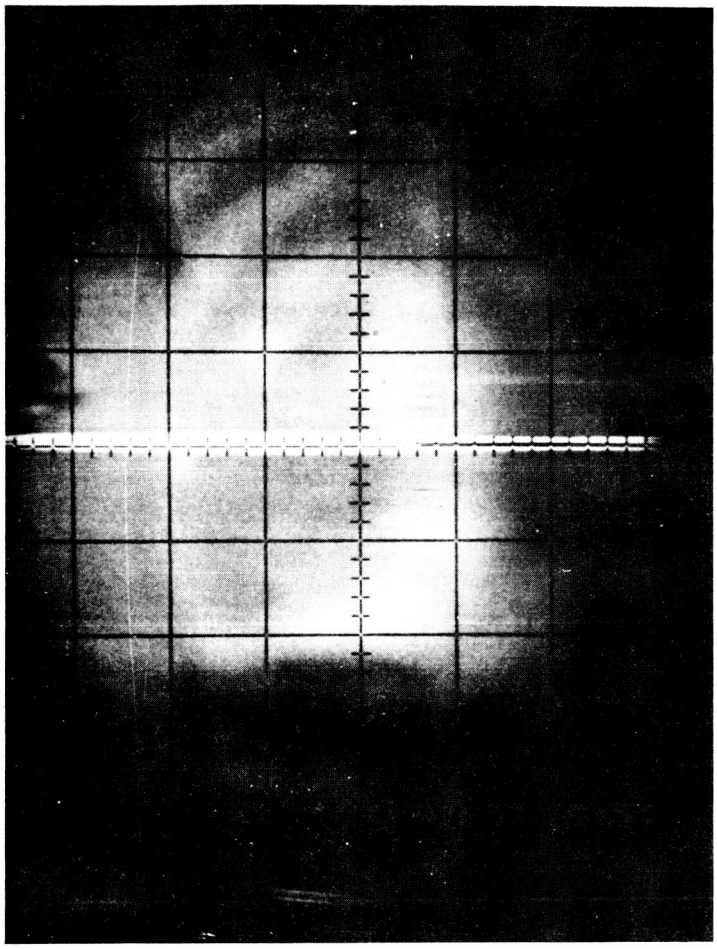

Figure II-2. Display Photo (No. 6).
$T = 1280\,°K$, $T_R = 425\,°K$

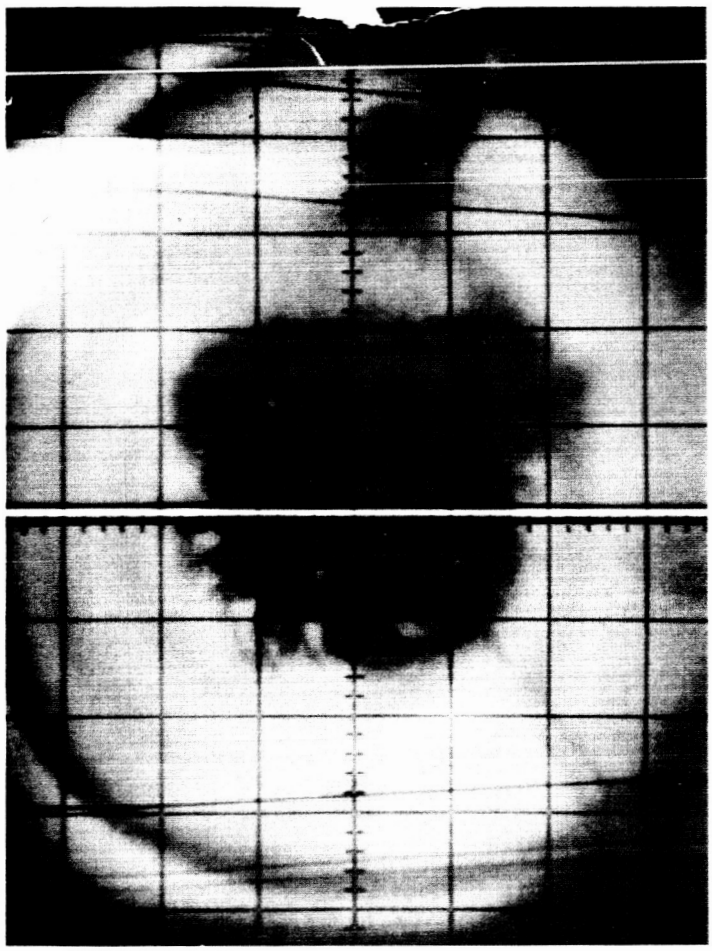

Figure II-3. Display Photo (No. 21)
$T = 1280^{\circ}K$, $T_R = 425^{\circ}K$, $T_A = 520^{\circ}K$

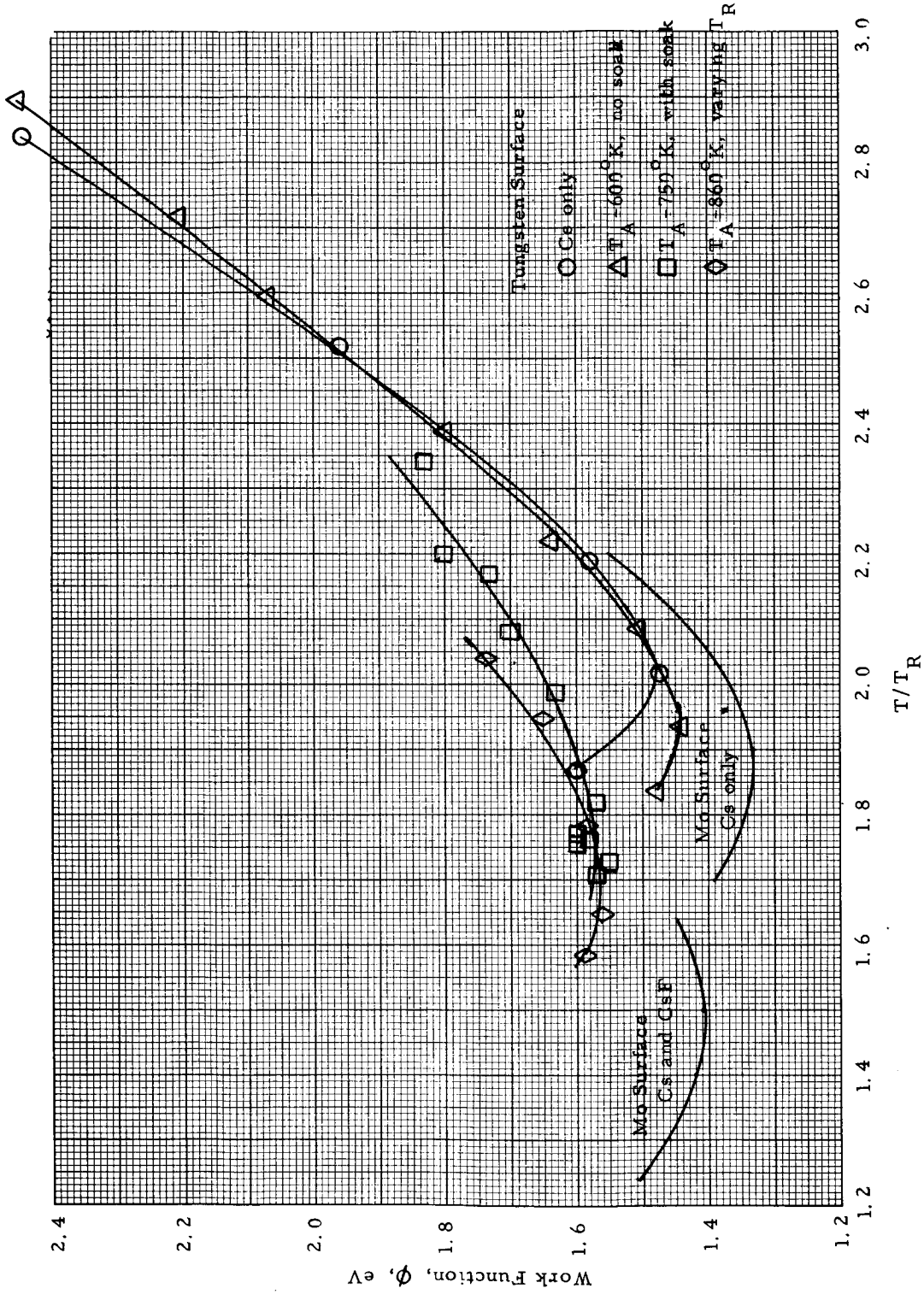

Figure II-4. Summary of Work Function Variations on Tungsten and Molybdenum Surfaces.

CHAPTER III

THE THERMIONIC SCANNING DEVICE

The thermionic scanning device uses strong magnetic fields to prevent radial flow of electrons in a converter-like structure. This, in effect, makes the device one-dimensional. Neighboring regions on the emitter surface are thus isolated from one another as far as the current flow into the plasma is concerned. Emission patterns on the surface are then reproduced at the collector and can be examined point by point. Operation with surface temperatures up to 1400°K and reservoir temperatures up to 520°K is achieved. The data is plotted against T/T_R, thereby extending its range of usefulness.

A. Principle of Operation

The elementary scanner shown in Figure III-1 releases electrons from the heated emitter, and with an applied accelerating field from emitter to collector, a glow discharge is produced in the cesium vapor. A strong magnetic field (B) in the direction parallel to the general flow will confine the electron paths to small-radius helices extending from emitter to collector. If the emitter is non-uniform, the same pattern will be present in the current reaching the collector because of the collimating effect of the magnetic field. A small diameter hole in the collector allows electrons to pass through and impinge on an auxiliary collector or probe to produce an output current. Changing the direction of the field by the addition of orthogonal fields B_x and B_y will deflect the helices so that the probe will in effect see a different portion of the emitter. In this manner the entire face of the emitter may be scanned. Surfaces to be tested are mounted as the emitter of the scanner test vehicle.

B. Test Vehicle Design

The magnetic scanner test vehicle design is shown in Figure III-2. The test surface (1), is mounted opposite the main collector (13, 14), with the surrounding space inside the shell (8) filled with cesium and additive vapor. There is a hole of approximately 3 mils diameter in piece (13) through which the scanned electrons pass to strike the probe or auxiliary collector (15). The chamber between the probe (15) and the main collector (14) is maintained at very low cesium pressure by direct cooling of the probe with water or liquid nitrogen. Any vapor passing the hole is immediately condensed and the work function of the collector remains relatively high, reducing stray emission from the heated collector to the probe. A sapphire window (17) is provided for visual observation of the discharge and the deflections.

Operating conditions in the tube are controlled by adjusting the temperature of the various elements. The test surface, mounted at the end of a thin wall spacer (3) to reduce heat losses, is heated by electron bombardment from a source filament connected to posts (30). Side emission is reduced by the action of an electrically floating shield (4). Temperature is measured either by viewing a blackbody hole in the side of the test surface through the sapphire window, or by using a thermocouple spark welded to the back of the emitter. The window may be calibrated for losses by observing a filament inserted in the vehicle with the emitter removed. Collector temperature is controlled by a balance between the power applied to the heater (27) and conduction to a water-cooled sink through rods (24). A thermocouple hole in the bottom of (14) is used to monitor the temperature. Cesium and additive pressures are controlled by adjusting the temperature of their respective reservoirs in

a manner similar to the collector heater. Vapor from the reservoir travels through tube (20) and into the chamber. The tube illustrated is the one for the additive. The cesium tube contains a small orifice which will restrict the flow of the very-low-pressure additive vapor without affecting the high pressure cesium vapor.

Leadthroughs (11) and (12) form a vacuum-tight seal while electrically isolating their various members by means of the ceramic rings (10). To prevent the condensation of vapor, the rings are thermally isolated from the cold probe (15) by the Kovar cup (22). An extra guard ring (19) is included in the lower leadthrough to aid in reducing electrical leakage to the probe. Because of the small currents involved, it is essential that the probe works into a relatively high impedance.

The test surface structure may be removed by grinding off flange (7) and removing the entire unit. The assembly may then be replaced by rewelding at flange (7).

A picture of the partially assembled test vehicle is shown in Figure III-3. On the left is shell (8) with the sapphire window mounting and flange (7) visible. The upper and lower leadthroughs as well as the collectors may be seen in the subassembly on the right. Since the probe hole piece (13) has not been mounted, the auxiliary collector is visible inside the main one. At the bottom is its Kovar cup (22) and cold sink connection.

Figure III-4 is a photograph of the complete device and mounting hardware. Visible in this figure are: the output lead (11), emitter radiator (21), body shell (31), sapphire window (4), probe connection and cooling strap (5), collector heater (6), additive reservoir (7), and the base plate (8). Thermocouples protected by ceramic tubes are provided

for measurement and control of the probe, additive and cesium reservoirs, shell, and test surface temperatures. The base plate supports the tube and contains leadthroughs for all the wires except the output lead, which is brought through a top plate to minimize the diameter of the upper section of the tube.

C. Deflection System

The magnetic fields required for collimation and deflection in the scanner are created by three sets of electrical coils oriented on orthogonal axes about the test vehicle. A schematic of this arrangement is shown in Figure III-5. Because of the defocussing effects which occur at the higher cesium pressures, large magnetic fields are required to produce good definition in this pressure range, and a compact coil and test vehicle structure is therefore necessary to counteract the very rapid fall-off of field strength with distance. The coils are wound from flattened copper tubing to provide simultaneously for water cooling and a favorable space factor. The main collimating field is generated by the tubing wound around the upper Vycor. The turns near the window have been spread to provide a clear view. Figure III-6 shows the device under vacuum with the deflection coils in place. They are potted in epoxy resin to ensure mechanical rigidity and connected in orthogonal pairs to provide a rectangular scanning pattern. Each coil is composed of two windings of flattened copper tubing, with parallel water feeds and series electrical connection. The discharge in the tube is observed through the central hole in one of these coils.

Power for the main or collimating field coil is obtained from a field rheostat-controlled, motor generator set. This source is capable of over 400 amperes. To reduce interference, the high current to this coil is

electrically isolated from the other circuits. The x deflection coils are powered from a programable dc supply, controlled with a sawtooth voltage obtained from the display system. A reversing switch is used to scan both emitter halves. About 1000 watts at 80 amperes is used to produce a maximum field of 600 gauss. Power for the y coils is obtained from the 60 cps power line through the step-down transformer. The current amplitude is controlled by a variable autotransformer in the primary. A variable phase output is provided for the display system to assure synchronization.

The fully developed magnetic scanner has performed quite well and has proven to be a most valuable tool for research in cesium vapor converters.

SCANNER REFERENCES

Reference S-1 Emitter Crystal Structure Study, Final Report on JPL Contract No. 950228, February 1964.

Reference S-2 Solar Energy Thermionic (SET) Conversion Development Program - Task III, Monthly Progress Report for November 1964, JPL Contract No. 950671.

Reference S-3 Thermionic Converter Life and Repeatability Investigation, Technical Report AFAPL-TR-65-17, Contract No. AF33(615)-1348.

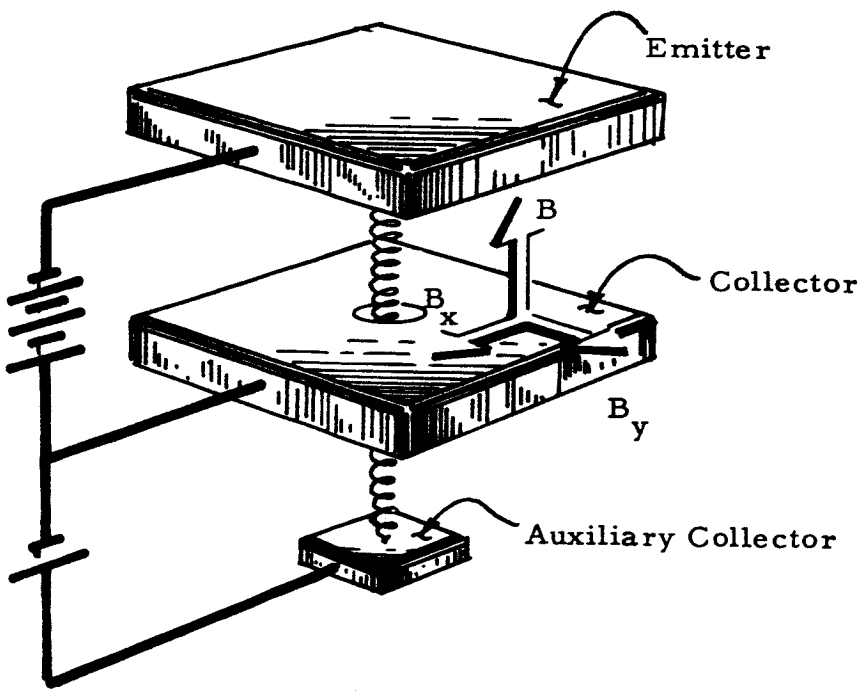

Figure III-1. Elementary Scanner in Magnetic Field

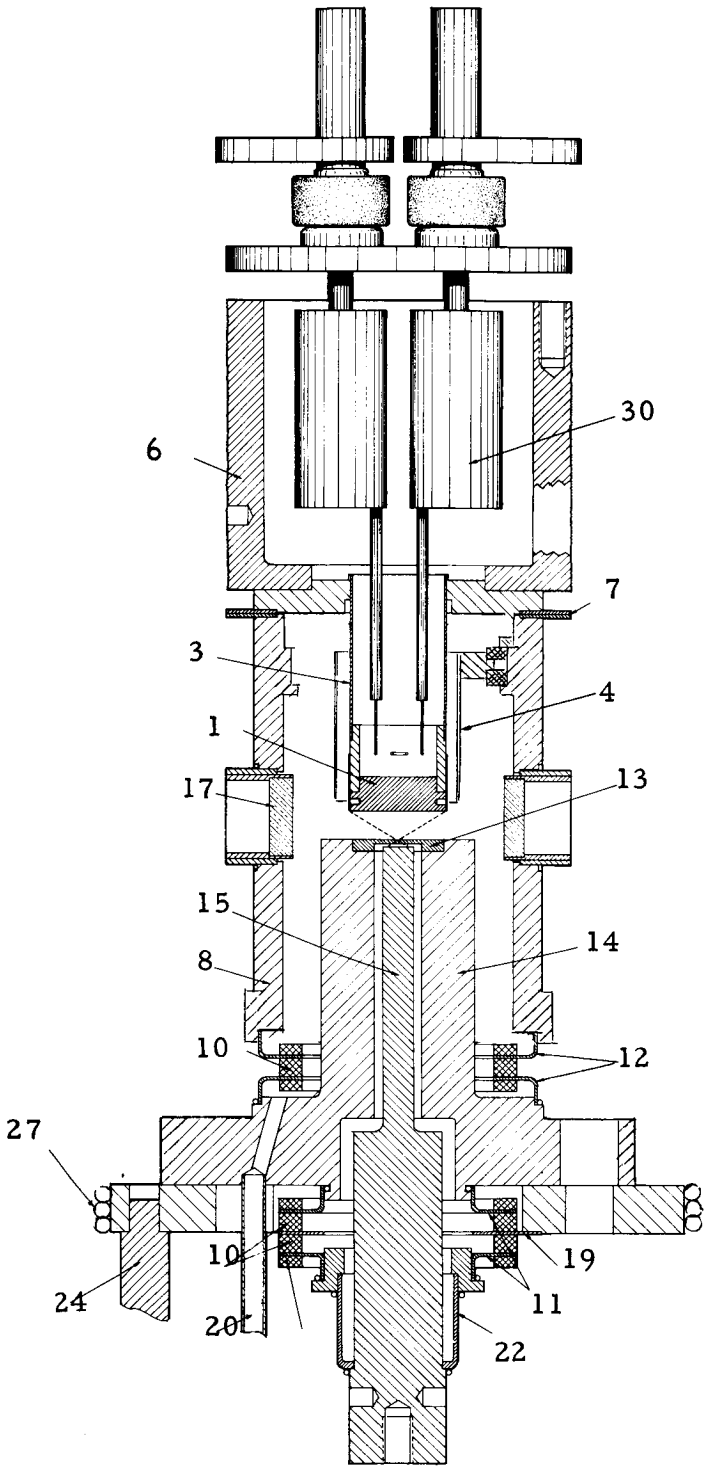

Figure III-2. Magnetic Scanner Test Vehicle

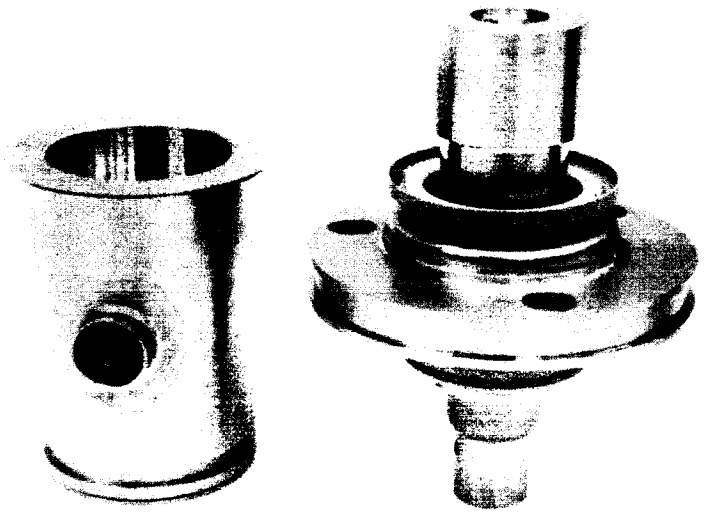

Figure III-3. Magnetic Scanner Partially Assembled

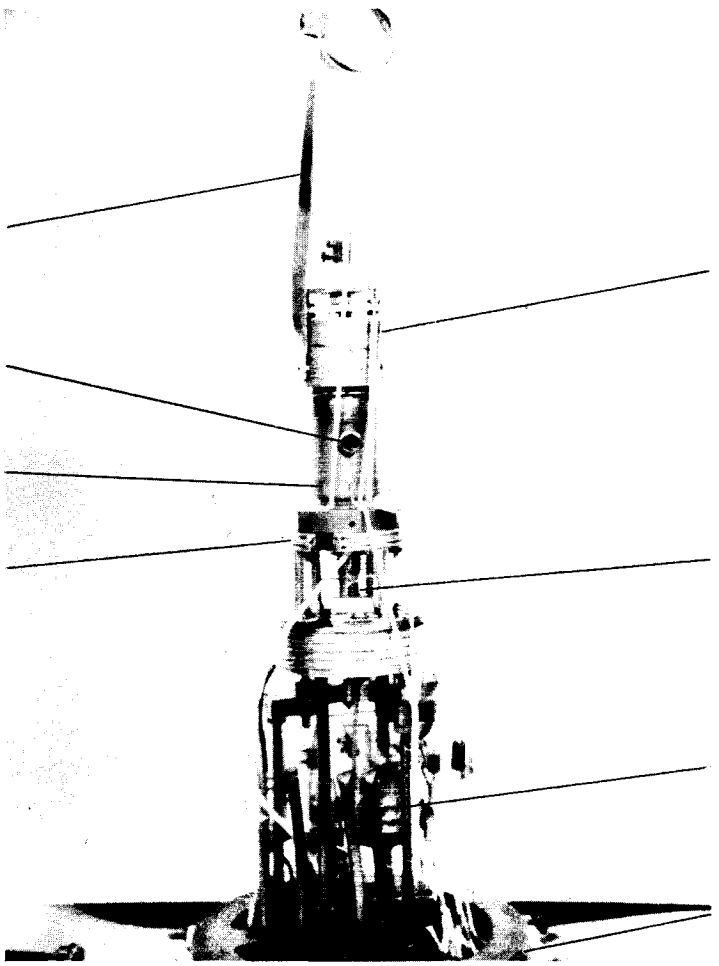

Figure III-4. Thermionic Scanner on Stand

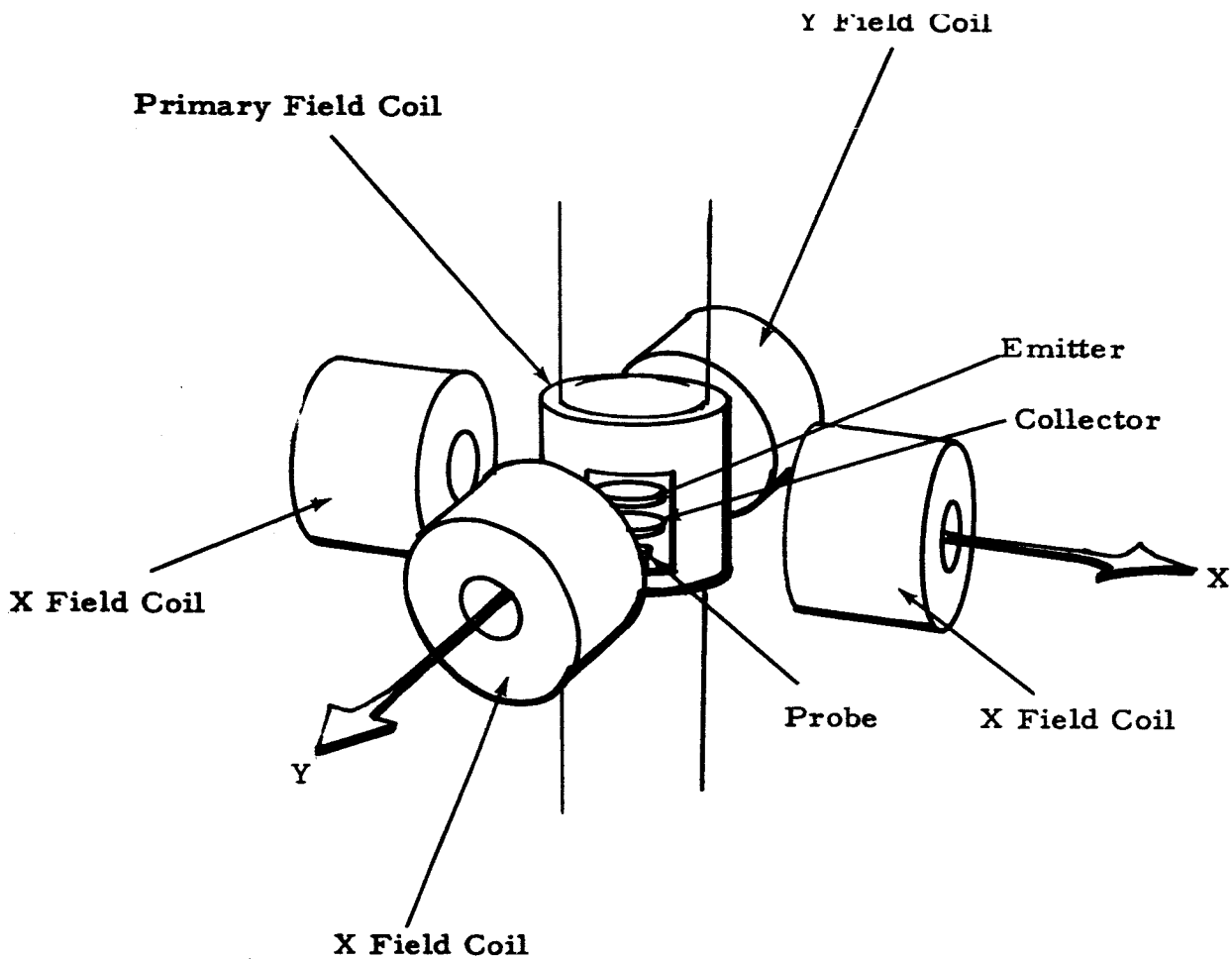

Figure III-5. Schematic of Thermionic Scanner Coil

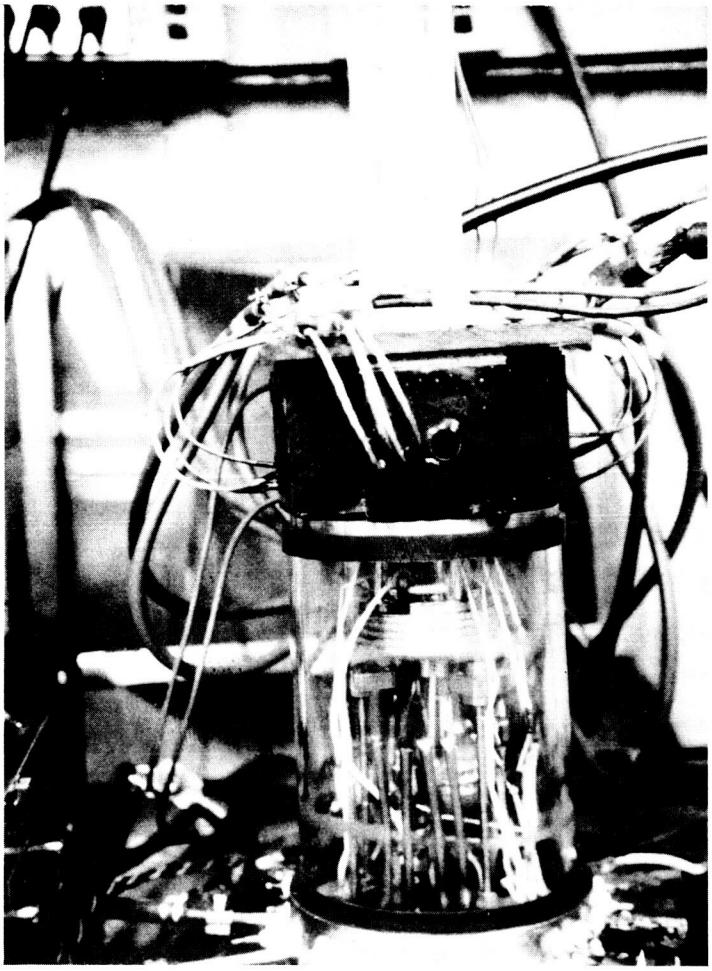

Figure III-6. Scanner Under Vacuum With Coils

CHAPTER IV

PHOTOELECTRIC SCANNING DEVICE

The photoelectric scanning device uses the photoelectric effect to examine the details of the surface work function variation. The device operates with cesiated surfaces but at low temperatures and pressures (surface temperature up to 900°K and reservoir temperature up to 360°K) where the thermionic currents are small and ignition effects do not occur. While these conditions are not similar to those found in thermionic converters, part of the collector temperature range can be covered and the surface behavior, unperturbed by plasma effects, can be examined. In addition, work function changes produced by varying Cs or CsF coverage can be determined.

A. Principle of Operation

A metal surface subjected to a beam of photons of sufficient energy to overcome the work function barrier will emit electrons, thereby producing a current dependent on the incident photon energy and the surface work function. Sweeping a very small area high intensity light beam over the metal surface will thus produce a photocurrent which is a function of the work function variation over the surface. Because of the low photoelectric yield, the device is limited to low electrode temperatures where thermionic currents do not mask the photocurrent. It should also be noted that this device determines work function only on a relative scale, since absolute values of work function can be determined photoelectrically with constant surface temperature only if a monochromatic light source is available. The problem of developing such a source with sufficient intensity to be useful for this work was beyond the scope of the program. The analytical techniques which are used to convert this relative information to a more useful form will be described later in this report.

B. Test Vehicle Design

The photoelectric test vehicle is shown in Figure IV-1. The test surface (1) is exposed to the light beam through the brazed-in sapphire window (18). Emitted electrons are collected by the ring (15), suspended over the surface, to produce the output signal. Wires (16) connected to ring (15) ensure that electrons from all portions of the surface have about the same path length and are subject to the same collection efficiency.

Operating conditions are controlled in a manner similar to that described for the magnetic scanner. The shell (8), however, is cooled through the radiator (6) to a water cooled sink. The additive restricting orifice is mounted in the tube (19) which connects to the cesium reservoir. It should be noted again that, because of the restriction caused by thermionic currents, the operating temperatures in this device will be much lower than those in the magnetic scanner.

The leadthrough (10) forms a vacuum tight seal while electrically insulating and shielding the collector (15). A guard ring is also provided (20). Proper temperature for the leadthrough is maintained by conduction from the shell (8).

Grinding off the weld on flange (7) allows the removal of the test surface structure for cleaning or replacement.

Figure IV-2 is a photograph of the emitter structure which consists of the molybdenum test surface with three notches filed in it for orientation purposes, the tantalum sleeve which supports it, and a radiator. The body shell with the collector leadthrough and guard ring is shown in Figure IV-3. In Figure IV-4, the test surface can be seen through the sapphire window, and Figure IV-5 shows the device mounted on the test stand under vacuum.

The cooling coil and electrical shielding are visible through the glass. The coil at the top of the bell jar is used to counteract the magnetic field of the heaters. The cesium and additive reservoirs are on opposite sides of the tube, below the cooling coil.

C. Deflection System

The deflection system contains the light source and optical components necessary to form the very-small-area spot, as well as the equipment required to deflect this spot over the test surface area. A schematic of this system is shown in Figure IV-6. The light source is a high-pressure mercury or xenon arc lamp. These lamps furnish a small-area, very intense light source, rich in the high-energy ultraviolet portion of the spectrum. Typical figures for brightness and arc size are: for mercury, 140,000 cd/cm^2 and 17 mils; for xenon, 100,000 cd/cm^2 and 15 mils. Light from the lamp is gathered by a concave mirror and focused on a 2-mil diameter aperture, the object for the optical system. The image on the test surface is formed by a sapphire lens mounted in front of the deflection system.

Two mirrors mounted on moving-coil galvanometers reflect the light beam onto the test surface. The first, or X mirror, responds to a saw-tooth output from the display system. The Y galvanometer, mounted to deflect orthogonal to the X, follows a 20-cps sine wave. These galvanometers are driven by special amplifiers, providing centering and amplitude controls so that any desired area of the test surface may be examined with the beam. A phase control in the sine-wave circuit allows synchronization of the galvanometer deflection with the display system.

D. Signal Circuits

Because of the small active area and low photoelectric yield, the output signal from this device is very small and special precautions must be taken to maintain a usable signal-to-noise ratio. Extraneous signals arising from ambient light conditions and amplifier drift are eliminated by mechanically chopping the light beam near the source aperture and using a low-noise ac. preamplifier for the resulting modulated photocurrent output. Since the photocurrent behavior is similar to that of a constant-current source, maximum output signal is obtained with a high-impedance load.

The chopper used for these experiments consisted of a 200-tooth anodized aluminum gear mounted on the shaft of a ball bearing dc. motor. The resulting current was sinusoidal in form, with a frequency of approximately 10 kilocycles. Slight adjustments in chopper speed were required to eliminate beat effects with stray 60-cycle fields and with the 20-cycle sweep rate. Variations in surface work function appear as amplitude modulation of the 10-kc carrier signal, and hum balance coils were used to counteract any stray power-line frequency interference. A high-pass filter with a cut-off frequency about 200 cycles reduced noise at the preamplifier input. Any additional filtering of the carrier resulted in a severe loss of resolution due to the reduction of bandwidth. An estimate for the bandwidth necessary can be determined as follows:

The Y direction sweep is sinusoidal with an amplitude of A/2 cm and a frequency of 20 cps. The velocity of the beam at any instant is thus $d/dt(A/2 \sin 2\pi \times 20t)$ or $20\pi A \cos 40\pi t$. At the center of an area A cm wide, $40\pi t = 0, \pi, \ldots n\pi$ and the beam velocity is thus $\pm 20\pi A$ cm/sec. To resolve two spots 10 mils or 0.25 mm apart with A = 0.5 cm requires a

rise time of about $\frac{0.025}{20\pi \times 0.5} = 0.8$ millisec. The precise value depends upon the characteristics of the phosphor and the desired contrast. The bandwidth required for amplitude modulation of a carrier by a pulse of rise time t_r is given by:

$$BW \approx 1/t_r$$

In the present case the bandwidth is approximately 1.2 kc. . With the carrier frequency of 10 kc the bandwidth becomes more than 10% of the carrier frequency, greatly restricting the filtering allowable to reduce the noise. The required signal-to-noise ratio is a function of the picture quality acceptable and the number of sweeps per picture. In these experiments a ratio of about two to one seemed necessary. For the cross-scan experiments where the fast sweep is not used additional filtering may be incorporated.

As the surface temperatures are increased, the thermionic currents emitted introduce two limitations on the usefulness of the device. The first and most important is the shot noise produced. If the signal current is of the order of 10^{-9} amperes, the mean square noise current is given by

$$\overline{i^2} = 2qIB$$

where: q is electronic charge; I total current and B bandwidth in cycles; i is the instantaneous noise current. The value of $\overline{i^2}$ must be of the order of 10^{-18} amp^2. With a bandwidth of 2 kc, as determined above, the thermionic current limit will be about 1.5 ma, corresponding to a maximum surface temperature of $900^{\circ}K$ at a work function of about 2 eV. The second restriction arises because of the shunting effect of the reduced dynamic impedance resulting from the thermionic current flow. This impedance represents an additional load on the photocurrent and thus reduces the available output.

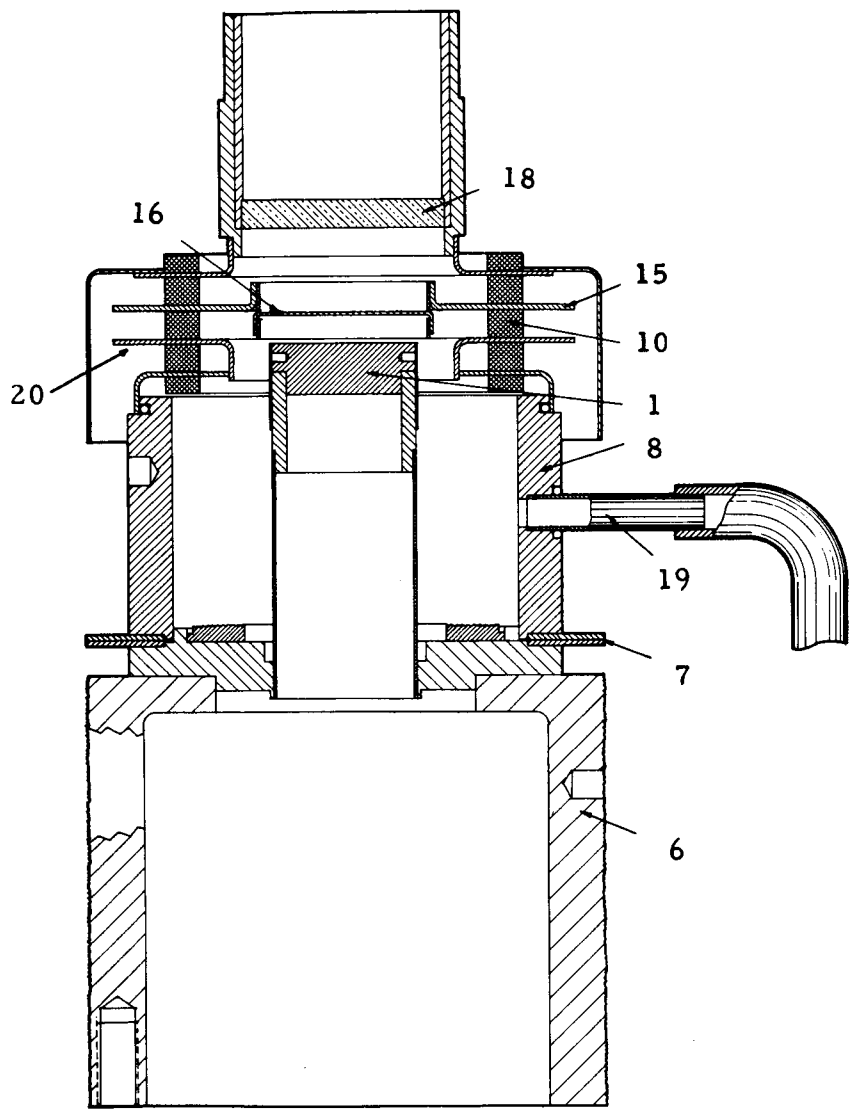

Figure IV-1. Photoelectric Scanner Test Vehicle

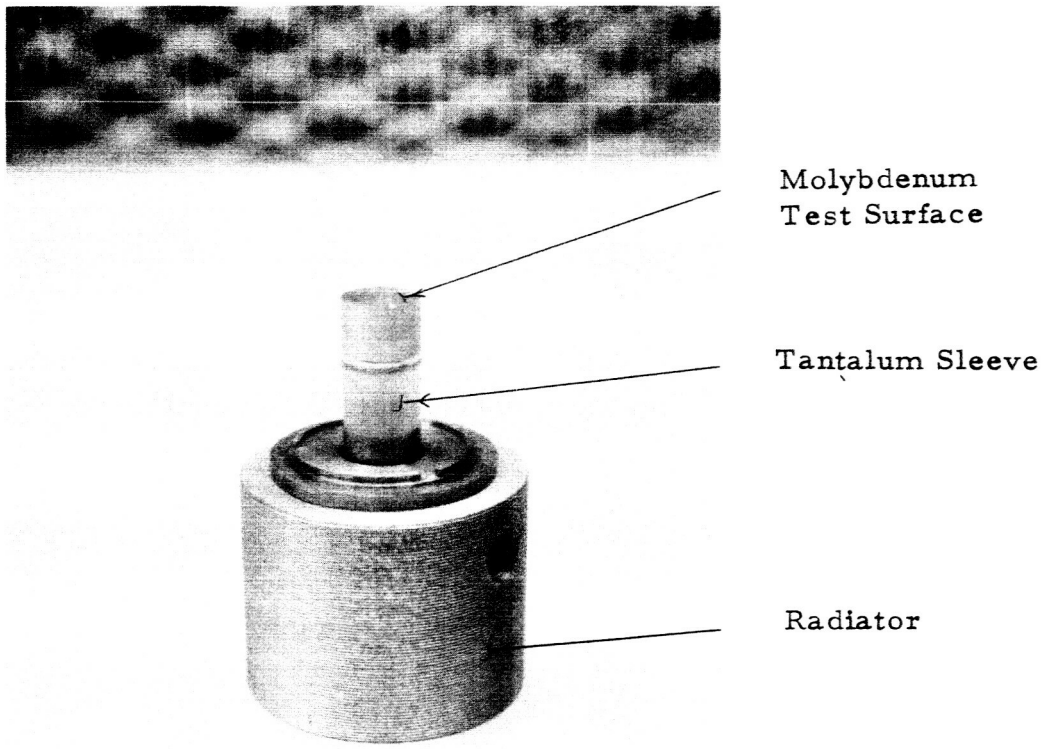

Figure IV-2. Emitter Assembly (Photoelectric Scanner)

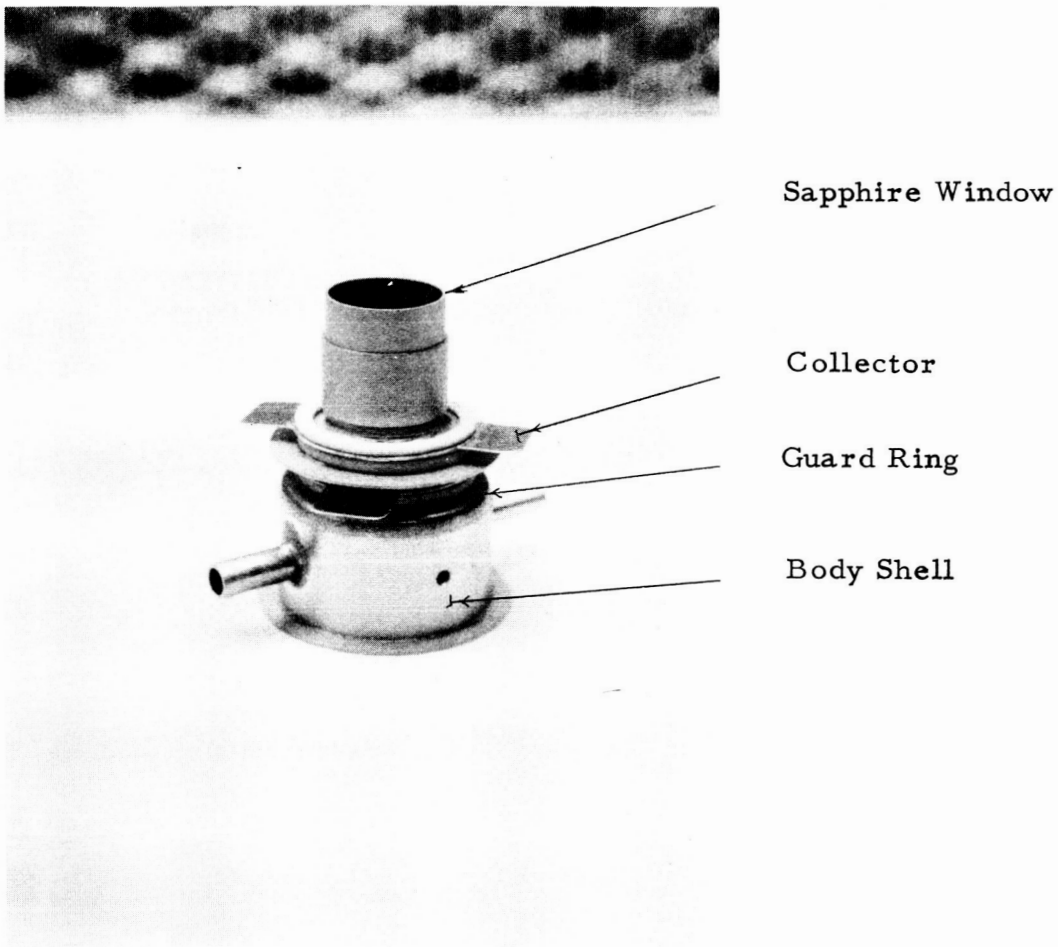

Figure IV-3. Shell (Photoelectric Scanner)

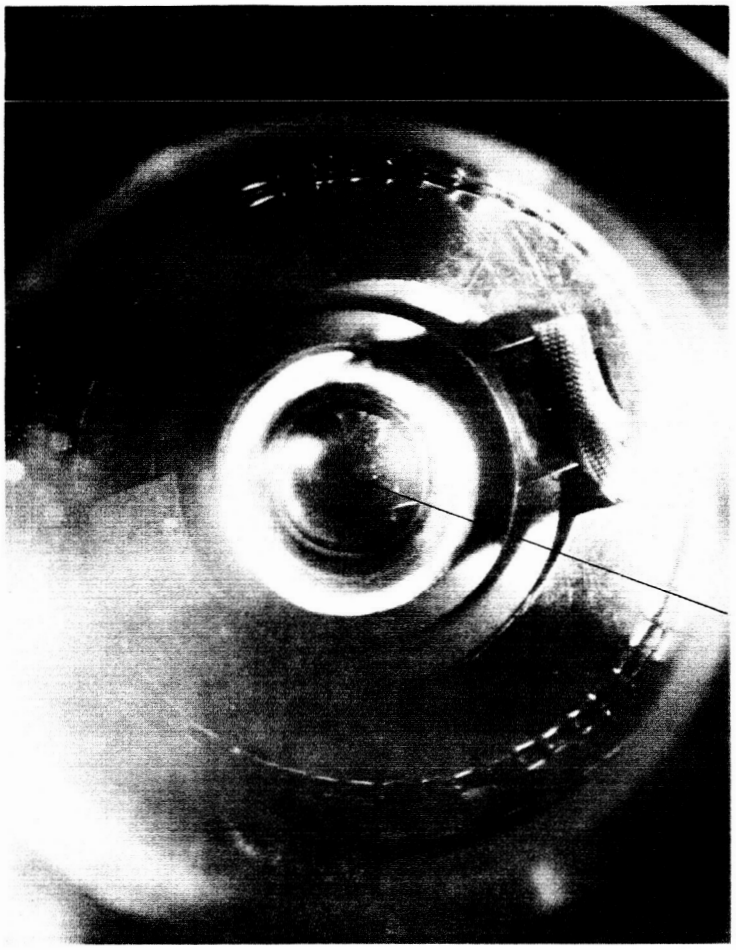

Test Surface

Figure IV-4. Top View (Photoelectric Scanner)

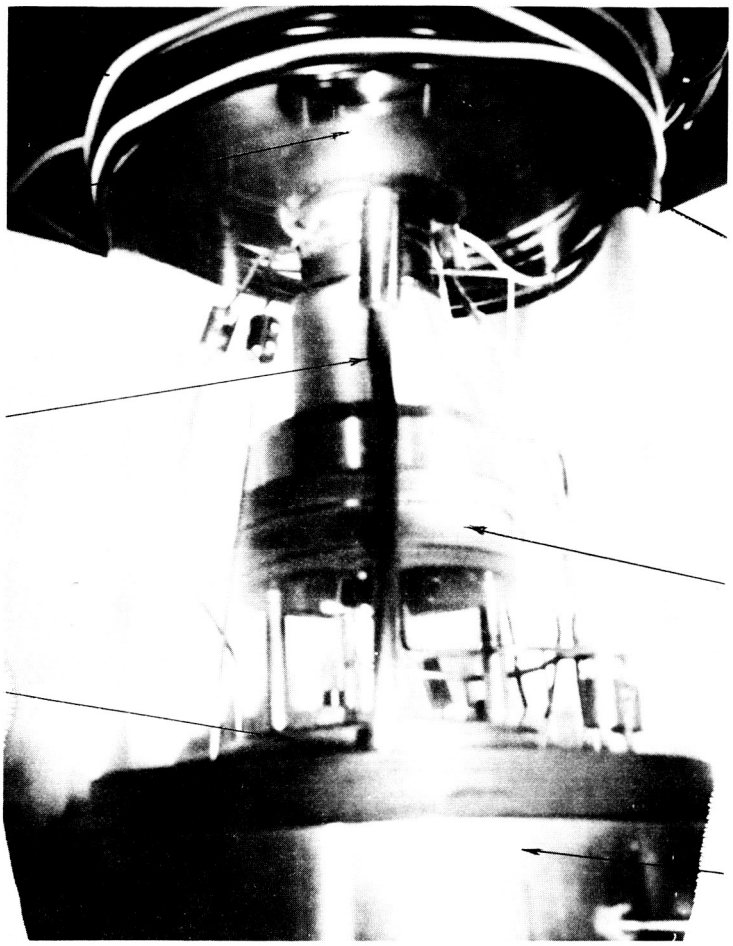

Figure IV-5. Photoelectric Scanner on Test Stand

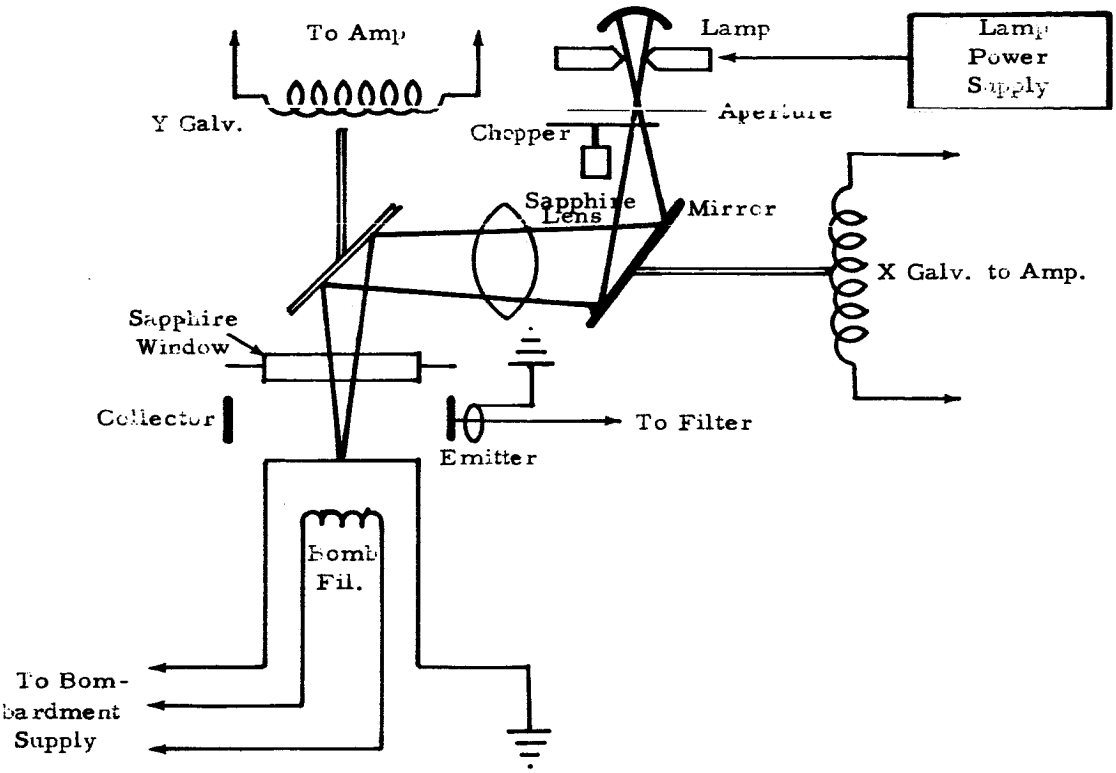

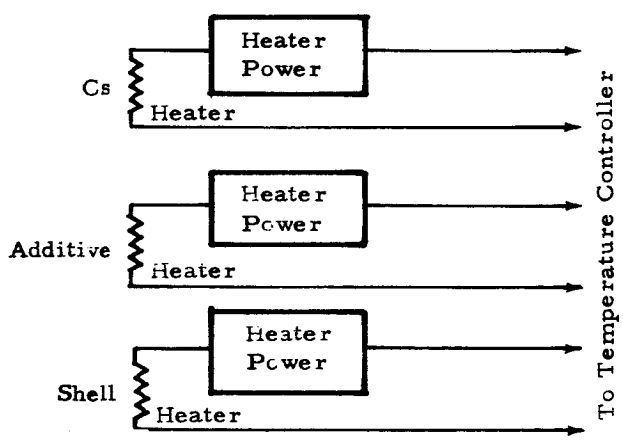

Figure IV-6. Schematic of Photoelectric Scanner

CHAPTER V

TEST PROCEDURES AND INSTRUMENTATION

Since one of the objectives of this program was to obtain data which would be useful in the design of future thermionic converters, it was essential that these experiments be conducted under steady-state conditions. Transient phenomena, while furnishing important clues to additive behavior, must be carefully separated from those intended to simulate the long-term behavior of converters. These considerations required that equilibrium conditions be established in the devices before the experiments were conducted. The factors forming the significant criteria that equilibrium had been established were: the stability of the Cs, additive, collector, and emitter temperatures; the repeatability of a series of tests; and the presence or absence of any hysteresis effects when the elements in the device were heated or cooled. The instrumentation necessary to maintain these temperatures and record the data from the test vehicles was centralized in a single unit, the display system. While steady-state temperatures were rapidly reached and readily stabilized in the photoscanner, the thermionic scanner with its high temperatures, changing magnetic fields, and large electrical energy transfers often presented difficulties in this process. The operating procedures and instrumentation used with each device are described below in greater detail.

A. Display System

The display system performs both temperature control and output functions for the two scanners. It contains heater power supplies which power and regulate the element temperatures in the test vehicle and which may be used with either scanner. The output equipment provides amplifiers and display devices which interpret the signals from the scanners and, with the aid of sweep drive voltages, synchronize the display with position on the test surface.

B. Heater Controls

The cesium, additive, and shell or collector heater supplies are each low-voltage, variable-autotransformer-adjusted, ac supplies. An on-off temperature controller with a thermocouple sensor mounted in the heater structure regulates the average power input to produce the desired temperature. The cesium and additive heaters can operate up to 10 amperes at 12 volts, and the collector heater can put out 20 amperes at 36 volts.

The test surface is heated by electron bombardment. A well filtered high-voltage dc power supply furnishes the bombardment current of up to 750 mA at 1000 V, while the filament is heated by an adjustable low-voltage ac supply capable of 50 amperes at 10 volts. Manual control of the power input is satisfactory for this operation.

C. Output Equipment

There are two modes of output presentation available: sweeping, in which a portion of the emitter is scanned in two directions producing a "map" or display picture with brightness corresponding to emitted current density; and cross-scanning, in which scanning takes place in one line only across the test surface and the waveform of the resulting voltage is displayed. Quantitative determinations of current can be made most easily by calibrating the cross-scan amplitude with a known signal.

In the sweeping mode, output signals from the test vehicle, after passing through a Z-axis amplifier, are applied to the intensity grid of a kinescope tube. At the same time synchronous scanning of the test surface and kinescope takes place, producing a one-to-one relation between the surface and display. The X sweep is controlled from a sawtooth generator contained in the output equipment,

while the Y sweep is driven by a properly phased sine-wave signal originating in the scanning equipment. Brightness of the resulting map is adjusted by the intensity control of the kinescope, and contrast by the gain control on the Z-axis amplifier. Photographing the display, after setting the brightness and contrast to match the film being used, provides a permanent record of the test surface emission patterns.

The cross-scanning mode uses only one scanning direction, the other sweep being shut off. Amplified output signals from the test vehicle replace the unused sweep on the kinescope. If the intensity modulation is left on, the output level corresponding to "black" in the display picture can be determined. In most cases, because a more stable display resulted and because of power supply requirements, the high-speed sine-wave sweep was used, and the sawtooth generator was replaced by a dc supply to allow the cross scan to be taken at any desired location on the test surface. A known constant-current source connected in parallel with the test vehicle output provides a calibrating signal for the cross scan which compensates for variations in gain or leadthrough resistance. Accurate records of the results are obtained by connecting an X-Y plotter in place of the kinescope. Either the sawtooth sweep or a sampler with the high-speed sweep must be used to reduce the rate to one suitable for the servo in the plotter.

A block diagram of the display system is shown in Figure V-1. On the diagram the connections to the scanners are shown as switches, but in actuality they are plugs to allow portability. At the lower right is the deflection equipment with its power supplies, drivers, and phasing controls. On the left are the signal components including the calibrating generators. In the upper center is the kinescope with its X, Y and Z amplifiers. Also shown here are the sawtooth generator and the blanking generator which is used to blank the retrace of the

sine wave, thereby increasing the resolution of the "map" by eliminating from the display any phase shifts caused by transit time in the devices. The reversing switches which enable scanning either half of the thermionic test surface are indicated. Also indicated are connections for the cross-scanning mode.

Appendix C contains detailed diagrams showing the point-to-point wiring for each scanner in each mode of operation.

The output oscilloscope is a Hewlett Packard 130C which has been modified to provide external ground-level outputs from its high-gain dc vertical amplifier. This amplifier now functions as the Z-axis amplifier. A dc coupled intensity-modulating input, necessary because of the low-speed sweep in the thermionic scanner, is provided through a connection to the unblanking circuit. To replace the original vertical amplifier, a Tektronix Type 59 preamplifier is connected directly to the deflection plates, and provides its own centering and gain control. A negative-going 30-volt output from the sweep generator, which has been arranged to operate independently of the horizontal amplifier, serves as the saw-tooth generator for the system. Additional power supplies have been connected to energize these added components. The major modifications are shown schematically in Appendix C.

D. Outgassing and Charging

When construction of the test vehicle had been completed, it was helium leak-checked and connected to the outgassing fixture. A getter ion pump attached to the additive tubulation evacuated the device, while the tube elements were heated to higher temperatures than were expected in use. The Cs was sealed in a glass capsule contained in its tubulation, and the CsF in a special capsule in the additive tubulation. Pumping was continued until a pressure no higher than

10^{-6} torr was reached, and there was less than an order of magnitude improvement upon cooling. The Cs capsule was then cracked, and after the pressure had recovered the pump was pinched off below the additive capsule. Heating the cesium capsule region to 220°C for 5 hours distilled the Cs into the device. Pinching off the Cs tubulation to remove the glass capsule prevented contamination of the test vehicle during testing. The device was then mounted on its test stand and was ready for use.

Since testing with pure cesium had to be accomplished before releasing the additive, a special cesium-resistant additive capsule was required. The capsule used in both scanners consisted of two pieces of 3/16-inch copper tubing brazed to a short piece of molybdenum tubing. One piece of copper was pinched off, and several grams of cesium fluoride, handled in dry atmosphere, were placed in the capsule. After outgassing at 125°C until a low pressure (10^{-6} torr) was obtained, the copper tube at the other end was pinched off. Molybdenum tubing is very brittle and may be easily fractured inside the additive tubulation when the cesium fluoride is to be released. A photograph of this capsule is shown in Figure V-2.

E. Thermionic Scanner

The steps required to conduct a series of experiments with a given test surface will now be detailed.

1. The test vehicle is warmed up to near the desired Cs, additive, test surface and collector temperatures.

2. A discharge is ignited by applying an accelerating dc field which biases the main diode into the emission-limited, i.e. saturated, portion of the J-V curve.

3. The cesium reservoir temperature is varied over a small range to ensure that the reservoir controls the Cs pressure in the test vehicle. Because of the additive-restricting orifice in the cesium tubulation, there is a long response time of the device to reservoir temperature changes, particularly at low pressures.

4. Time is allowed for stabilization of the element temperatures under the conditions of main current flow. A multipoint recorder monitors these temperatures and their variation.

5. If necessary, the heat input is adjusted to maintain the desired operating conditions.

6. A few J-V curves for both the probe and main diode are traced to ensure operation in the emission-limited region. These curves are compared with other saturation data obtained from converter-type experiments to establish their validity.

7. The main collimating magnetic field is energized and its effect on the discharge observed visually through the sapphire window. If collimation is satisfactory, the sweeping fields are energized and their action also observed.

8. Since the application of the magnetic fields has probably disturbed the energy balance in the tube, the heater power input is readjusted to re-establish the desired steady-state conditions.

9. Data can now be taken in the form of either cross scans or display pictures with confidence that the tube is operating in a stable uniform manner.

10. A new emitter temperature is then established and stabilized by regulating the heater power, and a new set of data can be obtained.

In a similar manner, a wide range of surface and reservoir temperatures may be investigated subject to certain limitations at both high and low current densities. As the main diode current density decreases, the current reaching the probe through the small hole becomes comparable with that arriving from the collector area opposite the probe body, and, since this current is also deflected, it appears on the display picture as a darkening of the central area. Furthermore, slight changes in collector temperature cause an exponential variation in this current, and result in severe drifting of the total probe current. When the high-additive-pressure tests are conducted, the high collector temperature required to maintain the pressure further aggravates this situation. An estimate of the limiting current ratio can be obtained by considering the relative areas of the probe hole and the interior collector area, a ratio of $1.35 \times 10^{-6}:1$.

At high currents there is a significant energy interchange taking place between the discharge and the tube elements, and, since the current is in turn dependent on element temperature, the device will be unstable in the region where the discharge energy is a significant fraction of test surface input. These conditions occur near the work function minimum on the T/T_R curves. The special test equipment described below was developed to permit stable operation in this region.

A reduction in the average power dissipated in discharge may be achieved through a pulse technique. If the accelerating field is pulsed to the saturation value with a low-duty-cycle source, the heating effect will be reduced, and the currents will still be emission-limited during a short period sufficient for measurement purposes. If the cross scan is taken using the slow sawtooth sweep, the accelerating pulse may be free-running and a sampling-type technique used to maintain the cross-scan amplitude for the X-Y plotter between pulses. Most of

the data taken uses the fast sweep which occurs at the line frequency; therefore a similar sampling method must be used to slow the effective speed for proper operation of an X-Y recorder. By synchronizing the sampling pulse with the accelerating pulse and varying the phase of the two pulses with respect to the 60-cycle line, a complete plot of a cross scan can be obtained on the X-Y recorder. Figure V-3 shows the J-V curve of the tube and indicates the pulse voltages. The curve is entirely in the power-absorbing quadrant because of the wide spacing. Figure V-4 illustrates the pulse and sample timing.

The accelerating pulse period corresponds to the 60-cycle sweep frequency, so that ignition always occurs at the same value of magnetic field. A delay of 0.8 millisecond between the start of the accelerating pulse and the sample time is provided to allow the discharge to stabilize and any turn-on transients to decay. The sampling pulse opens the sampling gate for a period of about 50 microseconds to record the sweep field and probe current at that time.

Figure V-5 shows a typical cross scan as it appears on the oscilloscope. The vertical sweep in the figure is derived directly from the 60-cycle deflection coil voltage, while the horizontal signal is obtained from the probe current. During the interval between accelerating field pulses, only spurious currents such as those emitted from the main collector reach the probe, and the resulting base line forms a zero reference. When the main discharge is ignited, the current from the test surface reaches the probe and appears as the current pedestal in the photograph. Figure V-5 is included here to demonstrate the timing and amplitude of the measuring current pulse. This type of observation is used as a monitoring technique while pulsed cross-scan data is being obtained. The scope trace itself is not used as data.

A block diagram of the instrumentation is shown in Figure V-6. A General Radio 1217B Pulser, synchronized to the line frequency through an adjustable phase shifter, provides the primary pulse source. This source drives the accelerating voltage gate and also triggers the sampling gates in the "waveform translator" through a trigger generator. X and Y signals for the recorder are taken through the sampling gates from the sweep and from the amplified probe current. Oscilloscopes monitor the tube voltage and cross-scan signals. One interesting aspect of the pulsing is its strobing effect on the discharge, which renders the high-speed sweeping action visible through the sapphire window.

The only current density restriction on the usefulness of the device arises at the low-current end of the scale; that is, at high surface temperatures where there is insufficient energy to overcome the work function barrier. There is an additional limit on the maximum Cs pressure allowable, due to the defocusing effect resulting from Cs interactions. Stronger magnetic fields, if available, may be used to extend the capabilities of the device.

F. Photoelectric Scanner

The only problem in reaching steady state with this device is that sufficient time be allowed for the heat flows to become stabilized. Once the device and instrumentation has warmed up, data may be taken. However, because of the restriction in the cesium tubulation, a period of about an hour is required for changes in Cs temperature to produce equilibrium pressure in the device.

Signal-level limitations in this device depend greatly on the ability to obtain very high leadthrough resistance, high values producing a better signal-to-noise level and finally better resolution. However, the thermionic noise limit which depends upon the relative currents is not affected. Useful data can be obtained up to temperatures where the shot noise becomes important.

The calibrating signal in this device is applied by reflecting the chopped light source onto a photocell connected in parallel with the output from the scanner. The amplitude of the calibrating signal compensates for changes in light source intensity or leadthrough resistance, reducing any drift problems.

G. General Procedure

Because of the long time period required to equilibrate the Cs pressure, most runs were made with constant Cs reservoir and varying test surface temperatures; thus it was not necessary to force a large amount of Cs through the restricting orifice in the tubulation. Each run consisted of a series of cross scans covering the range from low to high temperature and reverse until the low current limits were reached. To maintain equilibrium, only slow changes were made between steps and an equilibrating period of 15 minutes was allowed before taking a scan. A few display "maps" were taken to illustrate the general surface patterns.

During the initial tests, the CsF was contained in a special sealed capsule, allowing the test surface to be evaluated with Cs only. This data was then compared with results observed on converters and also served as a reference for the additive experiments. The capsule was then cracked to release the additive into the test vehicle. Additive pressure could then be controlled by varying the reservoir temperature. A series of runs similar to the initial ones was then made with each of several reservoir temperatures.

Appendix B contains a selection from the original curves and a list of the conditions at the time the data was obtained. For the tungsten data, which proved to be the most useful for studying the effect of the additives upon surface emission, runs 1-77 are for the cesium-only case, runs 78-185 are for cesium plus

cesium fluoride after short soaking times, and runs 186-231 are for cesium plus cesium fluoride after long soaking periods. (For the sake of brevity, we have included in Appendix B only a selection of typical curves which are significant to the discussion. All of these curves are available at the Lewis Research Center and at Thermo Electron.)

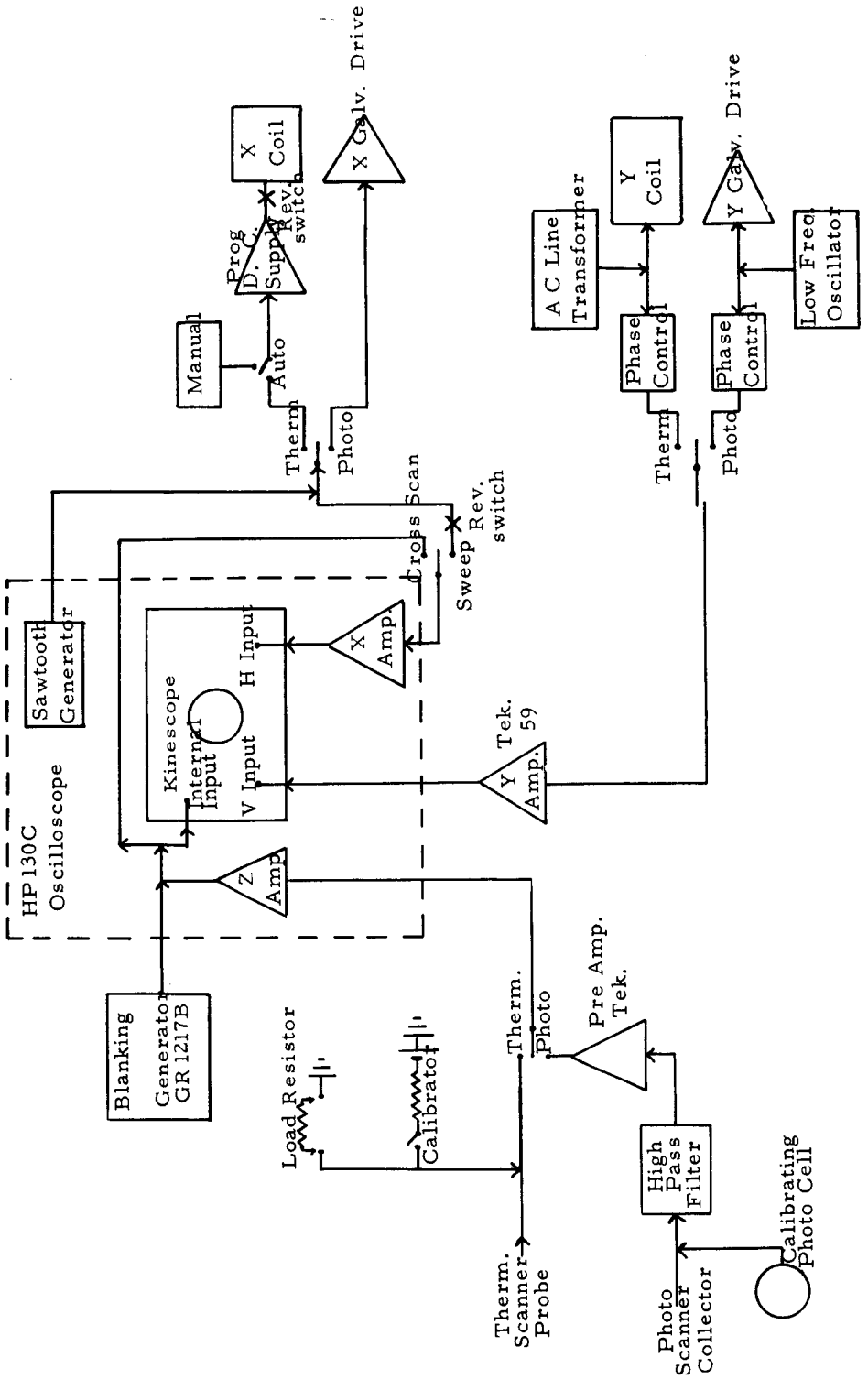

Figure V-1. Block Diagram of Display System

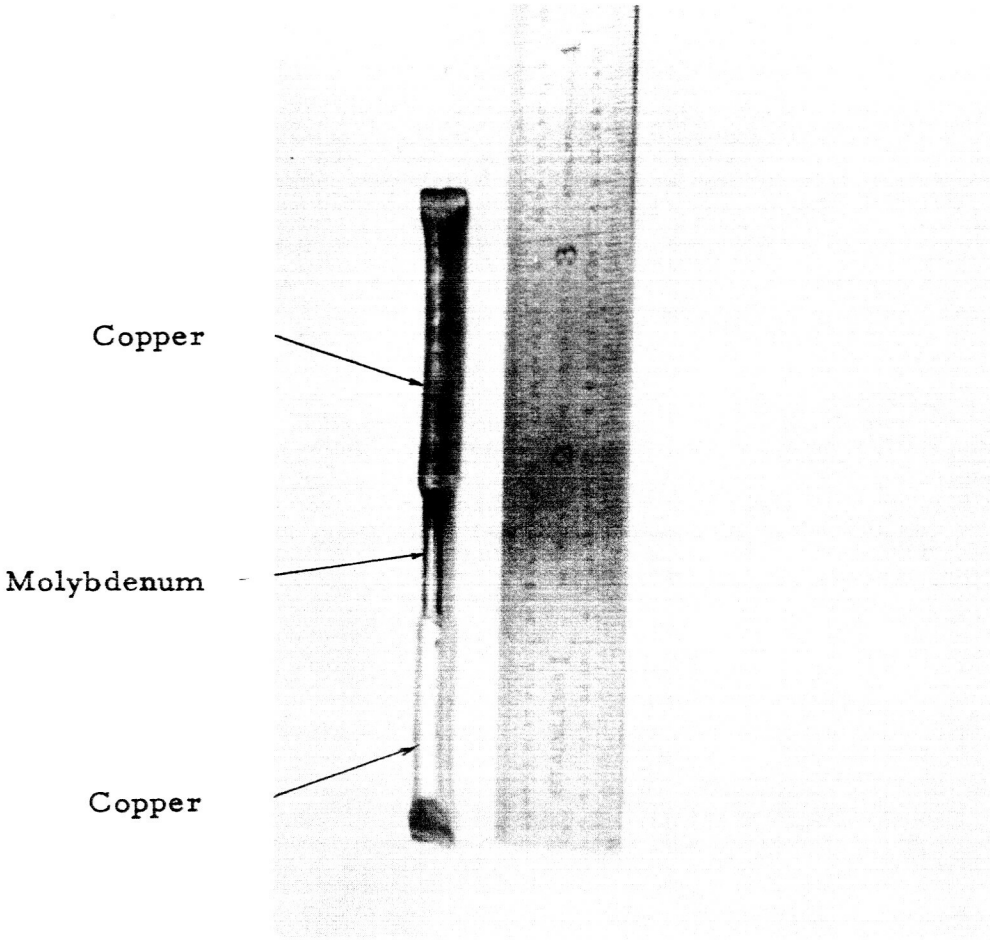

Figure V-2. Additive Capsule

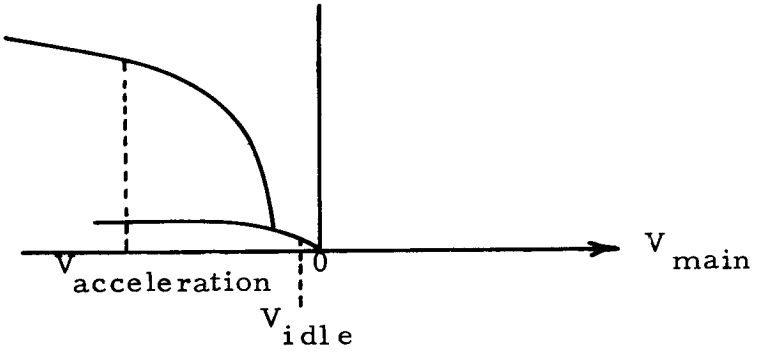

Figure V-3. J-V Curve

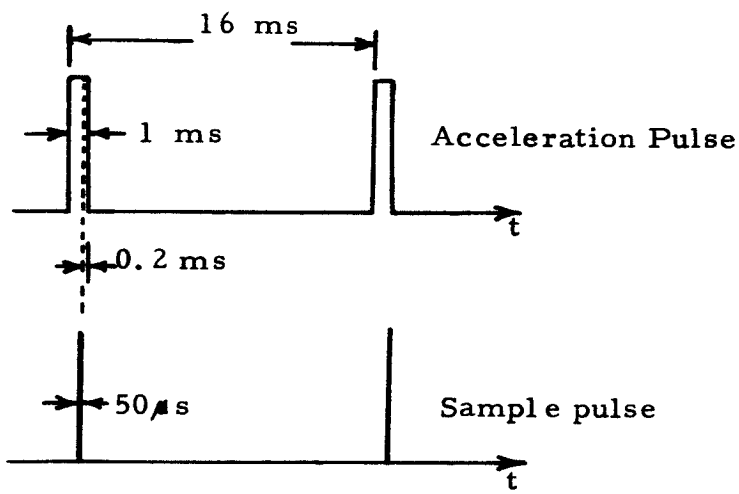

Figure V-4. Pulse Timing

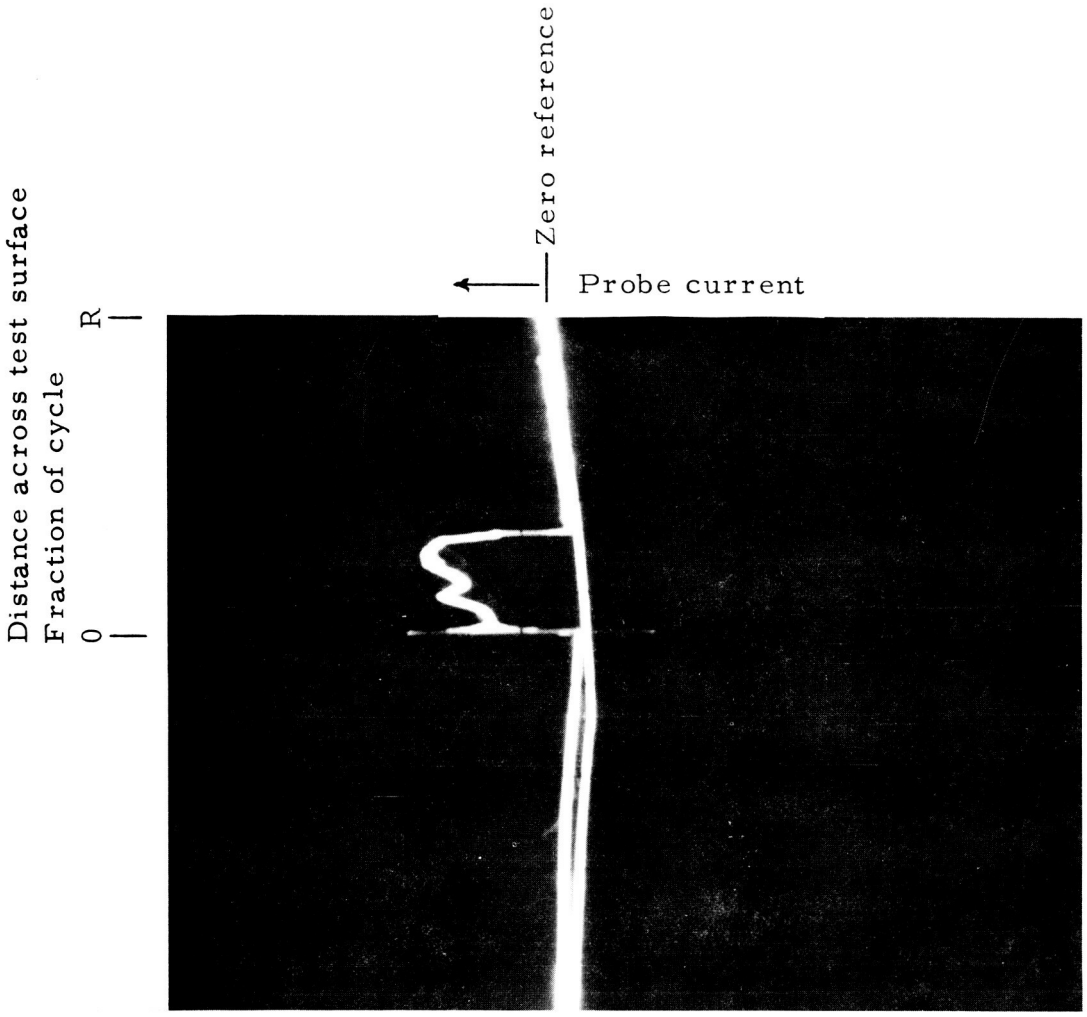

Figure V-5. Pulse Cross-Scan

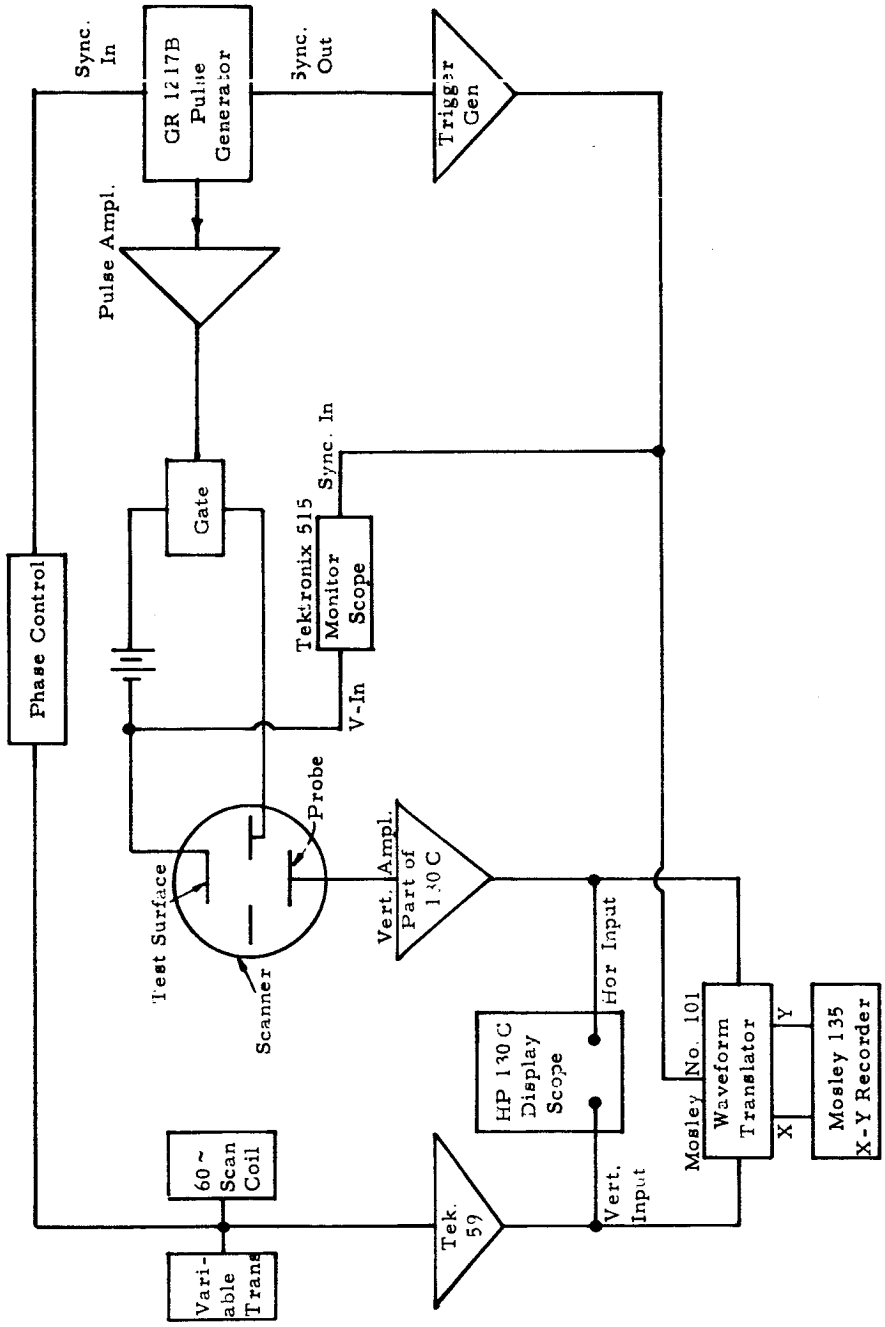

Figure V-6. Pulse Scanning Instrumentation

CHAPTER VI
EXPERIMENTAL RESULTS

A. General

Information from the scanning devices is obtained in either of two forms: a cross-scan plot showing the current amplitude along a single line across the test surface, or a display picture showing the emission pattern corresponding to a two-dimensional area on the surface. The display photographs, Figure VI-1, for example, are extremely useful in identifying the overall features of the surface under examination, and in perceiving the dependence of emission on the local features of the surface as defined by metallurgical examination. However, quantitative measurements cannot be obtained from such photographs. For this purpose, the single-line cross scans are far more suitable. Figure VI-2 is typical of a series of cross scans, each of which is obtained by scanning along a single chord on the face of the test piece. The designations "0," "40" and "60" are used to identify the three chords scanned. On the same figure, a calibrating signal is also recorded (lower line of Figure VI-2) to allow comparison between cross scans, or in some cases an absolute determination of emitted current density.

B. Methods of Data Analysis

Analysis of the test surface and additive behavior is based on the calculation of work function and its variations with position or temperature. The two techniques used in this work are: the construction of T/T_R plots, which relate work function to the ratio of surface temperature to Cs reservoir temperature and which can be compared with the Rasor theory predictions,[1] and the computation of

1. Rasor, N.S., & Warner, C., J. Appl. Phys., Vol. 35, No. 9, Sept. 1964.

distributions which illustrate the percentage of surface area having given work function values. A typical calculation of a T/T_R-vs-ϕ plot for each of the scanners will explain the reduction of cross-scan data to work function information.

Thermionic Scanner Typical Calculation

Figure VI-2 shows several cross scans at each of three different locations on a ⟨110⟩ tungsten test surface at a temperature of 1060°K, a Cs reservoir temperature of 425°K and no additive present. Let us choose point "A" on cross scan "0" for this example. The relative current at this point is given by the amplitude of the curve and is 71 graphical divisions. The calibrating current, which is identified graphically as the number of divisions between the two lines marked "Calibration" in Figure VI-2, has been previously determined to be 0.65 μA. Thus, the actual current at point "A" can be calculated. Dividing by the known area of the collector hole (4.6×10^{-5} cm^2) gives the current density through the hole. Repeating this procedure for cross scans covering a range of surface temperatures gives the values shown in Table I. The surface temperature and current density substituted into the Richardson equation give the effective work function of the cesiated surface, assuming the current is produced by saturated thermionic emission and all of the current in the hole area reaches the probe. These results are plotted in Figure VI-3. Similar plots were made for different additive and cesium reservoir temperatures.

Photoelectric Scanner Typical Calculation

Figure VI-4 shows a cross-scan plot produced from the photoelectric scanner. In this case, the calibrating signal is the output of a

TABLE I

Cross Scan No.	T °K	T_R °K	T/T_R	Current Ampl. Div.	Cal. Ampl. Div.	Rel. Ampl.	J A/cm^2	ϕ volts
61	800	425	1.88	20	44	0.455	.006	1.60
59	855	425	2.02	160	12	13.3	.174	1.48
57	930	425	2.19	244	13	18.8	.245	1.58
55*	1060	425	2.52	71	13	5.46	.071	1.96
53	1200	425	2.84	30	45	0.666	.009	2.45

*Cross Scan No. 55 is shown in Figure VI-2.
Other cross scans will be found in Appendix B.

standard photocell, onto which the beam used to scan the test piece is directed. Relative current for a series of similar plots may be calculated, but before this data can be translated to work function, the physics of this relationship must be considered.

Figure VI-5 is a plot of the relative electron current emitted by a surface of work function ϕ (indicated on the energy scale) when photons of a given energy strike this surface. It may be observed from this figure that photons of energy less than ϕ will not result in electron emission, while photons of energies slightly greater than ϕ will yield a given number of electrons independent of the actual photon energy (as a first approximation). As the energy of incident photons increases further, the actual number of electrons yielded decreases. For our purposes, however, we can assume that photons of energies less than ϕ yield no electrons whatsoever, while all photons greater than ϕ yield the same number of electrons. This assumption is shown by the dotted straight lines in Figure VI-5.

In the photoscanner experiments, a xenon lamp was used, and the characteristic of this lamp is shown in Figure VI-6. This figure is a plot of the relative number of photons versus the energy level. The curve of Figure VI-6 has been integrated and plotted in Figure VI-7 as the relative number of photons which have energies greater than E electron volts. Based on the assumption of Figure VI-5 and the relationship shown in Figure VI-7, we can state that the currents yielded by the incident photons will vary with the work function of the surface within the range of 1.2 to 4.3 eV. Surfaces with values less than 1.2 electron volts will emit the same amount of current, no matter what their work function, when this light strikes them, while

surfaces of greater than 4.3 electron volts will emit no current at all. Between these limits, the relative current may be approximated as

$$\frac{I}{I_{max}} = \frac{4.1 - \phi}{4.1 - \phi_o}$$

where ϕ_o is the minimum work function at which the relative current I_{max} is obtained, and I is the current at the work function ϕ. A surface having a work function of 3.5 volts will emit half as much as that emitted by a surface having a work function of 2.92 electron volts, since 20% of the incident photons have energies greater than 3.5 electron volts, and 40% of the photons have energies greater than 2.92.

Figure VI-8 shows a plot which relates relative photocurrent to T/T_R. This plot was obtained from a point A on cross scans PM1 through PM8, which are so designated in Appendix B. The actual value of the relative current (I) at each point is calculated by dividing I_o by I_c (see Table II).

Figure VI-8 shows that the current at point A rises as the surface temperature (T) is increased until a maximum is reached. Further increases in surface temperature then cause a decrease in the current. The shape of this curve is essentially the inverse of the relationship of the surface work function ϕ and indicates that ϕ goes through a minimum at the T/T_R ratio where the current goes through a maximum. This relative current plot can be translated into normalized work function by choosing a value for minimum ϕ (in this case the value of 1.3 eV, which is roughly the minimum value observed on molybdenum collectors) and using the relationship of the above equation to determine the values of ϕ for each data point. In actual calculation

TABLE II

PHOTO ELECTRIC SCANNER MOLYBDENUM EMITTER CESIUM-ONLY RUNS								
Run #	T °K	T_R °K	T/T_R	I_c	I_o	Relative Current		ϕ Normalized
				Calibrate Amplitude	Photocurrent Amplitude (Location A)	From Curve	$I=I_o/I_c$	
PM1	454	330	1.37	33	43.5	1.30	1.32	1.5
2	460	332	1.39	27	34.5	1.31	1.28	1.5
3	580	332	1.75	24	36.0	1.52	1.50	1.3
4	685	337	2.03	30	53.5	1.68	1.78	1.1
5	728	338	2.15	30	50.0	1.73	1.67	1.0
6	825	338	2.45	38	55.5	1.71	1.72	1.1
7	907	339	2.68	35	56.0	1.62	1.60	1.2
8	948	340	2.80	34	53.0	1.56	1.56	1.3

of the values of ϕ, the values of I were taken from the curve of Figure VI-8 at the values of T/T_R of the data points. These values of I are listed in column 8 of Table II. The normalized ϕ is then obtained by dividing all values of ϕ by $\phi_c = 1.3$. The normalized values are plotted in Figure VI-9 against T/T_R and are given in column 9 of Table II.

In comparing the display pictures and cross scans from the two scanners, it should be noted that in the thermionic device current is exponentially dependent on work function, while in the photoelectric device it is linearly dependent. For example, if a two-to-one current variation is observed in the thermionic scanner, when operating in the range of 1100°K (2 eV) the corresponding change in ϕ (from the Richardson equation) is 0.07 eV. For the photoelectric scanner we may use Figure VI-7 to determine the change in the amount of incident energy effective in bringing about a directly proportional change in photoelectric current. If we examine the change in ordinate as we vary the abscissa from 2.0 to 2.07 we find the change to be about 4%. This may be compared with the two-to-one (or 100%) change in current in the thermionic scanner.

The 4% change in the photoscanner is easily swamped by noise and other stray effects. The detail obtained is thus very much greater with the thermionic scanner than with the photoelectric device.

Distributions of Work Function Typical Calculation

A cross scan represents a slice of the test surface, and, if any one slice is assumed to be typical of the whole surface, a work function distribution calculation based on a single scan can be said to approximate

that of the whole surface. Based upon examination of many cross scans and many display photos, this assumption is deemed reasonable.

By relating relative current to work function, each cross scan becomes a plot of ϕ vs position. The values of ϕ are then used to prepare bar charts such as those of Figure VI-10. From the ϕ-vs-position plot, areas corresponding to small increments of work function (0.2 eV) are summed for the cross section. The resulting sums are converted to a decimal (or normalized) by dividing by 100 and plotted as a horizontal line over the range of work function chosen. The objective of this type of plot is to give a picture of the range and distribution of the work function as the temperatures (surface, reservoir and additive) are changed. Figure VI-10 illustrates a series of bar plots for a range of T/T_R values. Only results from the thermionic scanner were used for these plots, since its greater resolution and exponential dependence on work function produced a greater amplitude range and more clearly defined results. The results shown here indicate a strong variation of work function across the scan and a change in that distribution with emitter temperature.

No attempt was made to perform the same type of analysis for the non-additive case, but a visual comparison of several cross scans for additive and non-additive operation leaves no doubt of the change from uniform to non-uniform emission as a result of the additive. (For example, in Appendix B, compare cross scan #41 with #71 and cross scan #45 with #95.)

The uniformity of runs #1 through #48* is apparently characteristic of the nominally single-crystal tungsten where no additive effect is present.

---

*The original data for all of these runs is not included in Appendix B. Copies are on file at the Lewis Research Center and at Thermo Electron.

C. Data Analysis

The raw data obtained has been processed according to the methods discussed in the foregoing paragraphs. In the remainder of this section these data will be presented in summarized form.

Photoelectric Data

All tests in the photoelectric scanner used the Mo surface. When construction was completed an extremely low leadthrough resistance (20 Ω) had developed, apparently from deposits formed during outgassing. The resistance of the guard ring to ground, however, was high enough to allow data to be taken. Because of the long path length for electrons and the resultant lowered collection efficiency near the center of the test surface, all patterns from the device showed reduced output from this region. Comparison of patches could be made accurately only between neighboring areas. A photograph of a display is shown in Figure VI-11, and, although the resolution is poor and the noise level high, some grain structure can be discerned. By carefully filtering the output signal and taking repeated slow scans on the X-Y plotter, it was possible to obtain reasonably noise-free cross scans similar to that shown in Figure VI-4.

Initial runs made with Cs only are plotted as curve A in Figure VI-12. These points were obtained from cross scans PM1 through PM8, which appear in Appendix B, and are identified as "A." The results of series of scans made with T_{add} = 350°K, slightly higher than the cesium reservoir temperature (T_R = 330°K) are plotted as curve B of Figure VI-12. (These points result from reduction of data at points corresponding to vertical lines on cross scans PM 22-26.*

*The original data for these runs is not included in Appendix B. Copies are on file at the Lewis Research Center and at Thermo Electron.

A comparison of curve B with the cesium-only case (curve A) shows that only a very minor change has occurred in the T/T_R value at which the maximum current (minimum ϕ) is recorded.

Curve C was then produced by performing the same analysis on a series of cross scans (PM 27-35)* taken with the additive reservoir temperature at 400°K. Here the peak current (minimum ϕ) has shifted to much higher values of T/T_R. In fact, no minimum has yet been reached at the upper limit of T/T_R in our experiments. Curve D, which is a result of scans (PM 36-43)* taken with $T_{add} = 500°K$, shows a maximum current (minimum ϕ) at $T/T_R = 1.95$, which is a lower value of T/T_R than the cesium-only case.

It should be noted here that the value of relative current is of no significance, but the important feature is the value of T/T_R at which each curve peaks.

In Figure VI-13, all of the curves of Figure VI-12 have been converted to a relative work-function scale and normalized to a value of one (1) for the minimum work-function point. In this normalization, an approximate value of 1.3 eV was chosen for ϕ_{min} based on data obtained from the converter studies.

These results were taken as indicative of a trend which could be expected as additive pressure is varied. No attempt was made to correlate it in a direct manner with other factors, i.e. bare work function or crystal orientation. It was also tacitly assumed that, since the point on the surface (or position on the cross scan) was randomly chosen, the same kind of trend would be exhibited elsewhere on the surface. However, limitations of time and funds make it impossible

*The original data for these runs is not included in Appendix B. Copies are on file at the Lewis Research Center and at Thermo Electron.

to check this by additional reduction of data. Such work is recommended for future programs.

Thermionic Data

Tungsten

The nominally single-crystal tungsten test surface was examined in the thermionic scanner in the first tests. The initial runs described in an earlier chapter have been reproduced for comparison with those obtained after the admission of CsF additive to the device. Figures VI-14, VI-15, II-2, and II-3 illustrate the changes in surface patterns as surface temperature and additive pressures are varied. At a surface temperature (T) of 1280 °K and a cesium temperature (T_R) of 425 °K, the work function is comparatively uniform, as seen in Figure II-2. When the additive is introduced, the central region shifts to a significantly higher work function, as shown by the darker shadow in Figure VI-14.* At higher additive pressure (Figure II-3), this shift is more pronounced and the area more restricted. It should also be noted that, at lower surface temperatures, where the Rasor Plots for different bare-surface work function values approach each other, the patterns are much more uniform. This may be observed by comparing Figure VI-15 with Figure VI-14. Figure VI-16 shows the T/T_R plots for two patches and indicates their corresponding bare work functions.

Figure VI-17 shows ϕ-vs-T/T_R plots taken at 425 °K cesium and several additive temperatures. A similar plot is shown in Figure VI-18 for 475 °K cesium. These runs were all taken with only a short soaking period of about 3 hours at operating temperatures. Under these conditions, the effects of the additive were quite small. Another

---

*Of significance is the relative darkness of the portions of the figure, not absolute brightness. These comparisons, although more obvious in the original photographs, have not been reproduced in these printed reproductions.

run was therefore made after a 16-hour soak at additive temperature. During this period the emitter was maintained at a low temperature (870°K) and heated only during the run.

The additive curves of Figure VI-19 compare this data with the cesium-only condition. The additive has now caused a pronounced shift in the position of the minimum work function to lower T/T_R values.

Figure VI-19 also illustrates the shift obtained when surface temperature is held constant and T/T_R is varied by changing the cesium reservoir temperature. The available temperature range is small, however, and with this technique the work functions in the high range cannot be obtained.

A distribution function plot of the CsF without an overnight soak is shown in Figure VI-10.* The two peaks corresponding to the bright and dark areas of Figure VI-15 can be clearly seen in the cases corresponding to higher work function values.** Figure VI-20*** is a distribution function plot for a lower Cs temperature, 425°K, and shows behavior similar to that of Figure VI-10, but with greater resolution and work function spread. No attempt was made to draw similar plots for the cesium-only case since, as mentioned under the previous section (Photoelectric Scanning), cross scans of this emitter for the cesium-only condition are essentially uniform.

* The data of Figure VI-10 comes from cross scans Nos. 167, 169, 171, 173, 175 and 177.

** The two peaks merge, however, as the minimum work function value is approached, as expected from the Rasor theory.

*** The data of Figure VI-20 comes from cross scans Nos. 102, 104, 106, 108, 110, 112, 114 and 116 (not included in Appendix B).

Some difficulty with resolution at low currents was encountered, particularly after long soaking periods. This occurred because the collector emission tended to increase after soaking (possibly as a result of a lowering of collector work function). Collector emission then became a large fraction of the current collected at the probe and caused a significant drift as the collector went through small variations in temperature. In order to improve the signal-to-stray-current ratio, higher cesium pressure and test surface temperature were required, and the higher cesium pressure caused a decrease in resolution.

A special experimental technique was adopted to cope with this problem. Data at lower pressures was obtained only at the central point of the surface with the deflecting fields inoperative. By switching the accelerating electric field on and off, while plotting probe current versus time, the stray current could be separated from the central test surface current.

Since this procedure is time-dependent, the introduction of another variable (position), which would have been necessary to accomplish cross-scanning, was not possible without confusing the two effects. For this reason, cross-scanning was dropped. Much of the long-soak data was of this type.

Molybdenum

The Mo test surface was removed from the photoscanner and metallurgically examined, as described in Chapter VIII. The test surface was then incorporated into the thermionic scanner for further testing. Figure VI-21 illustrates the display patterns obtained on this material. Note the similarity of Figure VI-22, an enlarged

display of the central region, to Figure VI-11 from the photoscanner. Because of the large grain structure, the individual crystals in the surface can be observed and matched with those obtained from the metallograph, as can be seen by comparing Figures VI-22 and VI-23. In Figure VI-24 there is a pronounced pattern of concentric rings. These are due to a plasma effect which is dependent upon the accelerating electric field. At low fields, Figure VI-21, the pattern is not apparent.

The resolution in these pictures degrades as the Cs pressure is increased and improves as the magnetic fields are increased. Figure VI-25 at T_R = 475°K, compared with Figure VI-22 at T_R = 390°K, shows this decreased resolution. In Figure VI-26 both the Cs pressure and the main magnetic field have been increased, but there is still a net loss. A still larger field, Figure VI-27, illustrates the improved resolution. In each case where the field has been increased, the deflecting currents were held constant, thereby reducing the deflection angle and swept area and magnifying the display picture.

Cross scans of this surface with Cs only are shown in Figures VI-28 and VI-29. Figure VI-28 at T_R = 395°K consists of a series of plateaus, each of which corresponds to a traverse across an individual grain. Figure VI-29 at T_R = 475°K illustrates the loss of resolution at the higher cesium pressure and shows only the general shape seen in Figure VI-28, but none of the detail. Figure VI-30 is a T/T_R plot at T_R = 425°K for a dark and light area, locations A and B on Figure VI-28. The minimum work function is 1.7 eV, and there is a difference of about 0.07 eV over most of the T/T_R range. Also illustrated in this figure is a curve for T_R = 475°K. This curve was

shifted downward as the cesium pressure was raised.

Admission of additives to the device was then accomplished by cracking the metallic additive capsule and raising the reservoir temperature. The curve indicated by the squares in Figure VI-30 shows the work function produced with an additive reservoir temperature of 600°K and a Cs reservoir temperature of 400°K. The deviations from the Cs-only curves are not large enough to be significant. Another run made with a similar additive temperature and higher Cs pressure is shown by the circles in this figure. Again there is not a significant effect apparent.

The cross scans and display photographs, Figures VI-31 and VI-32, taken under these conditions, illustrate similar patterns to those obtained earlier with Cs only, except for a darkening of the central region caused by stray collector emission. These currents arise because of the relatively high collector temperatures required to prevent condensation of the additive vapor on the collector surface. Since this current is also deflected toward the probe by the sweeping magnetic fields, a dip in total probe current occurs near the center of the patterns. In Figure VI-31 this effect appears as the slope of the base line. This base line, irrespective of its shape, is the equivalent of a horizontal base line and is used in exactly the same manner when reducing the data. The same phenomenon occurred during tests involving the tungsten surface and is shown in Figure VI-33.

During the additive experiments using the molybdenum surface, difficulties were experienced with the control of the cesium pressure due to the restricting orifice in the tubulation. This is illustrated

by examining Figure VI-30. In this figure a comparison of the square symbols, which were the result of operation at $T_R = 400°K$, with the open circles, which were the result of operating at $T_R = 424°K$, gives an apparent difference. However, if the data of the open circles is replotted, using 400°K instead of 424°K, the results are identical to the previous 400°K points (squares). This supports the conclusion that the change of cesium reservoir temperature did not change the cesium pressure in the scanner chamber.

Before the conditions inhibiting cesium pressure control could be corrected, the thin-wall sleeve which supports the test surface developed a crack, and testing had to be discontinued. Thus equilibrium experiments could not be performed, and conclusive additive data was not obtained for the molybdenum surface under thermionic scanner conditions.

Examination of the results obtained with the molybdenum surface in the photoelectric scanner and of the data resulting from operation of the tungsten surface in the thermionic scanner lead to the prediction that, upon attainment of equilibrium, the molybdenum surface in the thermionic scanner would also show improved performance potential. It is therefore recommended that future programs include such experiments.

D. Interrelation of Emission Data and Metallurgy

The large grain size and irregular grain shape made it possible to match the thermionic emission map of the surface and its appearance under an optical microscope. A composite metallographic picture, an emission map, a sketch of the grains, and a cross scan are shown in Figure II-1.*

* All cross scans of the molybdenum surface were made along this same diameter.

Several important features of the patterns are evident from this figure. Within each grain the emitted current is uniform, as indicated by the flatness of the plateaus in the cross scan and the constant brightness in the display pictures. The darkening of grain boundaries on the emission map and the dips in the cross scan caused by low emission in these regions correspond to similar patterns appearing on the metallograph. The reduced emission areas correspond to areas denuded of surface precipitates, near the boundaries. Dark spots such as those appearing on grain No. 5 show up in both the emission and optical pictures, indicating that they are a feature of the grain, and they are believed due to a local contamination. Figure VI-34, a 75 x metallograph, illustrates the spotted grain identified by the arrow on the emission map in Figure II-1. These features and the width and geometrical form observed with the scanner correlate closely with those observed on the metallograph. Therefore it is clear that the shape of the pattern is the same on the thermionic map and metallograph, and emission is definitely related to the grain configuration.

As discussed in Chapter VIII, Laué photographs were taken of each of eight grains along the cross scan. Using these photographs it is possible to assign an angle to each grain, which represents the angle between the ⟨110⟩ pole and the grain normal and therefore is a measure of the misorientation of the grain surface with respect to the ⟨110⟩ plane. These angles are tabulated, with calculations of work function for the corresponding grains in Table III. In Chapter VIII the data of Table III is discussed in detail.

Two other observations can be made from the Laué patterns. The patterns are in each case quite simple, and can be interpreted

TABLE III

COMPARISON OF GRAIN ORIENTATION AND WORK FUNCTION

Mo Test Surface

$T_E = 790°K$

$T_R = 390°K$

$T/T_R = 2.0$

Grain Number	Orientation of ⟨110⟩ pole to surface normal	Work Function eV
4	23.5	1.65
1	20.5	1.67
6	18	1.65
2	16.5	1.60
3	12	1.60
5	11	1.60
8	1.5	1.61

as coming from only one grain. This means there are no concealed grain boundaries for, if there were, the Laué pattern would show two complete sets of spots, one for each grain.* Furthermore, the Laué spots are sharp. This means the grains show little substructure (they are in a well annealed condition). They do not have small local variations in orientation, which might be too small to produce two sets of Laué spots, but would smear out the existing spots. This uniformity of structure within the grain is reflected as a uniformity of emission in the scanner.

Therefore we can conclude that, although emission is a surface phenomenon, it is affected by the underlying crystal orientation.

* This is confirmed by the regularity of the array of precipitate particles in each grain. (See Figure VIII-6.)

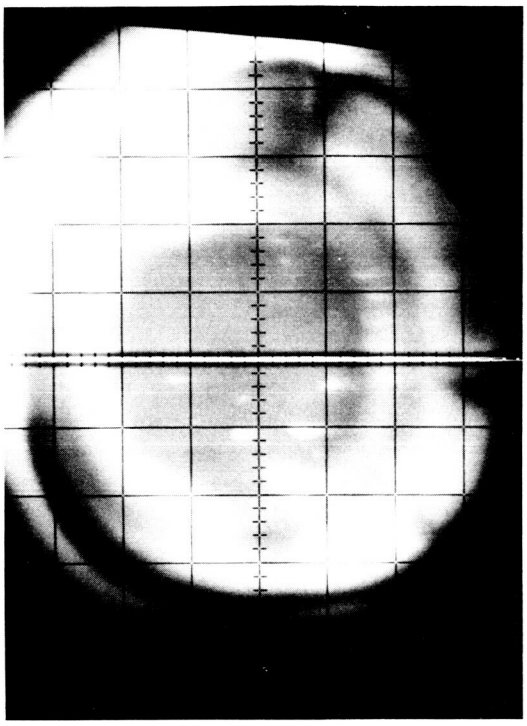

Figure VI-1. Typical Thermionic Scanner Display Photograph

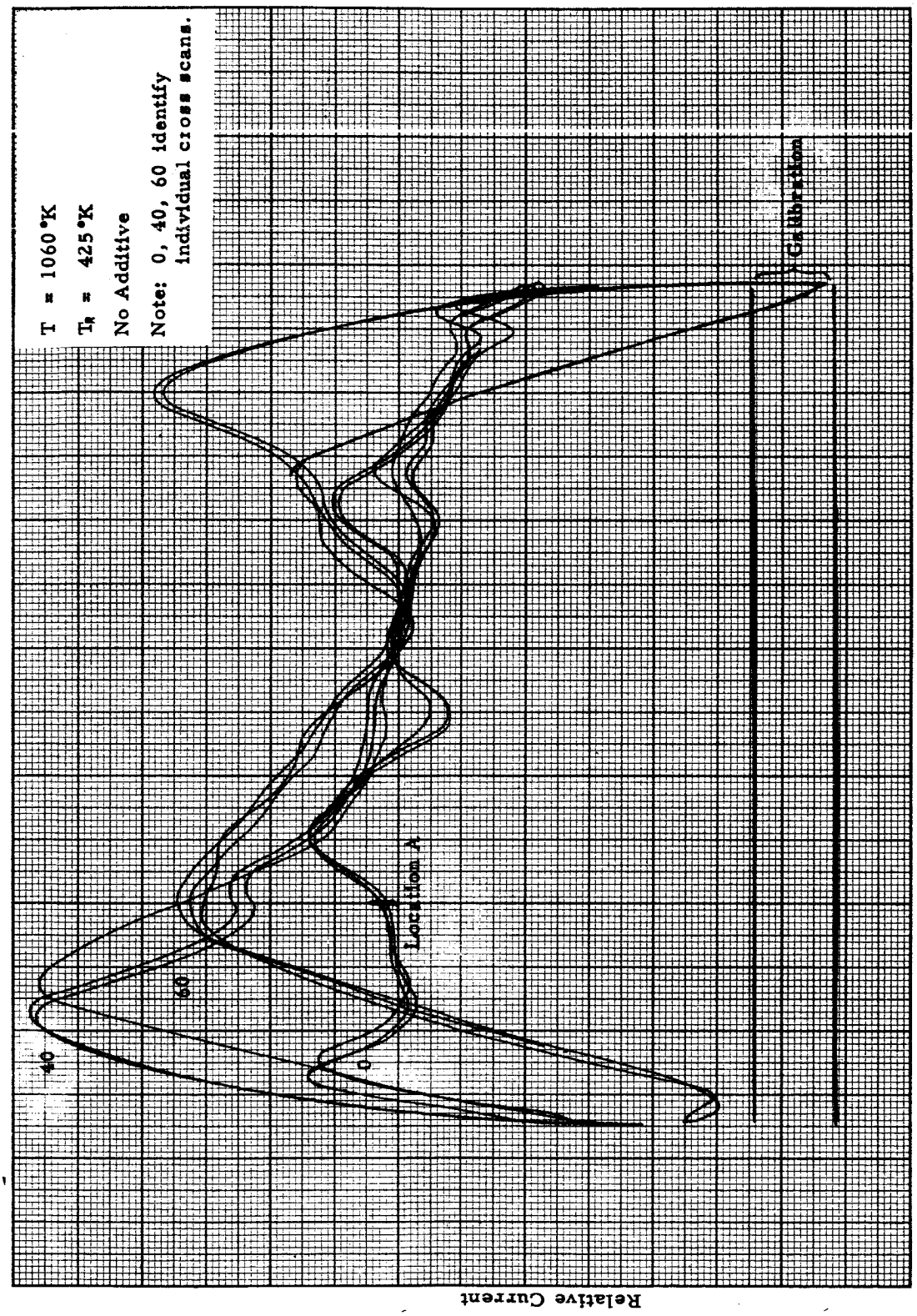

Figure VI-2. Cross Scan (No. 55) T=1060°K, T_R=425°K
Therminonic Scanner

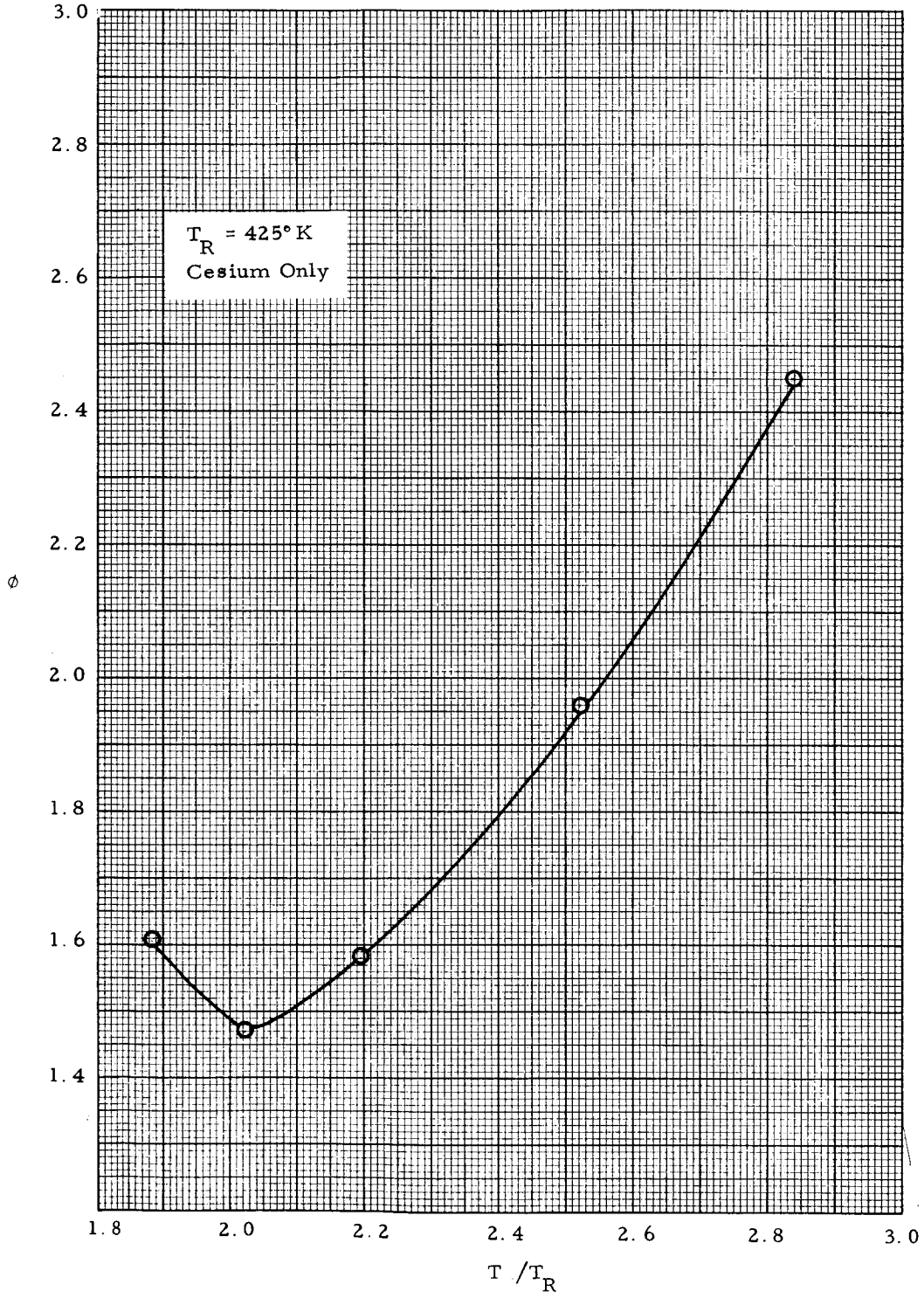

Figure VI-3. Ø vs. T/T_R, T_R=425°K, Tungsten Surface

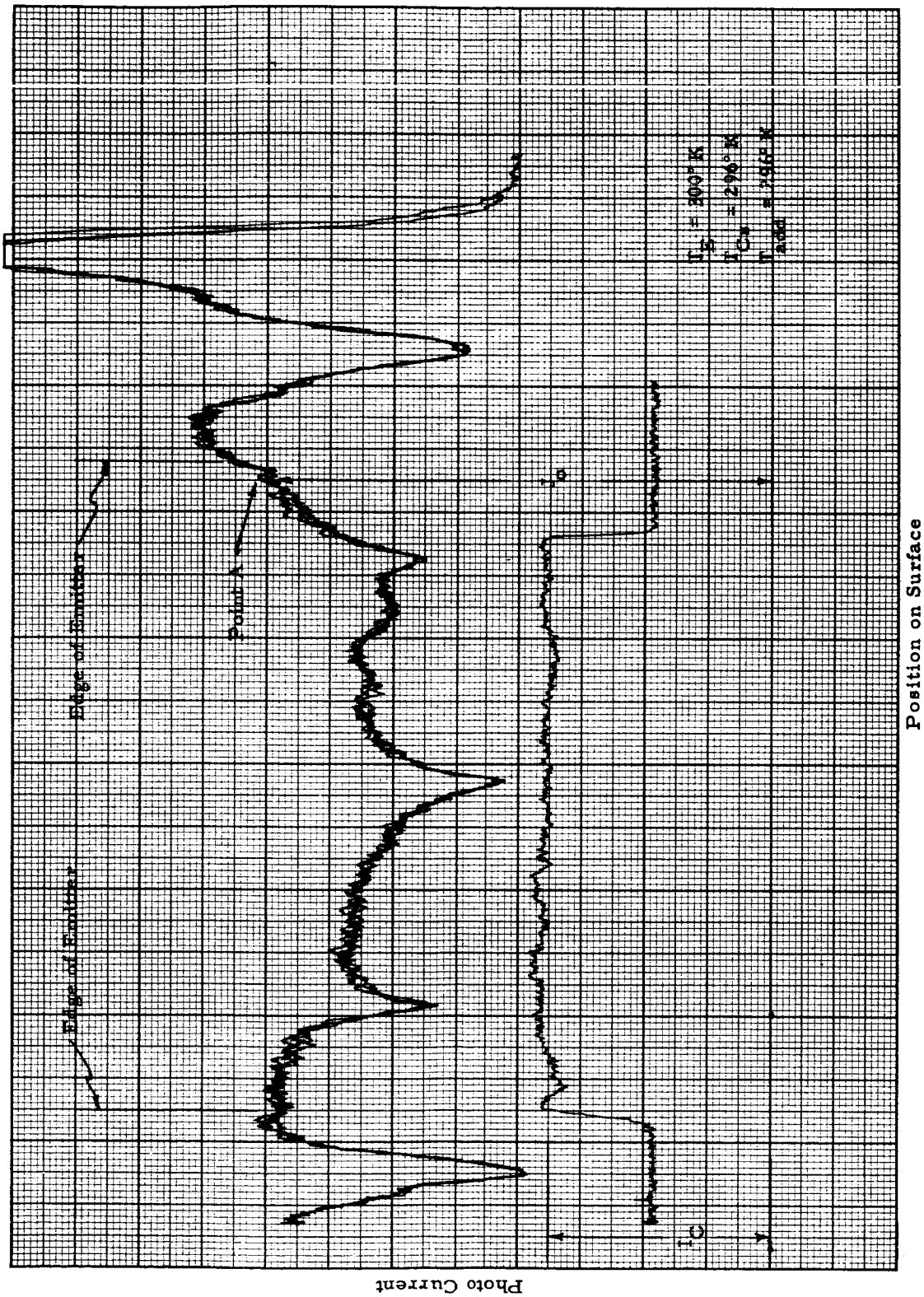

Figure VI-4. Typical Single Line Cross Scan (Photoelectric Scanner)

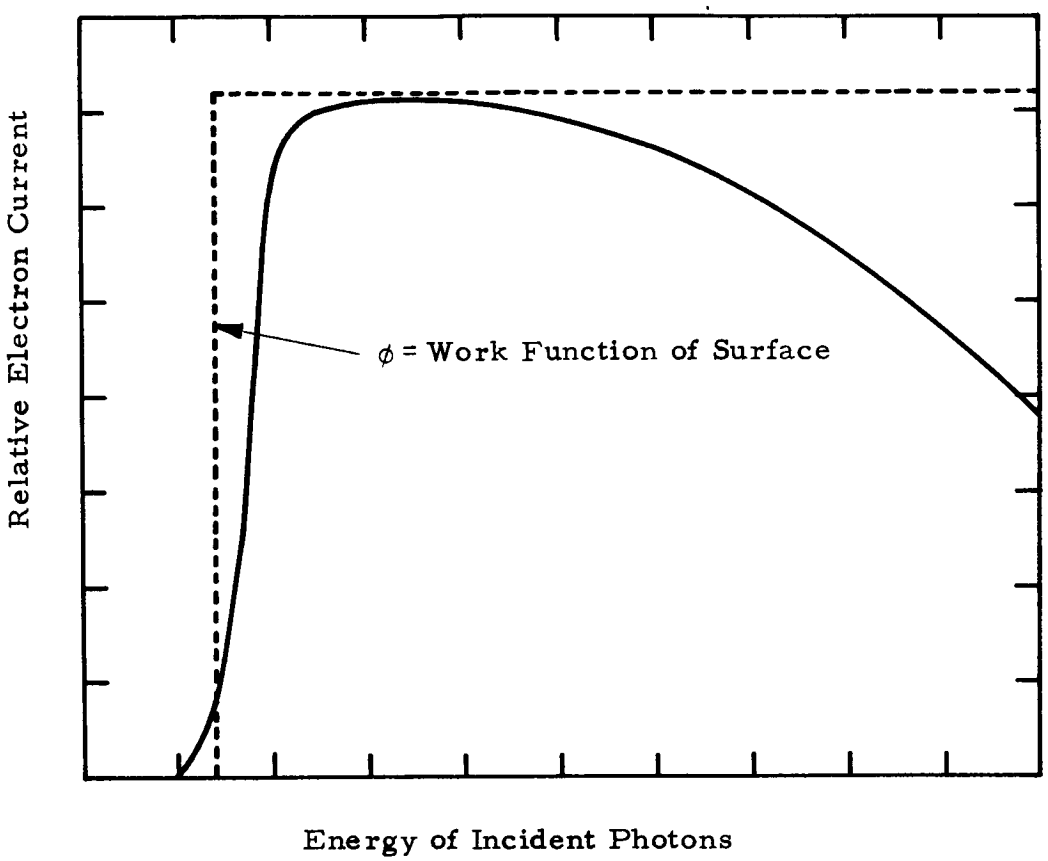

Figure VI-5. Quantum Effect Plot

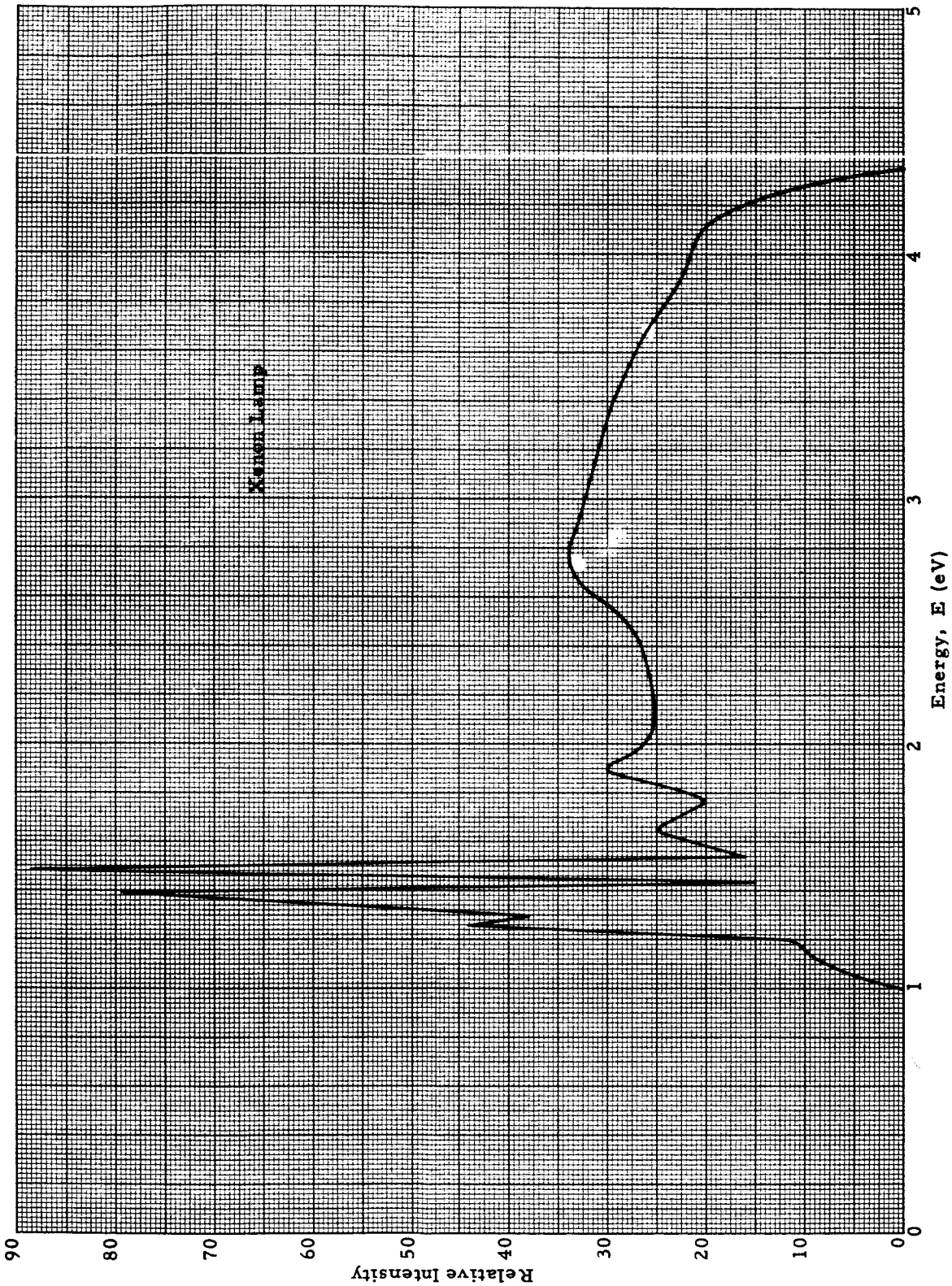

Figure VI-6. Xenon Lamp Spectrum

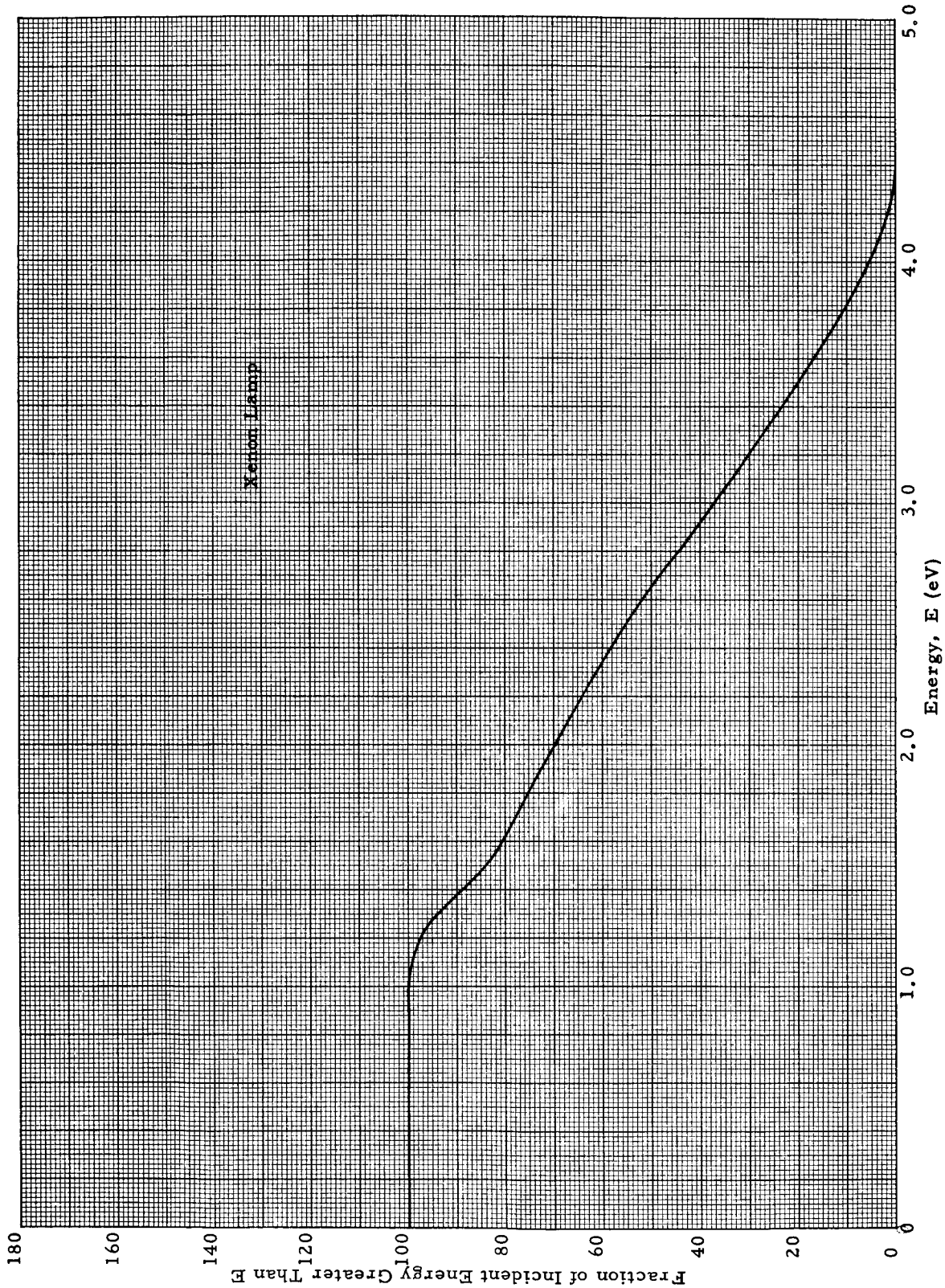

Figure VI-7. Integrated Xenon Lamp Spectrum

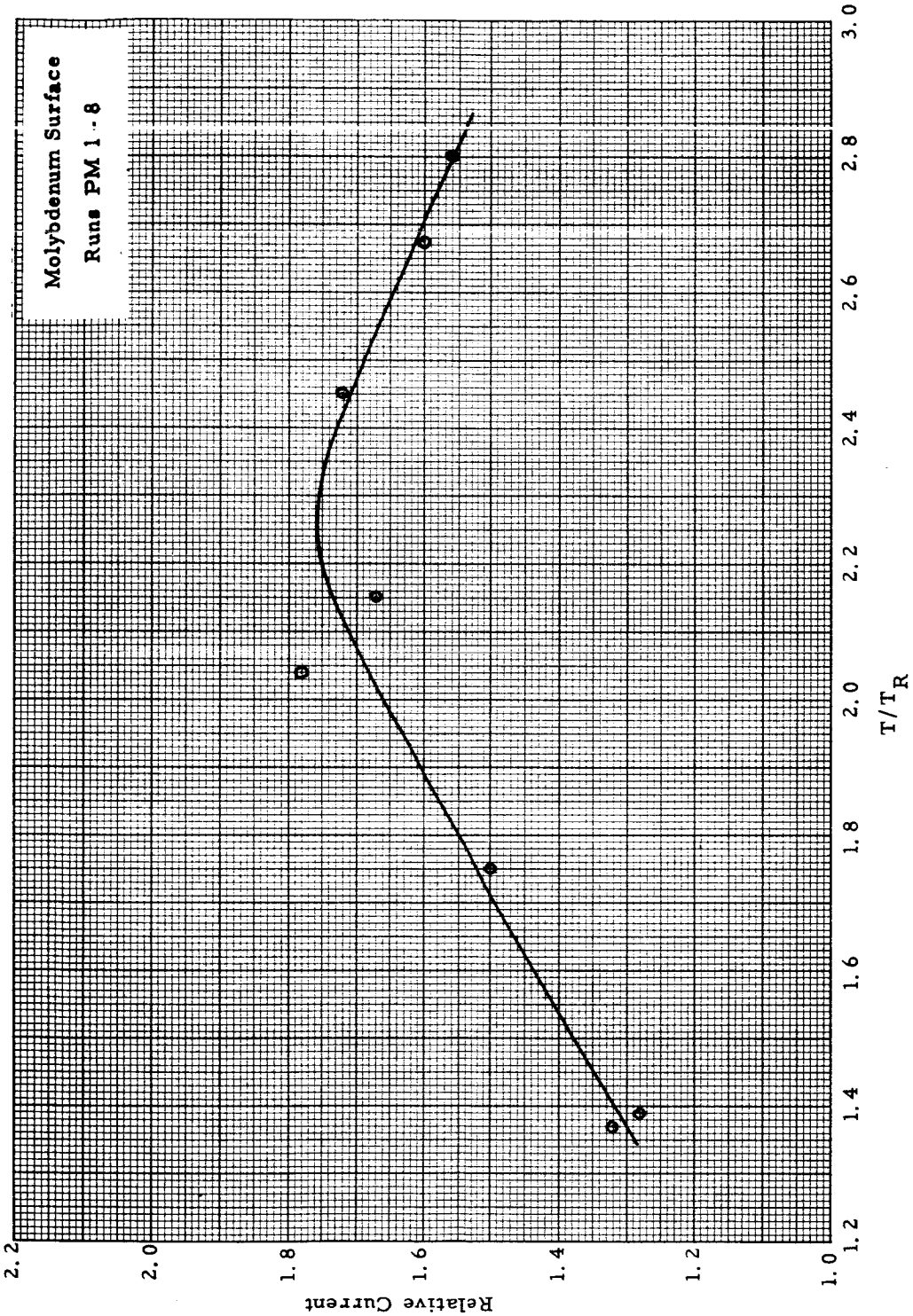

Figure VI-8. Relative Photocurrent vs. T/T_R

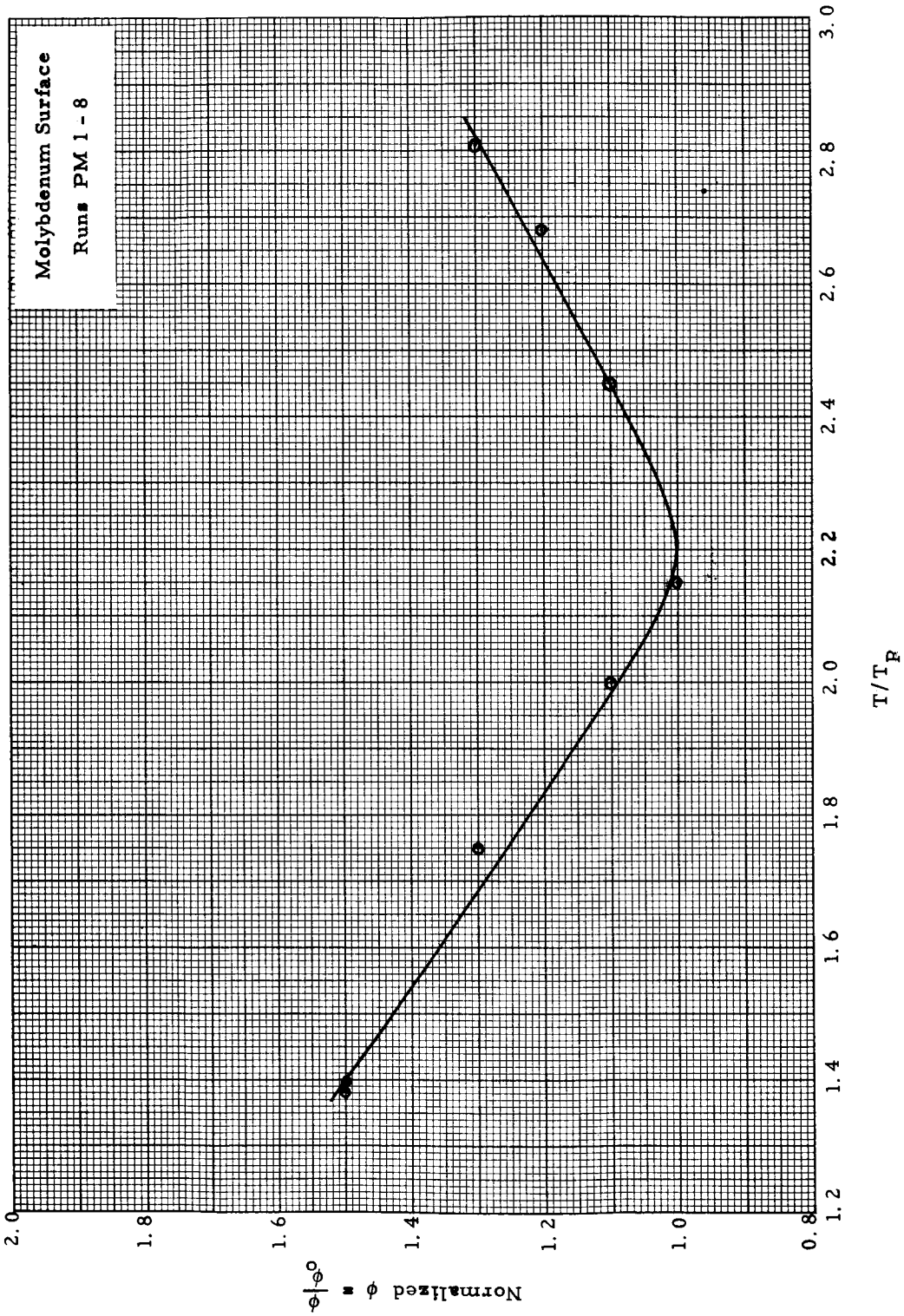

Figure VI-9. Normalized ϕ vs. T/T_R for Photoscanner

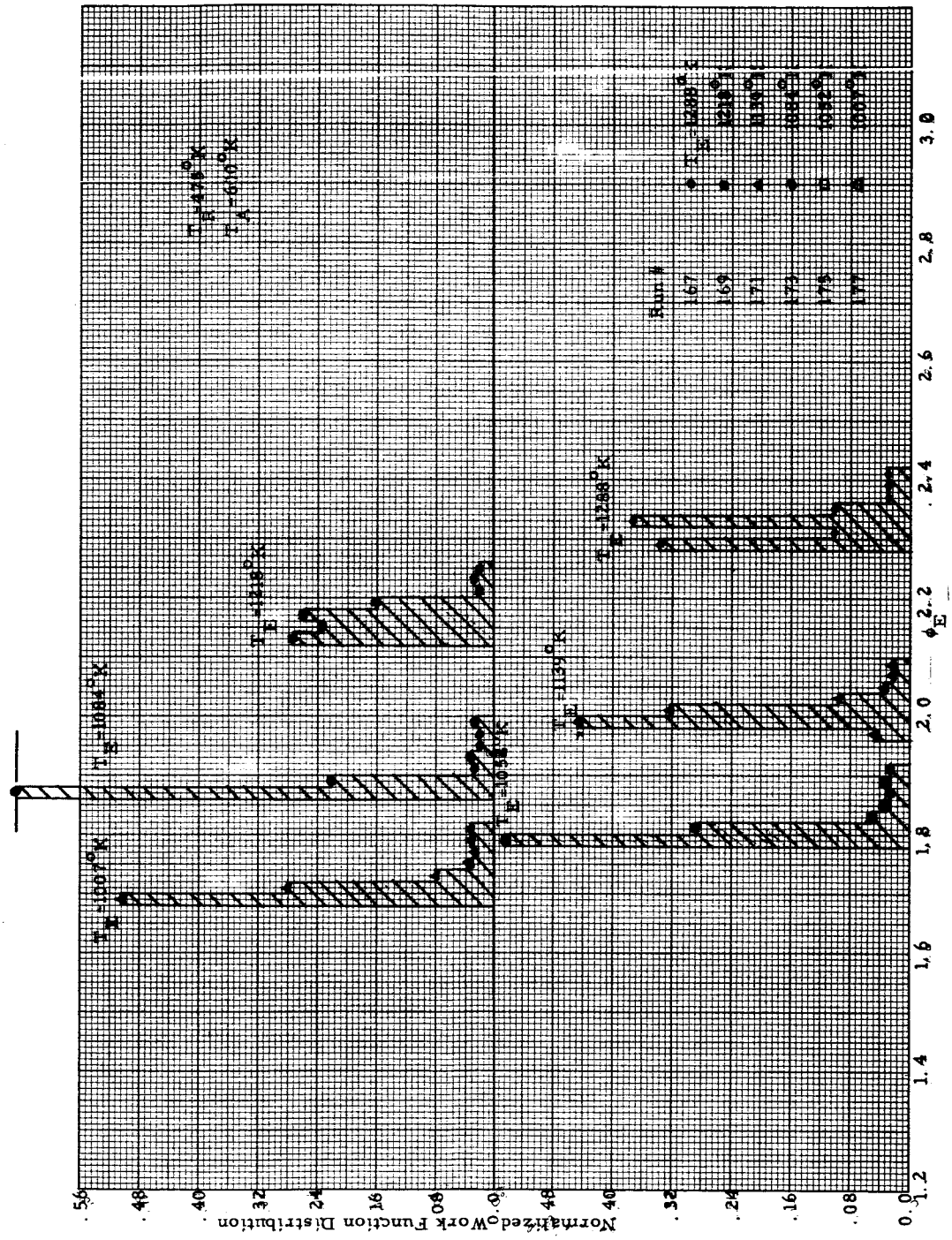

Figure VI-10. Work Function Distribution for Tungsten

Test Surface Edge

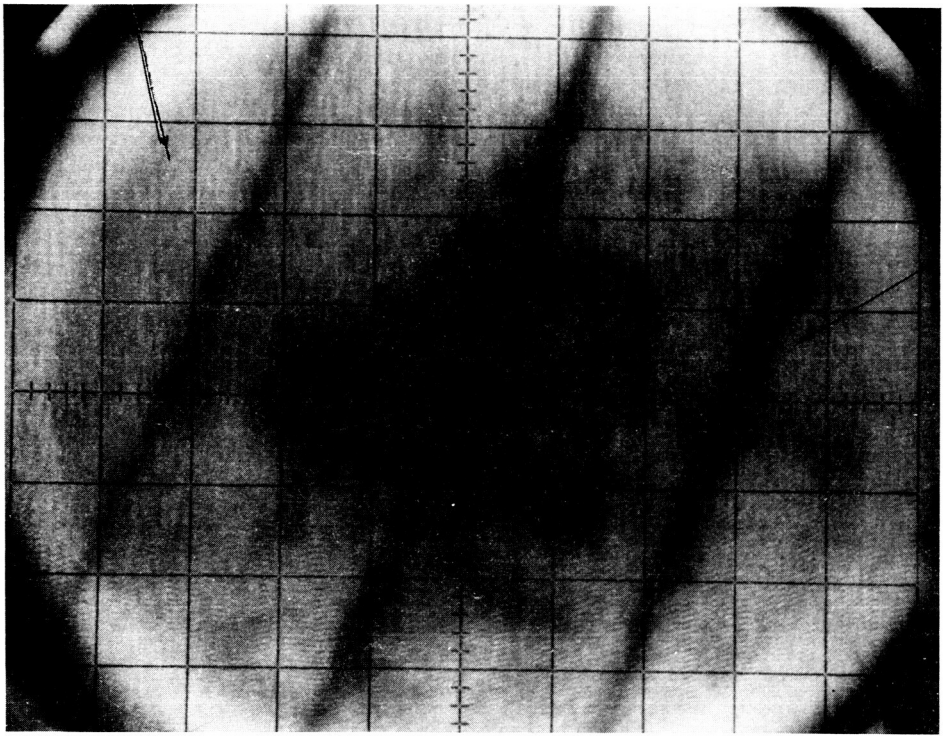

Wire Shadow

Figure VI-11. Scanner Display Photograph

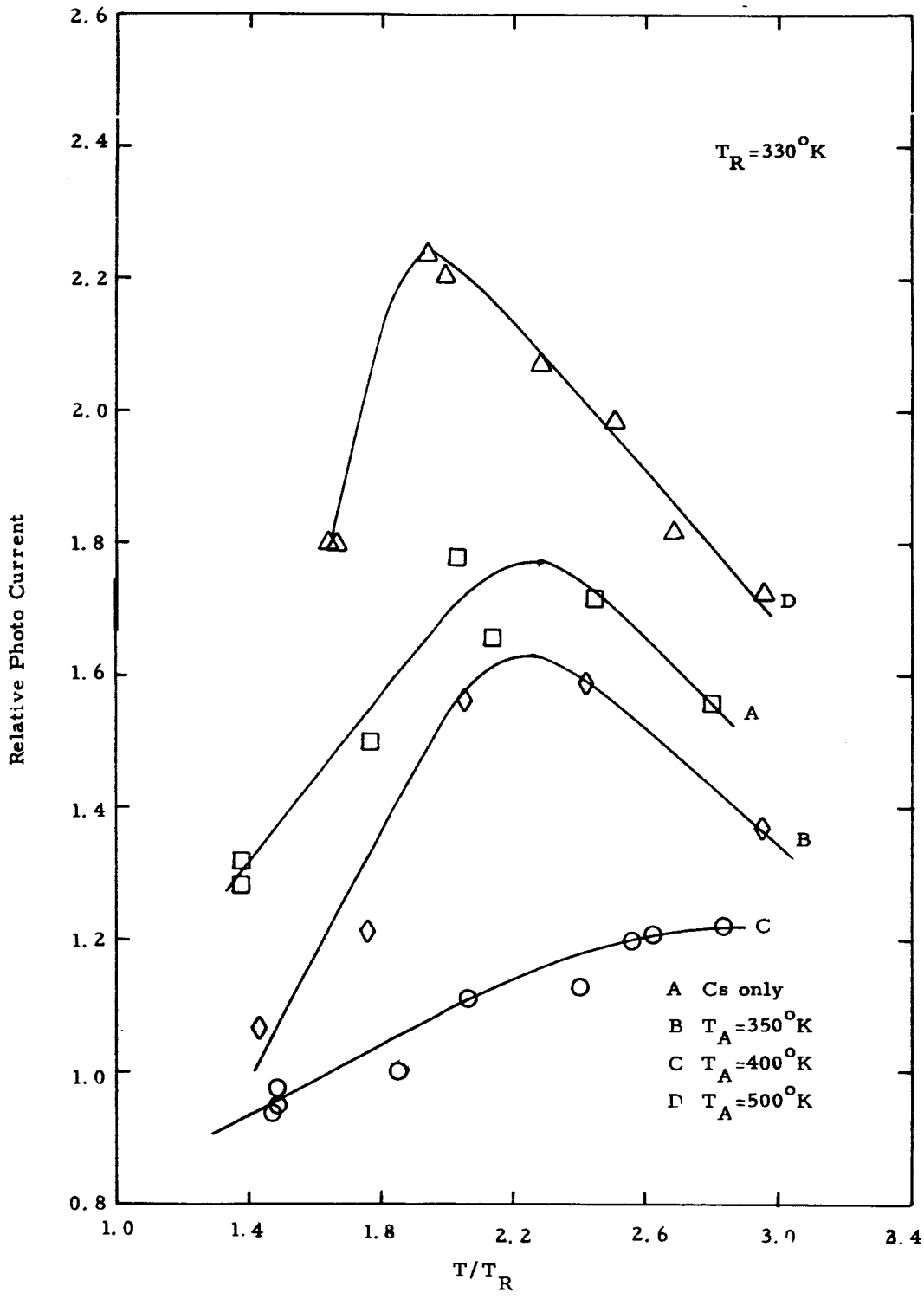

Figure VI-12. Relative Current vs T/T_R for Photoscanner.

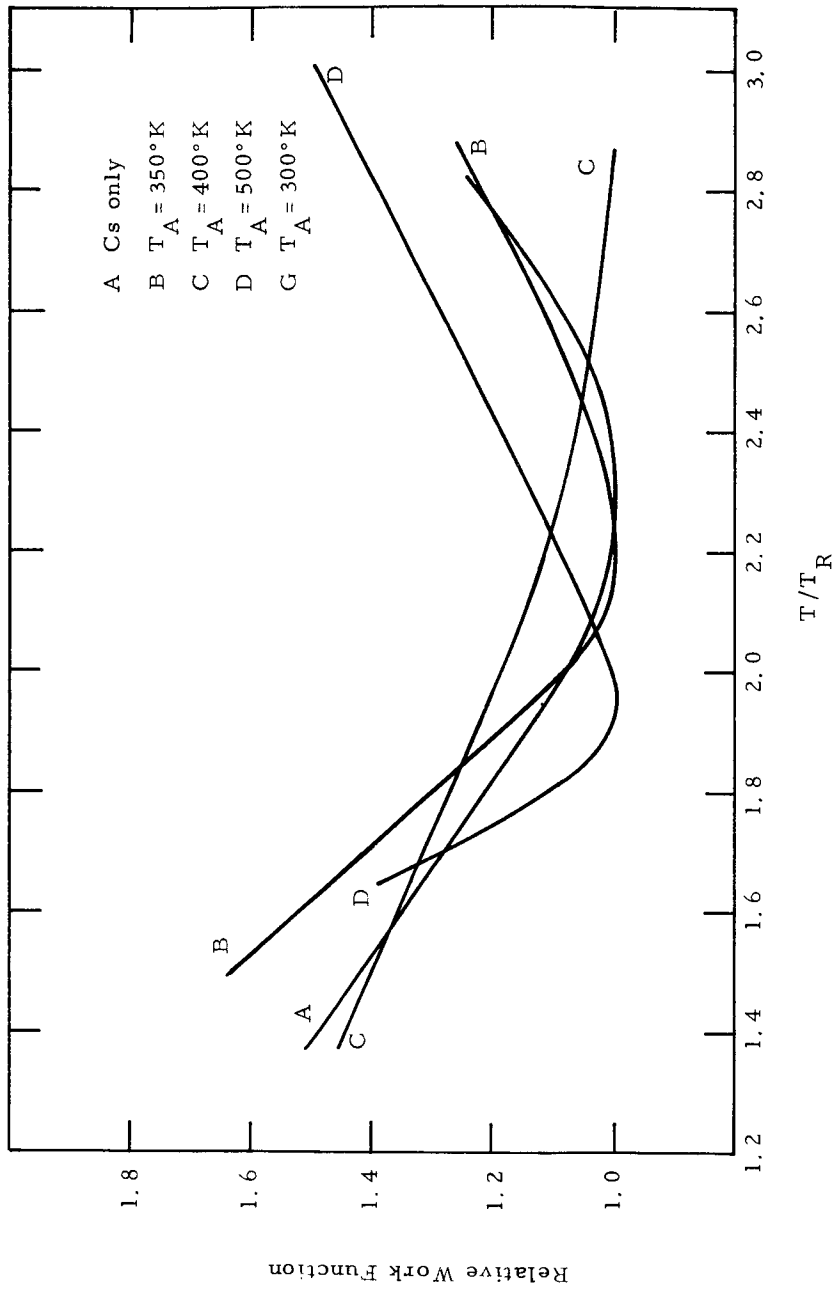

Figure VI-13. Relative Work Function vs T/T_R.

64-R-2-10

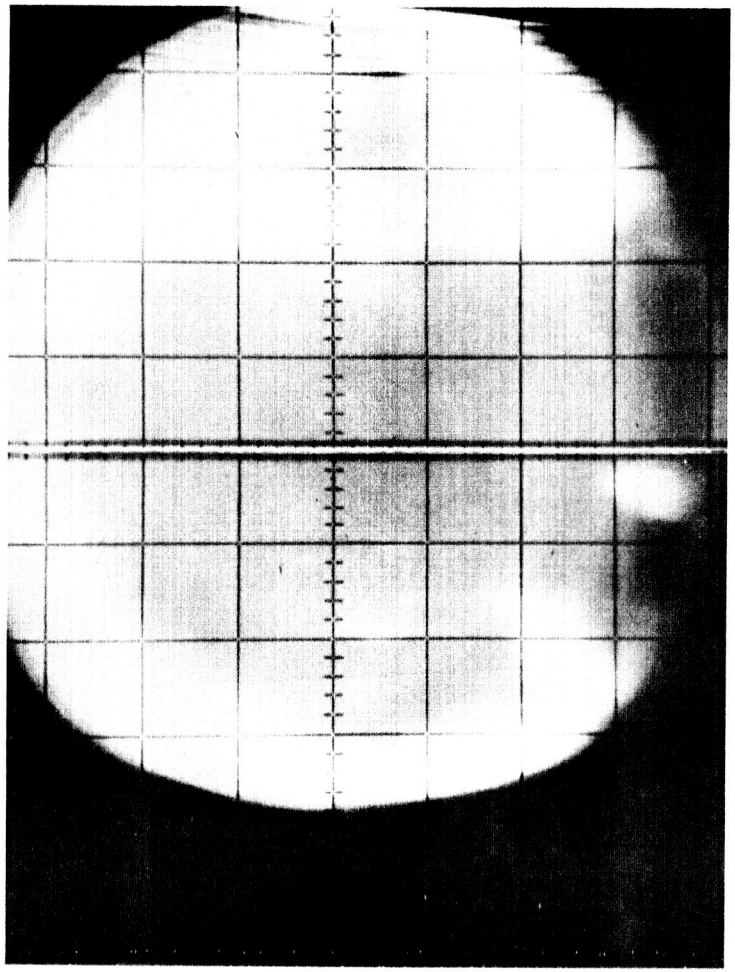

Figure VI-14. Display Photo (No. 12)
$T=1280^{o}K$, $T_R=425^{o}K$, $T_A=425^{o}K$

64-R-2-9

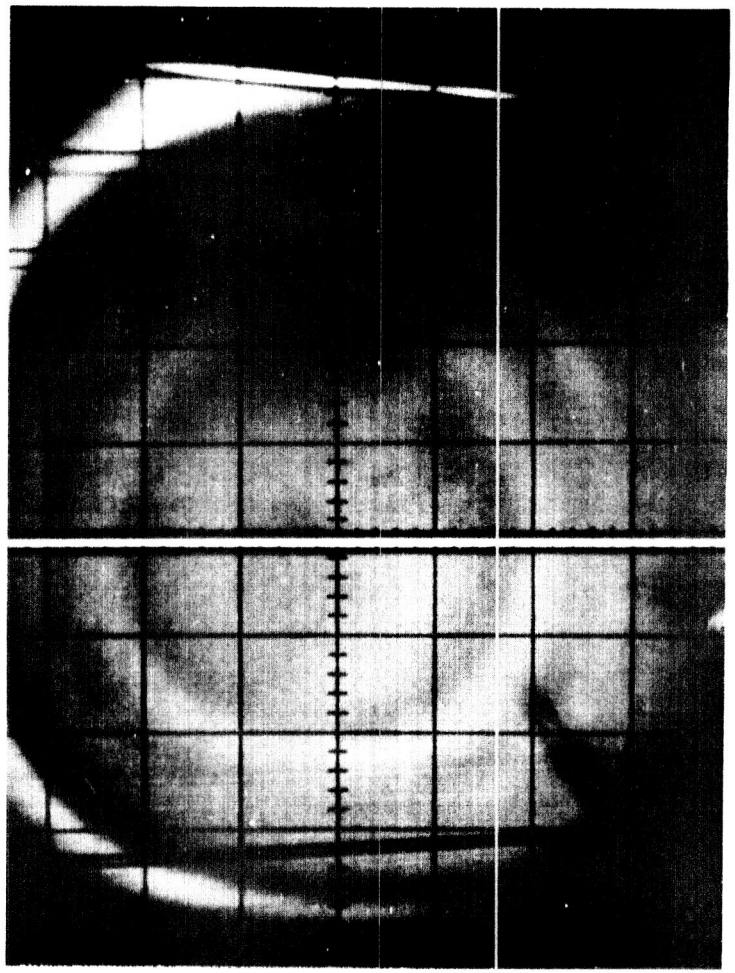

Figure VI-15. Display Photo (No. 19)
$T=1080^{o}K$, $T_R=425^{o}K$, $T_A=425^{o}K$

THERMO ELECTRON
ENGINEERING CORPORATION

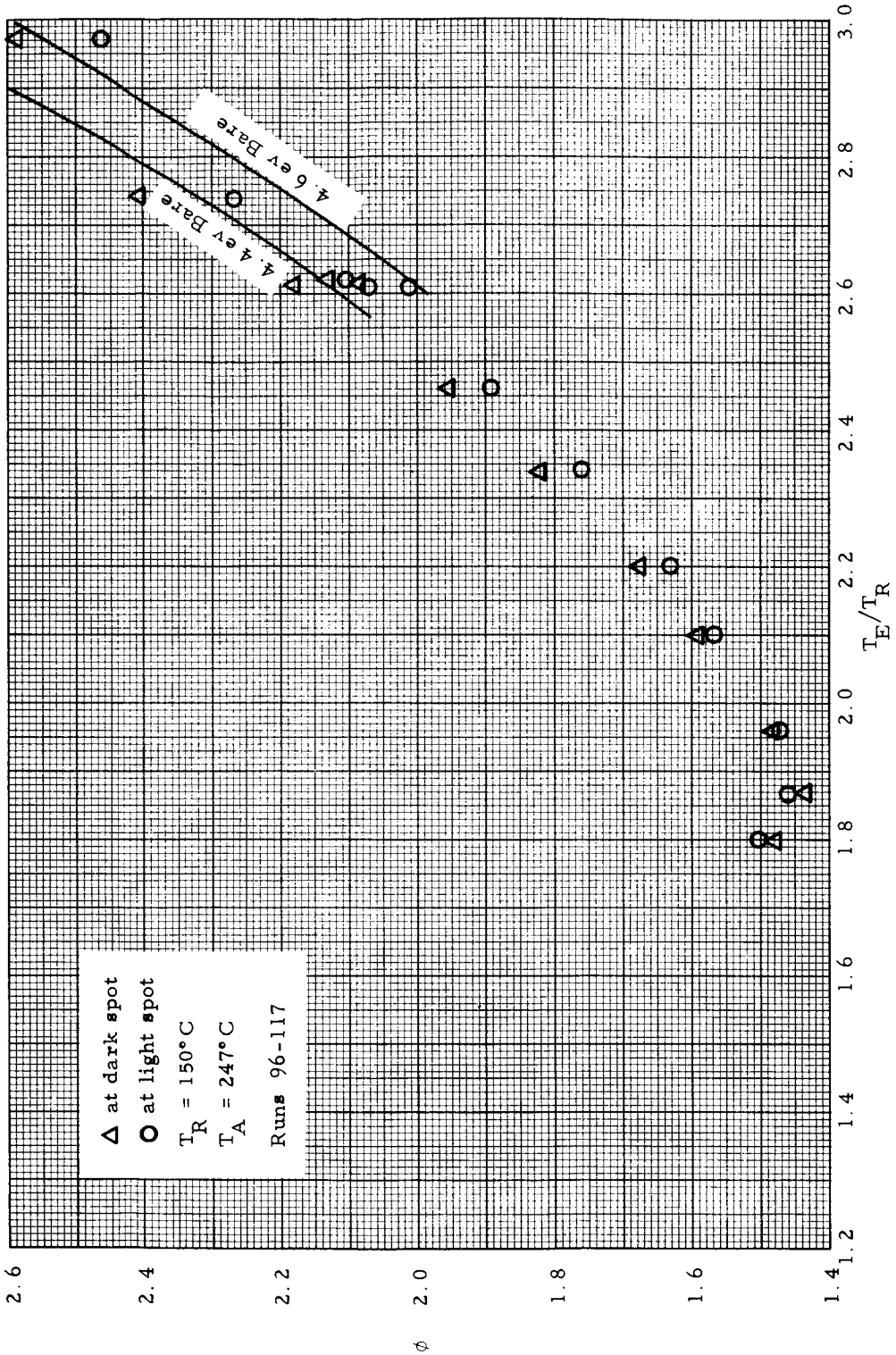

Figure VI-16. Work Function Plots of Two Patches

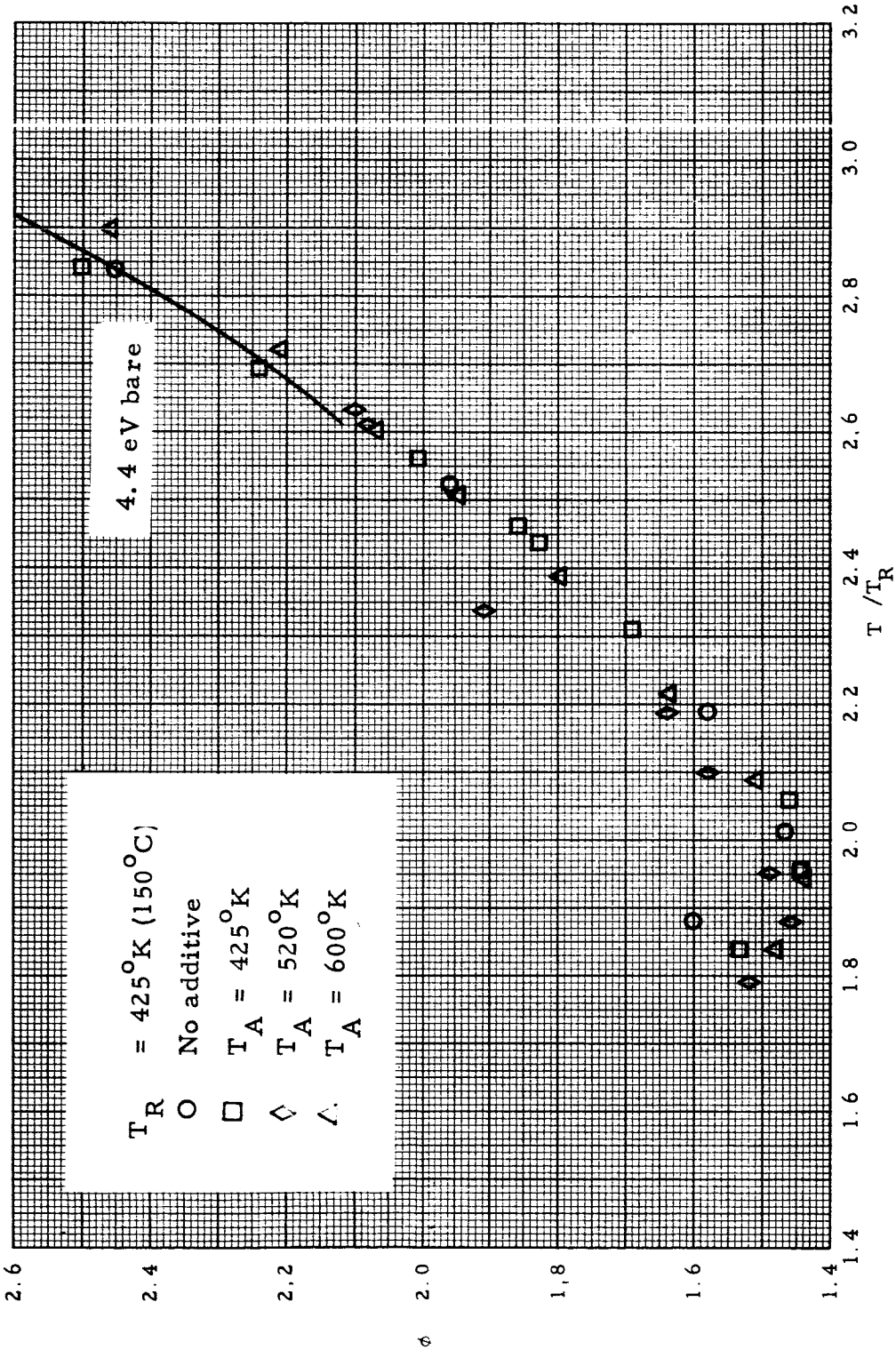

Figure VI-17. Φ vs. T/T_R T_R=425°K

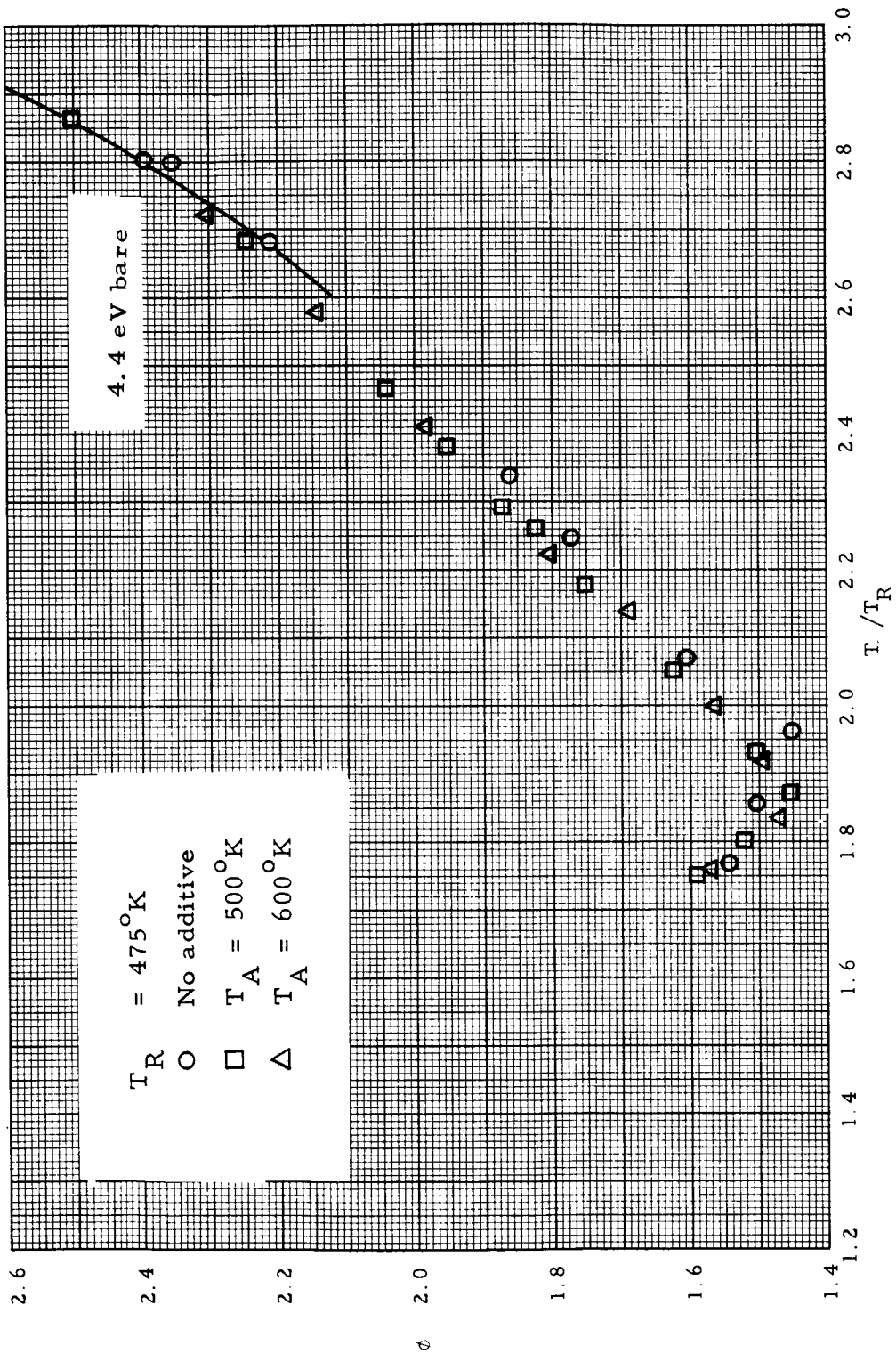

Figure VI-18. ϕ vs. T/T_R, T_R=475°K

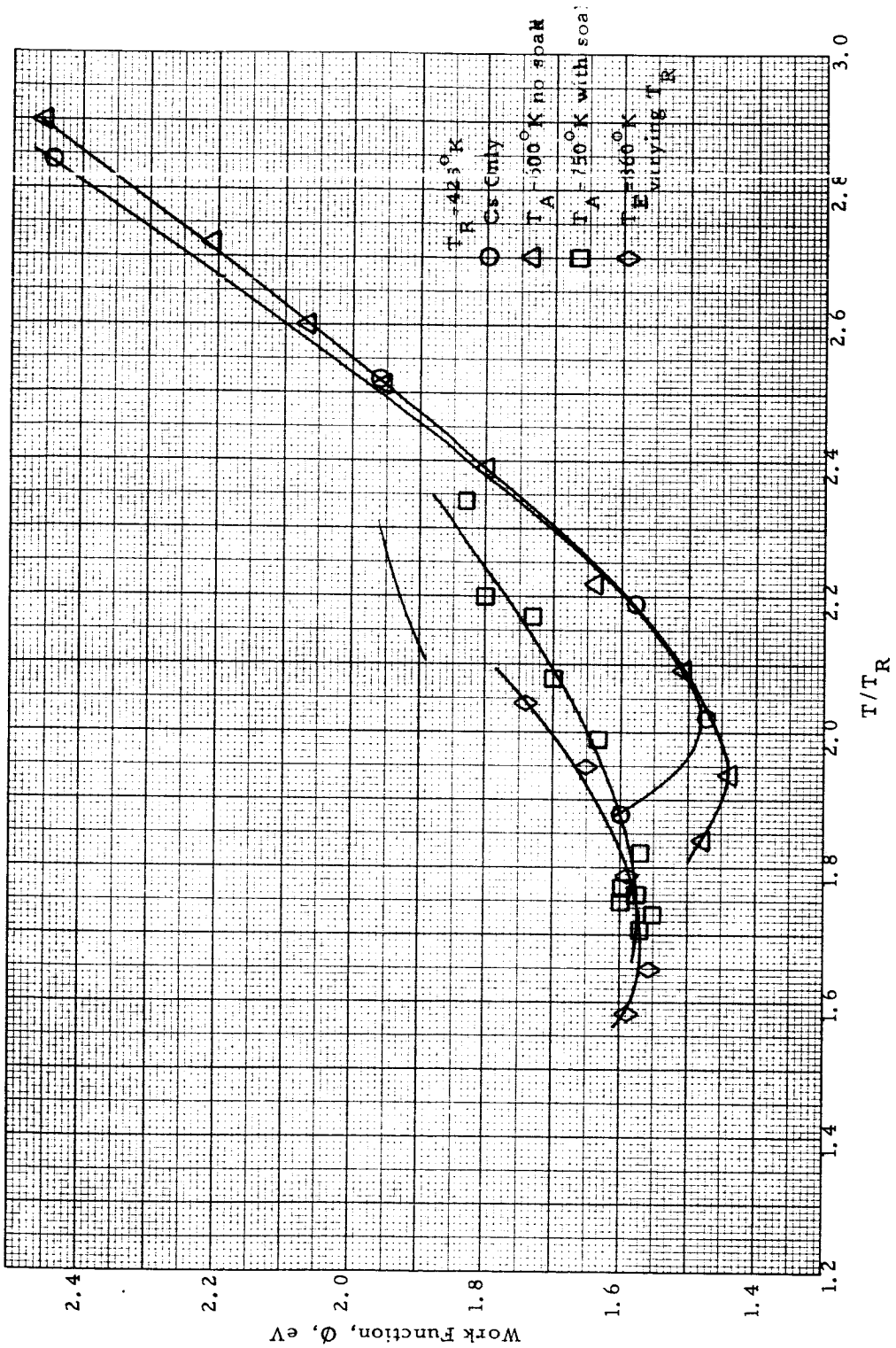

Figure VI-19. Summary of Work Function Variations on Tungsten Surface

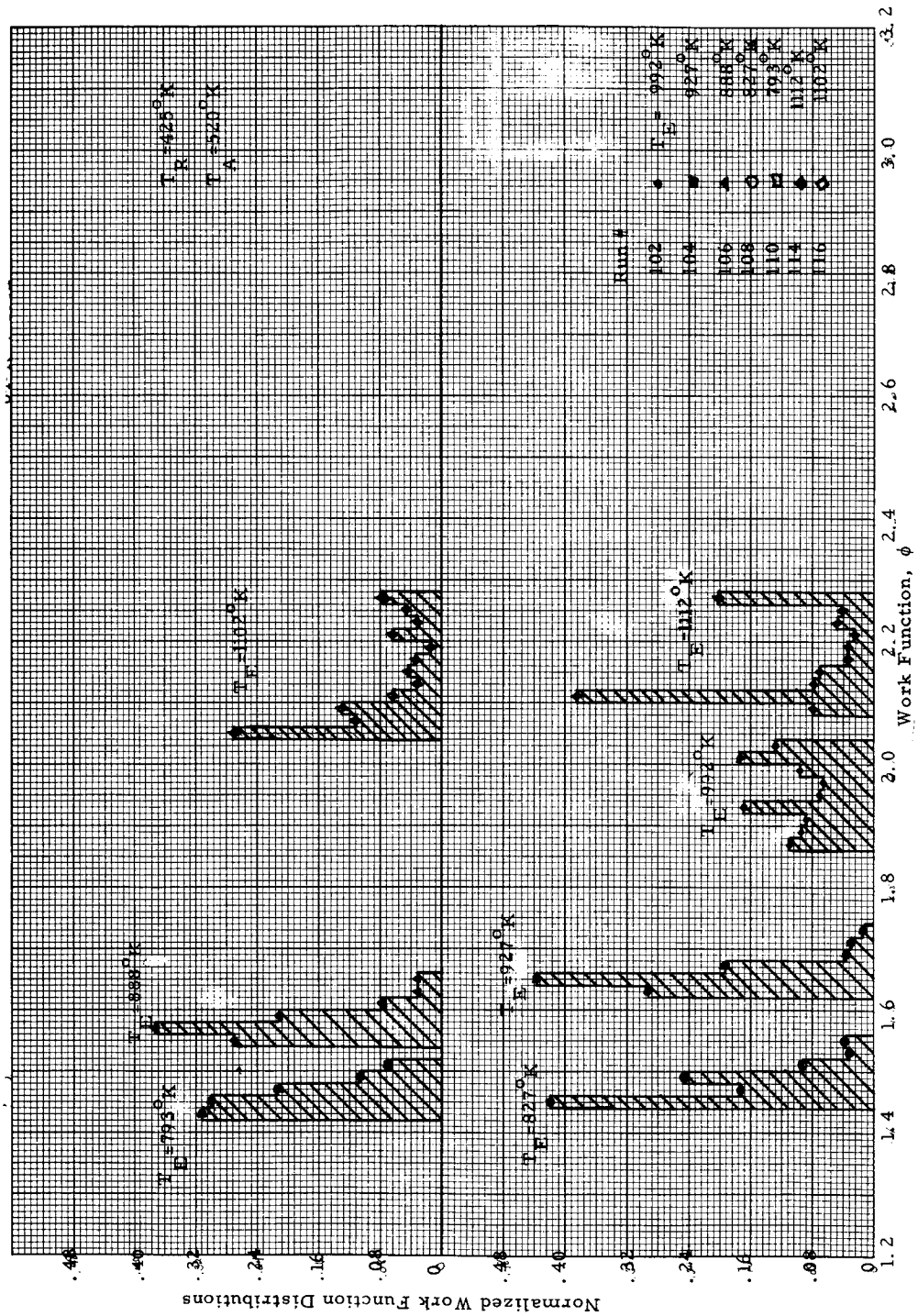

Figure VI-20a. Work Function Distribution for Tungsten

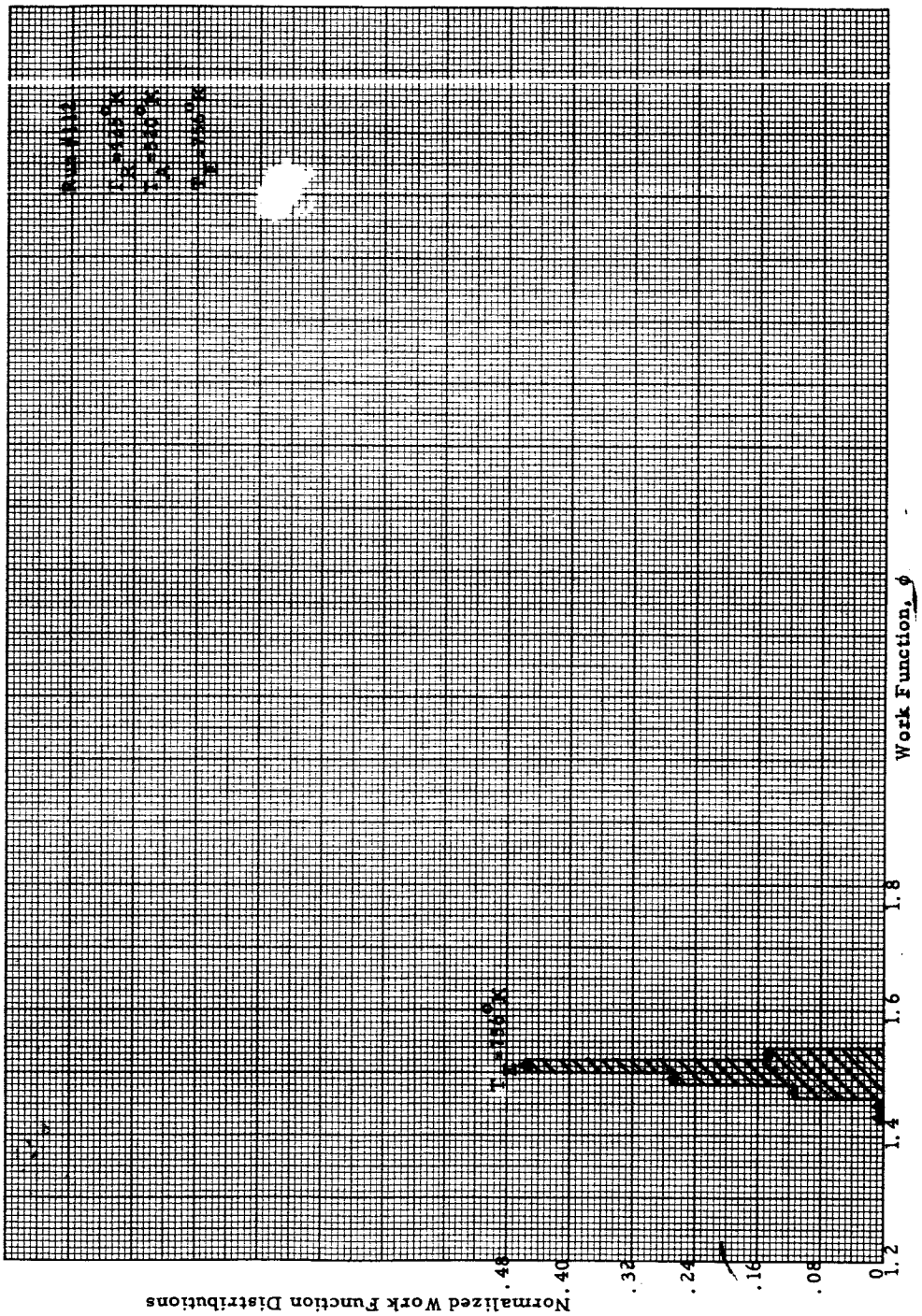

Figure VI-20b. Work Function Distribution for Tungsten

64-R-7-108

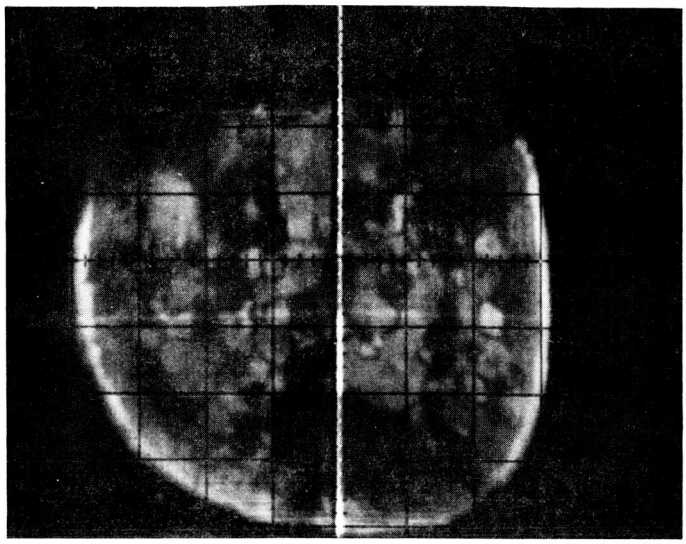

Figure VI-21. Overall Display of Molybdenum Emitter

64-R-7-109

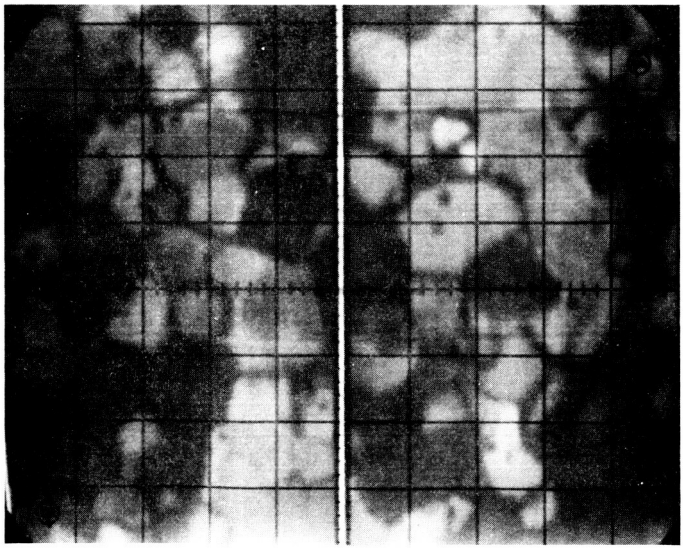

Figure VI-22. Enlarged Display of Central Region

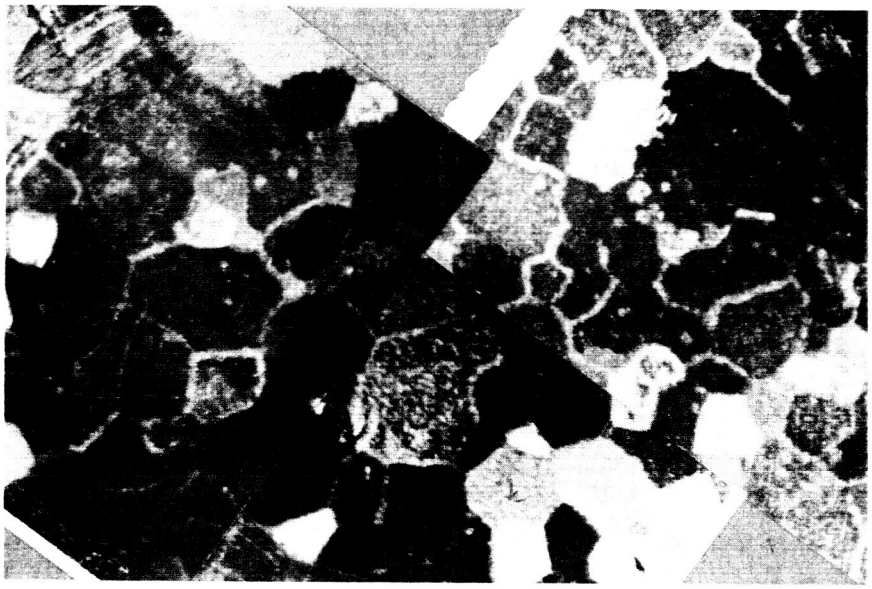

Figure VI-23. Composite Metallograph of Central Region

64-R-7-111

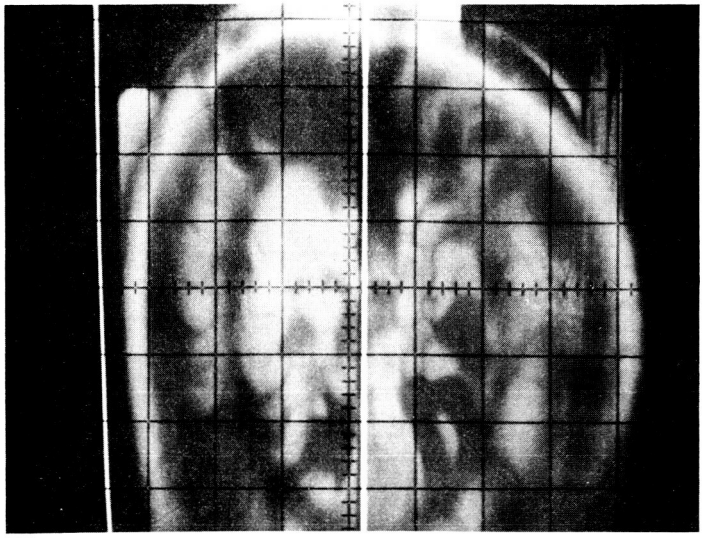

Figure VI-24. Concentric Ring Pattern at High Electric Fields

64-R-7-112

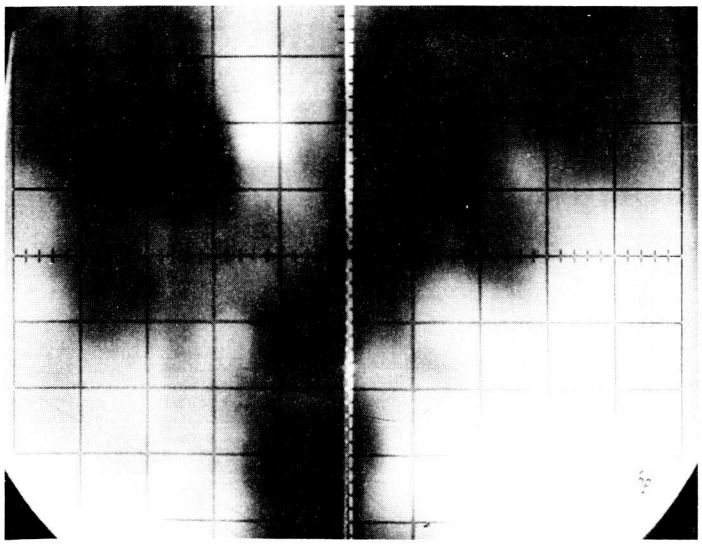

Figure VI-25. Central Region with Increased Cesium Pressure Showing Loss of Resolution

64-R-7-113

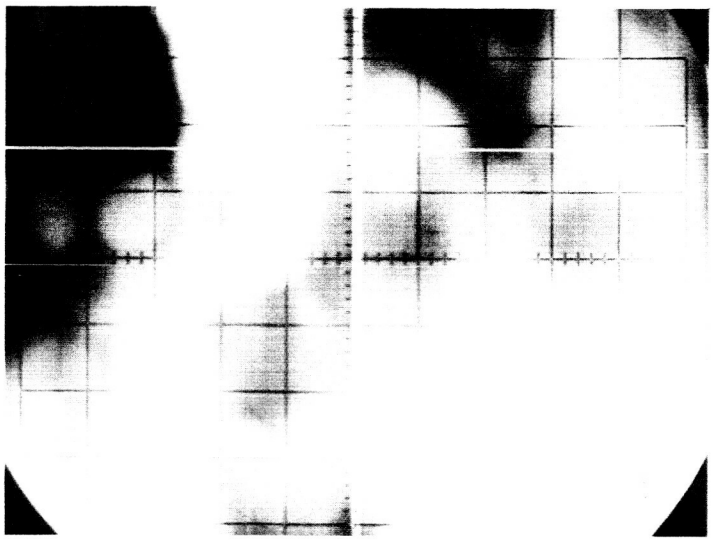

Figure VI-26. Same as VI-26 with Increased Collimating Field Showing Improved Resolution

64-R-7-114

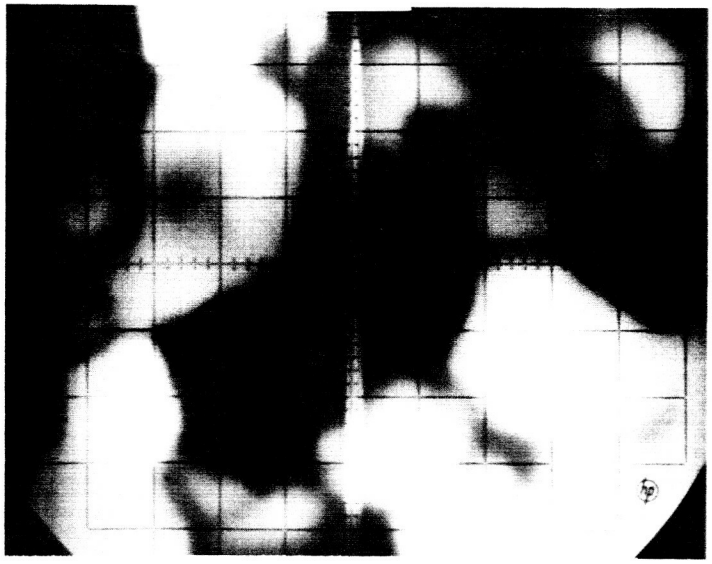

Figure VI-27. Central Region of Molybdenum Surface Showing Resolution with High Cesium Pressure and Large Magnetic Field

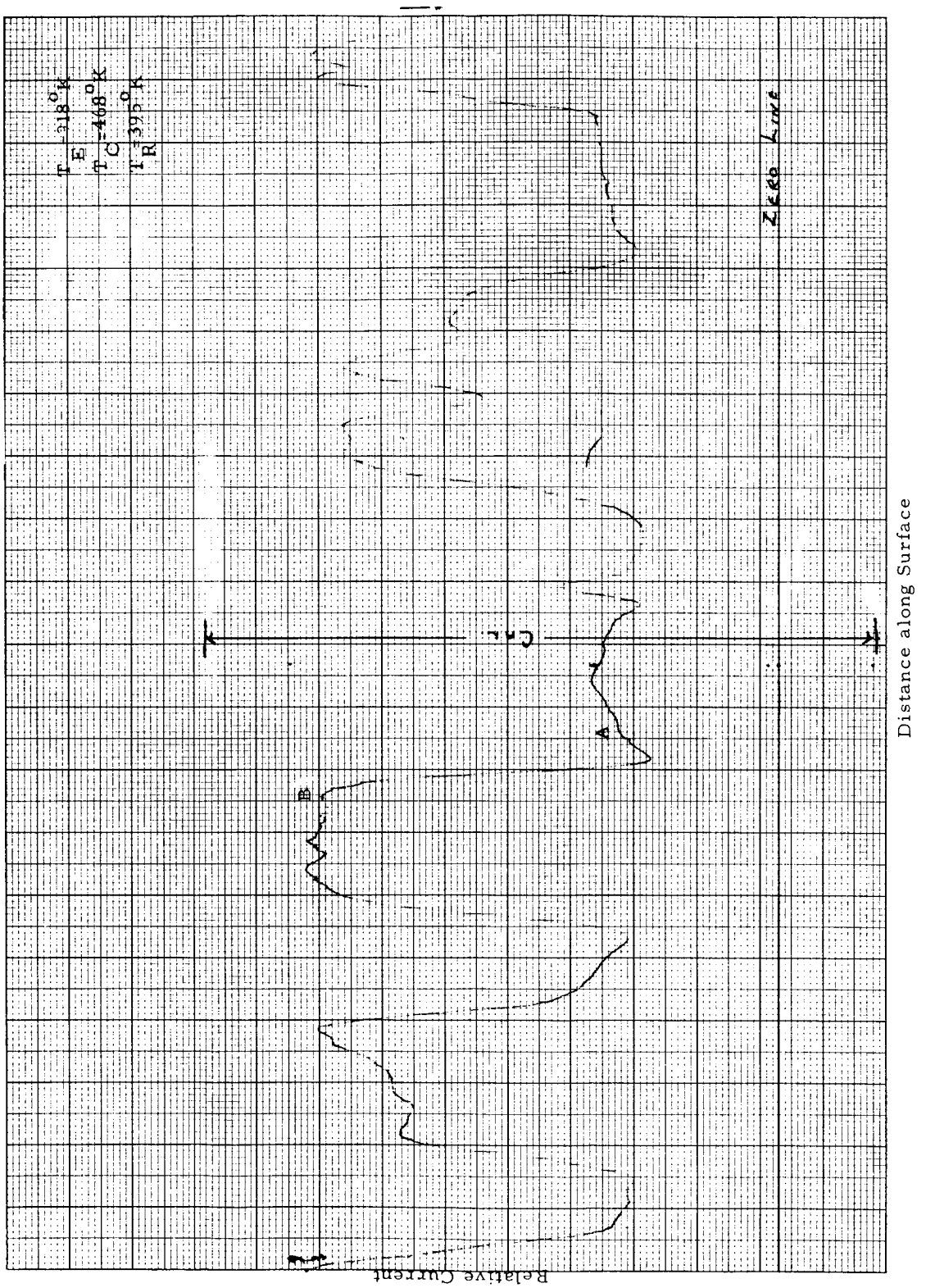

Figure VI-28. Typical Molybdenum Test Surface Cross Scan

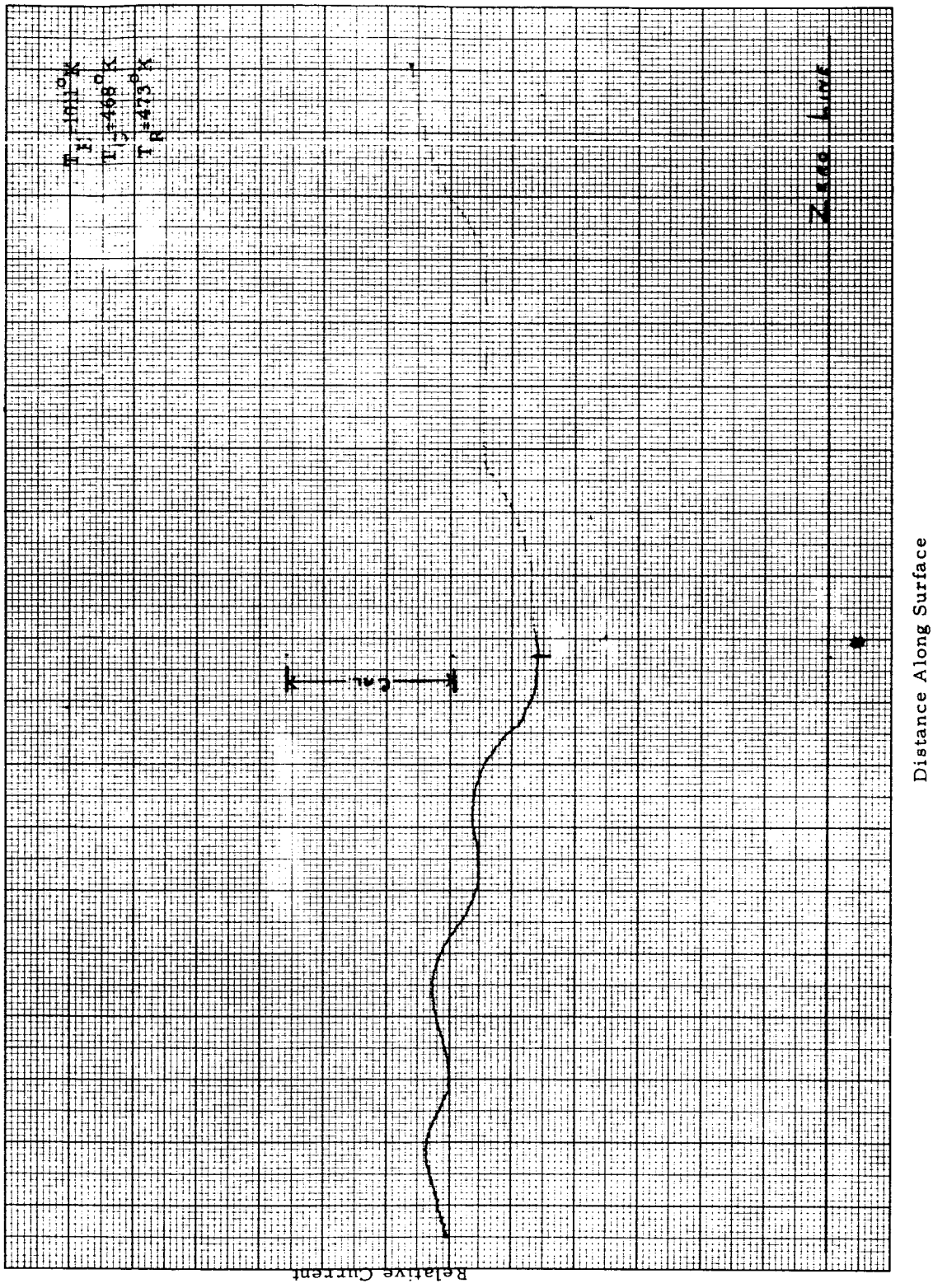

Figure VI-29. Typical High Cesium Pressure Cross Scan

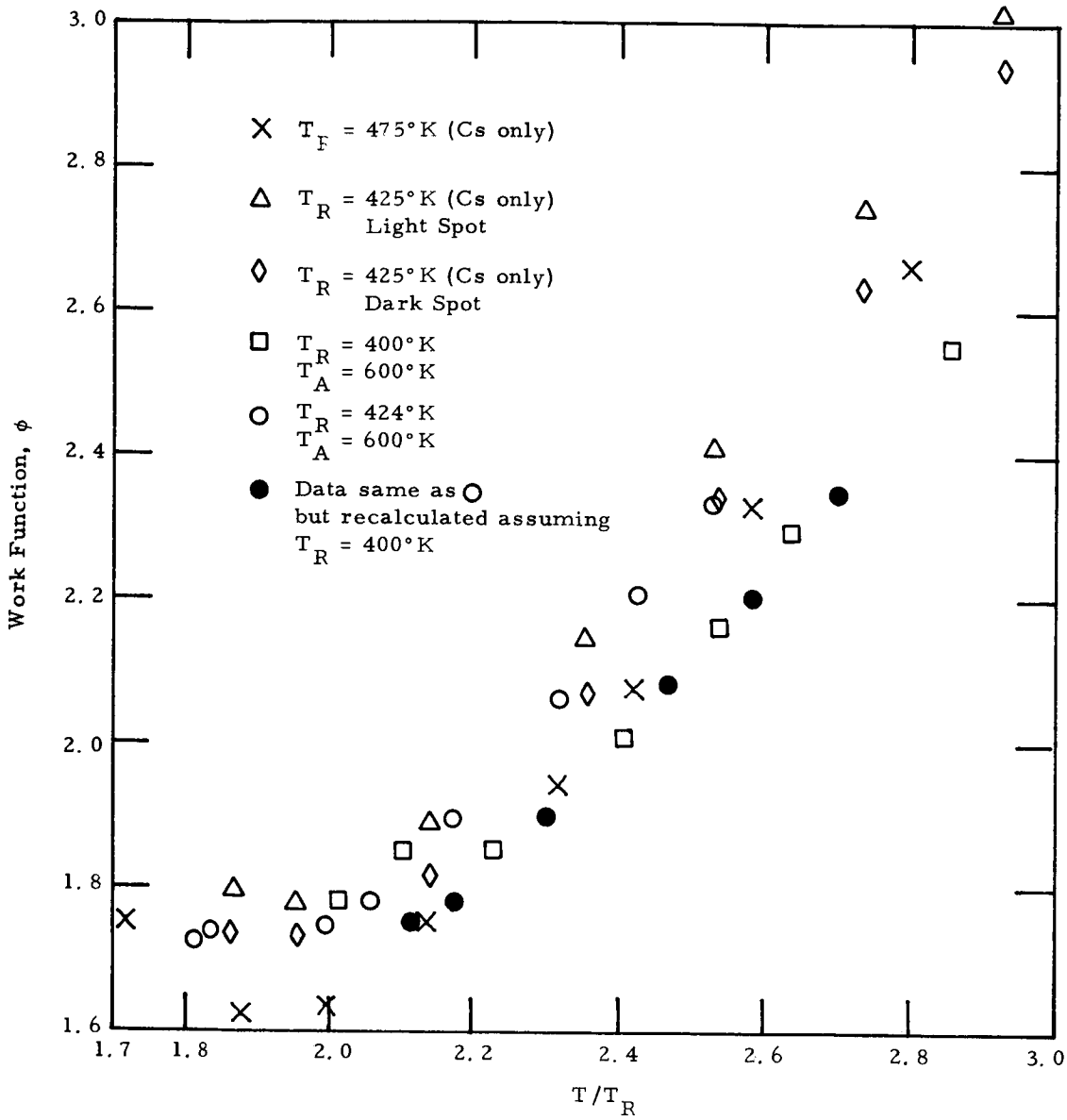

Figure VI-30. Work Function Plot for Molybdenum Surface.

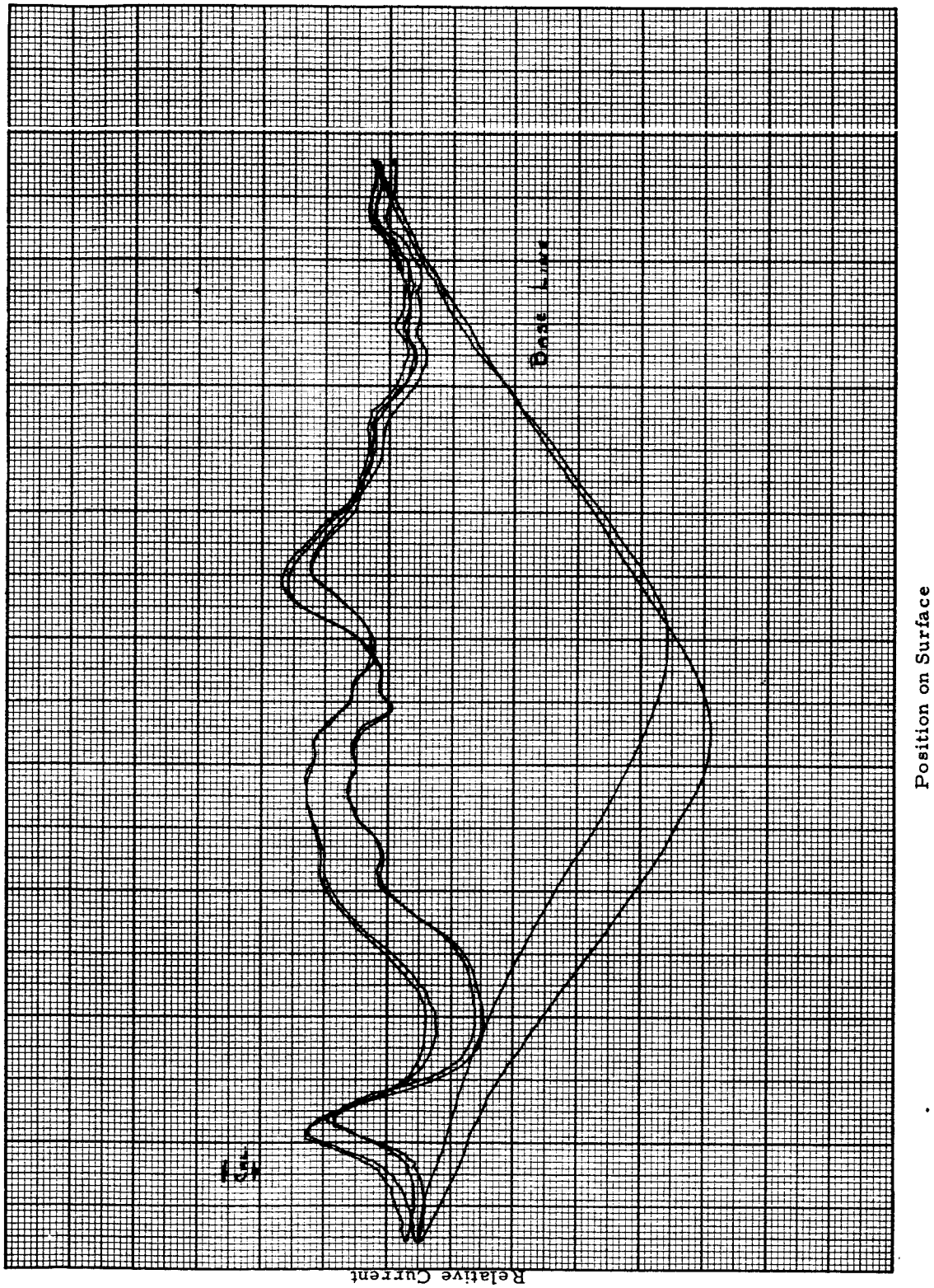

Figure VI-31 Cross Scan Showing Stray Collector Current

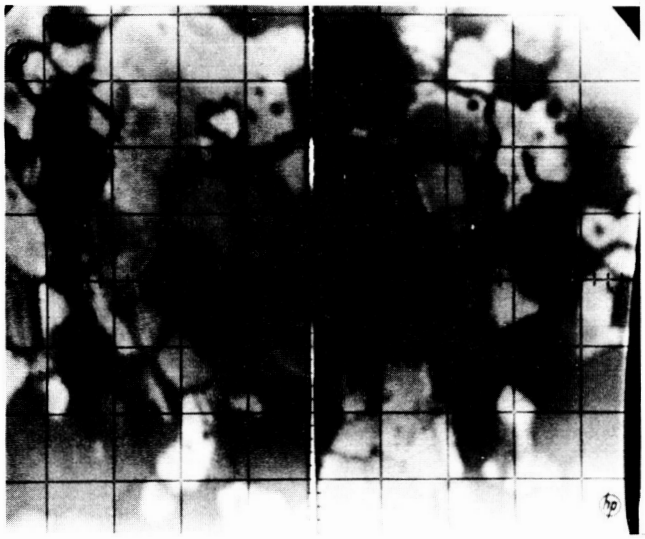

Figure VI-32. Molybdenum Display Photograph with Additive Present

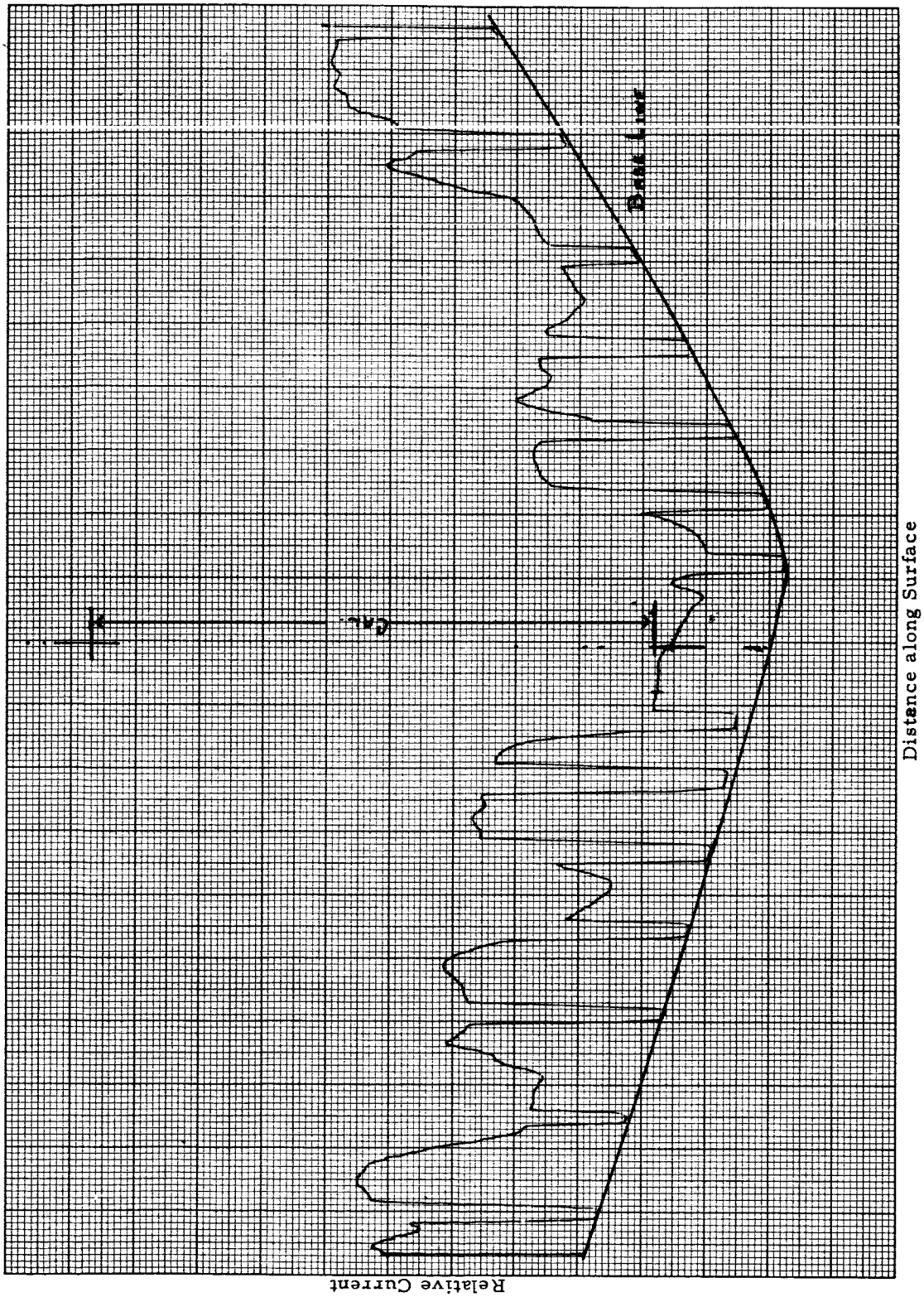

Figure VI-33. Cross Scan Showing Collector Emission

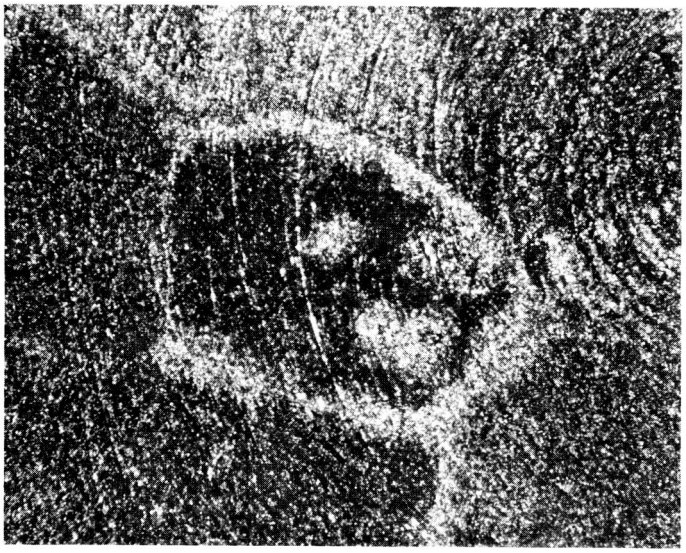

Figure VI-34. Metallograph of Local Contamination of Molybdenum Surface, 75X.

CHAPTER VII

NON-EQUILIBRIUM EFFECTS

A. General

The experiments under this program as well as those of an earlier one using converters[1] have shown that there are important time dependent processes involved in the additive effects. Two types of behavior were evident: a long range effect occurring when additives were introduced into the test vehicle; and a short term process appearing whenever surface temperature and therefore additive coverage was changed.

Because practical converters are essentially steady state devices it is important that equilibrium data be used in their design. A knowledge of the various time constants and their temperature dependence will be a great aid in establishing the requirements for the attainment of equilibrium in the experimental work. In addition this information will provide further insight into the physical phenomena involved in the action of the additives on a thermionic surface.

The short term effects observed in the thermionic scanner indicate that even better performance can be realized under special conditions. During transient changes a very pronounced temporary lowering of surface work function was observed. If conditions which maintain this change can be established in an operating converter, substantially improved performance can be realized. An understanding of the phenomena occurring will be a great aid in determining the required conditions.

---

1. Additive Converter Studies, Technical Documentary Report No. APL-TDR-64-2, January, 1964. TEECO No. 35-64.

B. Induction Time Phenomena

The use of additives in test vehicles, either scanners or converters, has shown that there are long time delays between the introduction of the additive (raising its reservoir temperature) and the appearance of an effect in the characteristic of the diode. Relatively long soaking periods (>10 hours) have been required before the device characteristics stabilized. The work performed on these scanners has further pointed out the features of this behavior.

In the photoelectric scanner, at temperatures up to 400°K, there appeared to be no significant delay effect, as shown by the fact that a single curve, C, of Figure VI-12 was formed by the composite of data taken after 3 hours and 24 hours at temperature.

Before any further changes were obtained, however, an overnight soak at temperature was required. Once the additive reservoir had been raised to a high temperature (approximately 500°K), a very significant lag time became apparent in that even several days after the temperature had been reduced to 350°K, the characteristics did not return to their original 350°K level. This is demonstrated by curve G of Figure VI-12 which was taken at $T_{add} = 300°K$.

Similar delays were observed with the thermionic scanner. Tests with additive reservoir temperatures of 500°K and 600°K did not show significant changes from those with Cs only (Figure VI-18). After an overnight soaking period, the results shown in Figure VII-1 were obtained with the T/T_R at minimum ϕ having shifted from 2.0 to 1.8. Once sufficient induction time had been allowed through the use of the long soaking period, an important reduction shift in the T/T_R curve was achieved. This result is extremely important to converter design and operation and deserves considerable attention in future experiments.

C. Short Term Effects

The interaction between the work function of the metal surface and the additives takes place by means of the adsorption of the CsF on the surface. Changes in temperature or additive pressure will, in turn, cause changes in the adsorption and desorption rates, thereby varying the coverage on the surface. In general, systems with this sort of physical adsorption have a rate and temperature dependence described by the Arrhenius equation:

$$K = A \exp\left(-\frac{E_a}{RT}\right)$$

where: K is the adsorption or desorption reaction rate; A, a frequency factor; E_a the activation energy; R, the gas constant; and T, the absolute temperature. A knowledge of the parameters in the equation will enable the calculation of time constants under various conditions and help to delineate the requirements for the establishment of equilibrium.

The activation energy may be evaluated by rewriting the equation after taking the logarithm of both sides:

$$\ln K = \ln A - \frac{E_a}{RT}$$

Differentiating with respect to 1/T gives:

$$\frac{d \ln K}{d\, 1/T} = -\frac{E_a}{R}$$

The slope of a plot of lnK versus 1/T will thus determine E_a. Assuming the change in ϕ is proportional to the number of adsorbed atoms, a rate k can be determined from the variation in ϕ with time. This procedure was carried out for CsF on the tungsten surface. All time constant experiments were conducted at a CsF reservoir temperature of 720°K.

Figure VII-2 illustrates the short time variations by showing the work function changes produced during a time and temperature cycle.

Starting at 930°K and T/T_R of 2.2, cross scans were taken at successively lower surface temperatures until the value of T/T_R for minimum work function was passed. About 15 minutes was allowed at each point to stabilize the readings. This data is presented as points 192 to 197. After soaking at the last point (745°K) for 30 minutes, the surface was rapidly heated to 800°K and a cross scan (point 198) taken. As the surface soaked at this temperature, the current gradually decreased. This corresponds to the work function increase indicated by the dotted line to point 200, which is the steady-state value reached after 30 minutes.

Work function changes with time produced by additive adsorption are plotted in Figure VII-3 for several different surface temperatures. These curves were determined by subjecting the test surface to a long soak at 700°K and then to rapid heating to the indicated temperatures. The current decay described above was recorded on a strip chart as shown in Figure VII-4. To eliminate drift the accelerating electric field was shut off periodically producing a set of zero reference pips. The work function change required to produce this decay was then calculated for use in plotting Figure VII-3. From each of these curves a rate constant, k, can be determined assuming the change in ϕ is proportional to the number of adsorbed atoms. These three values are then plotted in Figure VII-5 vs. $\frac{1000}{T}$. The activation energy for the adsorption of CsF on tungsten for this process is thus 2.2 eV from the slope of this line.

The time characteristics of the test surface also depend upon the particular region of the surface, as is evident in the cross scans of Figures VII-6, VII-7 and VII-8. All had 1100°K surface temperature and represent portions

of a time cycle. The original scan, Figure VII-6, was taken after a prolonged soaking to achieve equilibrium. The surface was then cooled slowly to 750°K while taking other scans. Rapid reheating to 1100°K produced the cross scan of Figure VII-7. In this scan the pronounced dip apparent in Figure VII-6 has disappeared. After soaking at this temperature for about 30 minutes, followed by a 5 minute period at about 1200°K, the scan in Figure VII-8 was obtained. The dip has now returned.

This evidence indicates a significantly different response between the central and the outer portions of the surface, and illustrates a previously unsuspected selectivity in the additive adsorption process. This central region was similar to the remainder of the tungsten surface both in terms of morphology and orientation. The differences that did exist are described in Chapter VIII. No correlation was possible, however, between the behavior of the central portion of the emitter with the additive and its metallurgical nature. (Data from this central region of the scans illustrated were used for the activation energy calculation described above.)

The physical or chemical changes associated with or responsible for the work function changes observed in the experiments described above are quite complex. It is expected that several years of intense research in surface physics will be required before a satisfactory model can be obtained for the refractory metal -Cs -CsF system.

Neither a detailed physical model nor the postulation of a specific reaction are prerequisite to a thermodynamic analysis such as the one just described. The conditions that are necessary for this treatment to be valid are:

a) Static or dynamic equilibrium exists when measurements are performed.
b) Work function is linearly dependent on the concentration of atoms taking part in the reaction.

The analysis, of course, does not yield any information on the detailed or microscopic structure of the surface; a quantum-mechanical treatment is necessary for that. What the thermodynamic treatment accomplishes is to allow the prediction of the behavior of the system under conditions other than those used in the experiments. Specifically, knowledge of the activation energy can be used to compute the time required for equilibrium at higher or lower surface temperatures, perhaps under conditions which result in time-constants too fast or too slow for direct experiment. This is accomplished through the use of the Clausius-Clapeyron equation.

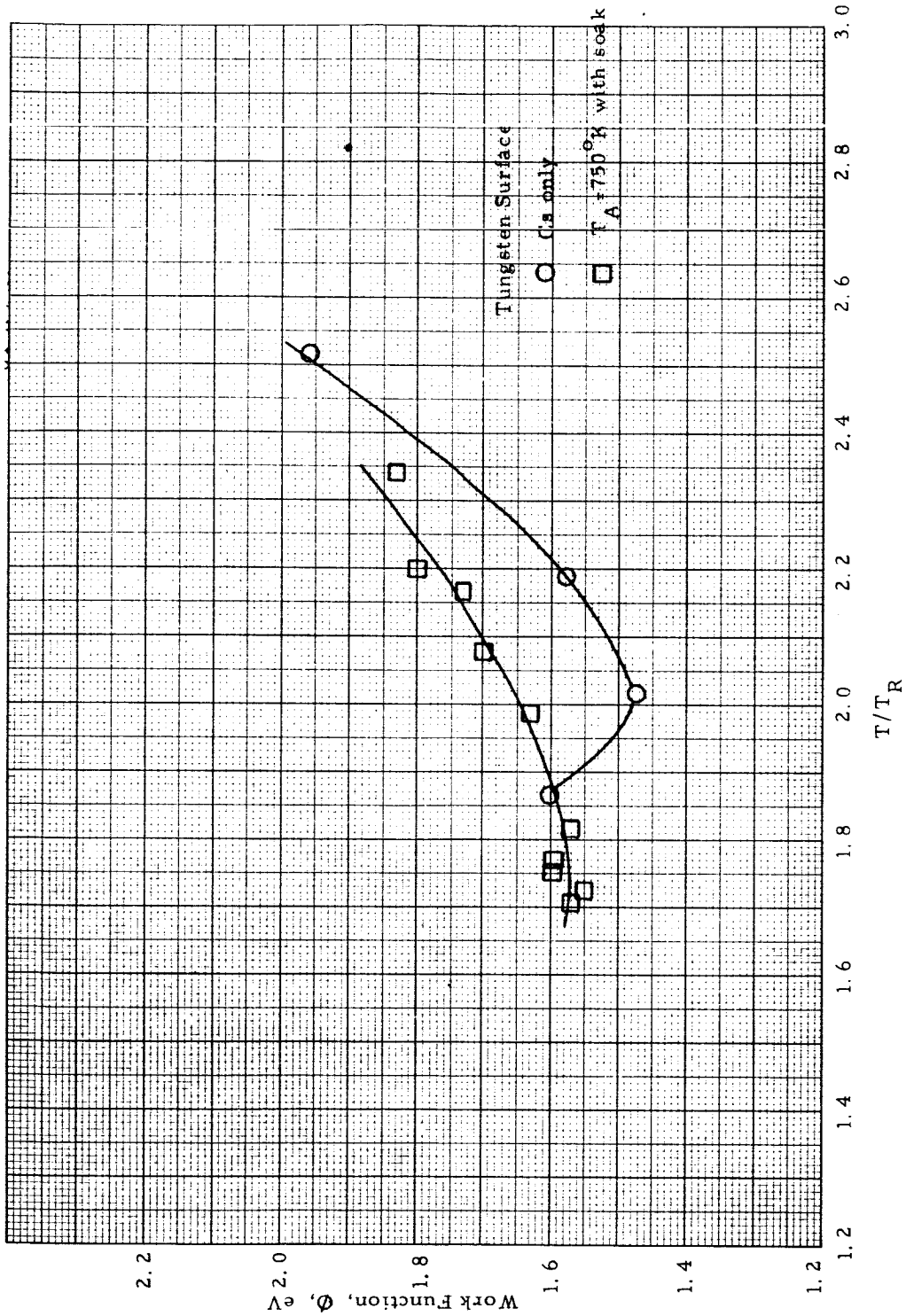

Figure VII-1. Work Function Variation on Tungsten Surface

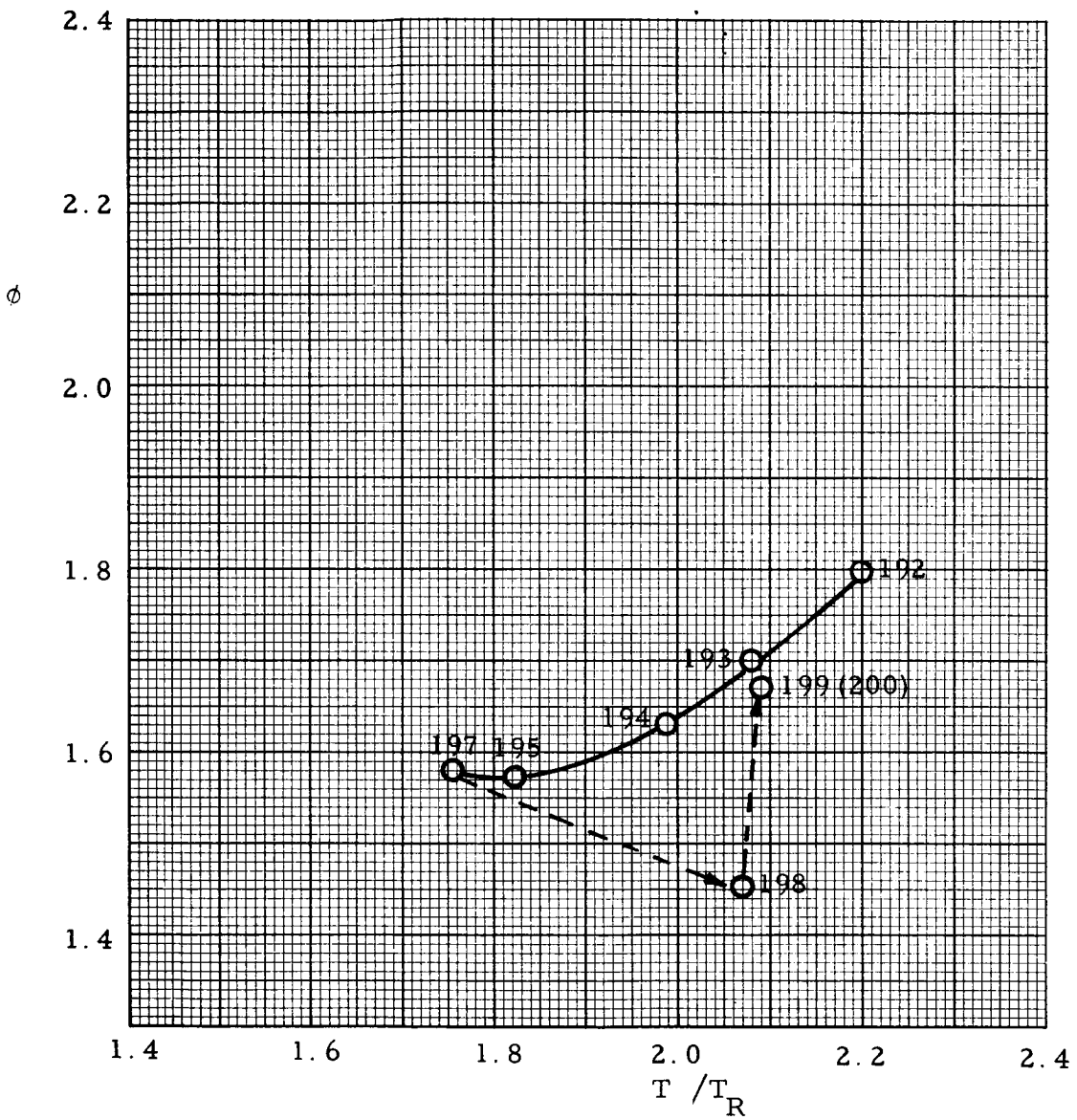

Figure VII-2. Time Effect With Additive

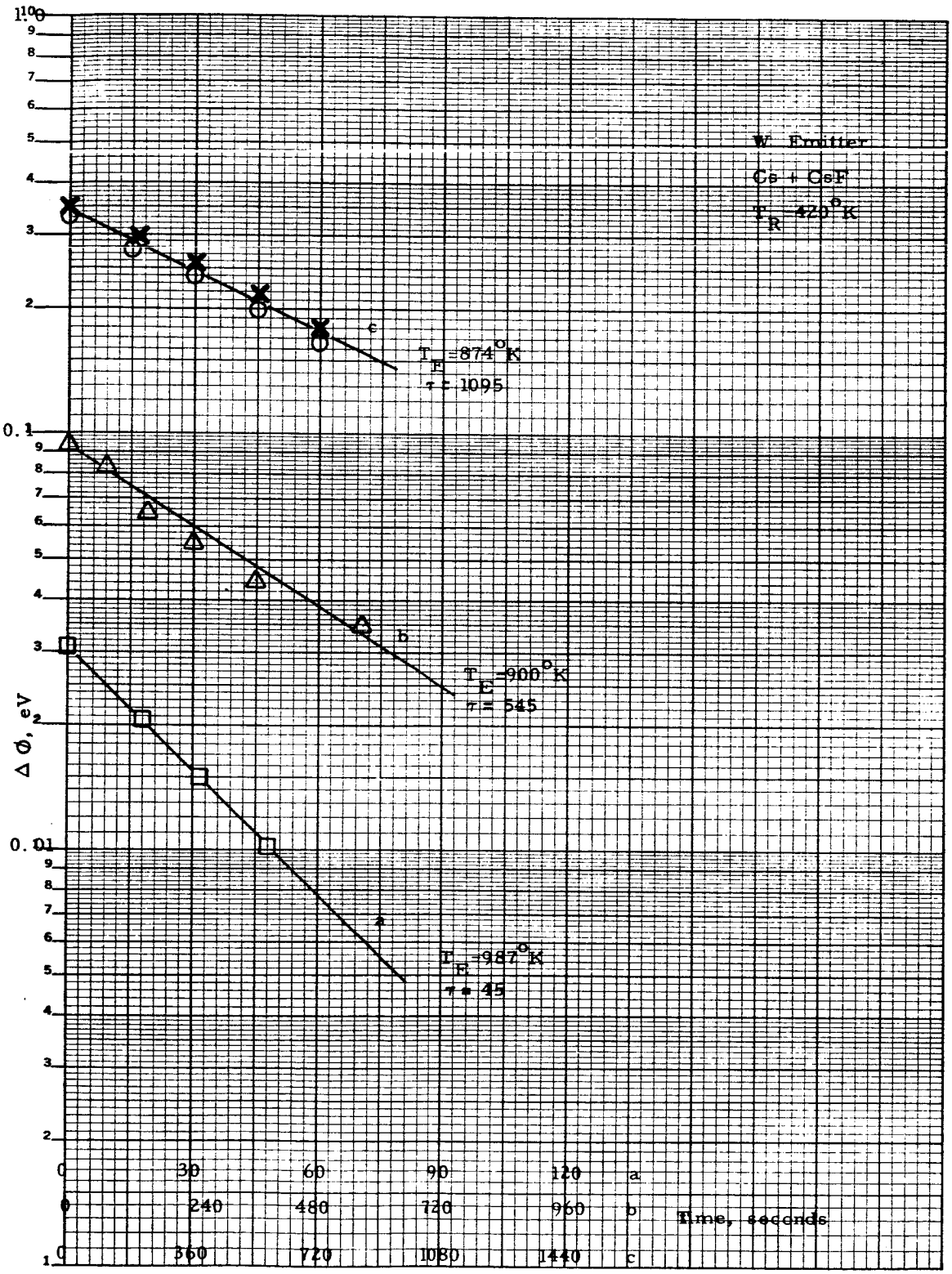

Figure VII-3. Work Function Change versus Time

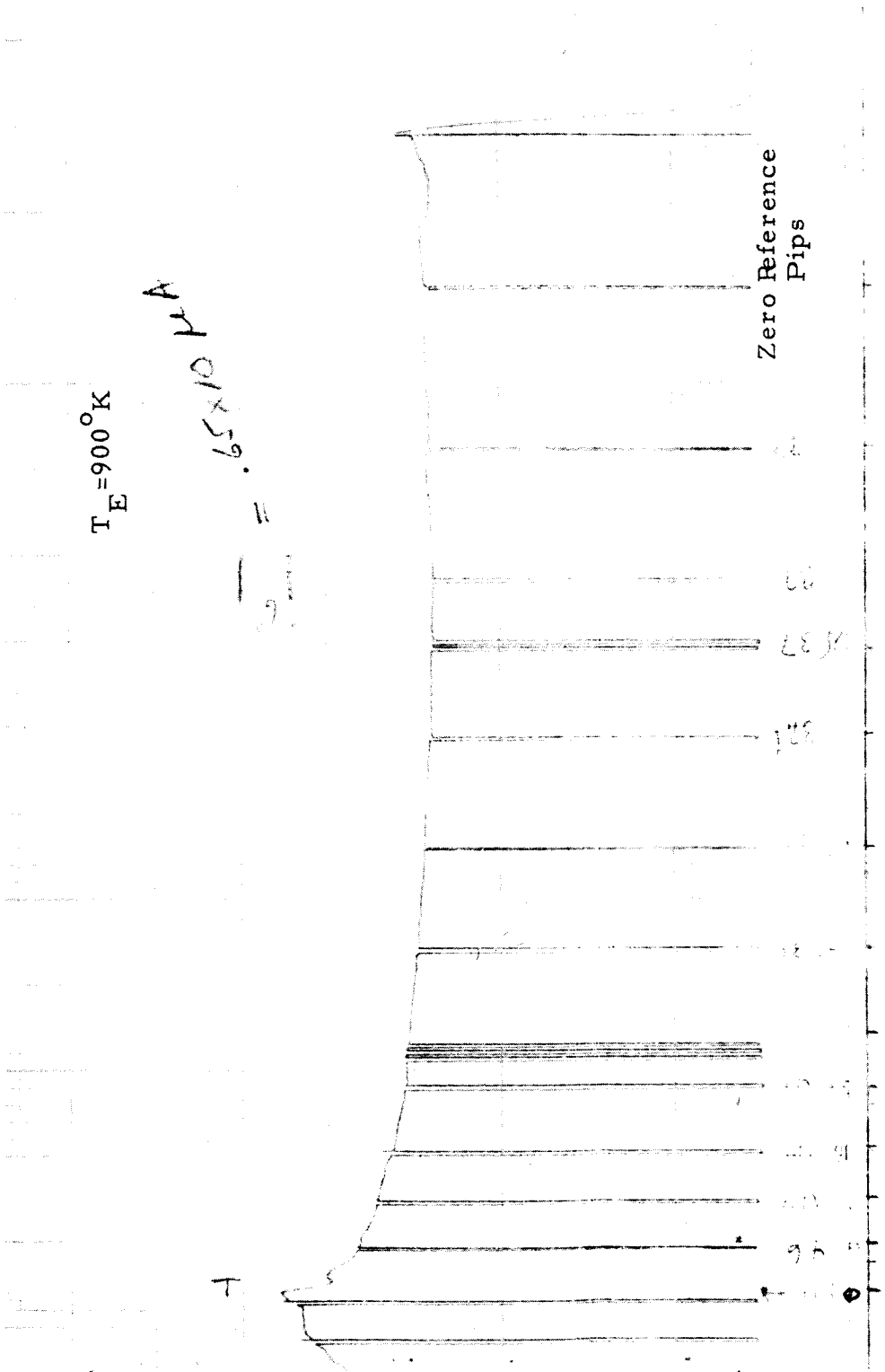

Figure VII-4. Exponential Decay of Current

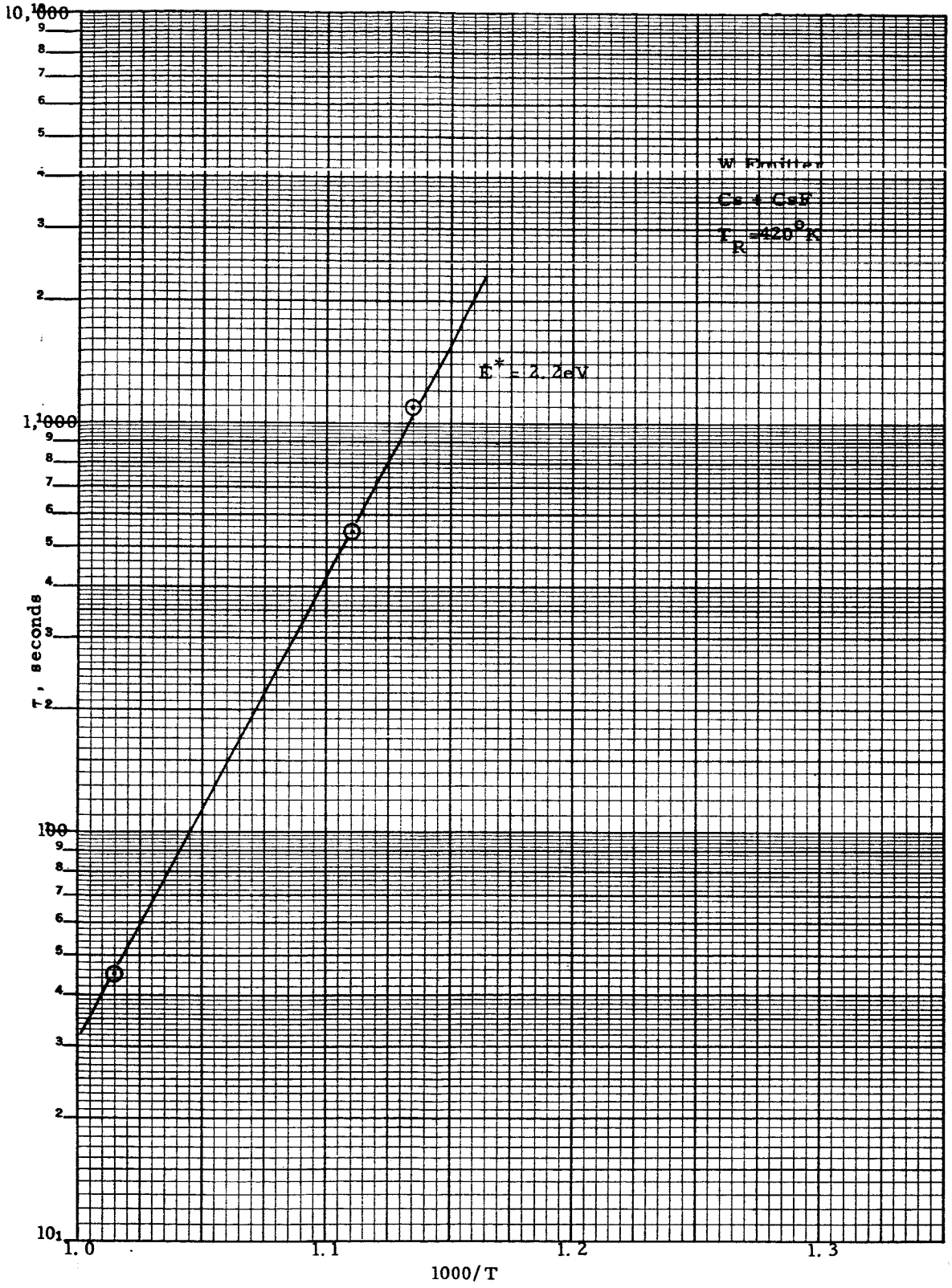

Figure VII-5. Desorption Time Constant versus Temperature

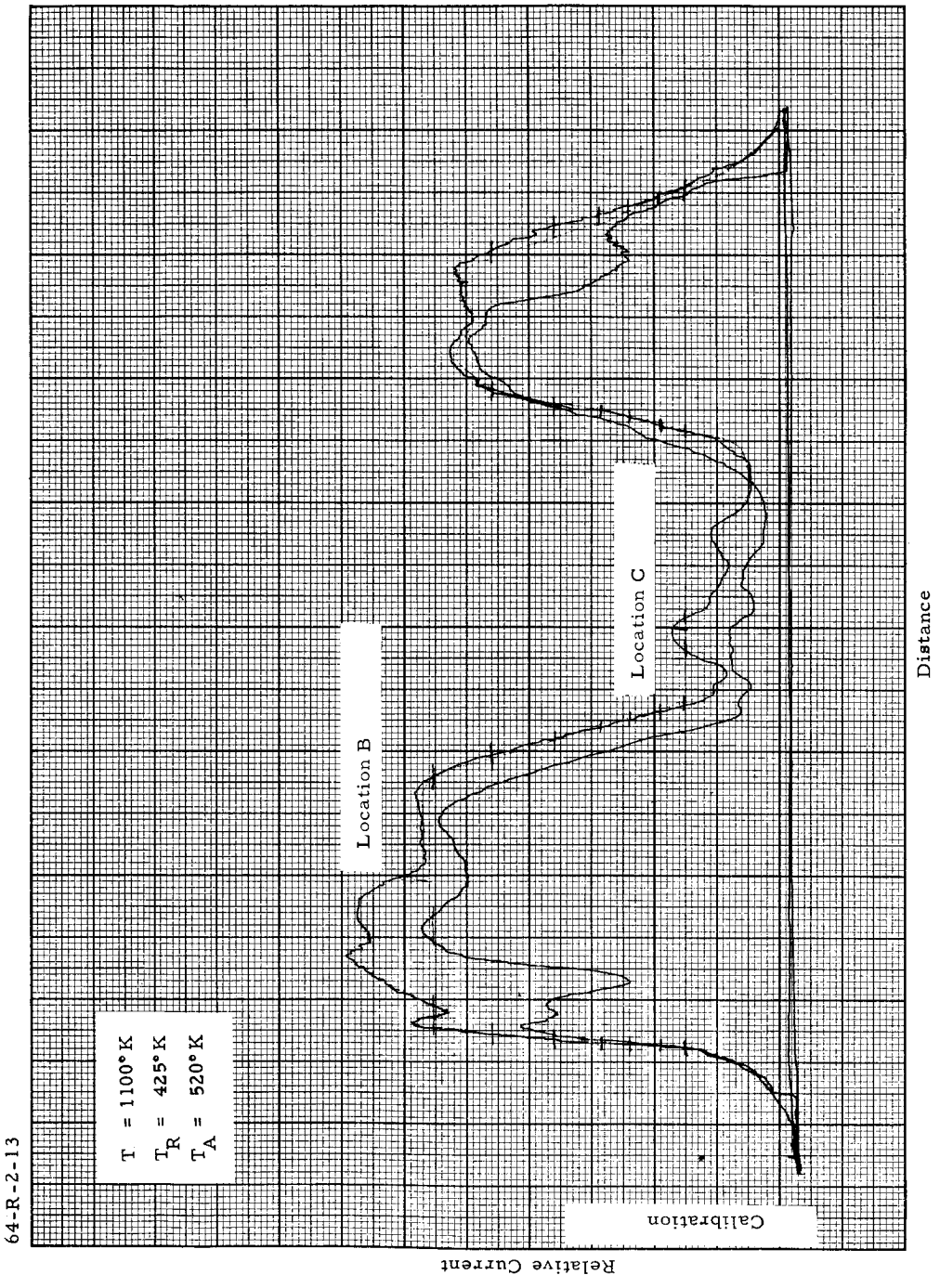

Figure VII-6. Cross Scan (No. 99), $T=1100^{\circ}K$, $T_R=425^{\circ}K$, $T_A=520^{\circ}K$

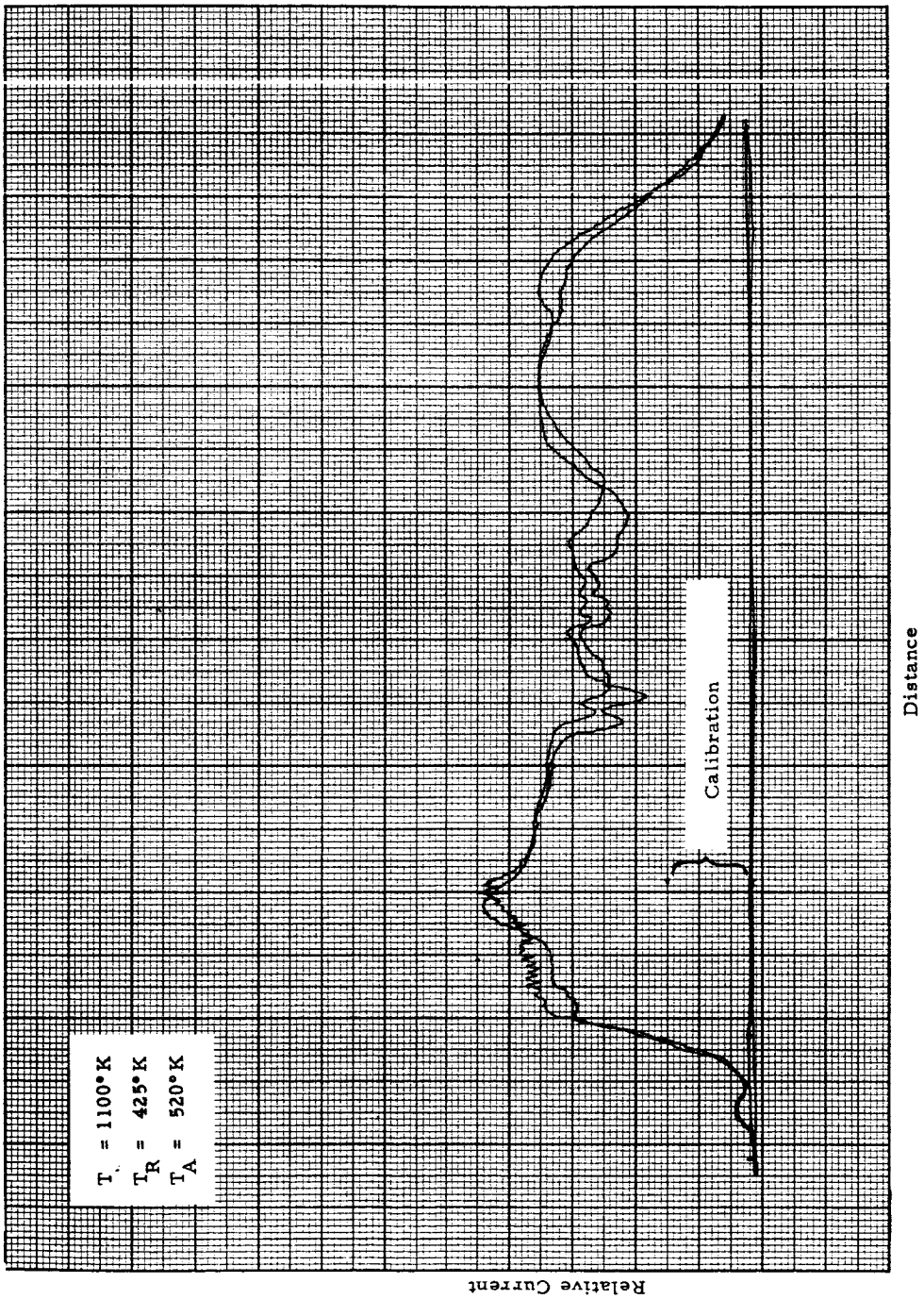

Figure VII-7. Cross Scan (No. 113), T=1100°K, T_R=425°K, T_A=520°K

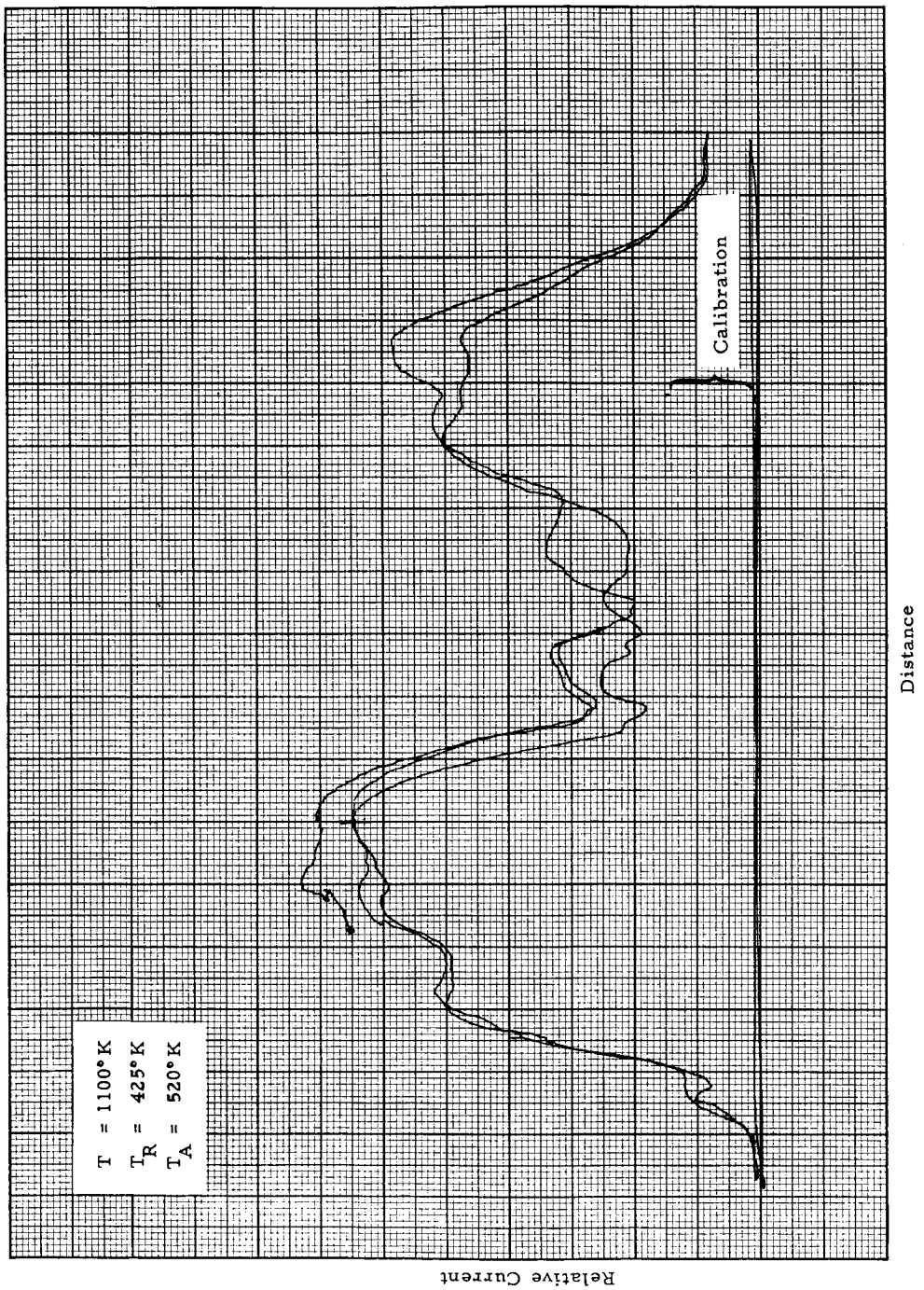

Figure VII-8. Cross Scan (No. 119), $T=1100^{\circ}K$, $T_R=425^{\circ}K$, $T_A=520^{\circ}K$

CHAPTER VIII

METALLURGICAL ASPECTS OF THE PROGRAM

Introduction

A careful analysis of this program reveals that the fundamental problem under examination is the effect that the adsorption of an additive on an electrode surface has on the work function of the surface. Since the adsorption is a strong function of the surface morphology, a sound attack upon the problem requires that the surface be defined and stabilized to the greatest possible degree. This documents the preparation and stabilization of the test surfaces and the techniques used for examining and defining the morphology of the surfaces and the changes which occur under specific types of treatment.

The correlation of emission with surface morphology has already been described in Chapter VI.

A. Preparation of Surfaces Studied

Tungsten (W3) - a half-inch diameter disc of tungsten was cut and electropolished, and then lightly etched in alkaline potassium ferricyanide. Three non-symmetrical notches were made at the edge. A comprehensive set of photographs of the surface was taken and the piece was vacuum fired for ten minutes at 2000° C. After additional photographs, the emitter was outgassed for fourteen hours at 1850° C. It was then welded to a molybdenum ring which was in turn welded to a tantalum thin-walled sleeve and thus connected to the rest of the assembly. The tungsten used was nominal ⟨110⟩ single crystal, containing several sub-grains misoriented by varying amounts with respect to the nominal orientation. When etched, these grains developed different surfaces - see Figures VIII-1 and VIII-2. It was hoped that subsequent differences detected in

thermionic emission might be correlated with these different surfaces.

After operation in a thermionic scanner, the emitter was extracted and rephotographed - see Figures VIII-3 and VIII-4. (Considerable scratching of the emitter visible on Figures VIII-3 was caused during removal of the emitter from the diode.) The changes are much as would be expected from past experience, and are discussed in Section B.

Molybdenum (M1) - A short piece was cut from 1/2" bar stock and machined into a cup whose outer flat face was the emitting surface. This had a machined finish. The part was then fired in vacuum for one hour at 2200°C, to establish a large grain size which would not alter during further heat treatment. The cup was welded to a tantalum spacer and further assembled, and carefully photographed. Again, three unsymmetrical notches were made in the edge, to aid in correlating metallographs and scanner pictures. One of these notches appears in Figure VIII-5. Figure VIII-6 at 310x shows a grain boundary, traces of tooling marks, smoothed by the heat treatment, and a network or array of markings which is discussed further in Section B.

The specimen was operated in the photoelectric scanner, and removed and photographed. Figure VIII-7 can be compared with VIII-5 and shows results of arcing on the surface. The arcing occurred while attempts were made to raise the lead resistance by applying a high voltage during the operation of the photoelectric scanner.

This emitter was later operated in the thermionic scanner.

B. Observation of Surfaces

1. Tungsten - It is found that the thermal stability of the surfaces, and the changes which occur thereon during prolonged heat treatment are consistent

with the theoretical results described in References 1 and 2. Briefly, the factors determining the shape taken up by a surface at a temperature where the atoms are mobile are as follows:

a. Surface free energy, which, in the simplest case, tends to a minimum represented by a plane surface. If the free energy varies with crystallographic orientation, the minimum energy may be achieved by a polyhedral surface instead of a plane. The total free energy of a surface is given by

$$\sum_{i=1}^{n} A_i \gamma_i,$$

where A_n is the area of plane surface with specific surface free energy γ_n. It is possible for an increase in A to be more than compensated for by a decrease in γ. This may occur on a surface which is slightly misoriented with respect to a low-energy plane and and breaks up into large areas of low-energy planes connected by small areas of higher-energy planes. This process has been observed to occur on several metals heated in vacuum and is known as thermal faceting. A special form of faceting is seen in Figure VIII-2, where a selective etch has attacked tungsten of approximately ⟨110⟩ orientation. Large areas of ⟨110⟩ surface, connected by small areas of complex planes, may be observed. In the present work, any variation in free energy with orientation appears to be dominated, at least on a visible scale, by

1. "Metal Surfaces - Structure, Energetics & Kinetics" Ed. W. A. Robertson & N. A. Gjostein, A.S.M. Seminar Report, 1963.

2. W. W. Mullins, J. Appl. Phys. 28 333 (March 1957) and J. Appl. Phys. 30 77 (Jan. 1959).

radius effects as the driving force for the transport mechanism.

b. Chemical potential, μ, which depends on the local curvature K of the surface, according to the relation $\mu(K) = K\gamma\Omega$ where γ = surface free energy p. u. a. and Ω = atomic volume (Reference 3).

Under the influence of one or the other of these forces, the mobile atoms will tend to form a surface of minimum energy, with the following transport mechanisms operating:

1. Surface diffusion
2. Volume diffusion
3. Evaporation
4. Viscous flow

Viscous flow is probably insignificant, but the balance of the other factors depends on the temperature considered. At diode operating temperatures evaporation is insignificant even into a live vacuum, and will be even less significant in a cesium-containing system. Volume diffusion coefficients are many orders of magnitude smaller than those for surface diffusion.

Thus all but surface diffusion may be eliminated as possible transport mechanisms in this work.

The radius and surface diffusion effects discussed above are illustrated by the rounding of corners and angles and the development of convex lips at the edges of etch pits. Figures VIII-9, -10, -11, and -12 show this sort of change on both (110) and (100) crystal faces of tungsten. The convex lip

---

3. C. Herring, Physics of Powder Metallurgy, McGraw Hill, 1951.

effect is a definite characteristic of surface diffusion. The original surface of Figure VIII-2 was developed by a selective etch, which converted the approximate (110) surface into perfect (110) sections connected by steps of complex plane. A slight difference in orientation across the boundary in the figure accounts for the different proportions of perfect (110) and complex step on the two sides. None of the scanner pictures in Figures VI-14, -15, II-2 and -3 can be correlated with the photomicrograph of the tungsten surface (Figure VIII-13). This may be due to the fact that most of the surface consists of (110) faces (with small variations in the proportion of the complex planes) which are responsible for almost all of the emission. Thus the small varying contributions of the complex plane are beyond the resolution of the instrument. For example, the group of three small patches, seen on Figures VIII-1 and VIII-3, is not visible in the scanner pictures, although their physical dimensions are probably within the resolving powers of the instrument. We thus conclude that, although small variations in the proportions of (110) and complex planes are readily visible under the microscope, corresponding differences in emission are not resolved by the scanners, since the change in (110) area per unit area is minute.

None of the above explains, however, why certain scanning pictures do show patches.

It should be noted here that the tungsten surface (W 3) was badly scarred during removal from the scanner. The result may be observed in Figure VIII-3.

2. Molybdeum – The grain boundaries in the mo test surface were quite stable during operation, Figures VIII-5, -6, -7 and -8, and changes in surface morphology are again only those that would be expected to occur on the machined surface. Some cratering occurred during accidental arcing. The most

interesting observations concern the array of markings on the surface (see Figures VIII-6 and -8). Similar markings have been observed widely (Ref. 4), without satisfactory explanation. Experiments at Thermo Electron have shown that (1) a light polish with alumina which removes the original surface does not remove all traces of the arrays, and (2) a very oblique section through a surface (made on a 2° angle-lapping jig) shows that the markings persist below the surface, decreasing in frequency with increasing depth. The markings are found on commercial Mo heated in the temperature range 1400-1900°C in vacuum. The results are the same whether the vacuum is obtained by oil diffusion pumps or getter ion pumps.

Mo is known to form Mo_2C and Mo_2N as well as the volatile oxide MoO_3 and a much less volatile oxide MoO_2. Other examples are known of an oriented precipitate formed in a refractory metal by contamination; e.g., Ta_2O_5 on (100) planes in Ta. It is suggested, therefore, that the markings are the traces on the surface of platelets of precipitated MoO_2 in the bulk. It is not perfectly clear where the oxygen in the precipitate comes from; it could conceivably be the traces of oxygen (generally 2-20 ppm) in the bulk material, which for some reason is redistributed as MoO_2 precipitates near the surface. It could also be picked up from the environment during heat treatment. Analysis of these alternatives is beyond the scope of this work.

Supporting evidence for the precipitate hypothesis is that there is frequently a precipitate-free zone along the boundaries of grains (see Figure VIII-5), suggesting that here the oxygen forms a grain boundary precipitate, not visible

---

4. See, for example, E.O.S. Final Report #3410, dated 25 Oct. 1963, on Contract NAS3-2529, Sections 2 & 3, and Pratt & Whitney Aircraft Report #PWA2306, dated 15 Feb. 1964, on Contract NAS3-2527, Figures 19 and 20.

as platelets. The alternative suggestion, of thermal etching as the cause of the markings (Ref. 4) does not explain the absence of markings in such a wide band along the grain boundaries. The changes in appearance between Figures VIII-6 and VIII-8 are explained by the fact that the temperature of photoelectric operation, in the range 100°C to 600°C, Cs reduces MoO_2, and the oxygen transferred from the emitter to the Cs probably comes to rest in the Cs reservoir which is the coolest part of the diode, leaving the emitter cleaner at the end of the photoelectric operation than at the start. At the higher temperatures of thermionic operation the situation is reversed so that Mo reduces CsO. Figure VIII-14, which shows how the free energies of formation of the various oxides change with temperature, explains the reversal (Ref. 5).

Figures VIII-15 and VIII-16 are included here for completeness, although they are of relatively little value to the surface study, due to heavy contamination. The contamination occurred during thermionic scanning and tends to obscure any surface effects which may have resulted from this operation.

C. X-Ray Analysis

The thermionic work function of a surface is known to vary with its crystallographic orientation. A close-packed surface, with a maximum number of metal atoms per unit area, has its electrons tightly bound, and therefore has a high bare work function. It also has more sites for cesium ions to adsorb, and a low cesiated work function. The closest-packed plane for the body centred

---

5. Since this report was drafted, Dr. C. N. Reid, while with the Metal Science Group at Battelle Memorial Institute, has established that this precipitate observed on Mo is in fact the carbide, Mo_2C (TAIME 233 (Apr 65) 834). Our conclusion about the markings being due to a precipitate is substantiated, but the surmise that it was MoO_2 was wrong.

cubic metals Mo and W is the (110) face. The (100) face has 71% and the (211) face only 58% as high an atomic density as the (110). Surfaces oriented close to (110) have somewhat lower atom densities. In an attempt to relate the results of the thermionic scanner with the crystal orientation of the grains scanned, a set of Laué back reflection x-ray photographs were taken of numbered grains on the cross scan. The numbers refer to those appearing on the metallograph portion of Figure II-1 and duplicated in the scanner picture, cross scan and outline picture of the same figure.

A Laué photograph is taken with a beam of highly collimated "white" x-rays incident on only one grain. The array of atoms in that grain reflects the x-rays selectively onto photographic film, forming a pattern of spots which has the same symmetry relations about its centre as the atoms have about the x-ray beam in the crystal. With a little experience, it is possible to identify spots on the photograph with the poles of planes in the crystal. That is to say, if the surface of the grain in the (cubic) crystal is approximately a (110) plane, the spot on the film corresponding to the ⟨110⟩ pole will be found near the centre of the film. Quantitative information about the angles between the grain pole (or normal) and the incident x-ray beam can be extracted from the photograph using a Greninger chart. Such information for the above grains is in Table III of Chapter VI. The angles (tabulated as γ) between the ⟨110⟩ pole and the centre of the film are a crude measure of the misorientation of the grain with respect to the (110) surface.

A more accurate representation of the grain orientation, which allows the grain normal to be plotted as a point on a unit stereographic triangle, is obtained as follows: For each grain, a stereographic projection is made, in which the grain normal is at the centre. The important low-index poles are plotted on this, starting with the ⟨110⟩ and ⟨112⟩ poles, plotted directly

from the x-ray data. Suitable zones and poles are developed according to standard crystallographic practice, until ⟨100⟩, ⟨110⟩, and ⟨111⟩ poles which enclose the grain normal are all present. The position of the grain normal is measured relative to these poles, in terms of angles. These angles are used to plot the grain normal on a standard unit stereographic triangle. The results of this are shown in Figure VIII-17, where the orientations of the ten grains which were examined are indicated on the unit triangle.

They are seen to cluster around the ⟨110⟩ pole somewhat. This is to be expected, as the extrusion process, used to fabricate the original molybdeum rod from which this is a slice, induces this type of preferred orientation. They do not, however, cover the whole triangle, and points near the ⟨111⟩ and ⟨116⟩ poles, which have particularly low bare work function, are conspicuously missing.

The stereographic triangle plots discussed above can be used to determine the surface free energies of given grains. This can be accomplished by making use of plots of surface energy versus position on the stereographic projection triangle such as the one of Ref. 6. It was hoped that these energy estimates would correlate better with the calculated ϕ values than the use of a simple angle did, but this did not prove to be the case. A simple monotonic relationship did not exist between estimated surface energy, or simple misorientation, and calculated cesiated work function. In both cases the ϕ values were found to fall into two mutually exclusive groups, centred around $\phi = 1.60 \pm 0.01$ and $\phi = 1.66 \pm 0.01$ eV. This grouping is also apparent from

---

6. From calculations on a second-nearest-neighbor model, supplied by B. E. Sundquist (of U.S. Steel Co.'s Fundamental Research Labs, Monroeville, Penna.), in accordance with the method of J. K. Mackenzie, A. J. W. Moore, & J. F. Nicholas, J. Phys. Chem. Solids 23 185 (1962)

the cross scans of Chapter VI. The low work-function group contains the poles closest to the ⟨110⟩ pole.

One possible explanation for this grouping is that the tendency to thermal faceting may depend critically on orientation; so that certain grains have developed submicroscopic facets with a high mean work function, while others have developed undetected facets exposing different low-index planes, and having a low work function. The comparatively rough surface makes the facets difficult to detect with optical microscopy.

A comparison of pairs of grains 1 & 8, and 9 & 10, each of whose Laué photographs are reproduced, Figures VIII-18, -19, -20 and -21 respectively, shows that emission behavior is closely linked to orientation with respect to the ⟨110⟩ pole, rather than the ⟨112⟩ pole. Grain 8 emits more than 1, and has its ⟨110⟩ pole very close to the centre of the Laué photo; while that of 7 is remote. The opposite is true of the ⟨112⟩ poles. Grain 10 is bright in the thermionic picture, while its neighbor 9 is dark; 10 has the ⟨110⟩ pole close to the centre of the Laué picture and the ⟨112⟩ remote, while 9 has the ⟨112⟩ close and the ⟨110⟩ remote.

In summary, the following conclusions can be drawn from the above:

1. The work fun ctions of the grains examined fall into two groups.
2. Despite rough surfaces and contamination, the bulk grain orientation has a large effect on the emission.
3. Proximity of the grain surface to a ⟨110⟩ plane rather than any other low-index plane, determines the cesiated work function.

The confused appearance of the emitter surface after thermionic scanner operation appeared to be due to contamination, and so an x-ray powder photograph was taken of the surface. This showed a number of fairly intense lines

not due to the Mo substrate. However, even with a considerable effort, the additional lines could not be attributed to any Mo compound or other obvious material. This may have been because the process of indexing lines on the powder pattern requires knowledge of their relative intensities in a fine-grained polycrystalline sample, and the intensities found here, for an oriented precipitate in Mo, may well have been misleading. It is clear, however, that there was some contamination present. In the light of the comments in Section B of this chapter, on arrays of markings in Mo, it is felt that the contamination was probably MoO_2, and additional experiments to elucidate this are anticipated. As mentioned in Chapter VI, Section D, there are also local spots of contamination which show up on the thermionic maps.

We wish to acknowledge the expert assistance of the staff of Advanced Metals Research, Inc., of Burlington, Massachusetts, in taking and interpretting the Laué photographs of individuals grains. A copy of their report is attached as Appendix A of this report.

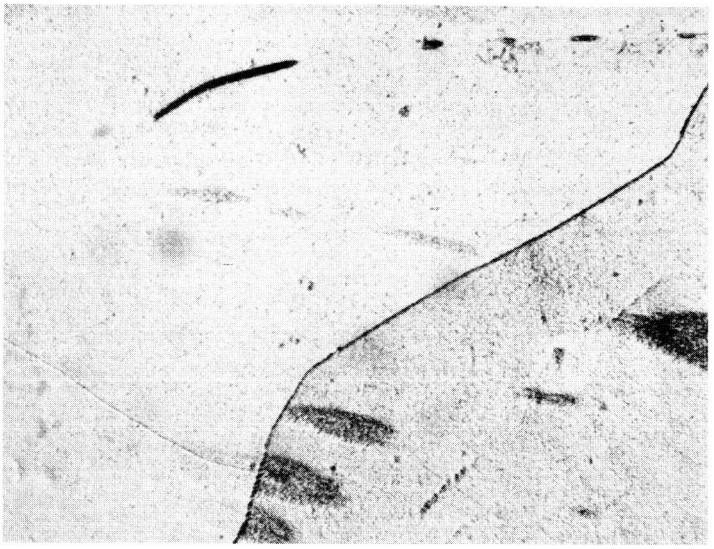

Figure VIII-1. Tungsten Test Surface (W3), Electropolished and Lightly Etched, 75X

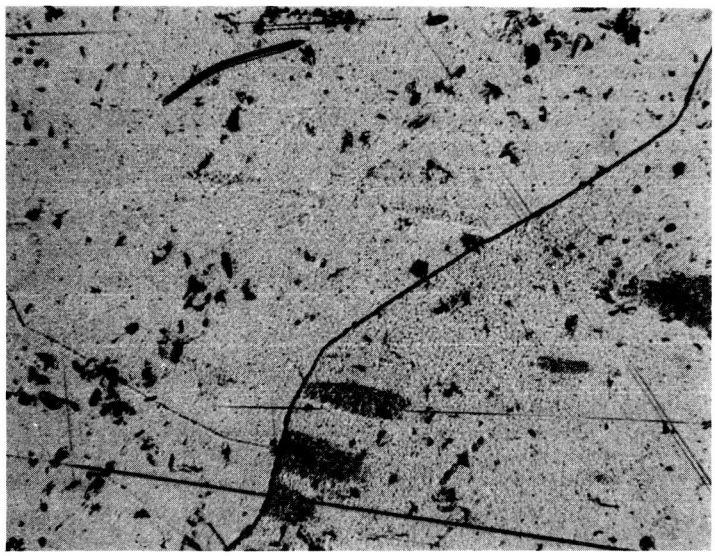

Figure VIII-3. Tungsten Test Surface (W3), After Operation, 75X

Figure VIII-4. Tungsten Test Surface (W3), After Operation, 560X

Figure VIII-4. Tungsten Test Surface (W3), After Operation, 560X

64-R-7-126

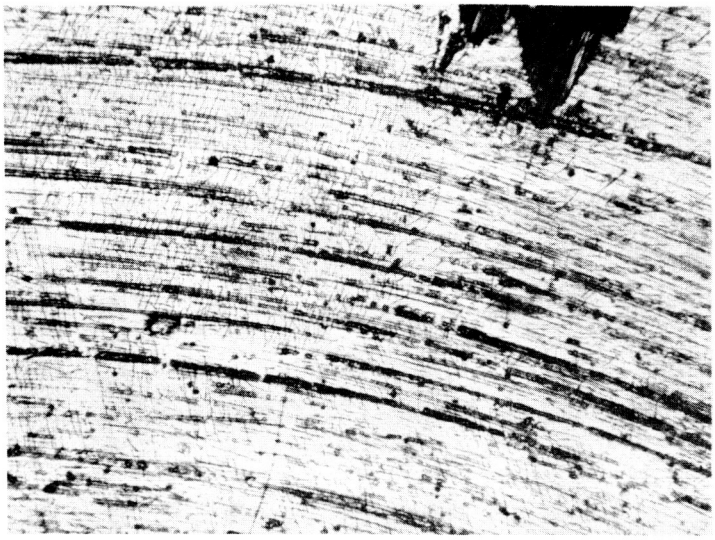

Figure VIII-5. Molybdenum Test Surface (M1) After Outgassing Showing Supposed Precipitate, 75X

64-R-7-127

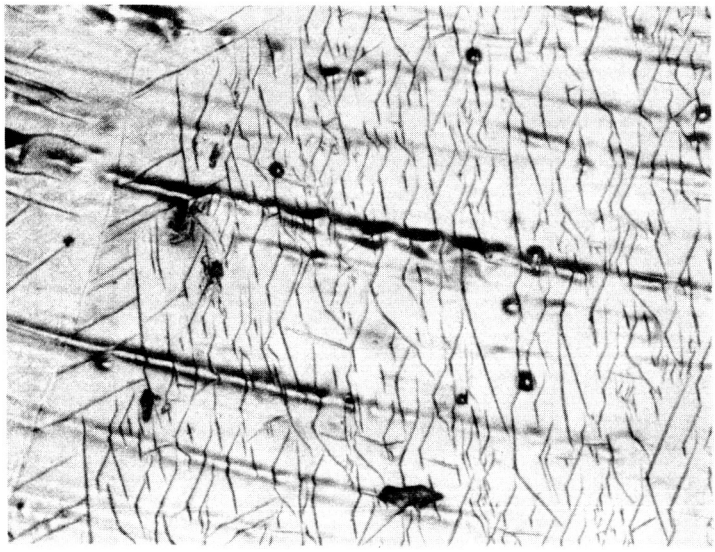

Figure VIII-6. Same as VIII-5, 310X

64-R-7-128

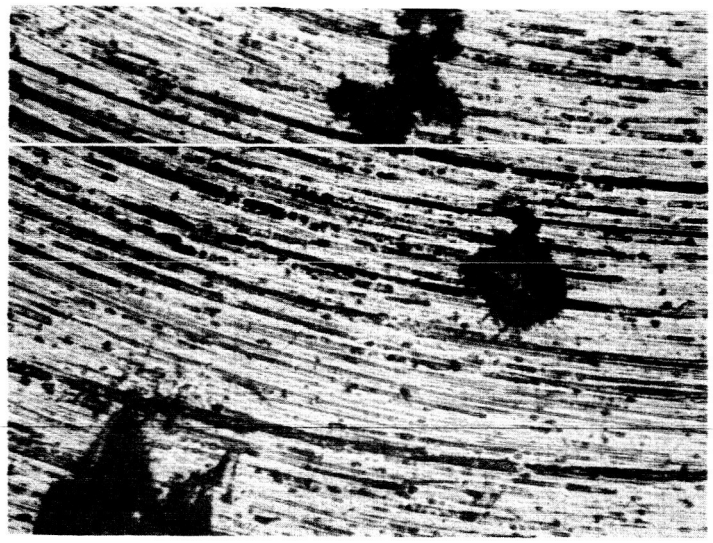

Figure VIII-7. Molybdenum Test Surface (M1) After Operation in Photoelectric Scanner, 75X

64-R-7-121

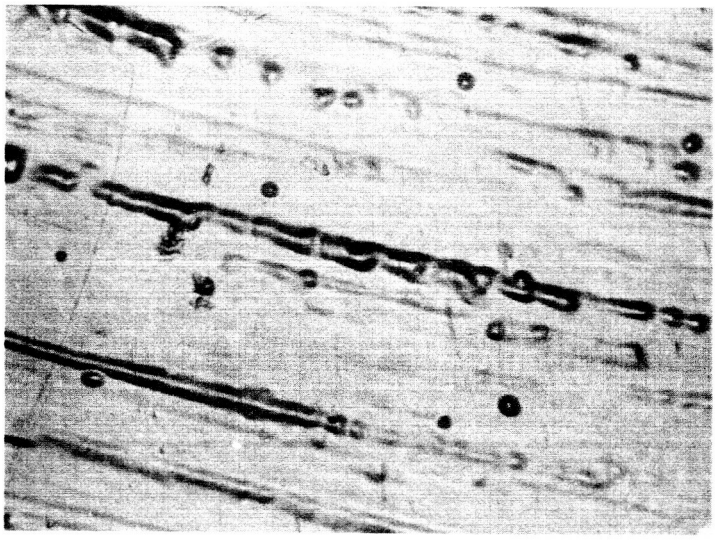

Figure VIII-8. Same as VIII-7, 310X

64-R-7-84

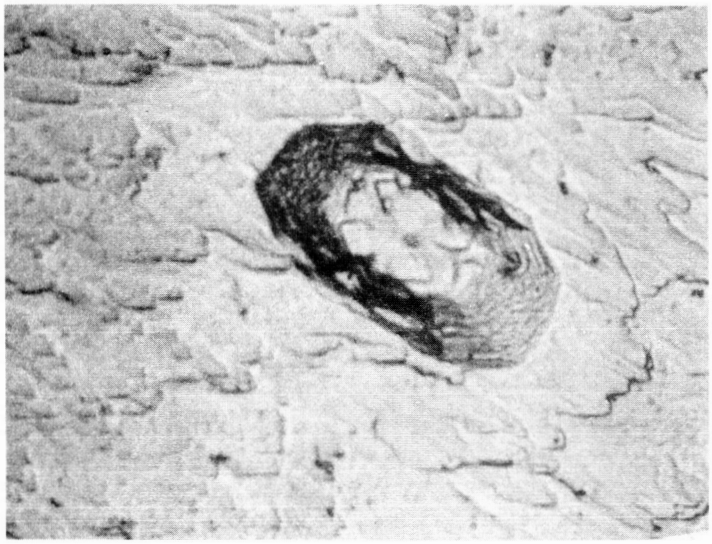

Figure VIII-9.

64-R-7-90

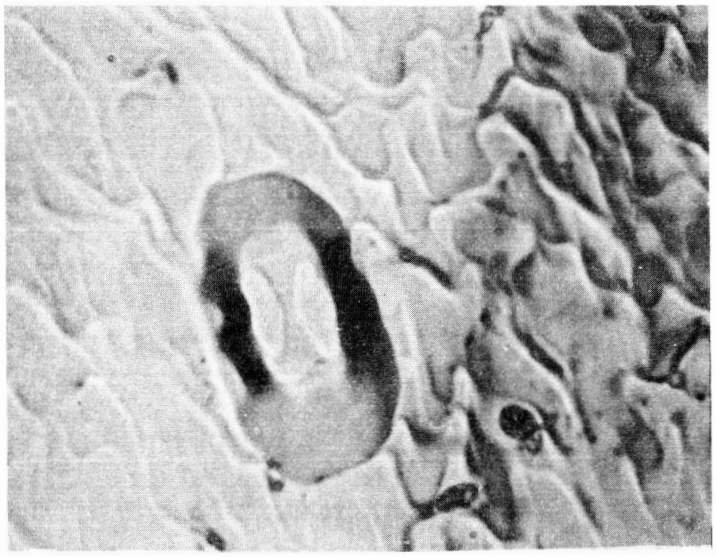

Figure VIII-10. ⟨110⟩ Tungsten Surface at 1084X with Green Light
A pair of photographs of an etch pit before and after firing at 2000°C for 1 hr. The first shows some structure on the floor of the pit, clearly "stepped" sides, and a background made up of ⟨110⟩ surface broken by sections of complex plane. The second picture shows marked rounding-off of all surfaces while the general outline of the features remains unchanged.

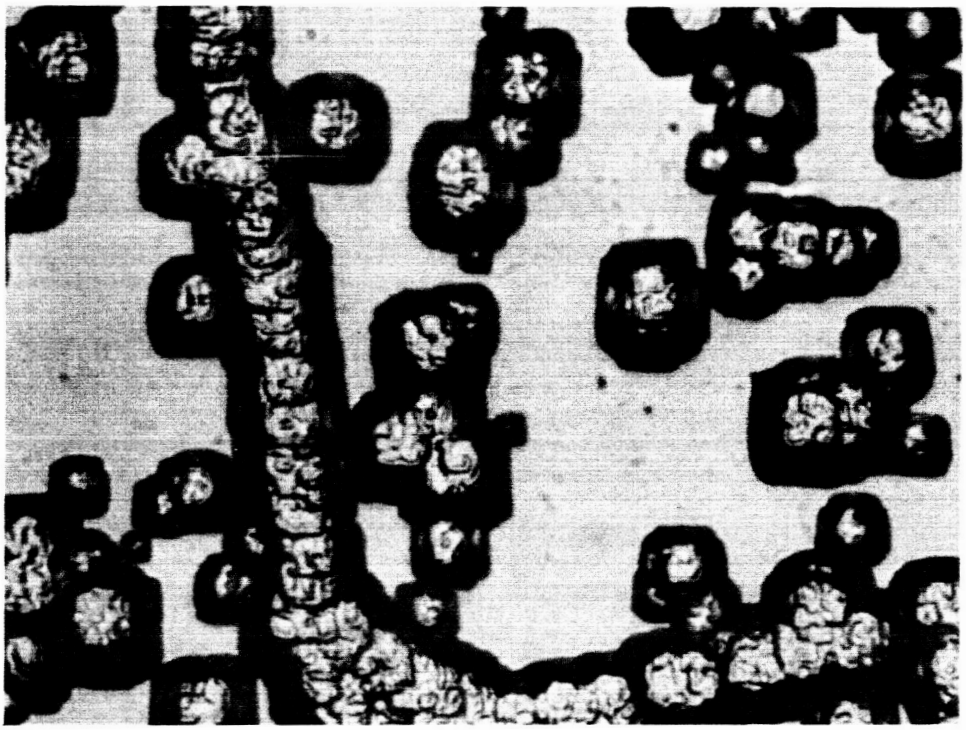

Figure VIII-11. Electropolished ⟨100⟩ Tungsten Etched in $K_3Fe(CN)_6$ to Develop Square Etch Pits with Structure Visible on Sloping Sides, Photographed at 760x after 5 minutes at 2100 °C.

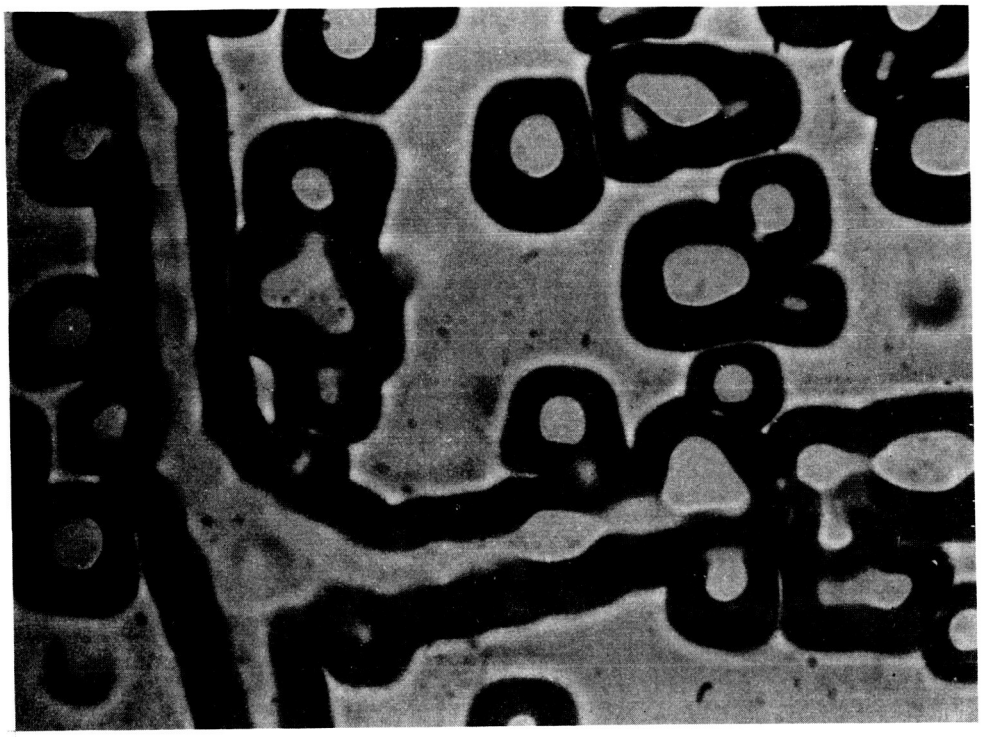

Figure VIII-12. Electropolished ⟨100⟩ Tungsten Etched in $K_3Fe(CN)_6$ after 7 Hours at 2550°C, 760x. This photograph shows the continuing process of smoothing of the bottom of etch pits, merging of pits, and rounding of their outlines.

Figure VIII-13. Photograph of Tungsten Emitter Before Firing, 5X

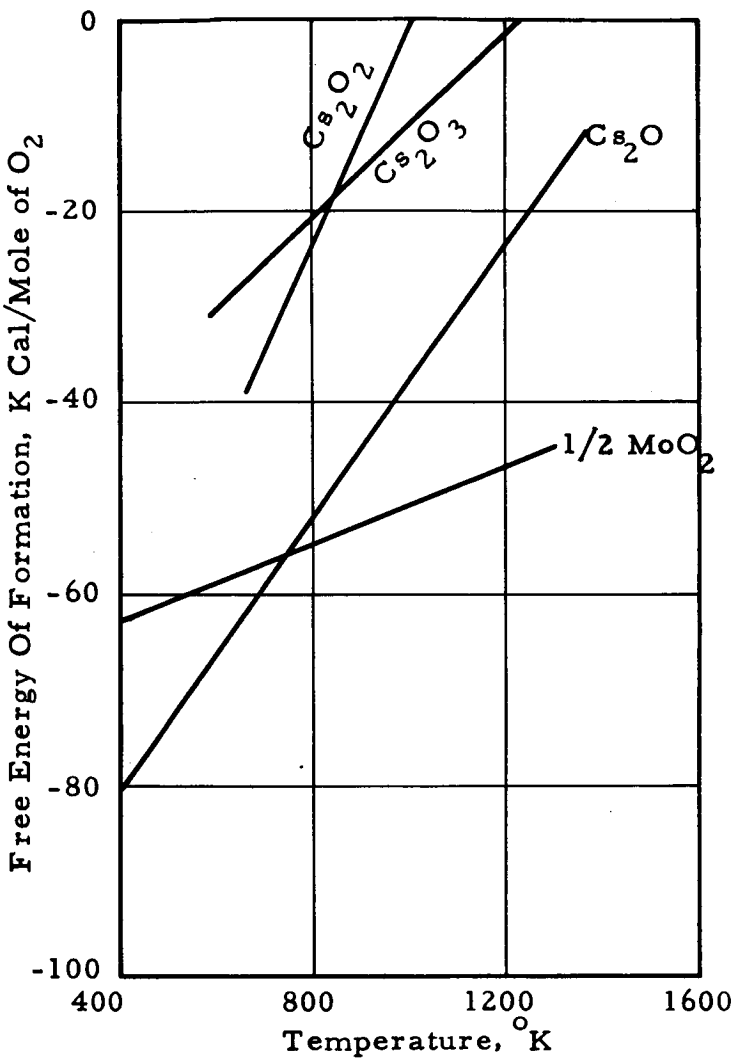

Figure VIII-14. Free Energy of Formation of Molybdenum and Cesium Oxides as a Function of Temperature.

64-R-7-130

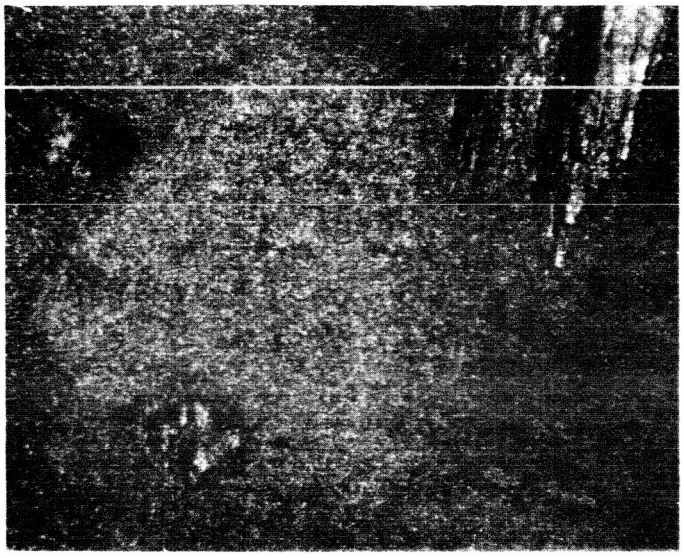

Figure VIII-15. Molybdenum Test Surface (M1) After Thermionic and Photoelectric Operation, 75X

64-R-7-131

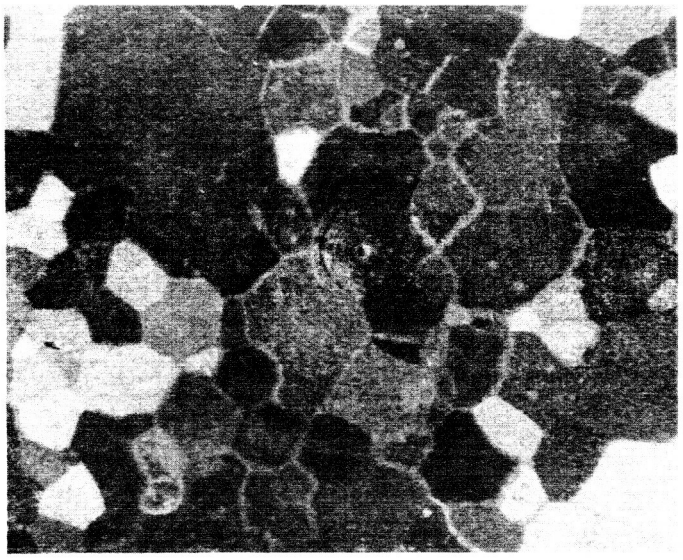

Figure VIII-16. Same As VIII-15, 7X

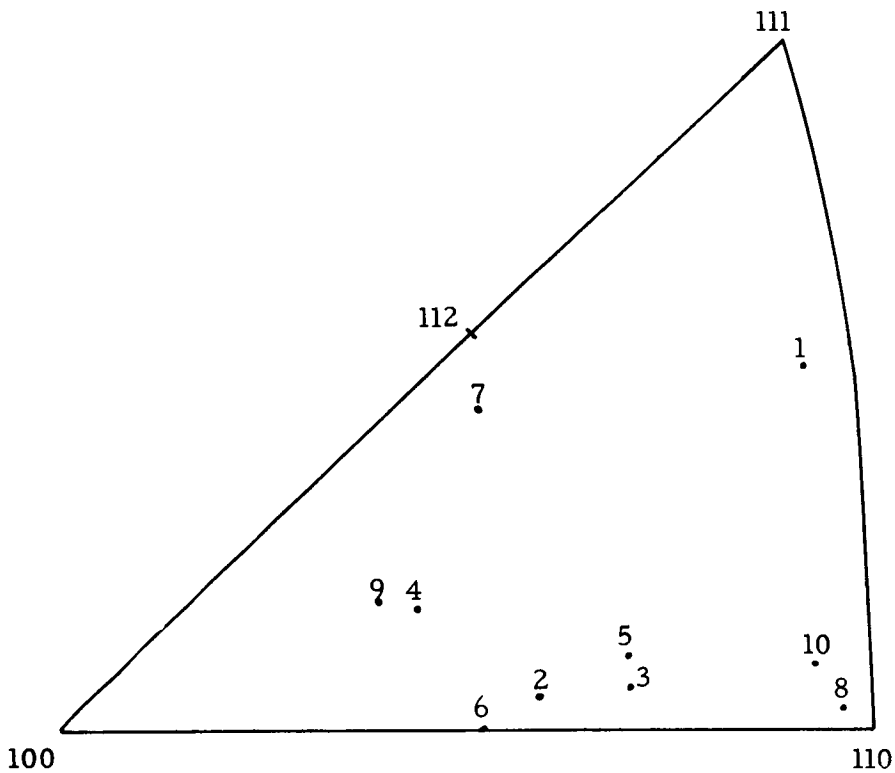

Figure VIII-17. Orientation of Large Grains on Molybdenum Emitter on Unit Stereographic Triangle

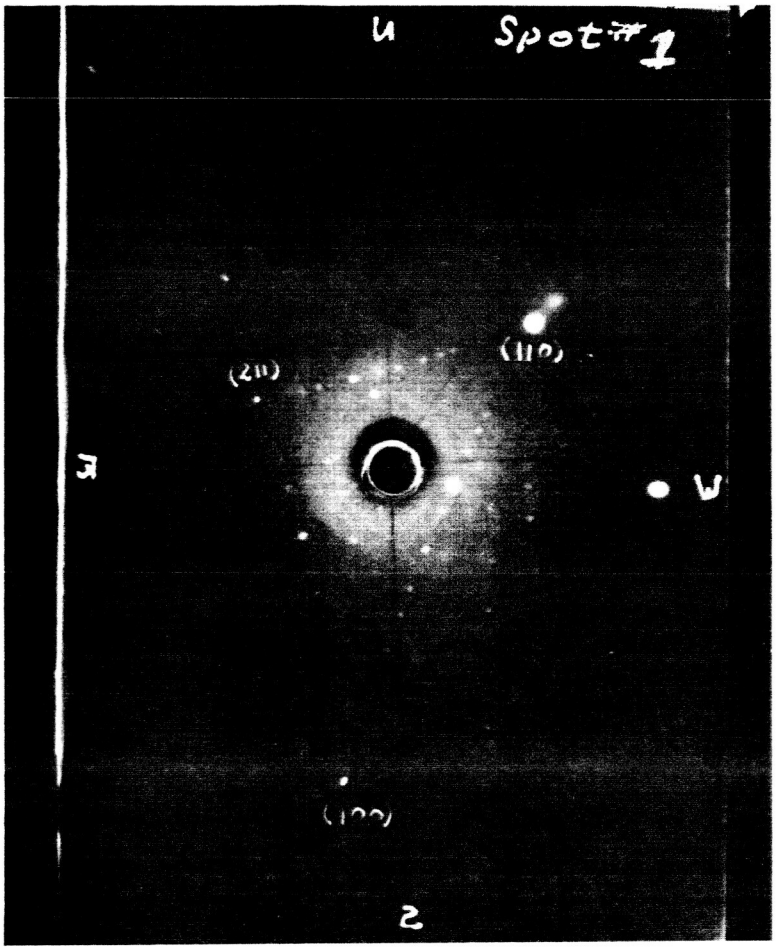

Figure VIII-18. Laue' Back Reflection X-Ray of Grain #1 Test Surface (M1)

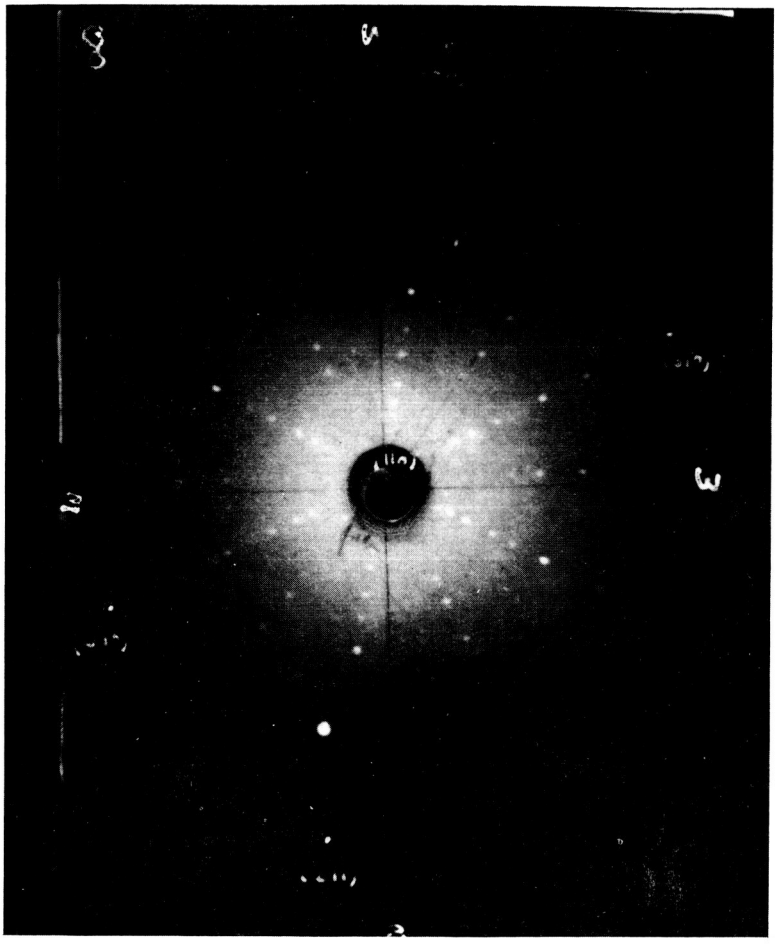

Figure VIII-19. Laue' Back Reflection X-Ray of Grain #8
Test Surface (M1)

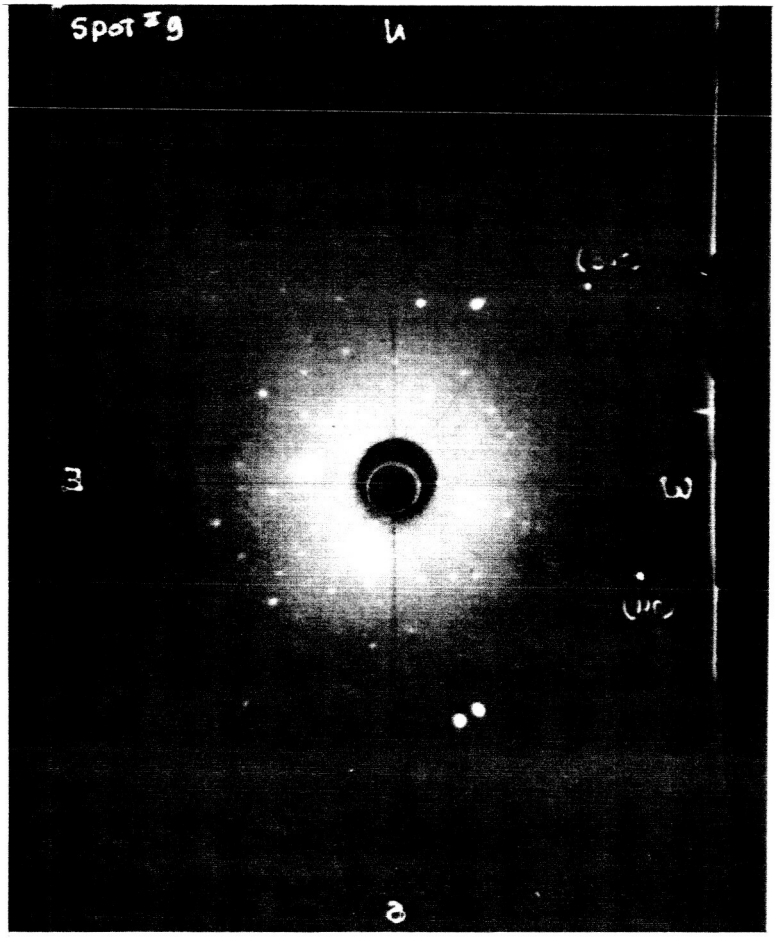

Figure VIII-20. Laue Back Reflection X-Ray of Grain #9
Test Surface (M1)

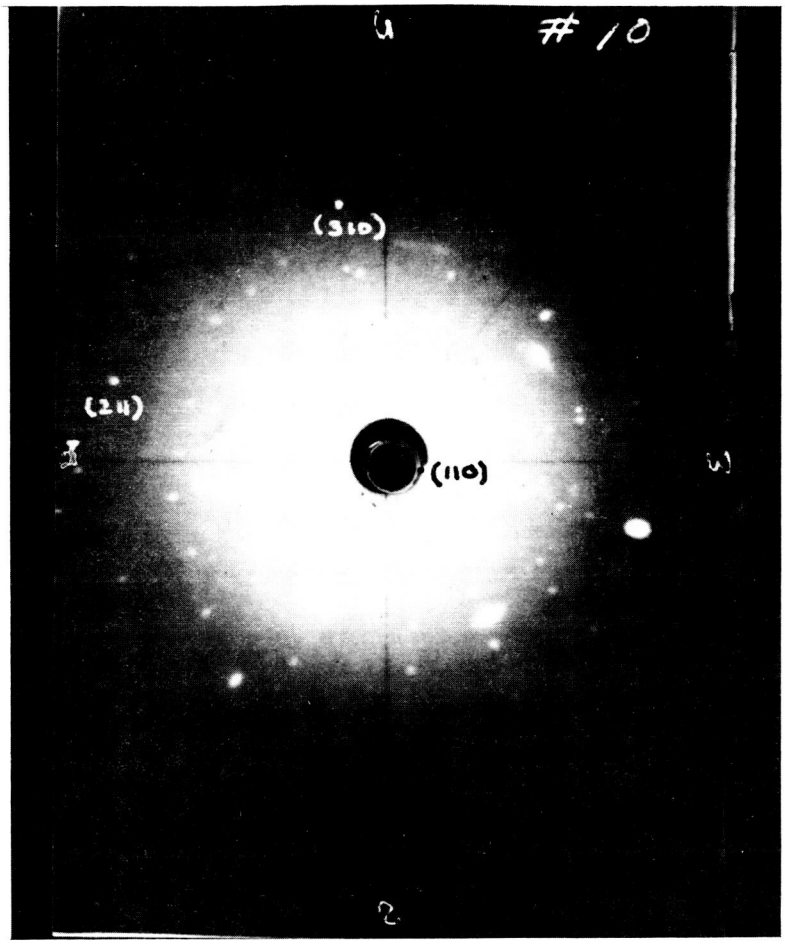

Figure VIII-21. Laue' Back Reflection X-Ray of Grain #10
Test Surface (M1)

APPENDIX A

Orientation Determination of Large Grains in Polycrystalline Mo

by

ADVANCED METALS RESEARCH CORPORATION

for

Thermo Electron Engineering Corporation

One sample of polycrystalline Mo was submitted for single crystal orientation studies. The sample consisted of large grains of the order of one mm. in size. Ten grains were outlined on a photomicrograph (75x) submitted with the sample for the purpose of obtaining their orientations with respect to the plane of the surface. Directions designated as north, south, east and west on the photomicrograph were maintained for the grain orientation studies.

In addition, an x-ray diffraction pattern of the specimen surface was taken employing a Norelco high angle diffractometer, Ni filtered Cu radiation, scintillation counter and pulse height analyzer.

Orientations were determined using the Laue back reflection technique and polychromatic Cu radiation. A 1/2 mm. collimator was employed to insure that the back reflection patterns were obtained from single grains. Only in one case (Grain No. 7) was a pattern obtained which was the result of the super position of the patterns from two grains (Grains No. 6 and No. 7). Using the pattern obtained from grain No. 6, it was still possible to isolate

the spots resulting from the diffraction from planes in grain No. 7, and thus determine the orientation of this grain.

To completely fix the orientation of a grain with respect to the plane of the surface, it is necessary to determine the angular relationship of two directions in the grain with respect to the surface normal. For this purpose the ⟨110⟩ and ⟨211⟩ directions were chosen.

Fig. 1 represents the angular coordinate system chosen to define the orientation.

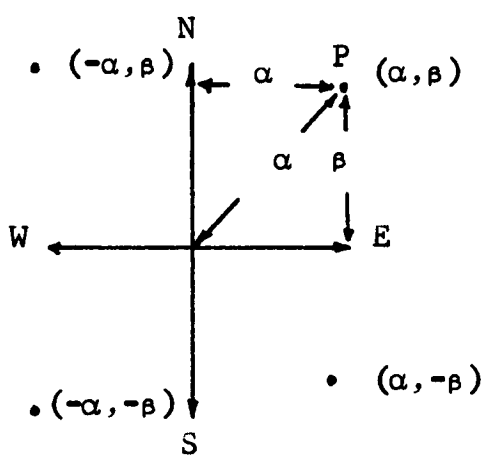

Specimen surface plane corresponds to plane of the paper.

Fig. 1 Coordinate System

If the specimen was rotated around the north-south axis through an angle α, and then around the east-west direction through an angle β, the planes normal to direction P would then be parallel to the plane which contained the surface prior to the rotation.

The angle between the surface normal and the ⟨110⟩ direction (designated as γ) is also listed in Table I.

Table I

Grain Orientations in Polycrystalline Mo

Grain	⟨110⟩ α°	⟨110⟩ β°	⟨211⟩ α°	⟨211⟩ β°	γ°
1	-14.5	14.5	14.5	7.5	20.5
2	5.5	-15.5	18.5	13	16.5
3	8	8	-22	4.5	12
4 *	-22.5	7	7	12.5	23.5
5	-11	-2	1.8	-29.5	11
6	15	-10.5	-15	-14	18.5
7	3	28	4	-3	28
8	0	1.5	5.5	-28.2	1.5
9	22.5	-9	4	5	24.5
10	-5	-1	24	8	5

* Two grains contributing strongest pattern chosen.

The diffraction pattern obtained from the specimen surface revealed the presence of an additional phase or phases. Attempts to index the pattern using the ASTM card index were unsuccessful. Table 2 lists the data obtained from this pattern in terms of interplanar spacing, d, and relative line intensities.

Table II

Diffraction Pattern from Mo Surface (Cu radiation)

line	d	I	(hkl)
1	2.778	7	
2	2.562	49	
3	2.506	31	

Table II (Continued)

line	d	I	(hkl)
4	2.473	100	
5	2.366	24	
6	2.231	28	(110):Mo
7	2.004	7	
8	1.816	4	
9	1.584	17	(200):Mo
10	1.403	5	
11	1.345	9	
12	1.296	2	
13	1.280	7	(211):Mo
14	1.251	2	
15	1.235	6	
16	1.181	6	
17	1.117	9	(311):Mo

It can be seen from the above table that the diffraction pattern obtained from the surface contaminant was quite strong. Contributions from this contaminant can also be seen in the Laue back reflection photographs.

However, the pattern obtained did not correspond to any compounds in the Mo-O, Mo-C and Mo-N systems or with any other Mo compounds listed. Using the relative line intensities, no other compounds could be found which corresponded to the pattern obtained. Because of the preferred orientation present in the sample, using relative line intensities to attempt to identify the contaminant may not be sufficient, since the ASTM index is

based on relative intensities from random powder specimens. If the contaminant is a mixture of phases, this means of identification would also be ineffective.

Donald M. Koffman

Sheldon H. Moll,
Laboratory Director

APPENDIX B

ORIGINAL DATA

DESCRIPTION OF CROSS SCAN PLOTS

A cross scan is a plot of current versus position along a line across the face of the emitter. The magnitude of the current is determined by comparison with a known calibrating current. On each plot the calibration amplitude is indicated either as a pair of vertically aligned points or as two parallel lines. The zero reference is shown either as a single point or as a line which may or may not be straight, depending on the conditions in the device and the drift in the signal. Figures B-1, B-2, and B-3 illustrate typical cross scans and have the calibration, zero, and signal identified. In cases where there is a large difference between the magnitude of the calibrating current and that of the signal, the scaling factors are indicated on the plot. In Cross Scan #240 of Figure B-3, for example, the calibrating amplitude is noted as x5, so the effective calibration current is 5 times the actual value of 0.65 μA.

The horizontal scale is linear with position on the test surface face. However, because of instability in gain from scan to scan, position in a scan should be related through the use of prominent features. The actual length can then be expanded or contracted proportionately. Features may also be identified with elements in the display photographs.

In those plots having more than one cross scan or taken at other than a central line, there is a location indicated, as in Figure B-2. This refers to the dc current used to bias the scan either to the right (R) or the left (L) of the display photograph.

The scans shown in the body of this appendix are similar to these examples and may be evaluated in the same way. The element temperatures in the scanner vehicles are indicated on each cross scan. These runs may be grouped as follows:

	Runs
Thermionic Scanner	
Tungsten Surface	
Cs	29 - 61
Cs plus CsF	71 - 212
Short soak	71 - 176
Long soak	191 - 212
Molybdenum Surface	
Cs	235 - 253
Cs plus CsF	263 - 268
Photoelectric Scanner	
Molybdenum Surface	
Cs	PM1 - PM8
Cs plus CsF	PM14 - PM21

In some cases the currents were too small to allow cross scans to be taken. In these runs the accelerating electric field was switched on and off while making a plot of current vs time. The resultant square-wave plot enabled the determination of much smaller currents by reducing drift and furnishing a zero reference. These runs were obtained at the center only without any deflecting fields. Runs 208 and 212 contain this type of plot.

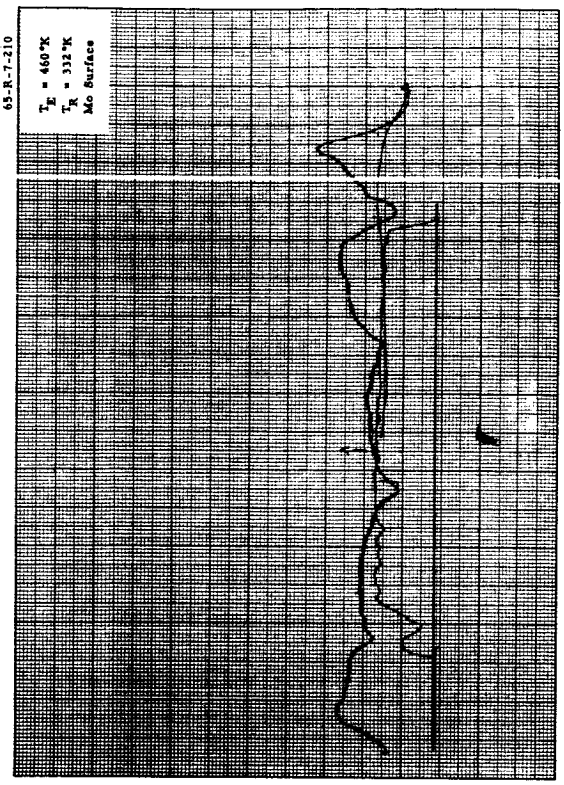

Photoelectric Cross Scan #PM2

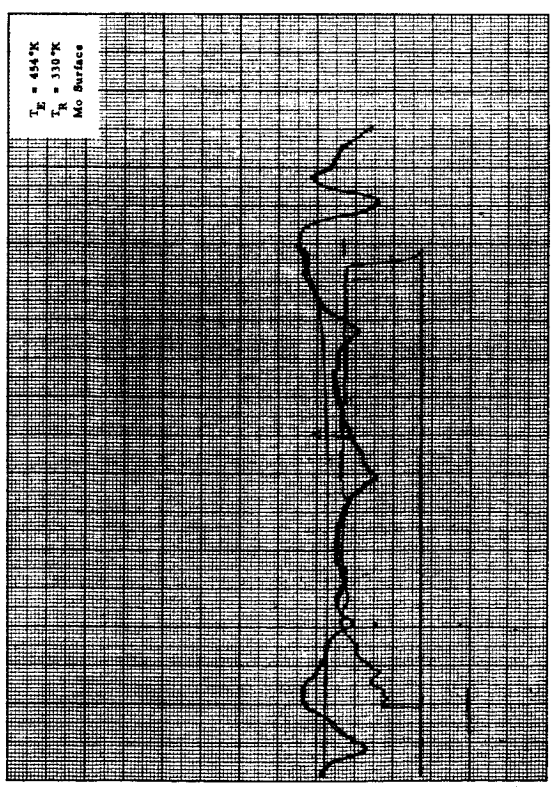

Photoelectric Cross Scan #PM1

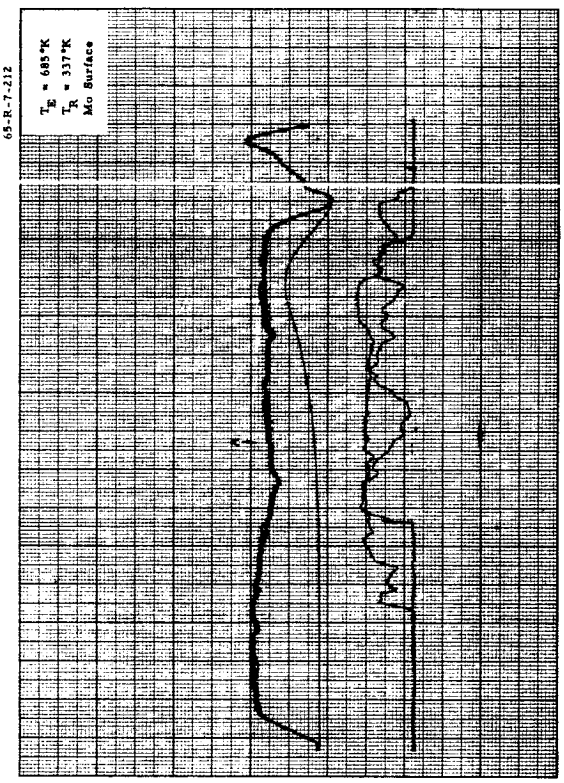

Photoelectric Cross Scan #PM4

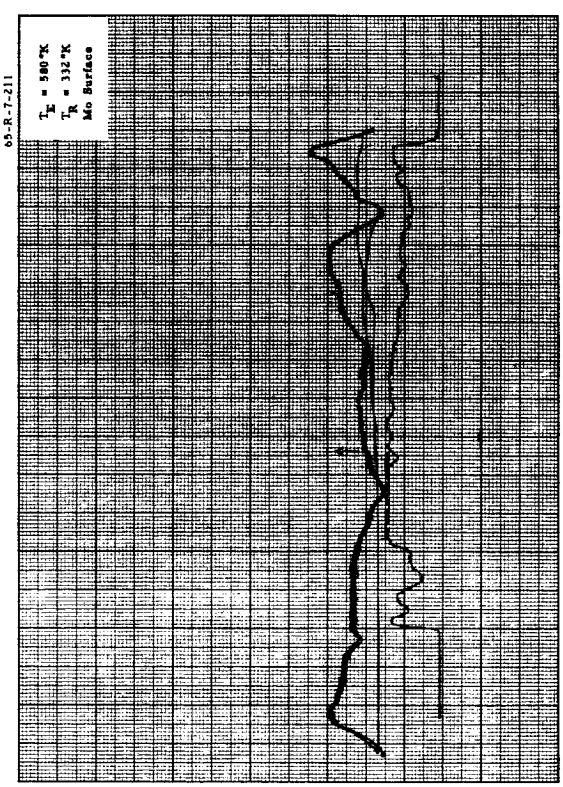

Photoelectric Cross Scan #PM3

65-R-7-214

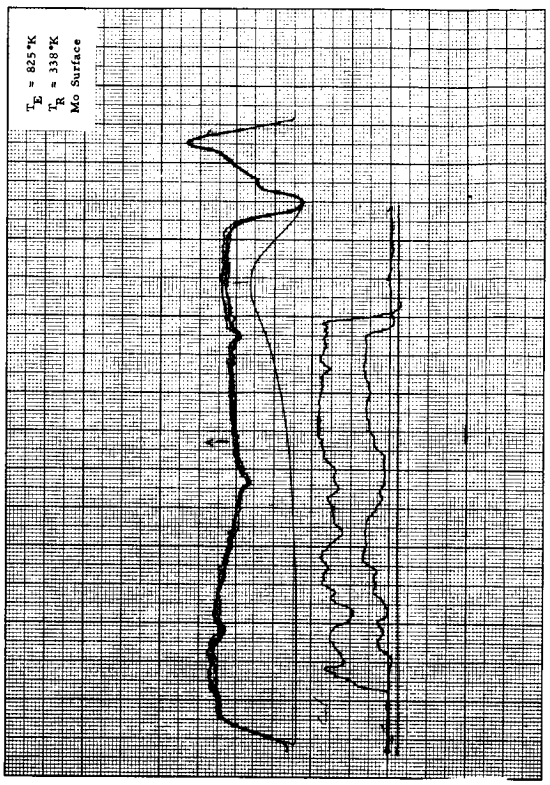

Photoelectric Cross Scan #PM6

65-R-7-216

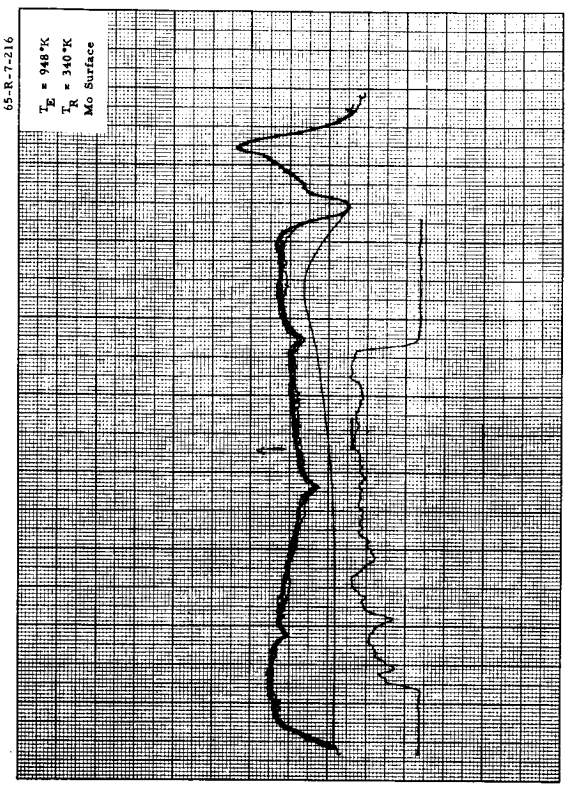

Photoelectric Cross Scan #PM8

65-R-7-213

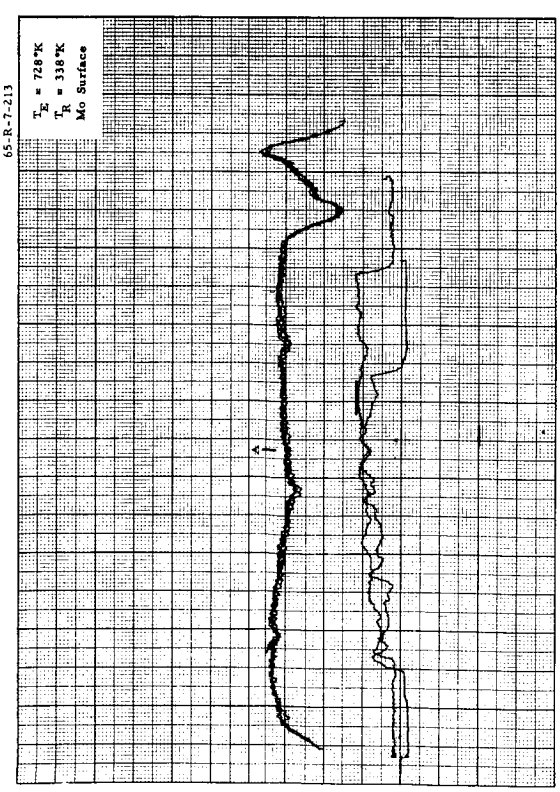

Photoelectric Cross Scan #PM5

65-R-7-215

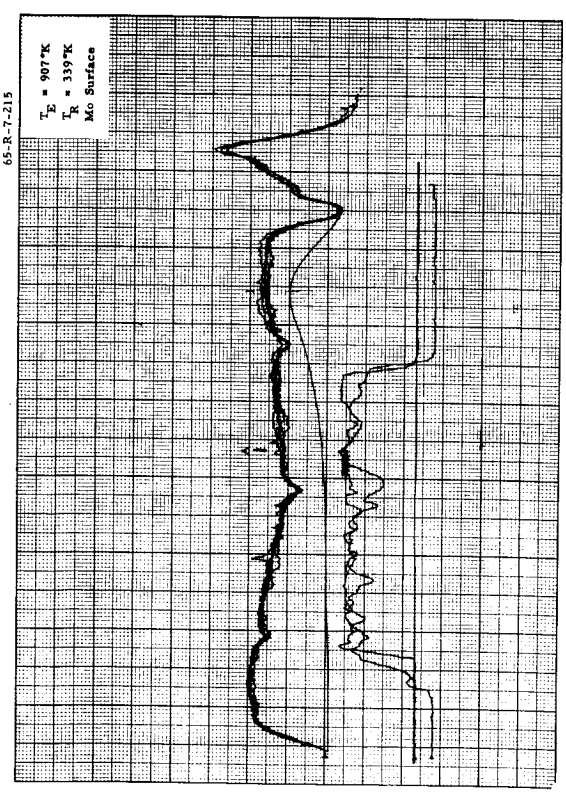

Photoelectric Cross Scan #PM7

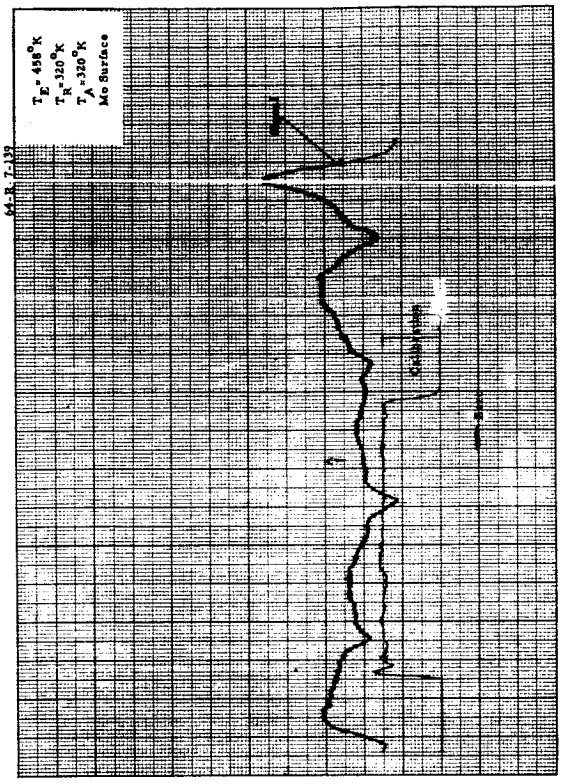

Photoelectric Cross Scan #PM 15

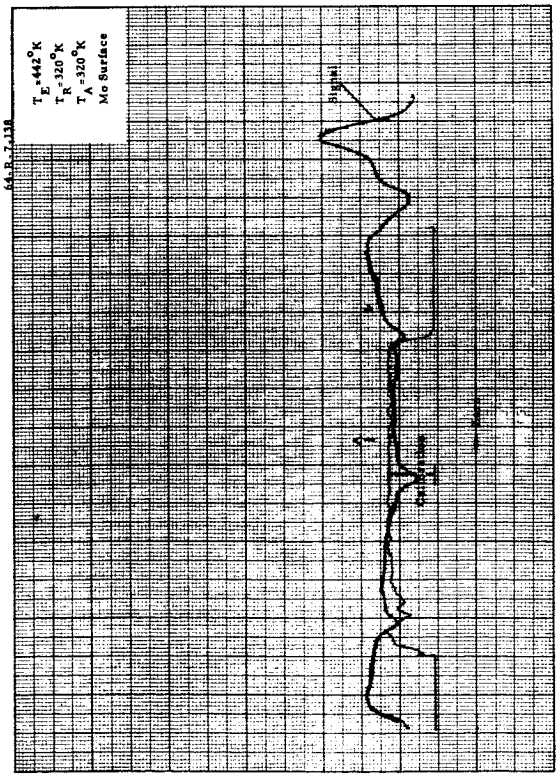

Photoelectric Cross Scan #PM 14

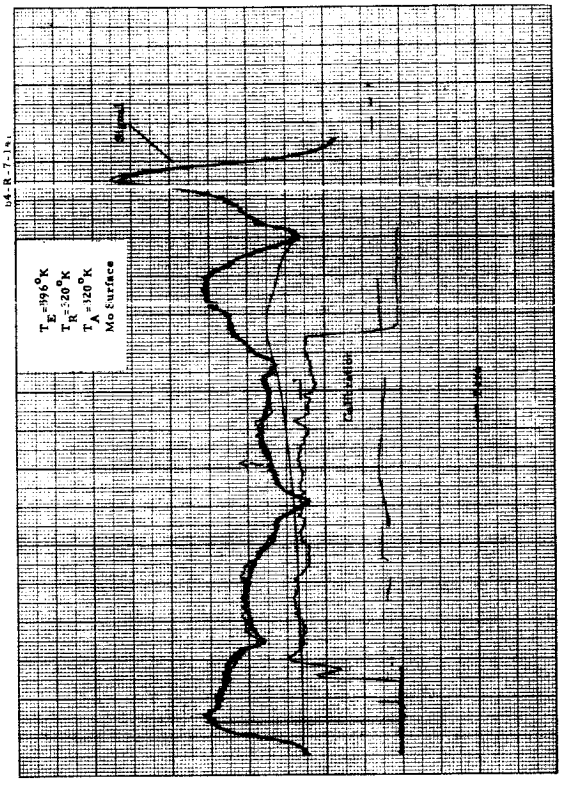

Photoelectric Cross Scan #PM 17

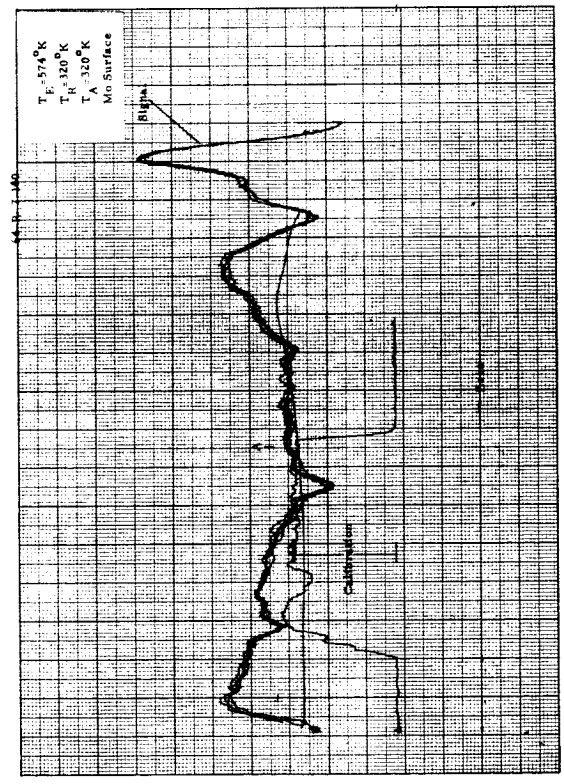

Photoelectric Cross Scan #PM 16

Figure B-1

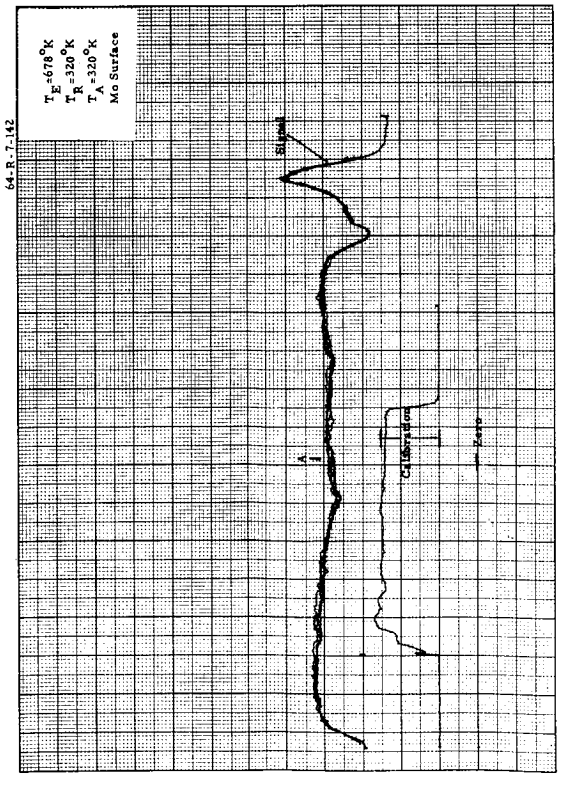

Photoelectric Cross Scan #PM 18

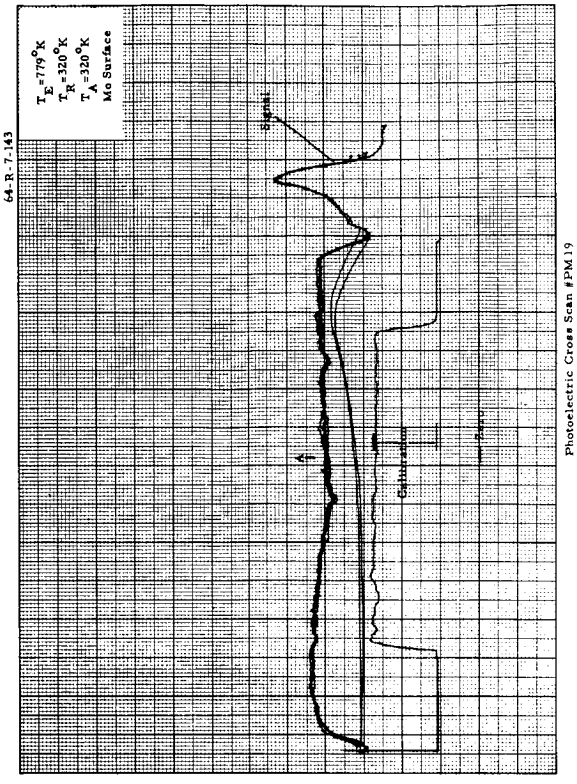

Photoelectric Cross Scan #PM 19

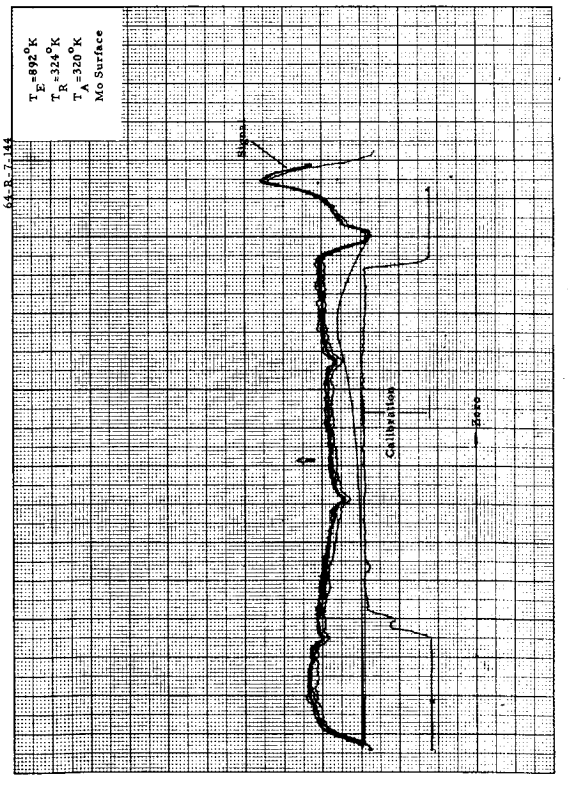

Photoelectric Cross Scan #PM 20

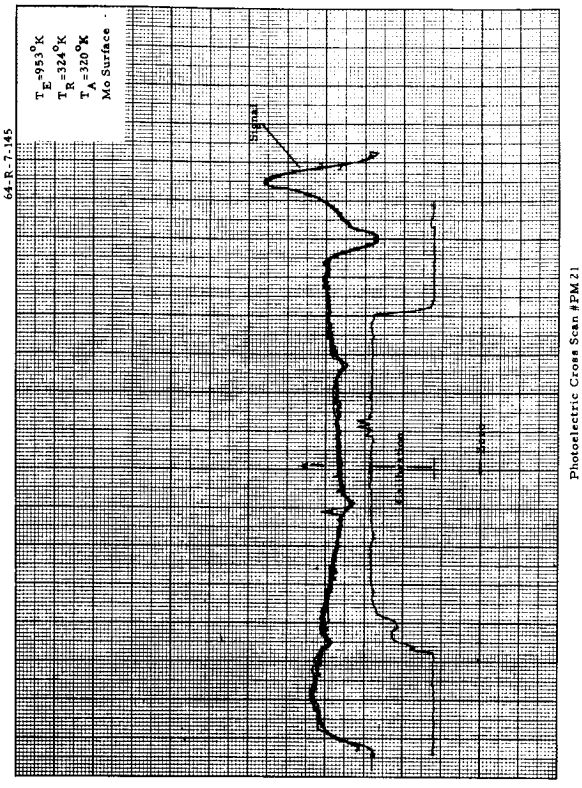

Photoelectric Cross Scan #PM 21

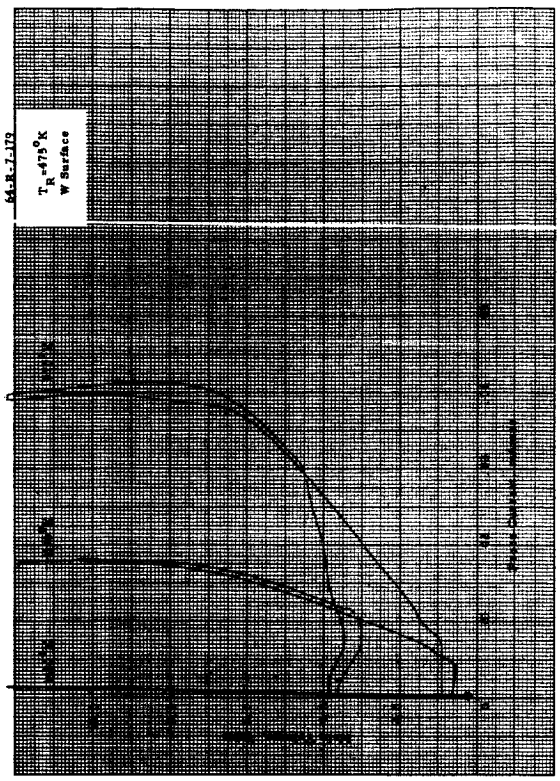

Main Voltage versus Probe Current, Cross Scan #30

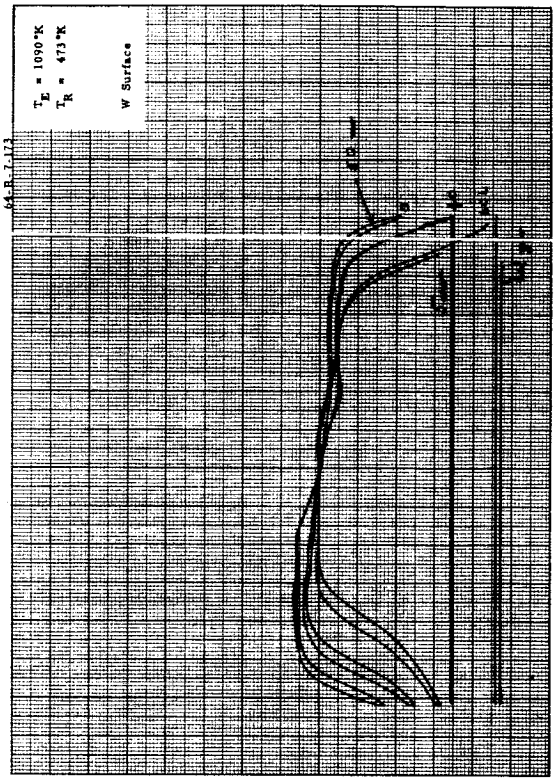

Thermionic Cross Scan #41

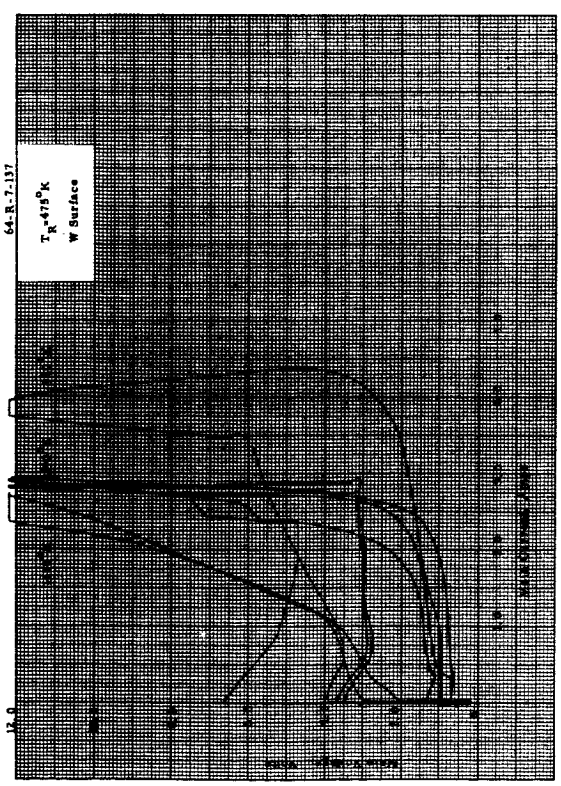

Main Current versus Main Voltage, Cross Scan #29

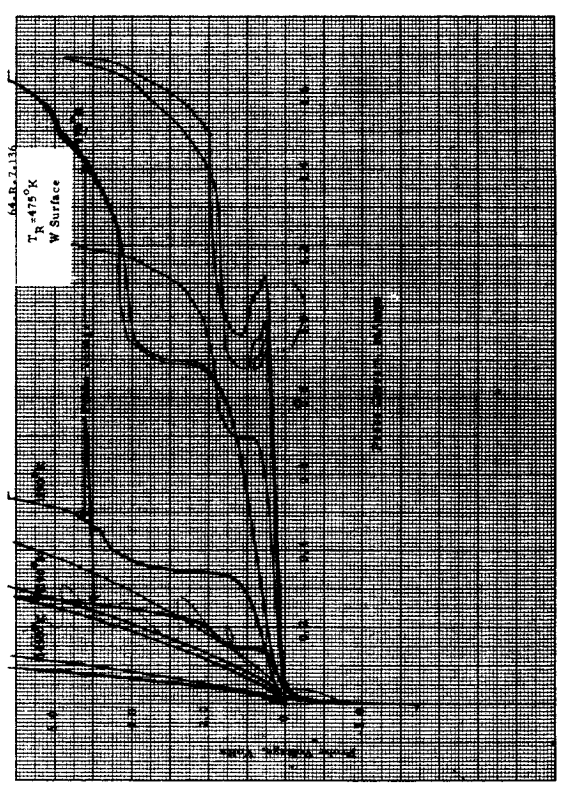

Probe Voltage versus Probe Current, Cross Scan #32

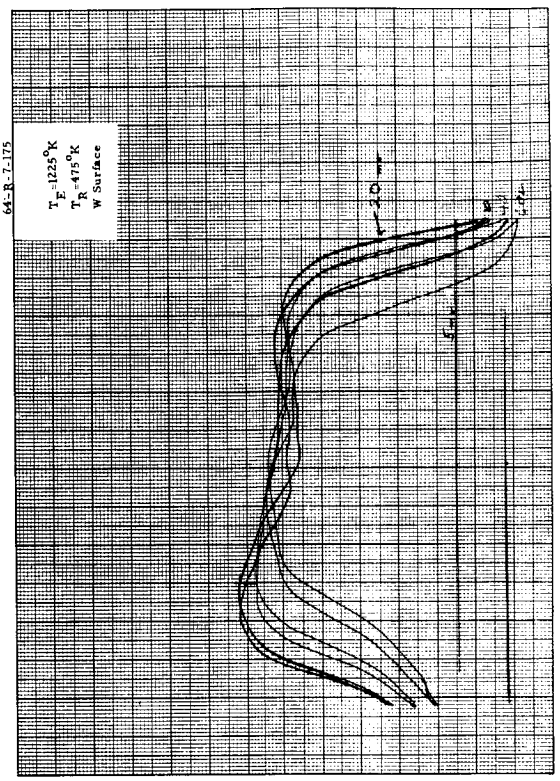

Thermionic Cross Scan #45

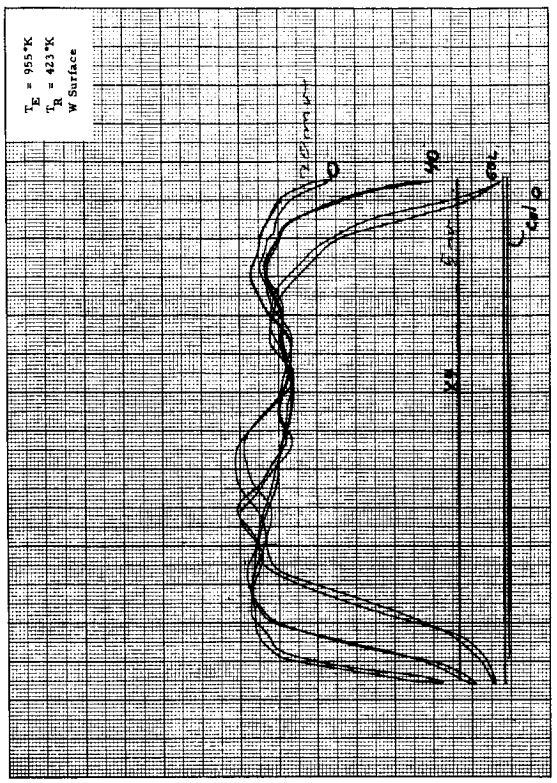

Thermionic Cross Scan #57

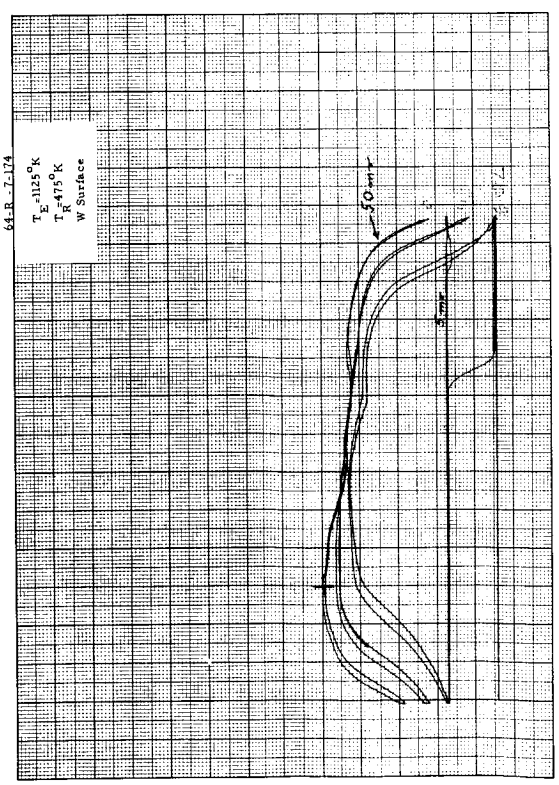

Thermionic Cross Scan #43

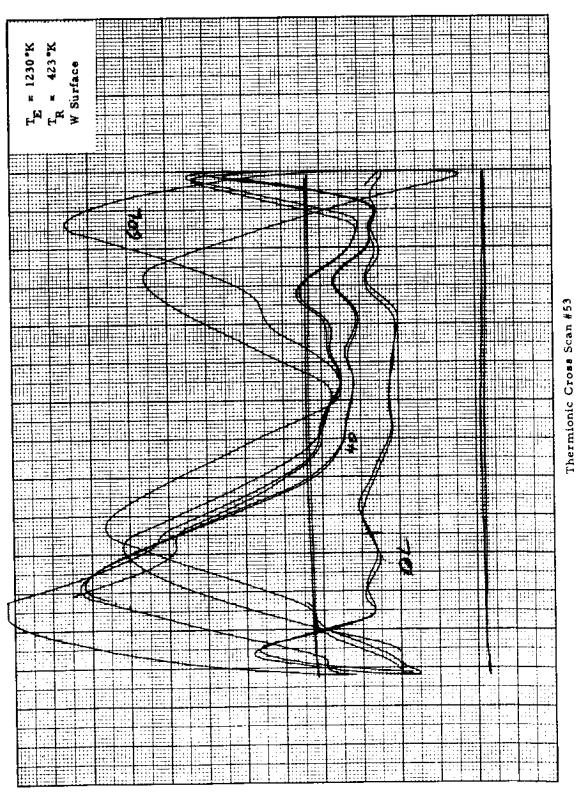

Thermionic Cross Scan #53

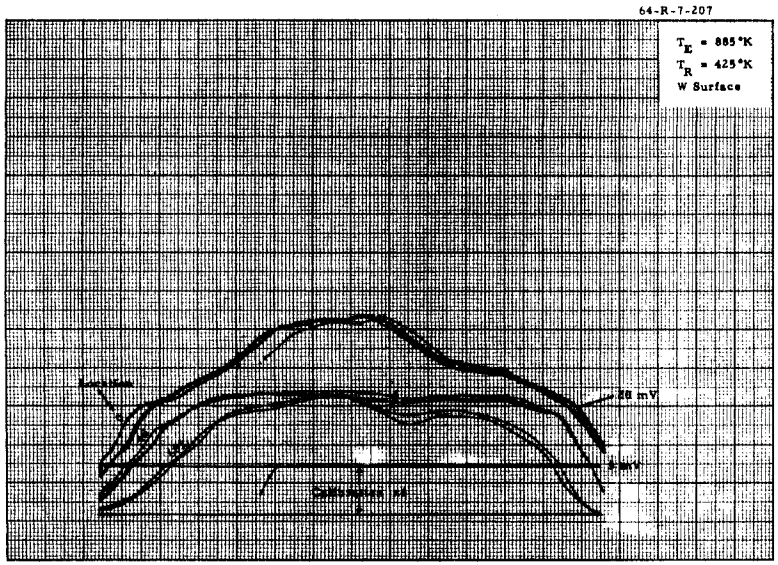

Thermionic Cross Scan #59

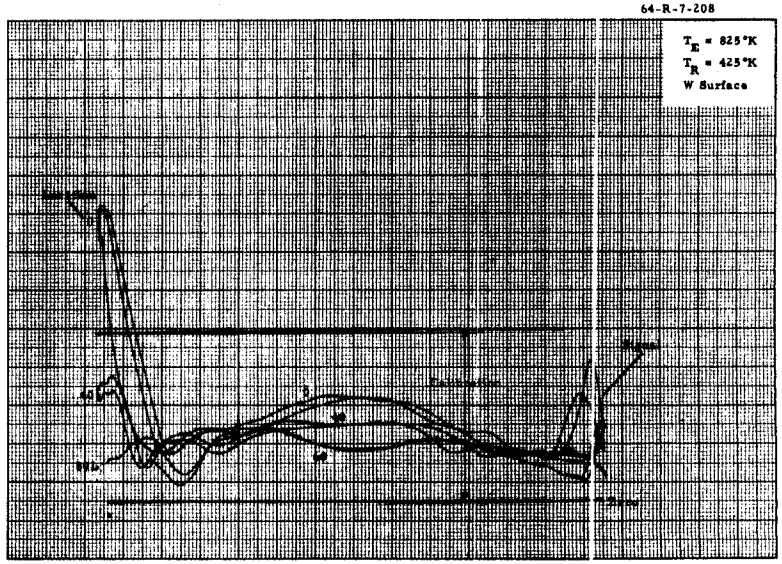

Thermionic Cross Scan #61

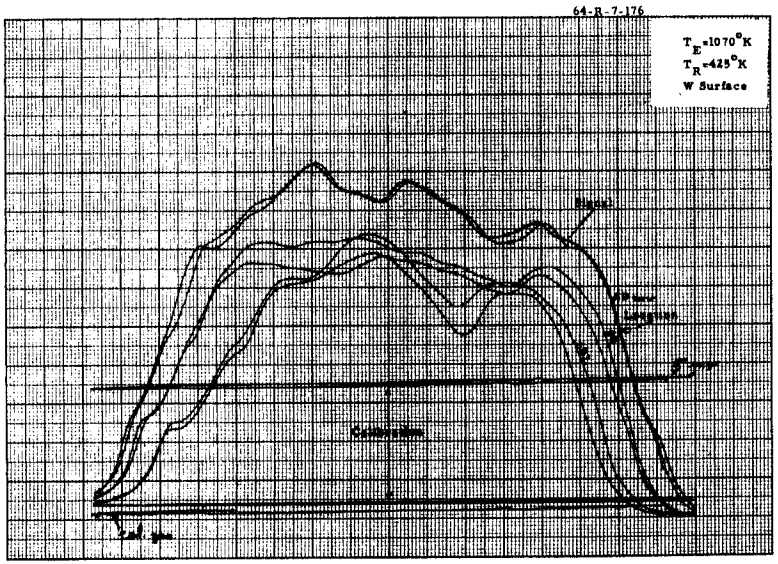

Thermionic Cross Scan #71

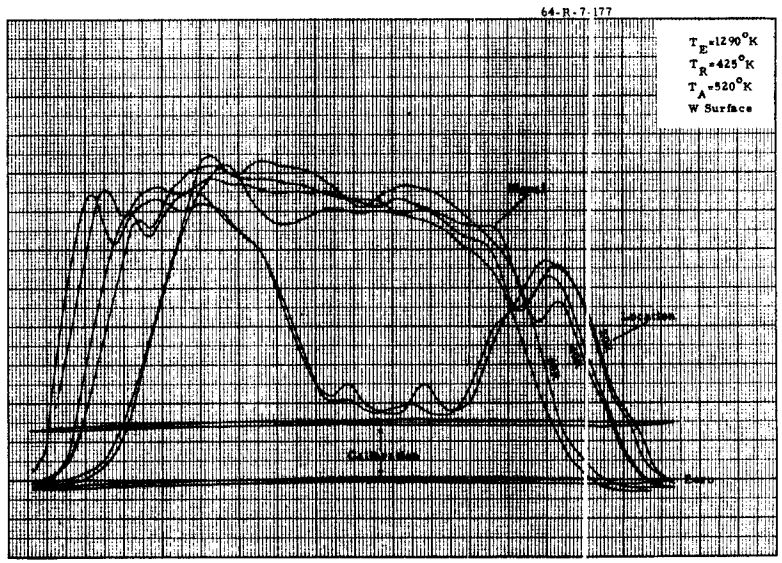

Thermionic Cross Scan #95

Figure B-2

THERMO ELECTRON
ENGINEERING CORPORATION

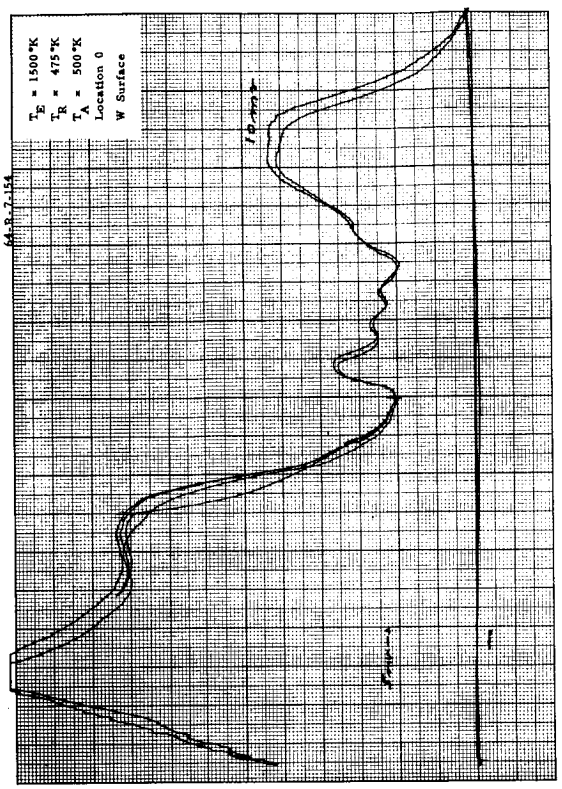

Thermionic Cross Scan #142

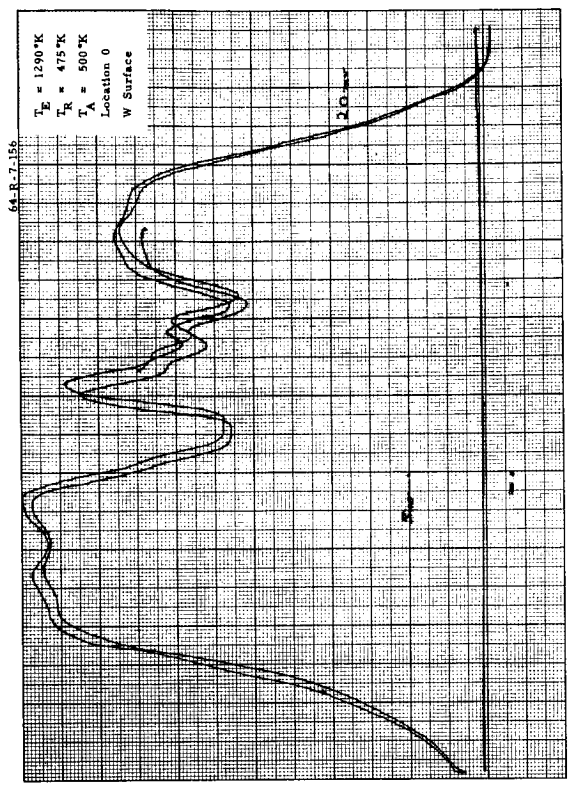

Thermionic Cross Scan #146

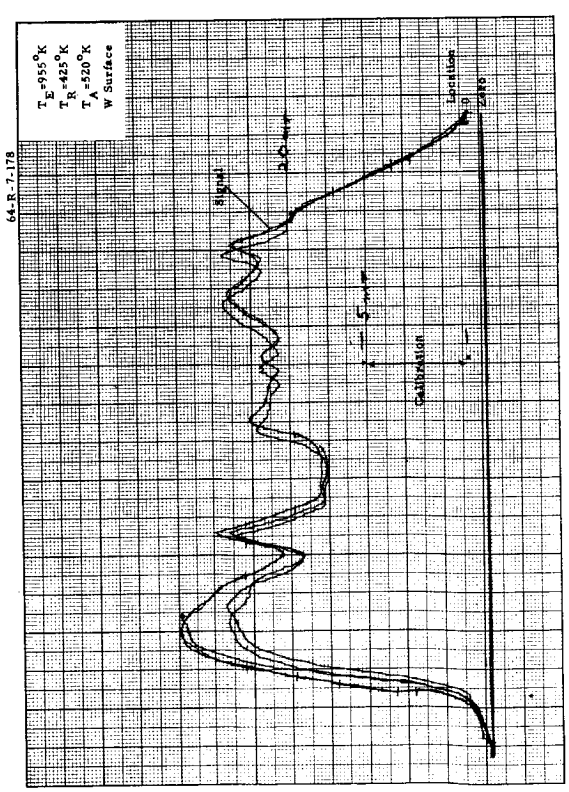

Thermionic Cross Scan #104

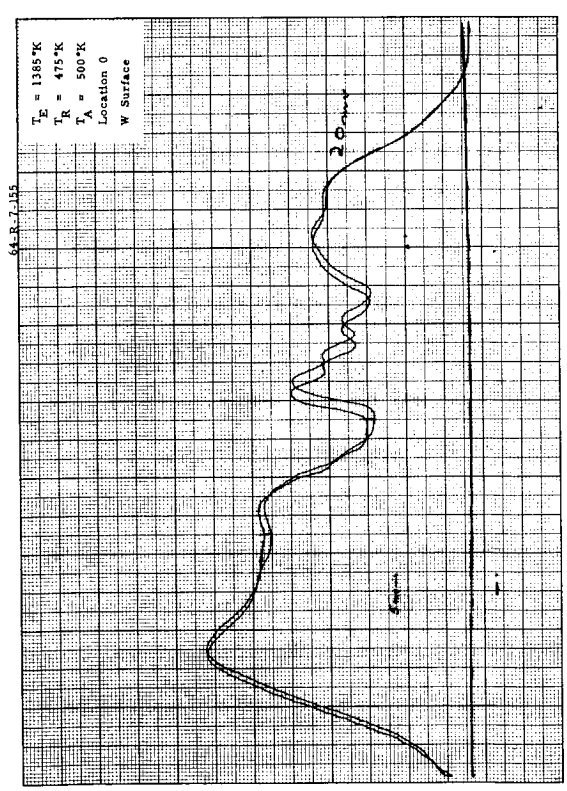

Thermionic Cross Scan #144

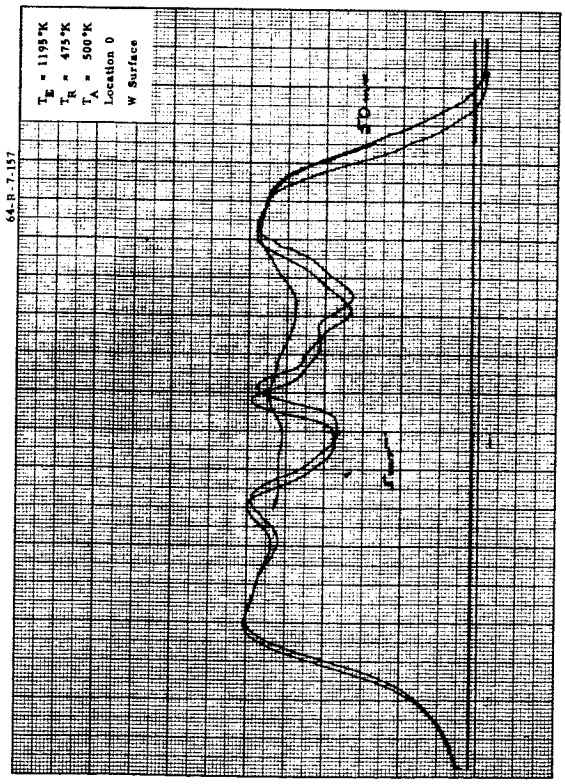

Thermionic Cross Scan #148

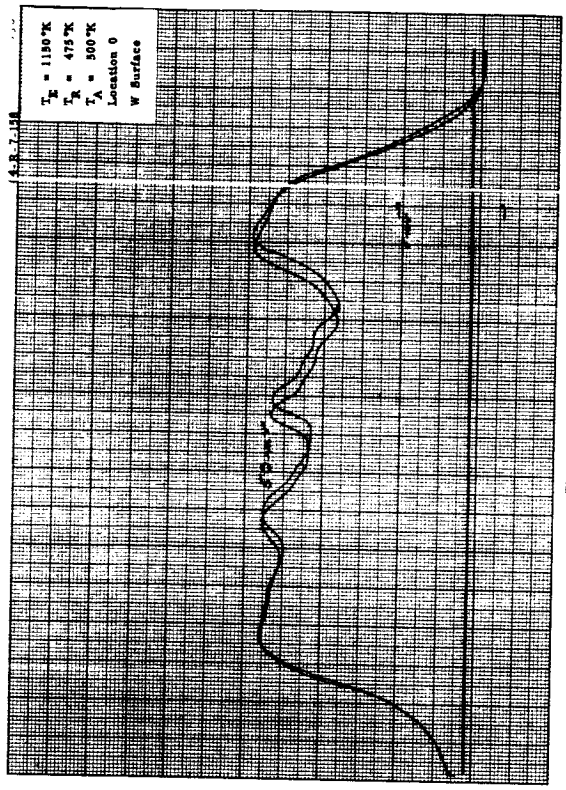

Thermionic Cross Scan #150

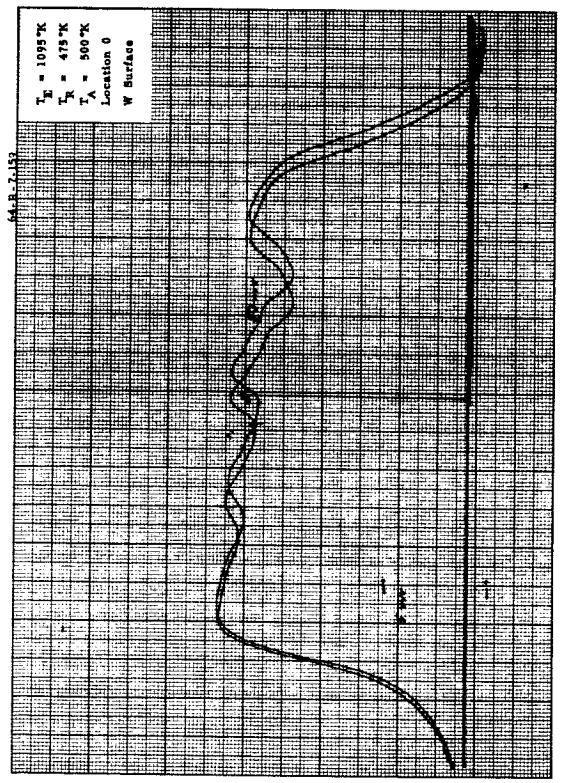

Thermionic Cross Scan #152

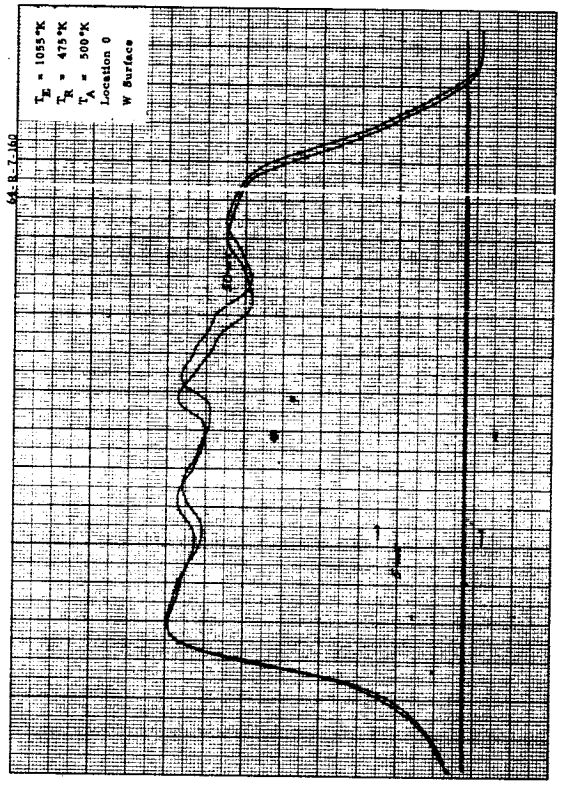

Thermionic Cross Scan #153

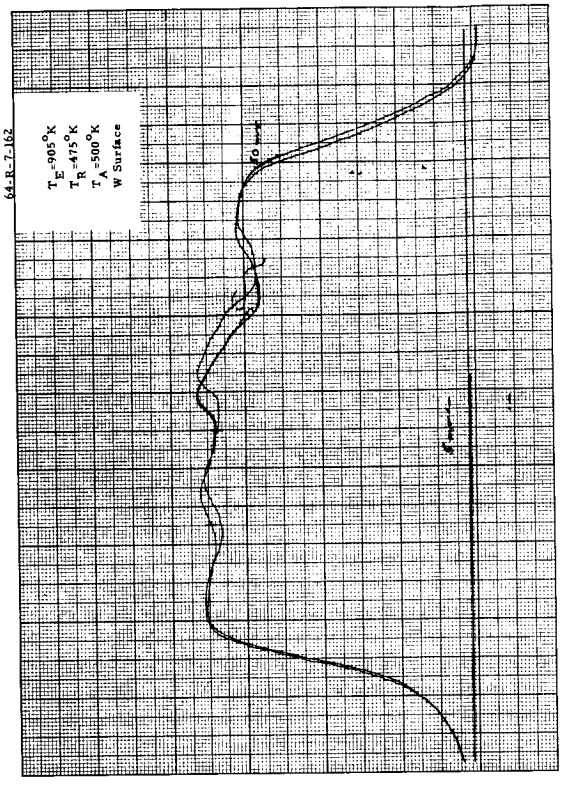

Thermionic Cross Scan #158

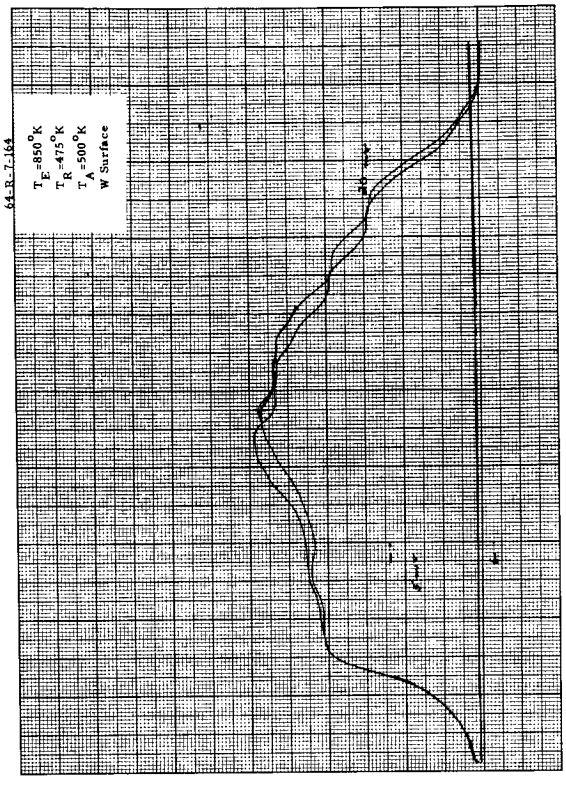

Thermionic Cross Scan #162

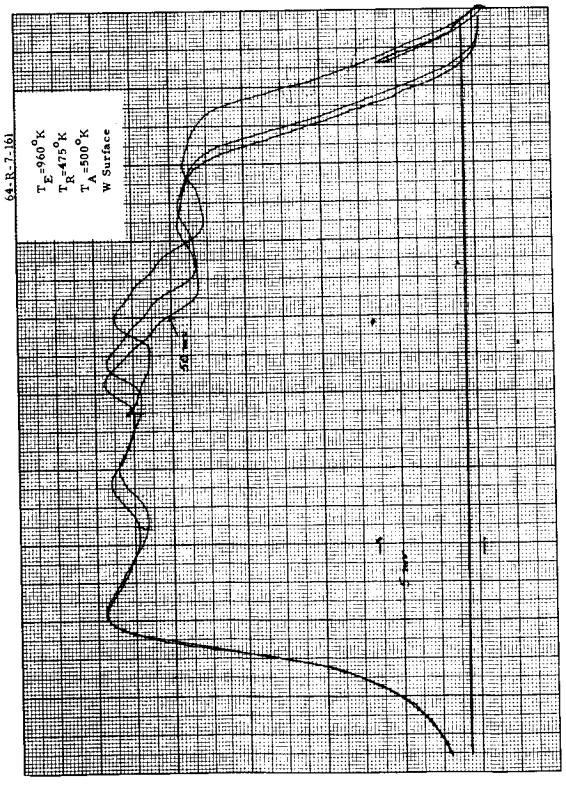

Thermionic Cross Scan #156

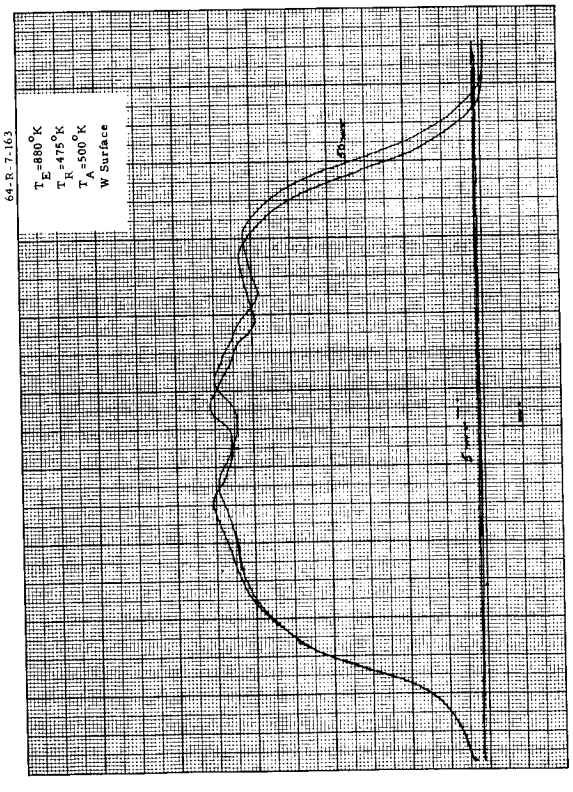

Thermionic Cross Scan #160

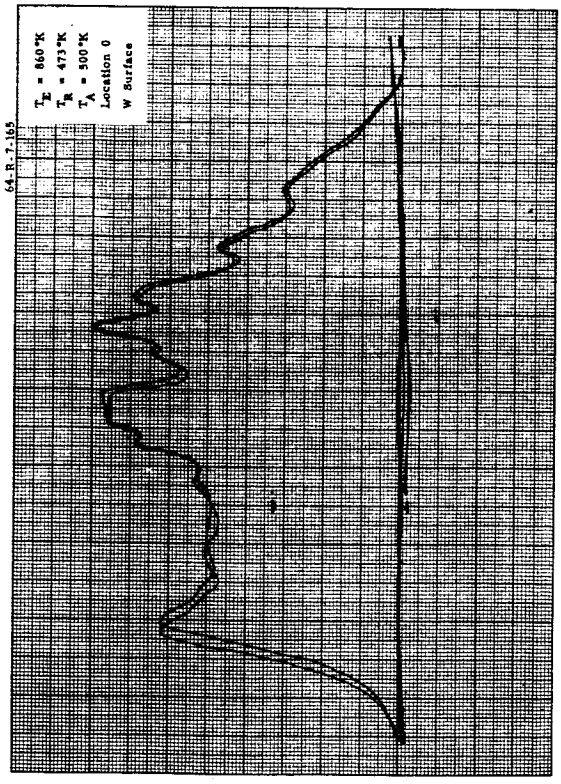

Thermionic Cross Scan #164

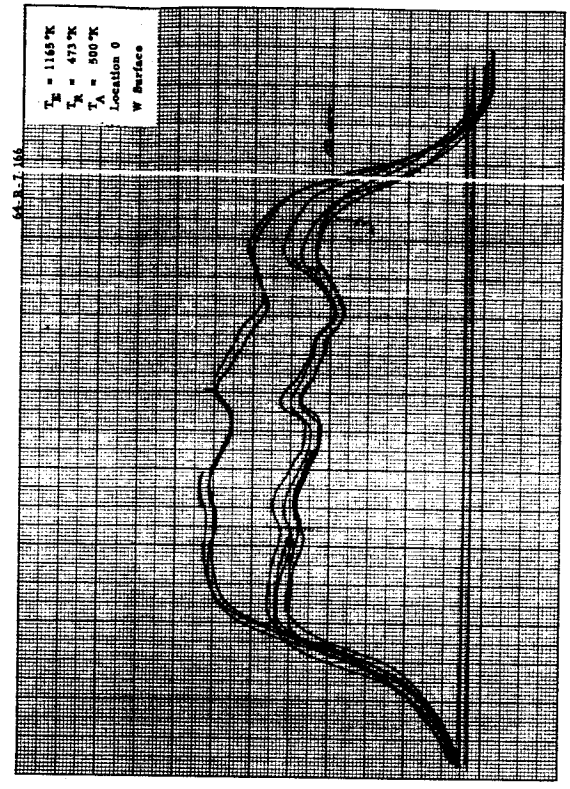

Thermionic Cross Scan # 165

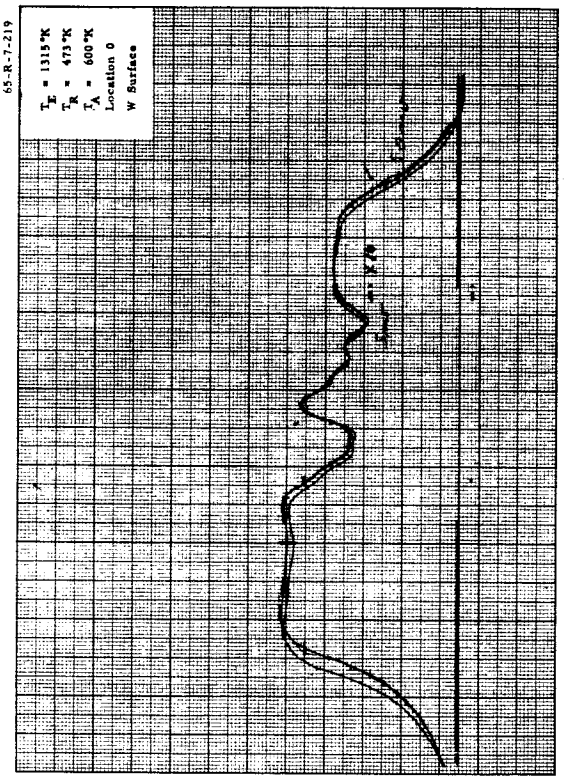

Thermionic Cross Scan #167

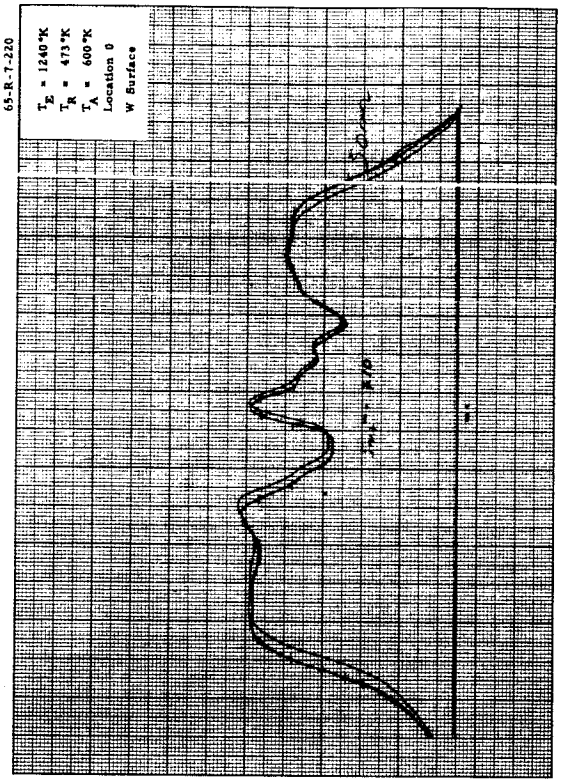

Thermionic Cross Scan #169

65-R-7-221

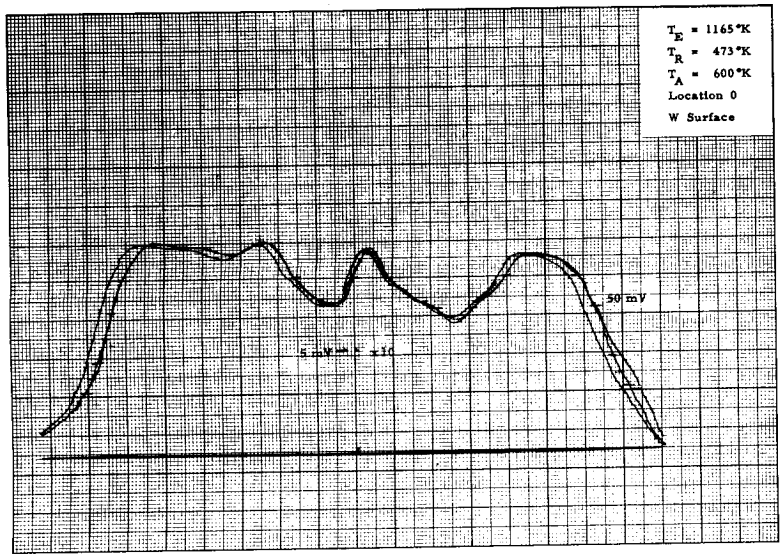

Thermionic Cross Scan #171

65-R-7-222

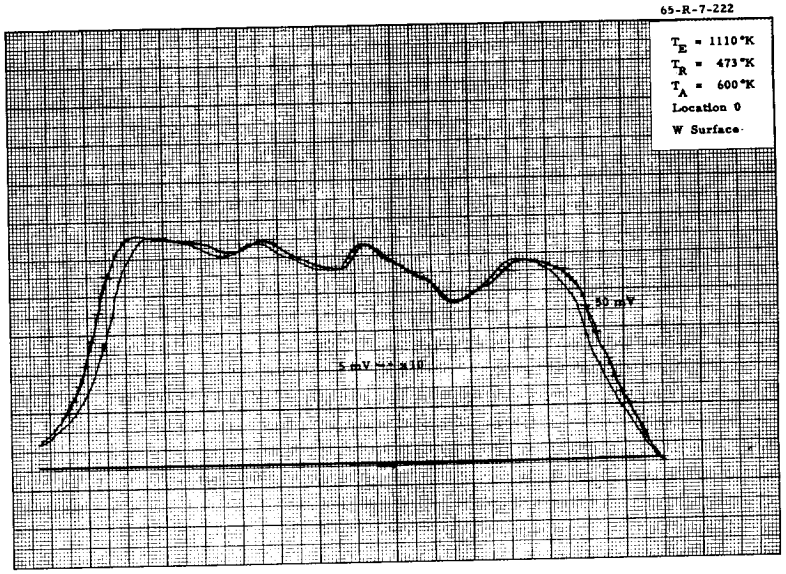

Thermionic Cross Scan #173

65-R-7-223

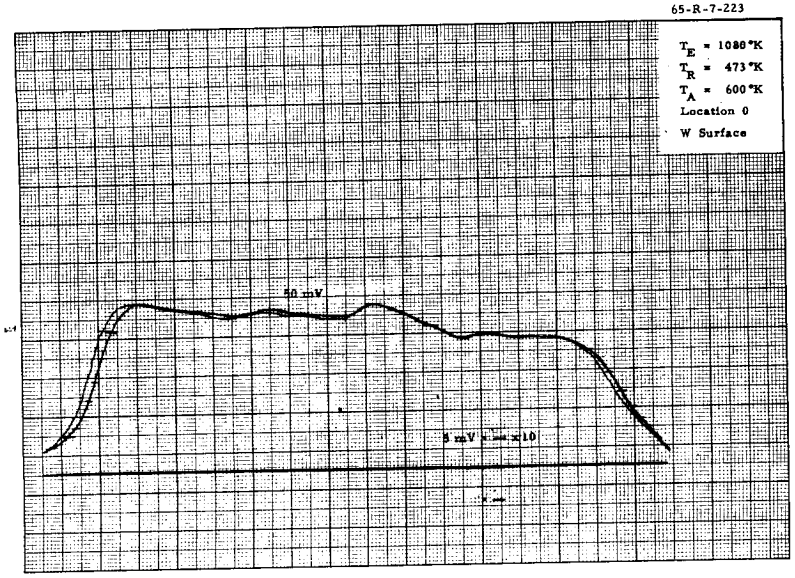

Thermionic Cross Scan #175

64-R-7-167

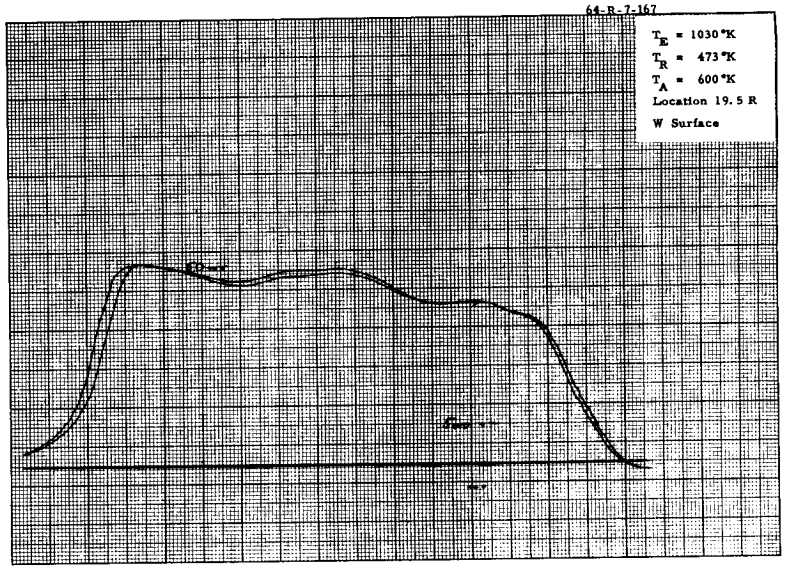

Thermionic Cross Scan #176

THERMO ELECTRON
ENGINEERING CORPORATION

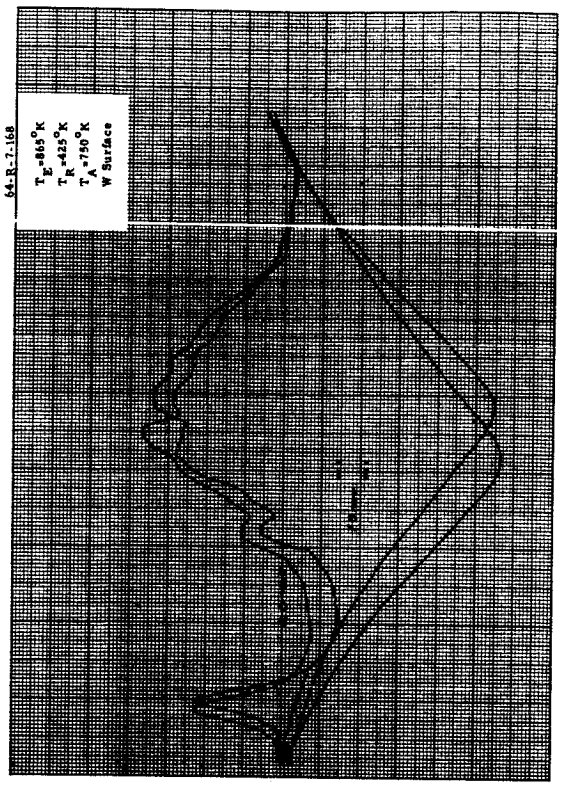

Thermionic Cross Scan #191

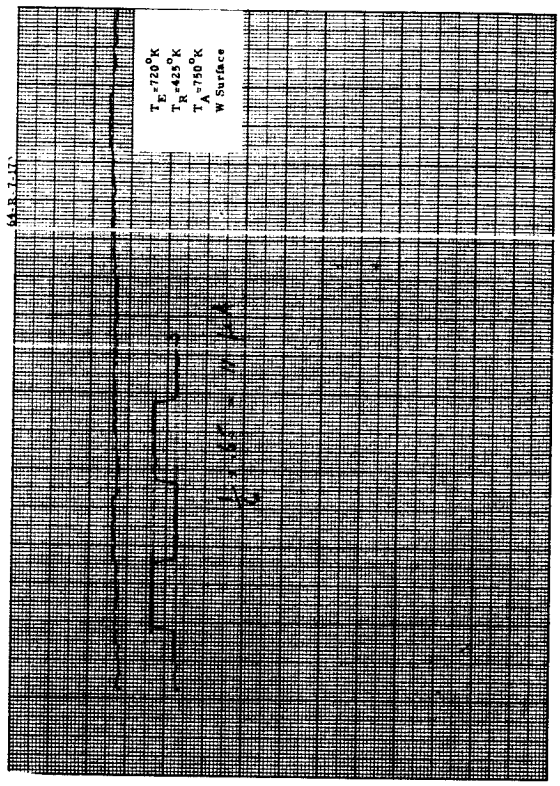

Thermionic Cross Scan #203

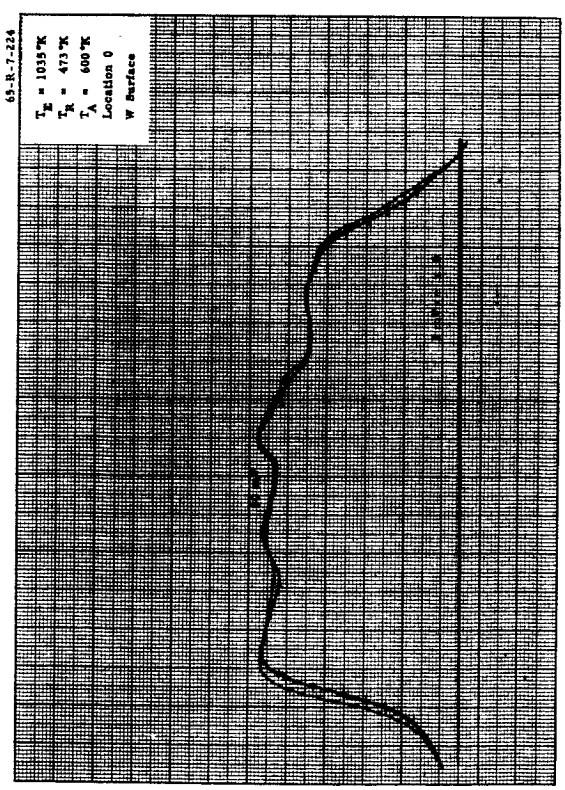

Thermionic Cross Scan #177

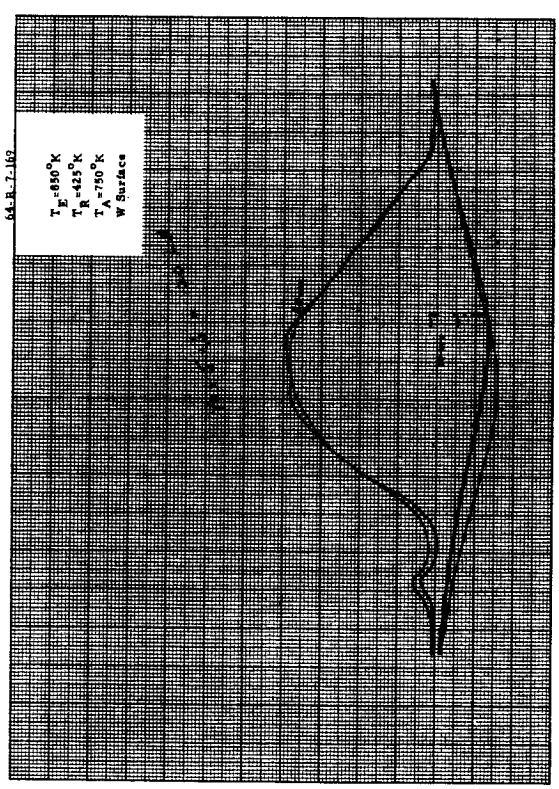

Thermionic Cross Scan #178

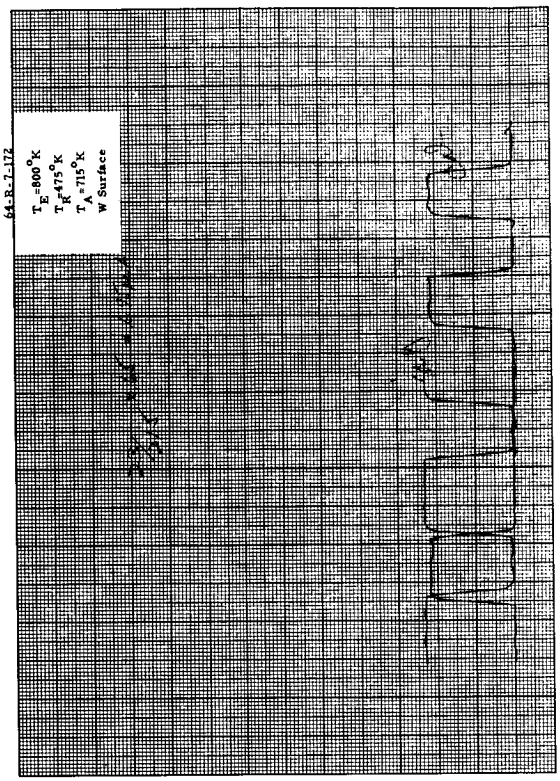

Thermionic Cross Scan #212

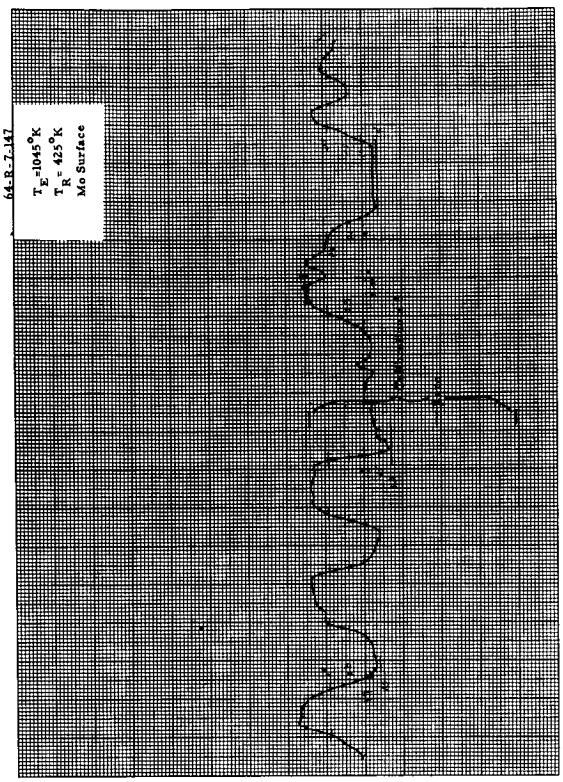

Thermionic Cross Scan #238

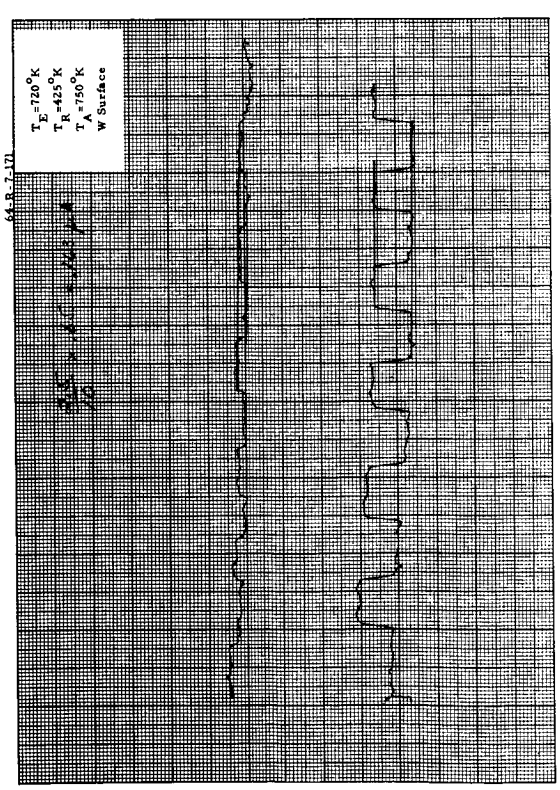

Thermionic Cross Scan #208

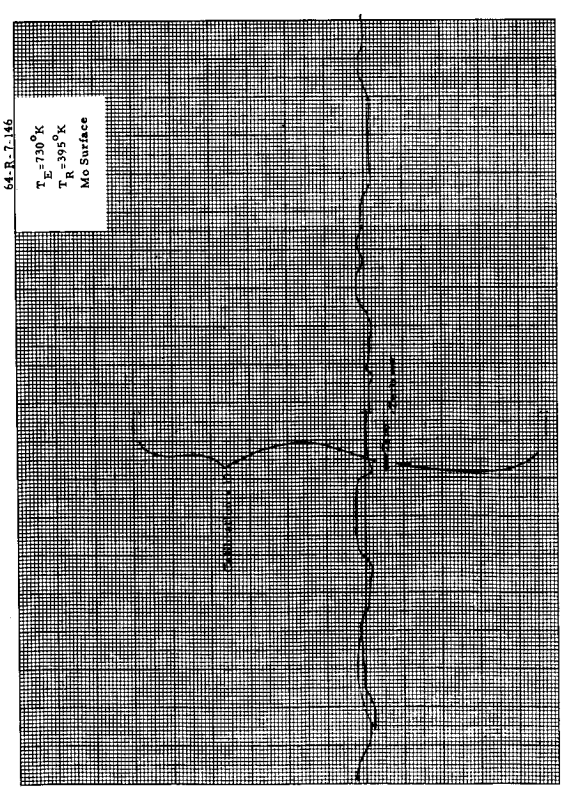

Thermionic Cross Scan #235

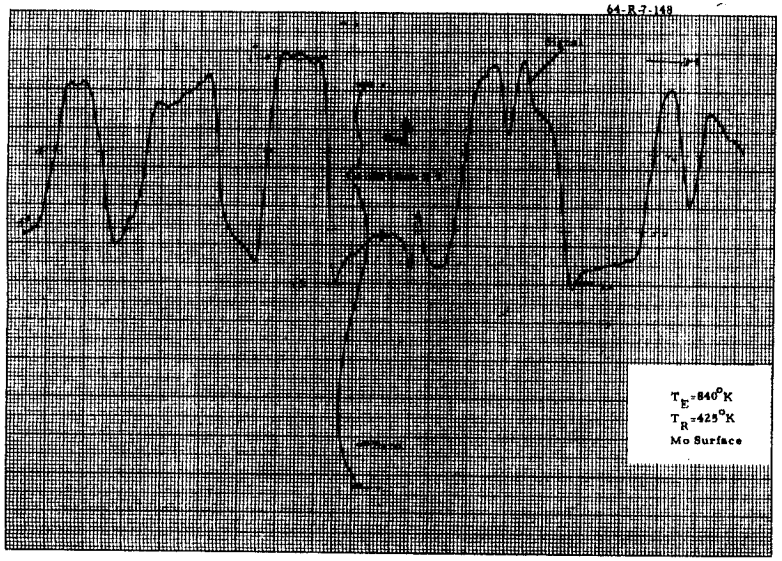

Thermionic Cross Scan #240

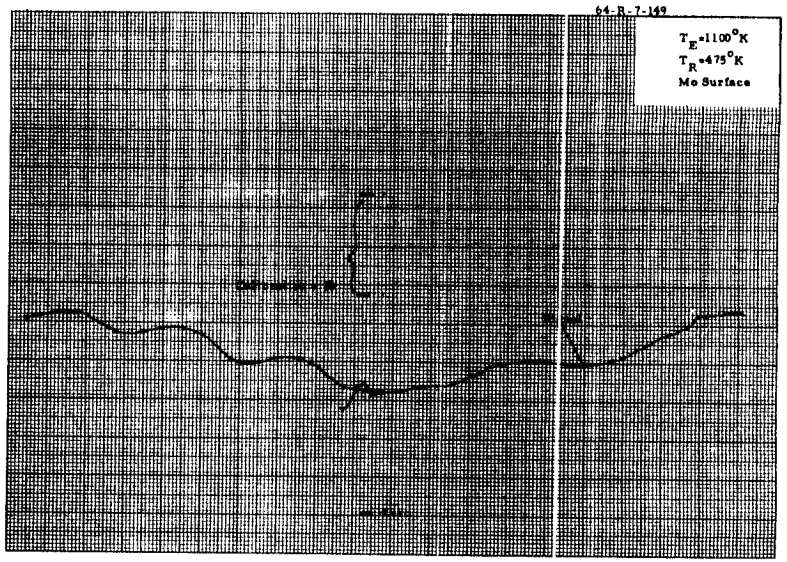

Thermionic Cross Scan #250

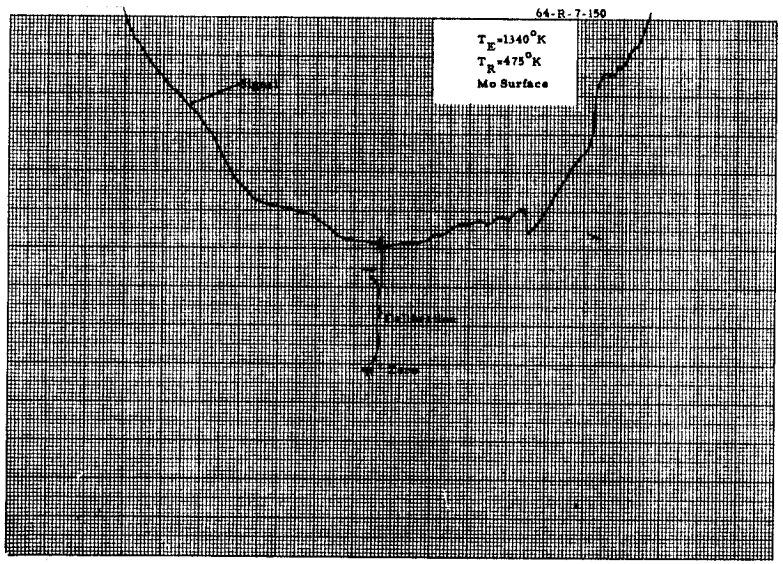

Thermionic Cross Scan #253

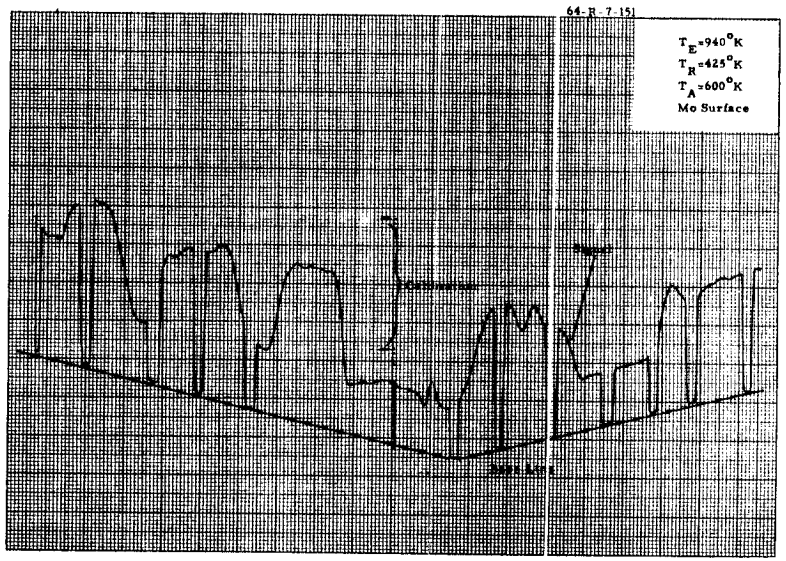

Thermionic Cross Scan #263

Figure B-3

THERMO ELECTRON ENGINEERING CORPORATION

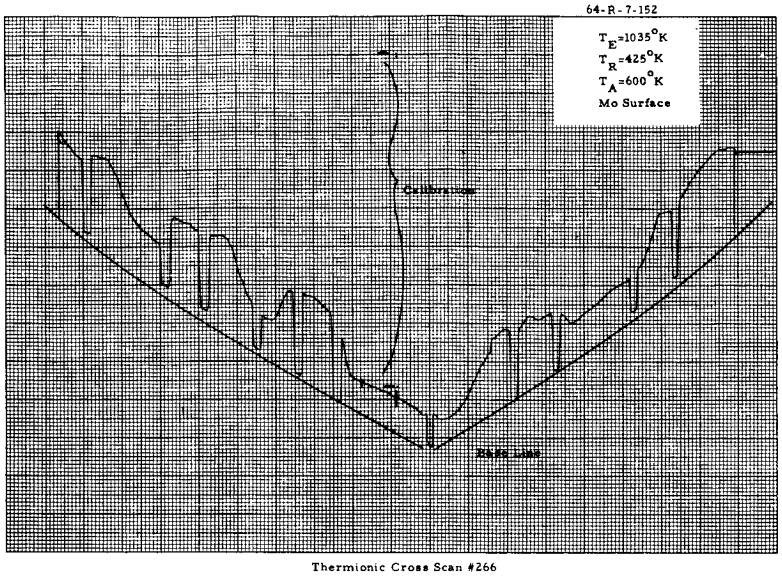

Thermionic Cross Scan #266

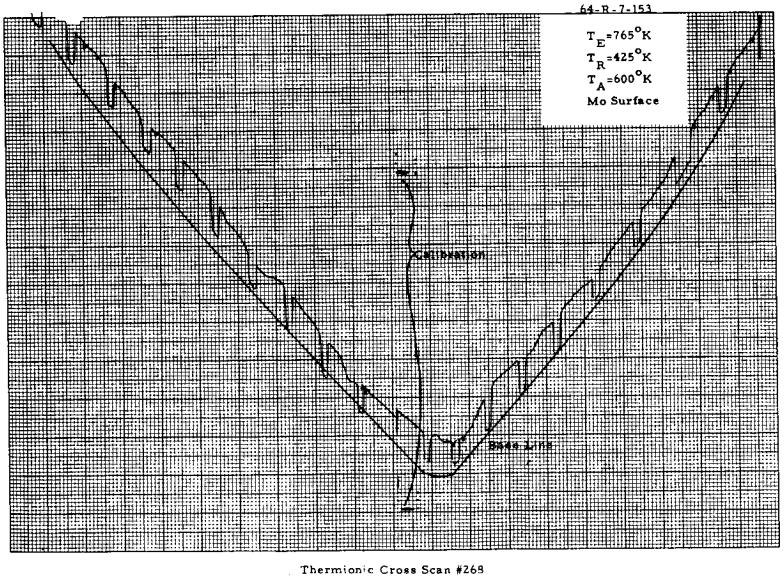

Thermionic Cross Scan #268

Photograph No.

1	Thermionic Scanner, W Surface, $T_S = 995\,°K$, $T_R = 375\,°K$, Cs only, 200A Main Field
2	Thermionic Scanner, W Surface, $T_S = 1000\,°K$, $T_R = 425\,°K$, Cs only, 150A Main Field
3	Thermionic Scanner, W Surface, $T_S = 1100\,°K$, $T_R = 425\,°K$, $T_A = 475\,°K$, 175A Main Field
4	Thermionic Scanner, W Surface, $T_S = 1100\,°K$, $T_R = 425\,°K$, $T_A = 475\,°K$, 175A Main Field
5	Thermionic Scanner, W Surface, $T_S = 1105\,°K$, $T_R = 425\,°K$, $T_A = 475\,°K$. 100A Main Field
6	Thermionic Scanner, W Surface, $T_S = 1255\,°K$, $T_R = 425\,°K$, $T_A = 520\,°K$, 150A Main Field
7	Photoelectric Scanner, Mo Surface
8	Thermionic Scanner, Mo Surface, $T_S = 990\,°K$, $T_R = 440\,°K$, Cs only, 85A Main Field
9	Thermionic Scanner, Mo Surface, $T_S = 990\,°K$, $T_R = 440\,°K$, Cs only, Reversed Magnetic Field
10	Thermionic Scanner, Mo Surface, $T_S = 990\,°K$, $T_R = 440\,°K$, Cs only, 125A Main Field
11	Thermionic Scanner, Mo Surface $T_S = 895\,°K$, $T_R = 390\,°K$, Cs only, 100A Main Field
12	Thermionic Scanner, Mo Surface, $T_S = 970\,°K$, $T_R = 425\,°K$, Cs only, 250A Main Field
13	Thermionic Scanner, Mo Surface, $T_S = 900\,°K$, $T_R = 390\,°K$, CsF, 250A Main Field
14	Thermionic Scanner, Mo Surface, $T_S = 900\,°K$, $T_R = 390\,°K$, CsF, 100A Main Field
15	Thermionic Scanner, Mo Surface, $T_S = 905\,°K$, $T_R = 395\,°K$, CsF, 250A Main Field

Photograph No.	
16	14x Metallograph of Mo Surface
17	14x Metallograph of Mo Surface
18	14x Metallograph of Mo Surface
19	14x Metallograph of Mo Surface
20	14x Metallograph of Portions of W Surface
21	14x Metallograph of Portions of W Surface
22	14x Metallograph of Portions of W Surface
23	14x Metallograph of Portions of W Surface

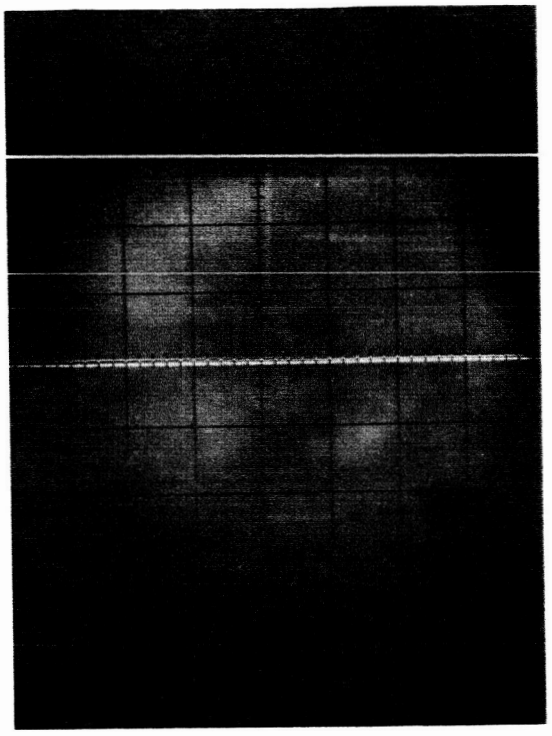

Photograph 1.

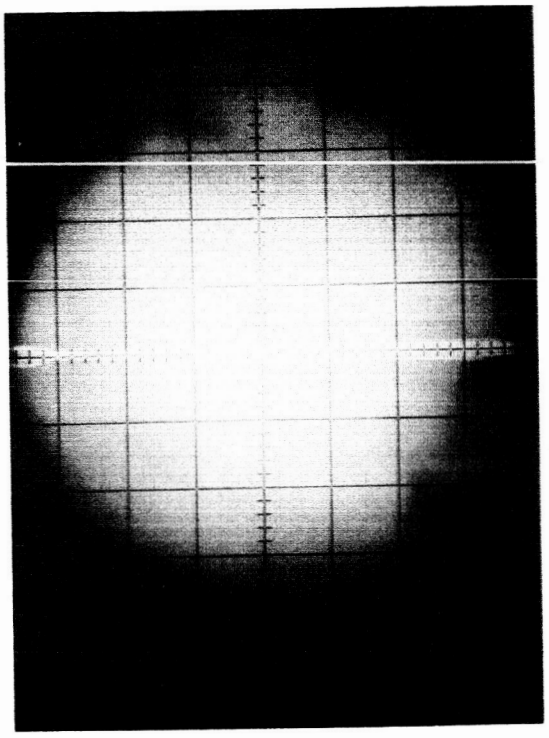

Photograph 2.

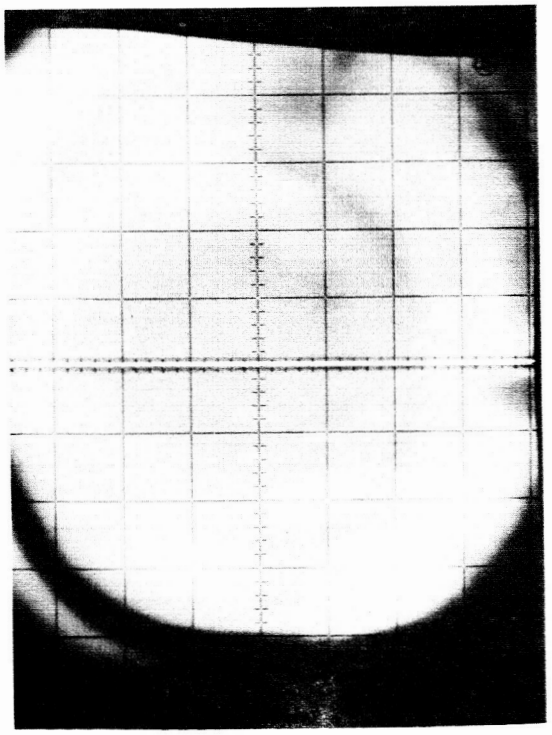

Photograph 3.

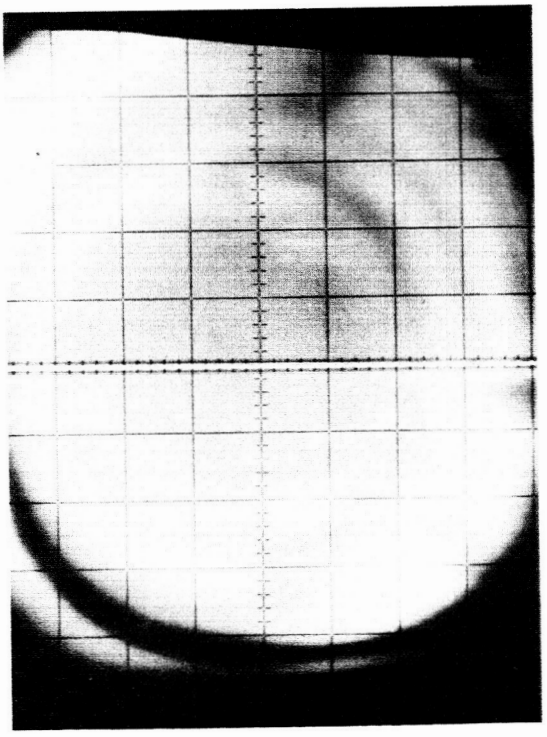

Photograph 4.

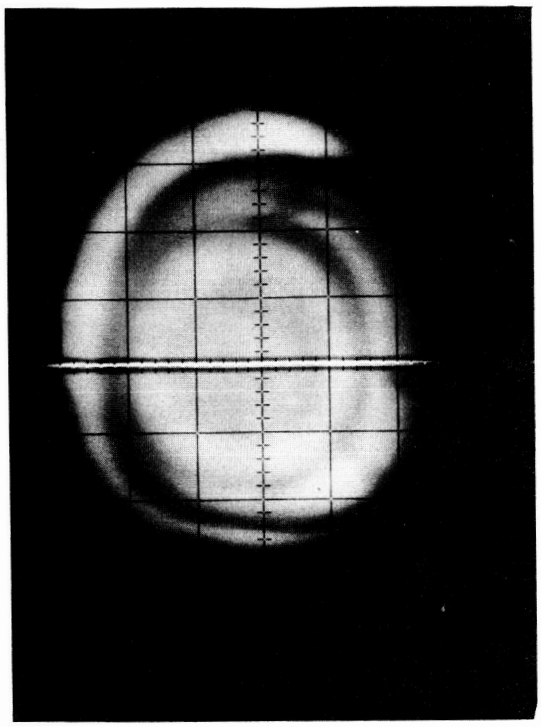

Photograph 5.

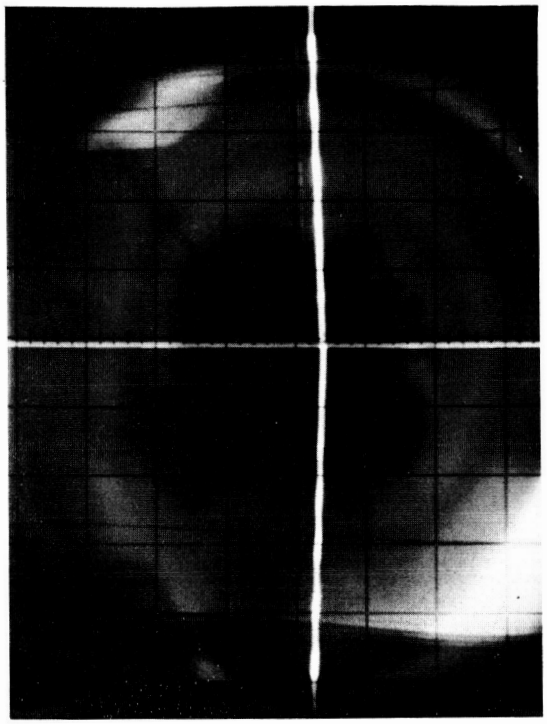

Photograph 6.

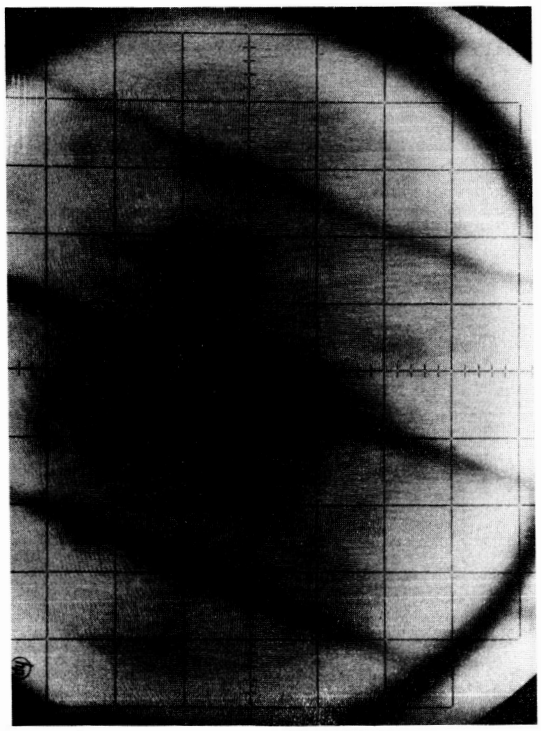

Photograph 7.

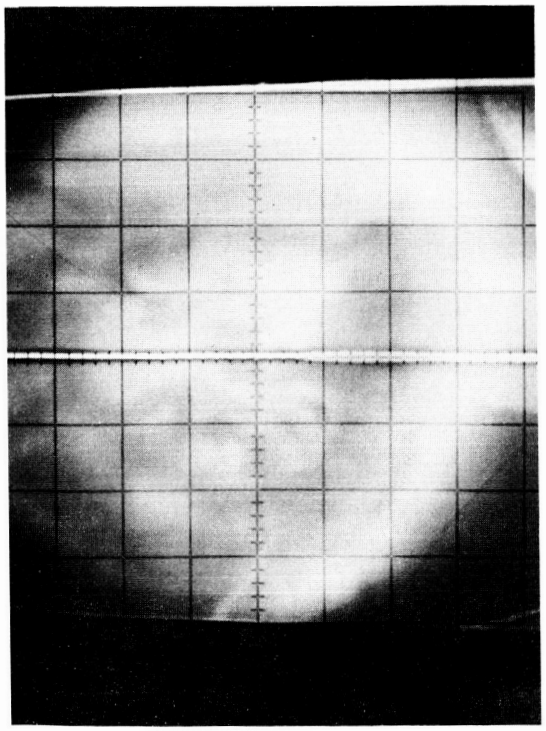

Photograph 8.

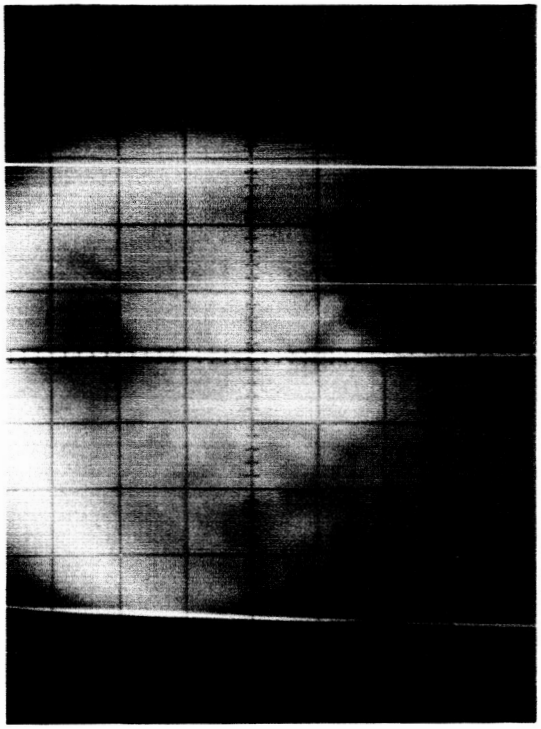

Photograph 9.

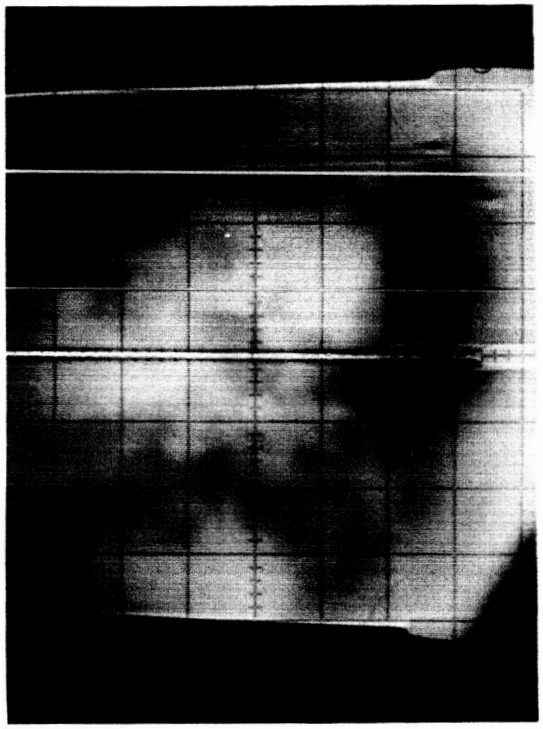

Photograph 10.

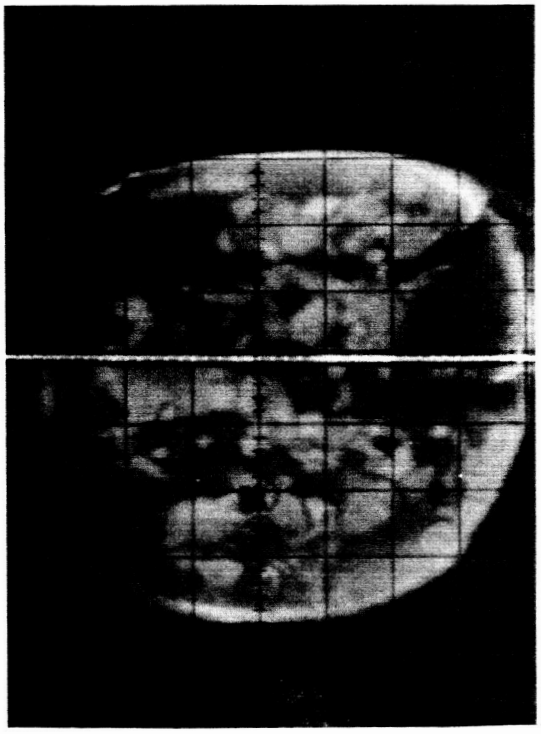

Photograph 11.

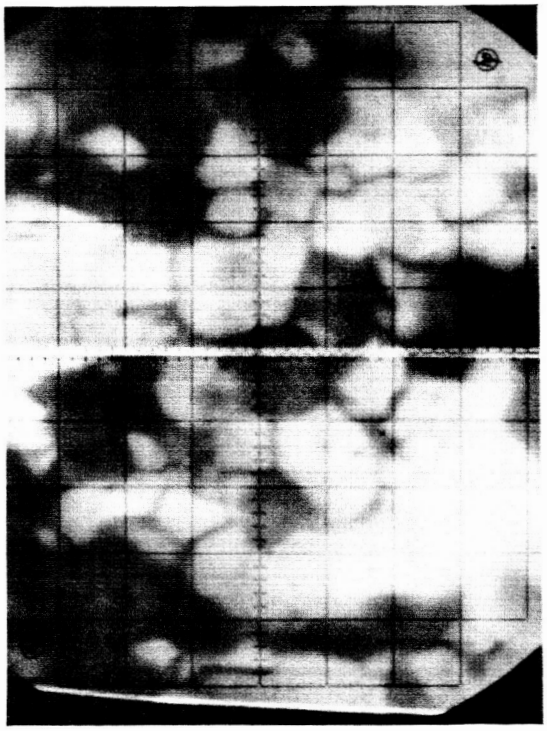

Photograph 12.

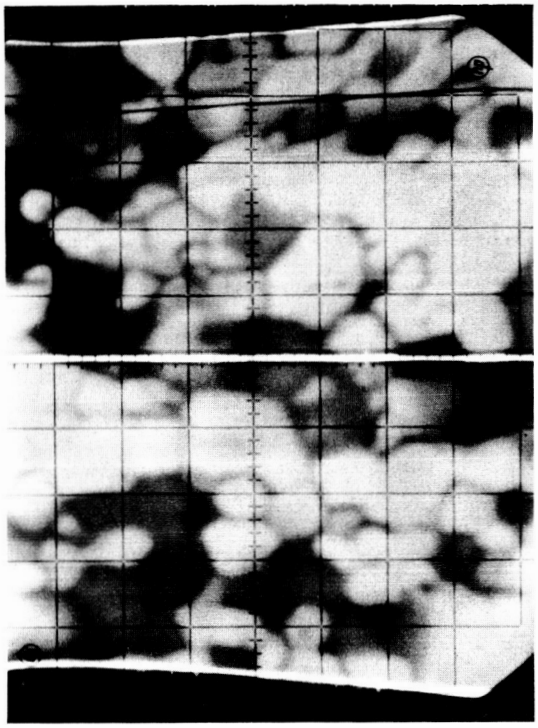

Photograph 13.

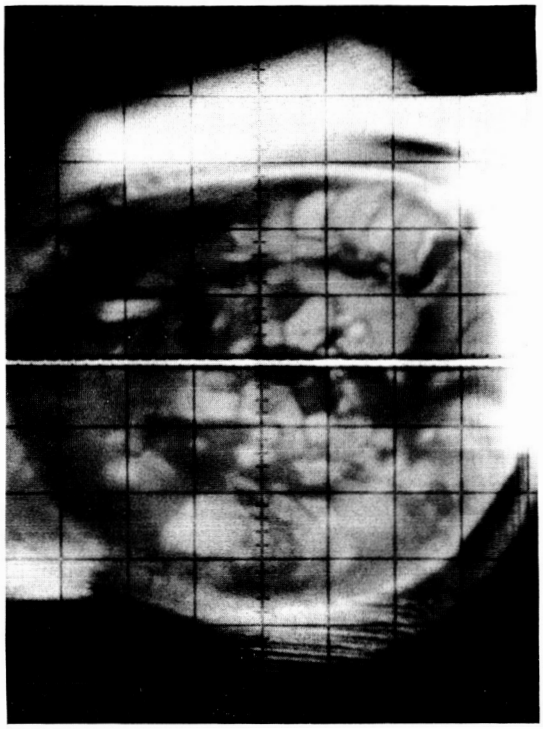

Photograph 14.

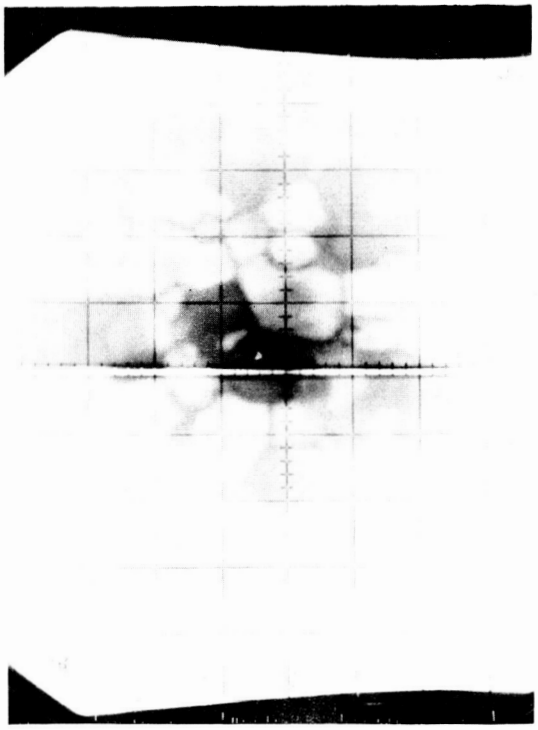

Photograph 15.

Photograph 16.

Photograph 17.

Photograph 18.

Photograph 19.

Photograph 20.

Photograph 21.

Photograph 22.

Photograph 23.

APPENDIX C

WIRING DIAGRAMS FOR SCANNER OPERATION

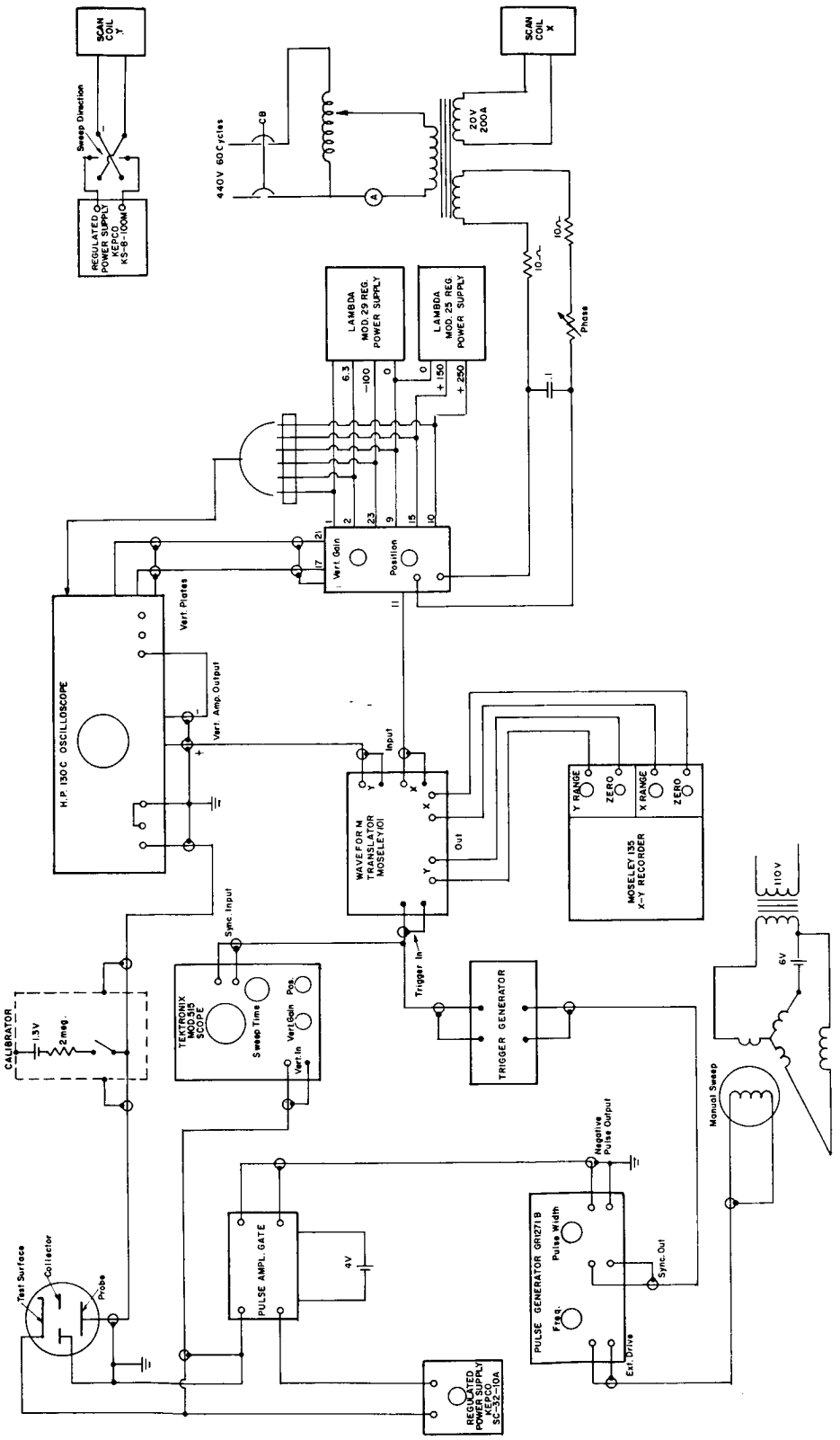

Figure C-1. Circuitry for X-Y Recording of Cross Scans using Thermionic Scanner (Includes Pulse Scanning Instrumentation).

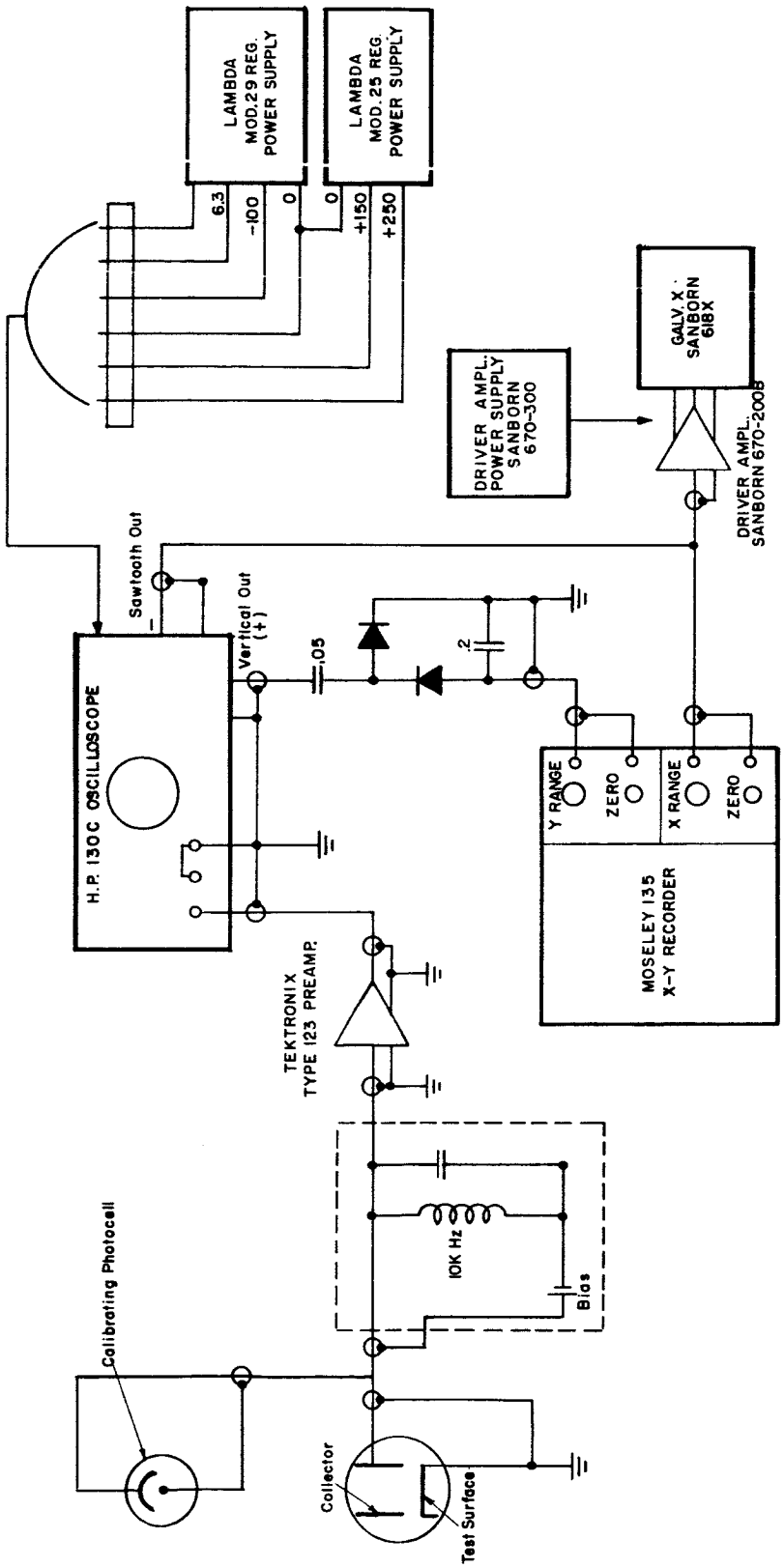

Figure C-2. Circuitry for X-Y Recording of Cross Scans using Photoelectric Scanner

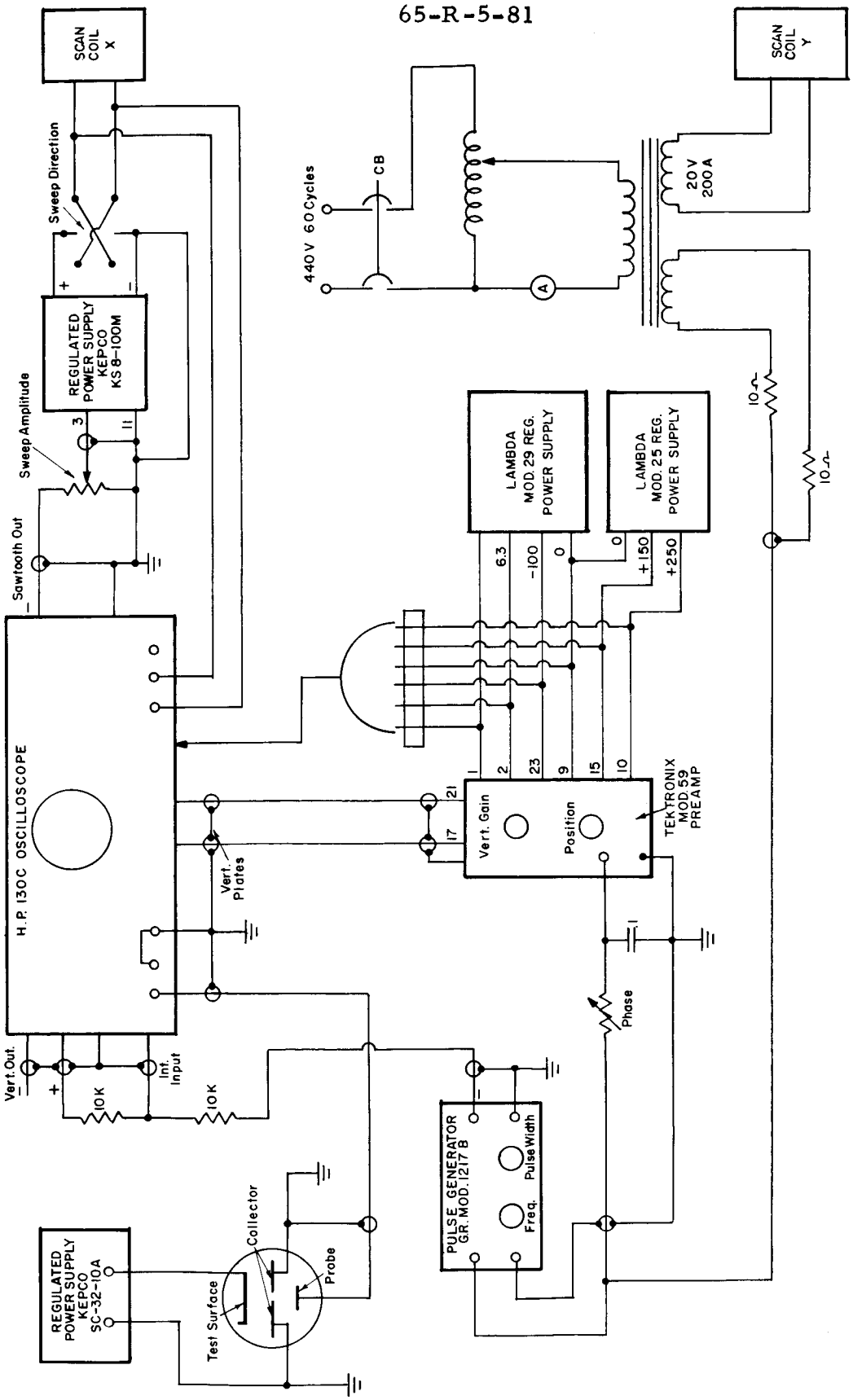

Figure C-3. Circuitry for Sweep Data (Display) using Thermionic Scanner.

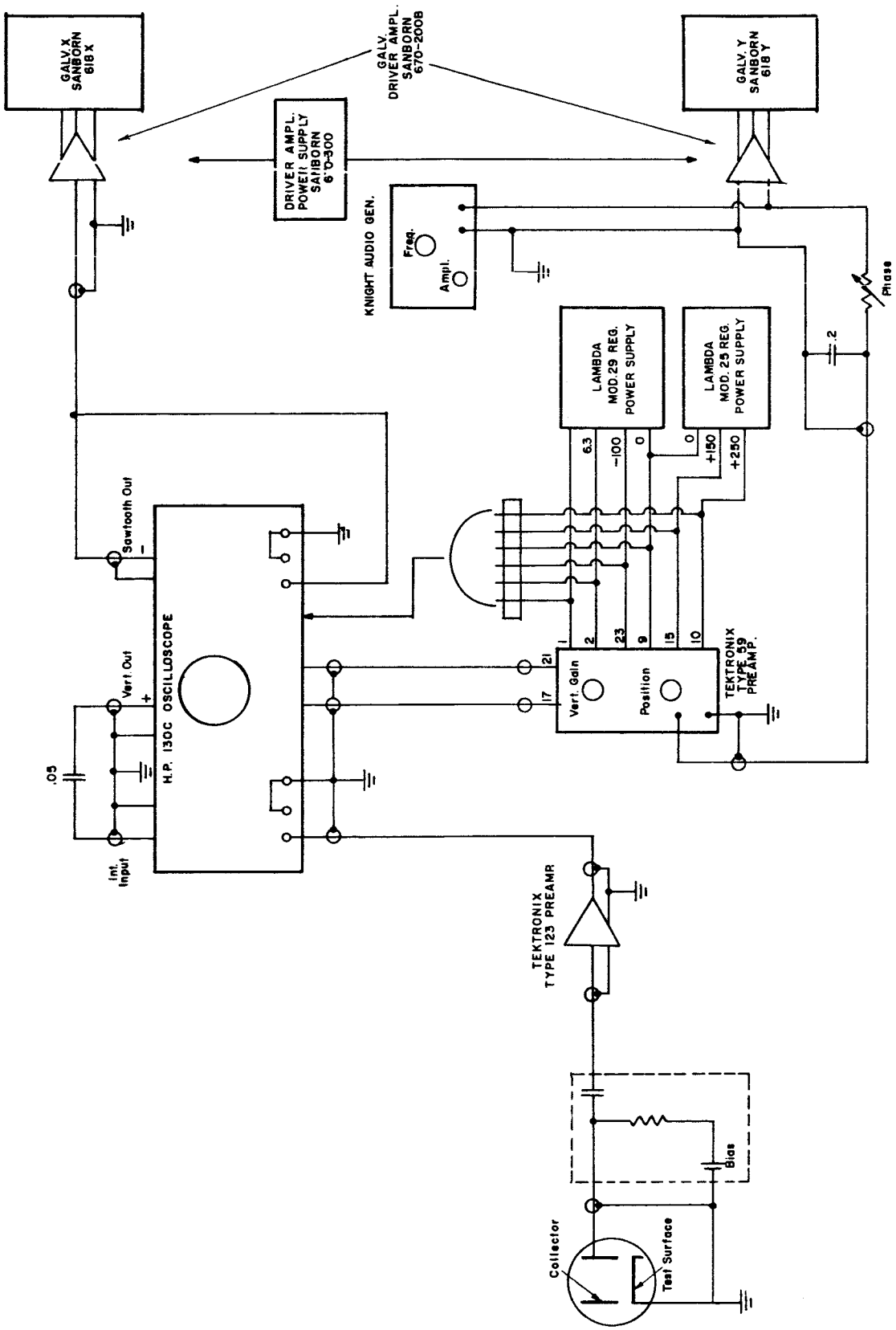

Figure C-4. Circuitry for Sweep Data (Display) using Photoelectric Scanner.